# JOURNAL OF APPLIED PHYSICS

# JOURNAL OF APPLIED PHYSICS

Vol. 21, No. 7 JULY, 1950


## *In This Issue*


Page

**Results of Recent Hypersonic and Unsteady Flow Research at the Langley Aeronautical Laboratory** JOHN V. BECKER 619

*Contributed Original Research*

**Modulation Conversion in a Wave Guide** PAUL S. ROGELL 629

**Measurement of Self-Diffusion of Silver without Radioactive Tracers** G. C. KUCZYNSKI 632

**Graphical Analysis of the Interference Patterns of an Elevated Ultra-High Frequency Antenna under Conditions of Atmospheric Stratification** F. R. ABBOTT AND C. J. FISHER 636

**Determination of the Impulsive Response of Variable Networks** LOTFI A. ZADEH 642

**Extension of Wiener's Theory of Prediction** LOTFI A. ZADEH AND JOHN R. RAGAZZINI 645

**Potential Flow into Circumferential Openings in Drain Tubes** DON KIRKHAM 655

**Determination of Modified Index-of-Refraction over the Gulf of Mexico from Radio Data** A. W. STRAITON AND A. H. LAGRONE 661

**Effective Permeability of an Array of Thin Conducting Disks** GERALD ESTRIN 667

**Stress Analysis for Compressible Viscoelastic Materials** W. T. READ, JR. 671

**Electrolytic-Tank Measurements for Microwave Metallic Delay-Lens Media** SEYMOUR B. COHN 674

**Role of Cathode Temperature in the Glow Discharge** HAROLD JACOBS AND JACK MARTIN 681

**Emission of Radiation from Diatomic Gases. I. Approximate Calculations** S. S. PENNER 685

**X-Ray Measurement of Long Range Order in β-Brass** D. CHIPMAN AND B. E. WARREN 696

**Resolving Power of an X-Ray Microscope** EDWARD PRINCE 698

**Metallic Evaporation and the Diameter of Tobacco Mosaic Virus with the Electron Microscope** H. KAHLER AND B. J. LLOYD, JR. 699

**Apparent Size of Objects as Observed in the Electron Microscope** STANLEY F. KERN AND RAYMOND A. KERN 705

**Current-Hysteresis of the Electrolytic Aluminum-Oxide Rectifier** A. J. DEKKER AND HELEN M. A. URQUHART 708

**Scheme for Analyzing Capillary Measurements on Non-Newtonian Liquids** ORRIN H. CLARK AND M. L. DEUTSCH 713

**Interpretation of Fracture Markings** J. A. KIES, A. M. SULLIVAN, AND G. R. IRWIN 716

**Letters to the Editor:**

**Absolute Measurement of Copper-Copper Interfacial Free Energy** G. W. SEARS 721

**Limiting Negative Pressure of Water** LYMAN J. BRIGGS 721

**Effective Permeability of Iron Dust Particles** LEONARD LEWIN 722

**Magnetically Controlled Wave-Guide Attenuators** THEODORE MILLER 722

**Note on the Error Coefficients of a Servo Mechanism** JOHN L. BOWER 723

**Erratum: Radiofrequency Mass Spectrometer** WILLARD H. BENNETT 723

**Use of Critical Point Phenomena in Preparing Specimens for the Electron Microscope** THOMAS F. ANDERSON 724

**International Congress on Electron Microscopy at Paris, September 14–22, 1950** 724

**Index to Advertisers** xxii



**BOARD OF EDITORS**

ELMER HUTCHISSON, *Editor*

*Associate Editors*

HOWARD H. AIKEN
OTTO BEECK
JAMES HILLIER
W. JAMES LYONS
PHILIP MORRISON
ERIC REISSNER
RAYMOND J. SEEGER
FREDERICK SEITZ
CHARLES S. SMITH

**Publication of the**

**American Institute of Physics**

**OFFICERS**

GEORGE R. HARRISON, *Chairman*
GEORGE B. PEGRAM, *Treasurer*

**GOVERNING BOARD**

J. W. BEAMS
C. PAUL BONER
WALLACE R. BRODE
W. F. FAIR, JR.
J. B. FISK
G. P. HARNWELL
GEORGE R. HARRISON
W. V. HOUSTON
RUDOLPH KINGSLAKE
PAUL KIRKPATRICK
PAUL E. KLOPSTEG
F. W. LOOMIS
PHILIP M. MORSE
J. R. OPPENHEIMER
GEORGE B. PEGRAM
HAROLD K. SCHILLING
FRANCIS G. SLACK
JOHN C. STEINBERG

**Consultant on Printing**

MELVIN LOOS

**ADMINISTRATIVE STAFF**

HENRY A. BARTON, *Director*
WALLACE WATERFALL, *Executive Secretary*
THEODORE VORBURGER, *Assistant Treasurer and Comptroller*
RUTH F. BRYANS, *Publication Manager*
BETTY HOFSTADTER, *Assistant Secretary*
EILEEN B. NEUBERGER, *Circulation Manager*



The JOURNAL OF APPLIED PHYSICS, published monthly at Prince and Lemon Sts., Lancaster, Pa., is devoted to physics in its role as the science basic to other natural sciences and to the arts and industries. Previous to 1937 this publication was known as PHYSICS. The JOURNAL OF APPLIED PHYSICS publishes editorials and reviews, as well as technical papers of applied physics. Articles appearing in it are indexed regularly, according to their field, by Physics Abstracts, Chemical Abstracts, Engineering Index, Inc., Industrial Arts Index, etc.

**Manuscripts** should be submitted to Elmer Hutchisson, Editor, Case Institute of Technology, Cleveland 6, Ohio. Unless otherwise stated, submission of a manuscript is a representation that it has been neither copyrighted, published, nor submitted for publication elsewhere. The authors' institutions are requested to pay a **publication charge** of $8 per page which, if honored, entitles them to 100 reprints without further charge. Instructions will be sent with galley proofs.

**Subscriptions,** renewals, and orders for back numbers should be addressed to the American Institute of Physics, 57 East 55 Street, New York 22, New York.

| **Subscription Price** | U.S. and Canada | Elsewhere |
|---|---|---|
| To members and associate members of the American Institute of Physics | $7.00 | $ 8.00 |
| To all others | 9.00 | 10.00 |

**Back Number Prices**

Yearly back number rate when complete year is available: **$10.00.** Single copies: $1.00 each.

**Changes of address** should be sent to the American Institute of Physics; **corrected proofs** should be sent to the Publication Manager, American Institute of Physics. **Advertising rates** supplied on request. Orders, advertising copy, and cuts should be sent to the American Institute of Physics.

Entered as second class matter January 22, 1937, at the Post Office at Lancaster, Pennsylvania, under the Act of March 3, 1879. Accepted for mailing at the special rate of postage provided for in paragraph (d-2), section 34.40, P. L. & R. of 1948, authorized May 2, 1932.

Journal
of
Applied Physics

Volume 21, Number 7 July, 1950

# Results of Recent Hypersonic and Unsteady Flow Research at the Langley Aeronautical Laboratory

JOHN V. BECKER

*Chief of Compressibility Research Division, Langley Aeronautical Laboratory, National Advisory Committee for Aeronautics, Langley Air Force Base, Virginia*

## INTRODUCTION

THE extremely high speeds and altitudes now contemplated in supersonic aircraft design involve many new compressible flow problems which, only a few years ago, were either unrecognized or of purely academic interest. This situation has naturally resulted in a greatly increased concentration of effort in basic compressible flow research at establishments such as the NACA. The purpose of this paper is to review briefly some recent results obtained at Langley in projects of this character dealing with hypersonic and unsteady flows. Similar exploratory work in small-scale facilities is in progress at the Ames and Lewis Laboratories of the NACA.

## THE 11-INCH HYPERSONIC TUNNEL

The eventual need for a wind tunnel capable of speeds in the range of 5 to 10 times the speed of sound was envisioned in 1945, and we undertook the development of a pilot model of such a facility at that time. The pressure ratios and other important design factors for hypersonic tunnels were then unknown, and this uncertainty pointed towards a blowdown type of tunnel sufficiently flexible in design to permit easy modification. A schematic drawing of the facility is shown in Fig. 1. The combination of a 50-atmosphere supply tank and a vacuum receiving tank affords a starting pressure ratio of several thousand. It was recognized that large reductions in the operating pressure ratio might be achieved through the use of a variable second throat provided that adverse flow separation effects did not occur. Provision was therefore made in the design for quickly reducing the second throat area after starting of the flow.

Two nozzles were designed by the characteristics method for $M=7.0$; one was a conventional single-step type as indicated on Fig. 1, and the second was a two-step design which expanded first in the vertical plane to a Mach number of about 4.5 and then in the horizontal plane to $M=7.0$. The test sections in each case are 10.55 in. deep by 10 in. wide. The single-step nozzle was found to produce acceptably uniform flow at the test section and a mean Mach number of 6.9 as determined from static and total-pressure measurements in the stream. Difficulty was encountered in the two-step nozzle caused by non-uniform boundary layers at the entrance to the second step.

During the preliminary design studies, it became obvious that the temperature in the test section would drop to the liquefying temperature of air at a Mach number of about 4.5 if the air in the settling chamber were maintained at room temperature. For higher speeds, the air temperature would fall far below the liquefying temperature, even if large degrees of supersaturation were assumed. Experience with water-vapor condensation suggested that considerable supersaturation might exist in air. However, the uncertainty as to what would actually happen in air led us to incorporate a heater which can maintain stagnation air temperature up to 1300°F abs. The possibility of air liquefaction can thus be eliminated in our tunnel for Mach numbers up to approximately 8.0. Incorporation of the heater has the obvious additional advantage of making possible studies of temperature effects not only in connection with the condensation phenomena, but also in heat transfer research in this tunnel. As an incidental advantage, the heater also appreciably lengthens the test runs. A water-cooled heat exchanger installed ahead

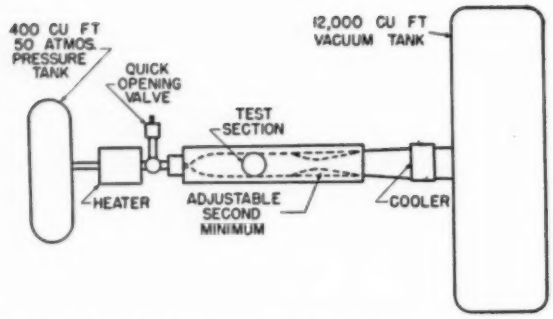


FIG. 1. Schematic drawing of NACA 11-in. hypersonic tunnel.

of the vacuum tank has a similar beneficial effect on the running time. Runs of about 25 sec. duration are obtained without the use of the adjustable second throat. With the second throat immediately adjusted to a reduced area after starting, runs of 60 to 90 sec. are obtained, the time varying with model support configuration.

The tunnel functioned satisfactorily during its first runs on November 26, 1947.

## AIR CONDENSATION EXPERIMENTS

Pressure-distribution data have been obtained along the parallel sidewalls of the nozzles of the 11-in. hypersonic tunnel for stagnation temperatures ranging from high values for which condensation is impossible to low values for which the components of air must either be highly supersaturated or condensed. It was found that even for the lowest stagnation temperatures the longitudinal pressure distributions were smooth; no condensation shock was apparent. In this respect, our data agree with results obtained in the 5-in. hypersonic tunnel at California Institute of Technology and in the 2.5-in. $M=4.5$ tunnel at Princeton. Had it been impossible for us to vary temperature, the lack of any apparent condensation shock probably would have led us to the conclusion that no condensation was occuring. Further analysis of the pressure data, however, reveals that, while no discontinuities occurred along the nozzles, there was a significant change in the pressure at all stations along the nozzle when the temperature was allowed to fall below saturation values. Figure 2 shows this effect for various stations along the two nozzles. The left diagram of Fig. 2 shows the results for three stations in the forward part of the nozzle at which the Mach numbers at high temperatures were 5.47, 5.75, and 6.09. The right diagram shows the results for the test-section stations of the two nozzles investigated where the Mach numbers as determined from wall static pressures were 6.56 and 6.76. The pressure ratio at any of these stations was not much affected by decreasing the temperature until the saturation region was reached. Here a marked increase in pressure (decrease in Mach number) was noted. In the entire first step of the two-step nozzle in which the temperature never fell below saturation values, there were no appreciable pressure variations with temperature. These results seem to indicate that condensation, if it is actually present, is a gradual process occurring along the entire region of the nozzle where the temperatures are appreciably below the saturation value. The possibility that these pressure ratio changes are due to viscous or heat transfer effects rather than condensation has not yet been eliminated. However, tests made over a range of stagnation pressures at temperatures above the saturation level indicated no appreciable Reynolds number effects. Instead of the indicated decrease in Mach number with decreasing $T_0$ in the saturation region (Fig. 2), the effect of the corresponding Reynolds number increase produced a small increase in Mach number.

In recent years, the nucleation theory developed by Volmer,[1] which successfully predicts the condensation of water vapor, has been used by several investigators,[2-4] for example, to estimate the degree of supersaturation of oxygen that might be expected. These calculations, when applied to our conditions, predict high degrees of supersaturation terminated by a condensation shock. An assumption common to all of the theoretical work is that no foreign particles are present which might act as condensation nuclei and thus reduce the probability of high degree supersaturation. In our air stream, there are three possibilities: carbon dioxide crystals, water crystals, and oxide dust from the heater. Water is present only to the extent of about two parts in a million, and thus probably can be neglected. It is also doubtful whether enough oxide particles are present

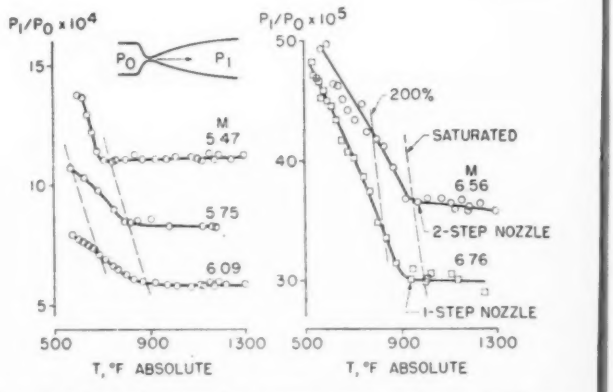


FIG. 2. Effect of stagnation temperature on the static pressure at each of several stations along the nozzle. (The stations are designated in terms of the roughly constant Mach number existing at each station for temperatures above saturation.)

[1] M. Volmer, *Kinetik der Phasenbildung* (Theodor Steinkopff Verlag, Dresden, 1939).

[2] A. E. Puckett and R. Schamburg, "Hypersonic wind-tunnel progress," Report No. 5 (U. S. Army Contract W-04-200 Ord-1963), Guggenheim Aero. Lab., California Institute of Technology, August 8, 1946.

[3] P. Wegener, "On the experimental investigation of hypersonic flow," U. S. Naval Ordnance Lab. Memo. No. 9629, July 29, 1948.

[4] S. M. Bogdonoff and L. Lees, "Study of the condensation of the components of air in supersonic wind tunnels. Part I—Absence of condensation and tentative explanation," Princeton University Aero. Engineering Laboratory Report No. 146, May 25, 1949.

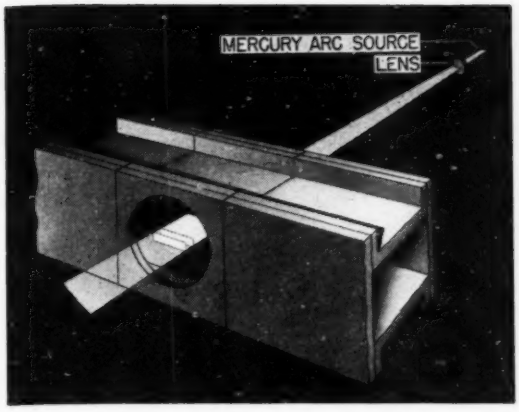


FIG. 3. Set-up of light-scattering experiment.

to be significant. If the carbon dioxide solidifies without becoming highly supersaturated, a significant number of solid particles would form in the flow at temperatures somewhat below those corresponding to the saturation of oxygen. Under these circumstances, the theoretical predictions of high supersaturation and condensation shock would have to be modified.

A simple optical experiment has been made which is of interest in connection with the condensation question. Figure 3 shows the experimental setup. An approximately parallel beam of light is passed through the test-section windows with the test chamber darkened. For the no-flow condition, all that can be seen are the reflections where the beam passes through the windows. When the stagnation temperature is at its usual elevated value, 1160°F abs., there is no evidence of any particles in the flow, the oxide particles apparently not being numerous enough to show up (Fig. 4). When the flow is not heated, however, strong scattering of the light beam occurs suggesting the presence of a large number of small liquid or solid particles. Near the walls in the high temperature region of the boundary layer, the light scattering disappears entirely. It is conceivable, of course, that this phenomenon is caused by $CO_2$ particles rather than by liquid oxygen or nitrogen particles. The possibility has also been advanced that the scattering is caused by liquid oxygen particles of subcritical size, as considered in the Volmer theory. Another conceivable explanation is that photo-nucleation is occurring. This test, therefore, does not provide completely conclusive evidence of condensation of the components of air.

Additional experimental work on the condensation problem is planned but there is a limit to what can be accomplished in the tunnel. It appears to us that cloud chamber techniques can be used to advantage in the study of this problem. Another possibility suggested by Donaldson at Langley is to utilize the sudden expansion in a suitably designed shock tube to simulate the rapid changes in temperature and pressure of a supersonic nozzle. The experimental information obviously needed includes degrees of supersaturation, condensation time factors, and the effects of gas mixtures and foreign nuclei on the condensation phenomena.

## FLOW VISUALIZATION AT LOW PRESSURES

Our experience with the 11-in. tunnel indicates that the limit of usefulness of the schlieren method of flow visualization is reached at a pressure of about 1 mm of mercury for slender test models at $M=7.0$. To obtain significant results at these conditions, we use a sensitive system in which the light is passed through the test section twice. A single 10-in. mirror is used located close to one side of the tunnel and ground to the rela-

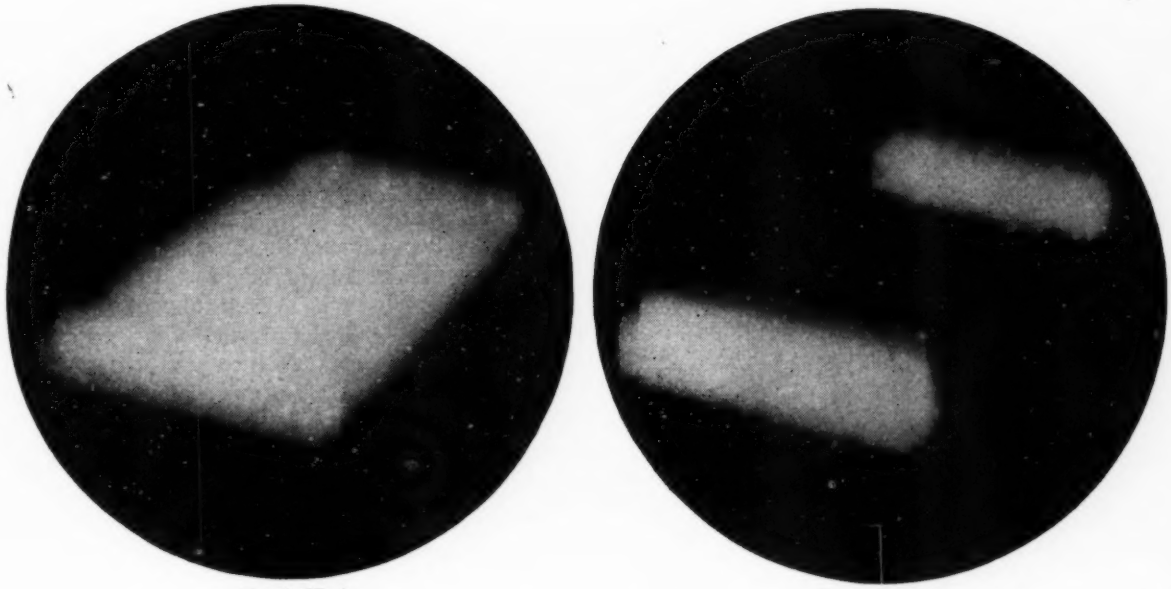

$T_0=540°F$ abs. $T_0=1160°F$ abs.

FIG. 4. Photograph of light beam passing through test section taken from same viewpoint as Fig. 3.

tively long radius of curvature of 20 feet. In terms of Mach number, the estimated limiting value for this schlieren system is about $M=10$ for a 50-atmosphere stagnation pressure. For higher hypersonic tunnel speeds, and also for low density aerodynamic research at all speeds, other methods of flow visualization are needed.

We were fortunate to have Dr. Joseph Kaplan as a consultant on this problem during the summer of 1948. He suggested use of the little-understood phenomenon of the afterglow that persists in nitrogen which has been excited by an electrical discharge as a means of flow visualization. Acting on this suggestion, Williams and Benson set up a low pressure supersonic nozzle in which the afterglow principle was applied successfully for the first time[5] in August 1948. The apparatus used is shown on Fig. 5. Nitrogen is ducted through the exciting discharge tube, through a grounded screen which greatly reduces the number of ions present but affects the afterglow only slightly, and thence into the supersonic nozzle. The brightness of the glow can be increased by increasing the energy of the exciter, either by the addition of more arcs or by increasing the power. It is interesting to note that the grounded screen has little effect on the brightness. Figure 6 shows the nozzle flow for three pressure ratios less than that required for starting, which was about 20 to 1. The uniform brightness of the afterglow after starting and the patterns about a 15° double-wedge model are illustrated in Fig. 7. The high pressure region behind the shock has greater brightness than the main stream. Separation occurs at the point of maximum thickness of the wedge-shaped model at the low static pressure of this test, 3 mm of mercury.

The nitrogen afterglow appears to be usable at static pressures as low as 100 microns and perhaps lower. We have also successfully used other gases including dry air, oxygen, and argon, although their afterglows are not as bright as that of nitrogen. A small amount of iodine vapor appreciably increased the brightness of nitrogen afterglow. It is probable that other combinations can be found having more intense afterglows.

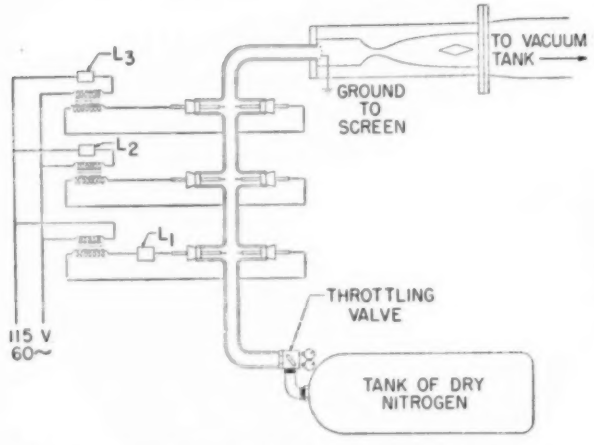


FIG. 5. Apparatus used for generating nitrogen afterglow in a supersonic nozzle.

[5] T. W. Williams and J. M. Benson, Preliminary Investigation of the Use of Afterglow for Visualizing Low-Density Compressible Flows, NACA RM I9A24a, February 15, 1949.

The question arises as to whether the presence of the glow has any aerodynamic effects on the flow. Studies made by Rayleigh[6] indicated that the decay of the glow was accompanied by a high rate of heat release, a phenomenon which would be expected to produce important aerodynamic effects in a supersonic nozzle. This possibility has recently been investigated by Benson at Langley. He finds that in our application for which the glow has a life of about one sec., the temperature rise is of the order of 30° to 90°C. This corresponds to a temperature rise of only a small fraction of a degree during the transit of the gas through a supersonic nozzle. Thus the aerodynamic effect is expected to be negligible. Benson also finds no appreciable change in viscosity due to the presence of the glow. Schlieren and afterglow photographs obtained for static pressures of 6 to 9 mm of mercury correlate satisfactorily. In summary, the afterglow technique at its present stage of development appears to be a reliable and convenient method of flow visualization for low pressure aerodynamic research.

## BOUNDARY-LAYER EFFECTS AT HYPERSONIC SPEEDS

It is well known that the effect of the boundary layer on the pressure distribution about aerodynamic bodies at both subsonic and supersonic speeds is restricted to the rear or trailing portion of the body. In this region, adverse pressure gradients occur which cause the boundary layer to thicken greatly or to separate from the surface, with associated large effects on the surface pressures. Over the forward part of the body, the boundary layer for Reynolds numbers in the practical range is too thin to have a measurable effect on the pressures. This fact is well established for the entire speed range for which pertinent data are available in aeronautical literature.

The change from low supersonic to hypersonic speeds involves a many-fold increase in boundary-layer thickness for a given value of the Reynolds number. Recent calculations and tests in the 11-in. hypersonic tunnel at $M=6.9$ have brought to light the fact that the thickness becomes so great as to cause a large distortion of the pressure diagram over the forward portion of airfoils. The usual separation effects over the rearward portion are also present.

Figure 8 shows the calculated growth of the laminar boundary layer on a flat plate as a function of Mach number. The calculations are based on the usual compressible-flow boundary-layer assumptions with the added assumption of a linear velocity profile. The latter

[6] S. K. Mitra, *Active Nitrogen—A New Theory* (Indian Press, Ltd., Calcutta, 1945).

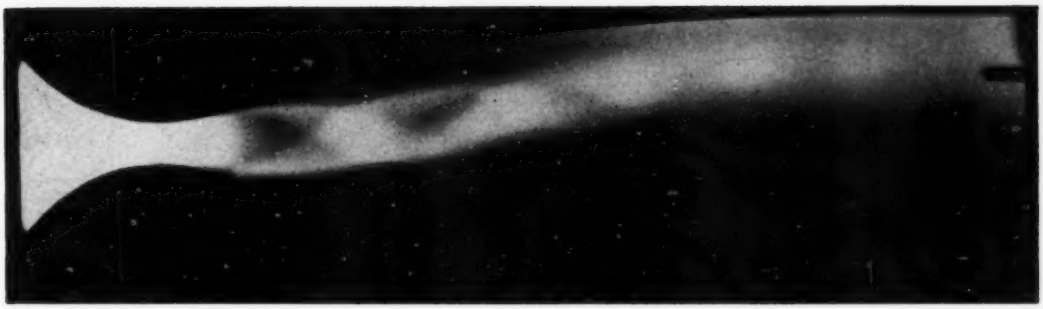

(A) Pressure ratio approximately 9 to 1

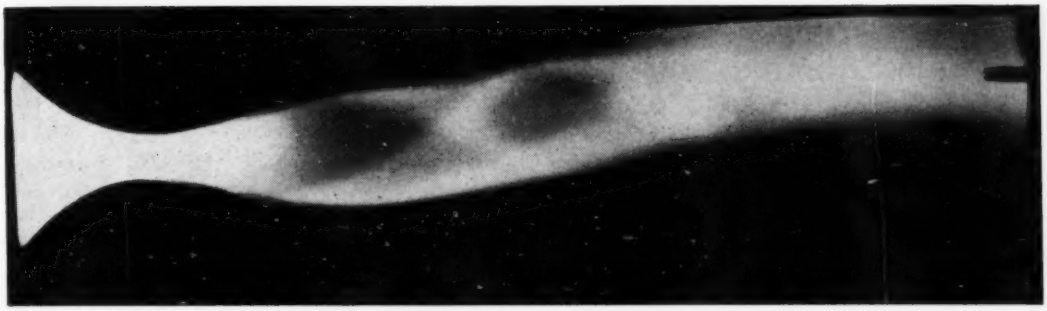

(B) Pressure ratio approximately 10 to 1

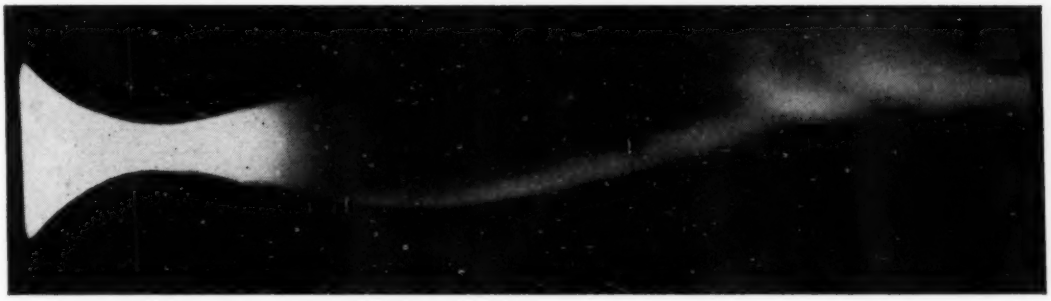

(C) Pressure ratio approximately 11 to 1

FIG. 6. Nozzle flow patterns obtained with nitrogen afterglow at pressure ratios below that required for starting.

assumption is justified on the grounds that over the forward part of a flat plate at our test Reynolds number the boundary layer is known to be laminar and that theoretical considerations[7,8] reveal that the profile is expected to be nearly linear at hypersonic speeds. (See upper diagram on Fig. 8.) Furthermore, the calculated chordwise growth of the displacement thickness is insensitive to the profile shape chosen. Figure 8 shows that the displacement thickness at $M=7$ is about 10 times that at $M=1.0$ for a constant value of $x/(R_x)^{1/2}$, where $x$ is the distance from the leading edge of the plate and $R_x$ is the Reynolds number based on the length $x$. The increase is associated with the large temperature rise in the boundary layer at high Mach numbers and to the corresponding viscosity increase near the surface.

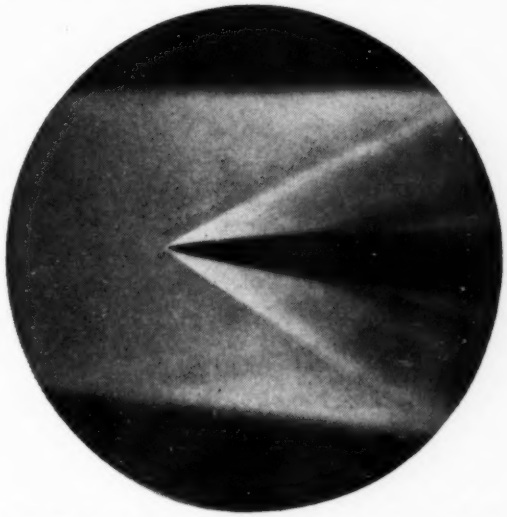

FIG. 7. Flow pattern for wedge-shaped test model obtained with nitrogen afterglow. $M=2.6$. Absolute static pressure, 3 mm of mercury.

[7] A. Busemann, "Gas Stromung mit Laminarem Grenzschlict Entlang Einer Platte," ZAMM 15, S23, 1935.

[8] Th. von Karman and H. S. Tsien, "Boundary layer in compressible fluids," J. Aer. Sci. 5 No. 6 (April, 1938).

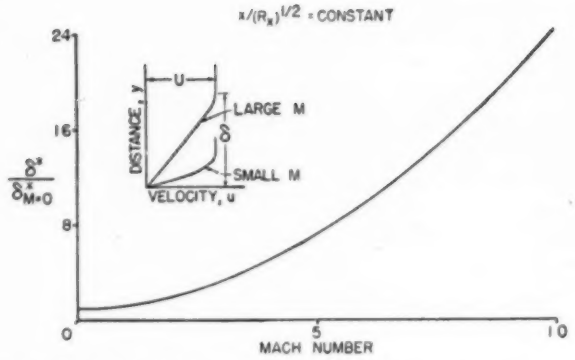


FIG. 8. Effect of Mach number on the displacement thickness of the laminar boundary layer on a flat plate.

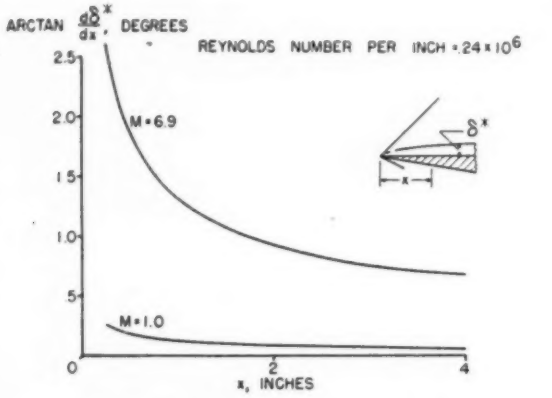


FIG. 9. Slope of the effective surface of the boundary layer along a flat plate.

Figure 9 presents the effective change in slope of the surface of the plate due to growth of the boundary layer. The effect, of course, is a maximum near the leading edge. At the 0.20-in. station, for example, the slope increase is about 2.3° or the equivalent of a four-percent-thick wedge.

The calculated pressure increments corresponding to the slopes of Fig. 9 are plotted on Fig. 10 as fractions of the stream static pressure. For comparison, the results of actual measurements for a flat surface parallel to the stream in the 11-in. hypersonic tunnel are also given. It will be seen that the pressures near the leading edge are markedly altered by the boundary-layer effect; a pressure rise of about 0.7 of stream pressure occurs at the 0.25-in. station. The agreement between theory and experiment appears surprisingly close when it is considered that no account was taken of the effect on the boundary-layer development of either the bow shock or the streamwise pressure gradient.

A schlieren photograph of the flow over a flat surface, taken at a static pressure of 5 mm of mercury, abs., is shown on Fig. 11. The significant part of this photograph is the upper surface of the wedge, alined so as to be accurately parallel to the flow. The lower shock in Fig. 11 is due to the inclined lower surface and has no significance in the present discussion. The shock caused by the boundary layer can be seen to be curved near the nose as required by the effectively curved surface corresponding to the chordwise growth of the boundary layer. The thick boundary layer itself can also be seen; the apparent thickness agrees approximately with the calculated values.

Two obvious practical effects of this phenomenon are to increase the pressure drag of hypersonic airfoils and to alter appreciably the characteristics of leading-edge control devices.

## UNSTEADY FLOWS

Research in the field of unsteady flows is receiving increasing attention partly because of the possibilities of using unsteady flows to advantage, for example, in compressors, pulse-jet engines, and high speed wind tunnels, and partly because of serious adverse effects due to unsteady flows on the performance of supersonic inlets, diffusers, and other aircraft components. In the field of useful applications is the familiar "comprex" compressor, designed by Seippell, in which moving compression and expansion waves perform the func-

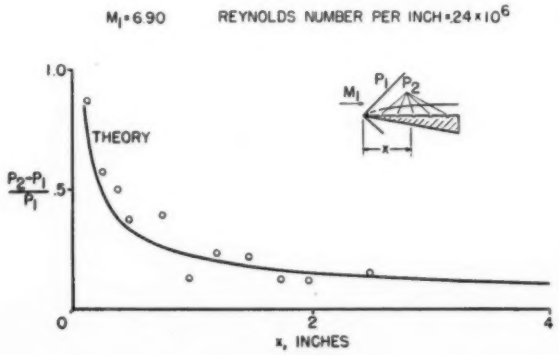


FIG. 10. Effect of boundary layer growth on the pressure distribution along a flat plate.

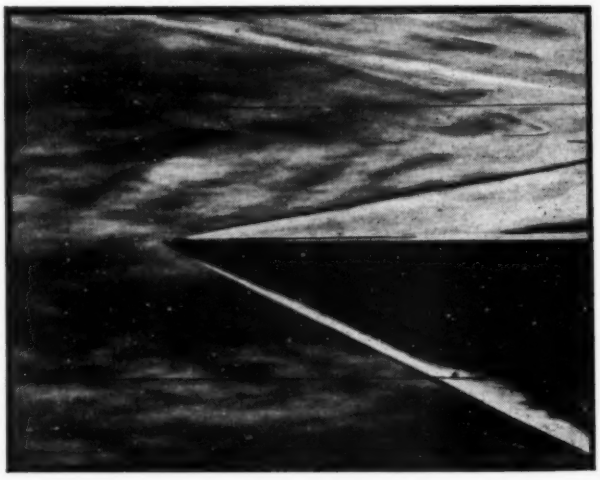

FIG. 11. Schlieren photograph of the boundary layer and shock on a flat surface aligned with the flow. $M = 6.9$. Absolute static pressure, 5 mm of mercury.

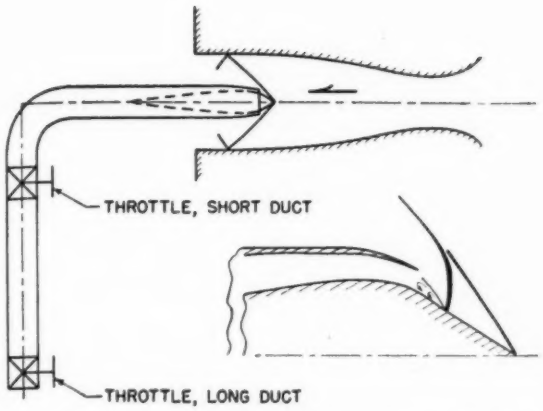


FIG. 12. Supersonic inlet test configuration and sketch of shock-induced separation on conical nose.

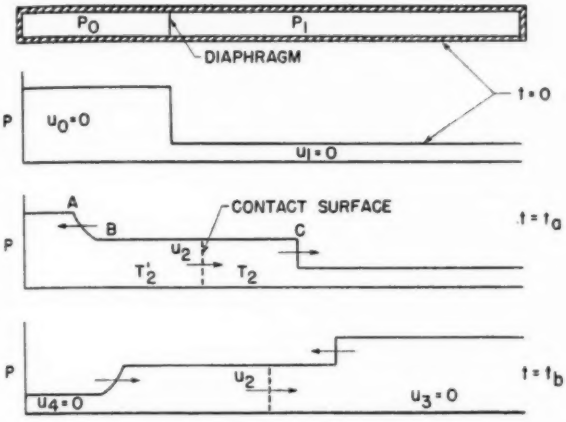


FIG. 13. Illustration of shock tube pressure distributions.

tions of a mechanical piston.[9] Another useful unsteady flow device is the shock tube, which has been used, for example, by Smith at Princeton to study shock reflections[10] and by Geiger and others at the University of Michigan as an intermittent flow wind tunnel.[11]

Adverse unsteady flow phenomena on aircraft wing sections arising from shock boundary-layer interaction at high speeds have been studied for a decade or more and these phenomena continue to present some of the most difficult problems of high speed research. Recently Ferri at Langley has discovered an interesting case of unsteady flow due to shock boundary-layer interaction at the entrance of an axially symmetric supersonic inlet. Figure 12 illustrates the experimental set-up used. The inlet is shown inserted in the test region of a supersonic nozzle which produced a Mach number of 1.90. Back pressure in the duct was varied by means of a throttle, and tests were made with two alternate throttle locations as shown on Fig. 12. The flow pulsations occurred when it was attempted to reduce the mass flow into the inlet by closing the throttle and thereby forcing the normal shock to move from its design location (just inside the inlet) to an external position on the conical central body, thus permitting spillage of some of the approaching air. The external position of the shock is illustrated on the lower sketch of Fig. 12. The basic cause of the pulsations was the abrupt occurrence of shock-induced separation resulting from failure of the boundary layer on the cone to negotiate the strong normal shock in its external position. This separation produced an abrupt reduction in the mass flow entering the inlet and a corresponding drop in back pressure in the duct. The sudden drop in back pressure is equivalent in its effect to a sudden opening of the throttle and thus the shock was momentarily drawn into the inlet again, after which the process repeated itself. The phenomenon was initiated solely by the external shock-induced separation and was in no way connected with internal diffuser or burner disturbances. As would be expected, however, the length of the internal duct had a marked effect on the frequency and character of the pulsations once they had started. The "long duct" configuration (Fig. 12) had lower frequency but larger amplitude pulsations. For both duct configurations the pulsations were of such violence as to prohibit any useful applications of this inlet. Various means of preventing periodic separation on the cone are being studied and there is promise that this type of unsteady flow can be eliminated.

As a basis for experimental study of some of the more difficult unsteady flow problems previously mentioned, Huber has investigated in some detail the phenomena in a simple shock tube.[12] The objectives of this work were to develop suitable pressure-measuring equipment

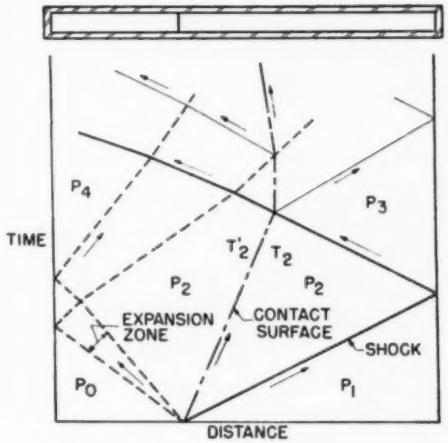


FIG. 14. Position histories of shock-tube phenomena.

[9] C. Seippell, Pressure Exchanger, U. S. Patent Office 2,399,394, Pat. April 30, 1946.

[10] L. G. Smith, Photographic Investigation of the Reflection of Plane Shocks in Air, OSRD Report No. 6271, November 1945.

[11] F. Geiger and C. W. Mantz, "The shock tube as an instrument for the investigation of transonic and supersonic flow patterns" Contract N6-ONR-232, Project M720-4, Engineering Research Institute, University of Michigan, June, 1949.

[12] Huber, Fitton, and Delpino, "Experimental investigation of moving pressure disturbances and shock waves and correlation with one-dimensional unsteady flow theory." NACA TN 1903, July, 1949.

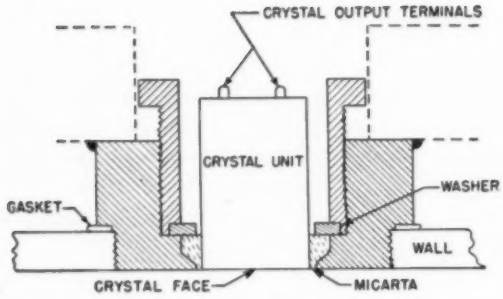


FIG. 15. Method of mounting pressure measuring crystal in wall of shock tube.

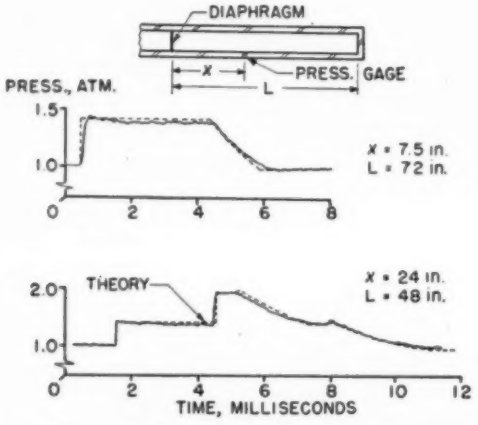


FIG. 16. Pressure histories in the shock tube for two crystal positions and two lengths of tube.

and to determine how closely the one-dimensional theory predicts the actual phenomena in the tube. For the benefit of those unfamiliar with the shock tube, Fig. 13 has been prepared to illustrate its action. The tube has two chambers separated by a diaphragm and containing a gas (or two gases) at different pressures. When the diaphragm bursts, a shock proceeds towards the low pressure end of the tube at a low supersonic speed and a rarefaction wave proceeds in the opposite direction at the speed of sound. Between these disturbances, the pressure is constant at the value $P_2$ and a flow is produced of velocity $u_2$ in the direction of the low pressure end. The surface of contact between the gas originally at high pressure and that at low pressure represents a temperature and entropy discontinuity, since the air to the right has increased in temperature due to the shock passage, while that at the left has decreased in temperature due to the action of the rarefaction. When the shock strikes the end of the tube, it is reflected and proceeds in the opposite direction, reducing the flow velocity in the tube to zero and increasing the pressure. The rarefaction wave has a similar action at the opposite end of the tube. It is important to note that any compressive disturbance behind the shock quickly catches up with it because of the velocity $u_2$ and the higher speed of sound behind the shock. The initial rarefaction wave tends to spread out, however, because the velocity of advance of a wave

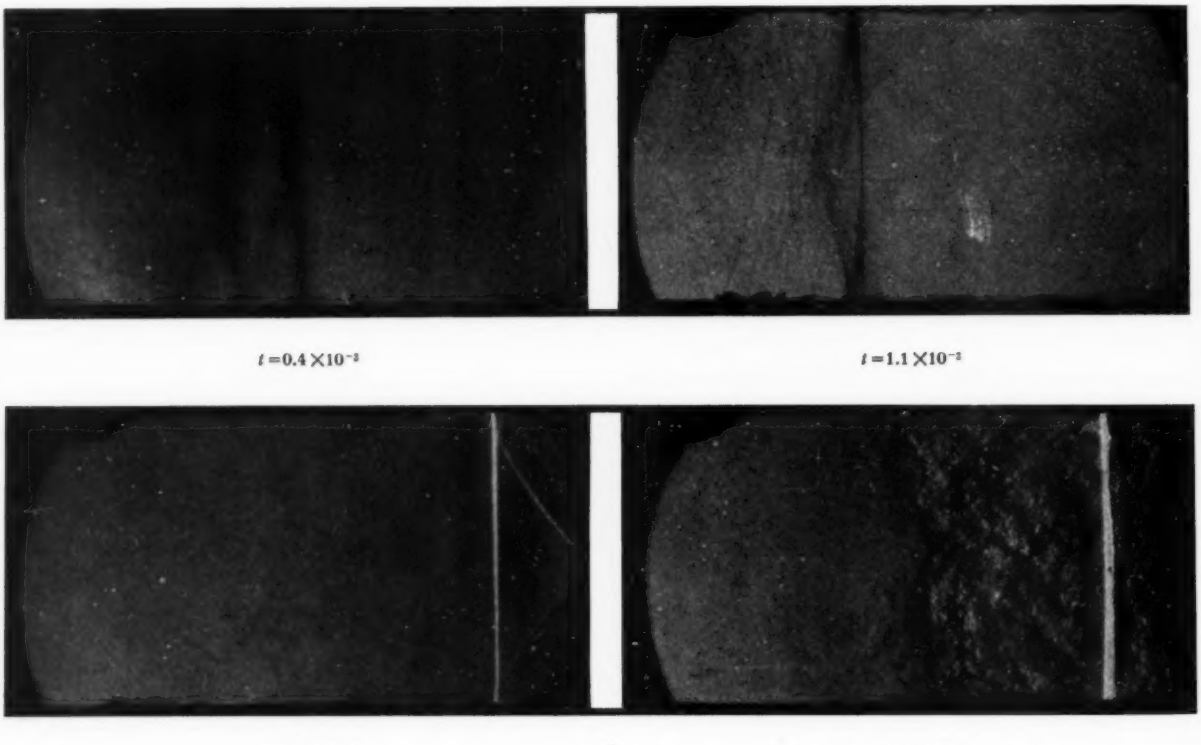


FIG. 17. Schlieren photographs of the shock-tube phenomena at various times (seconds) after bursting of the diaphragm.

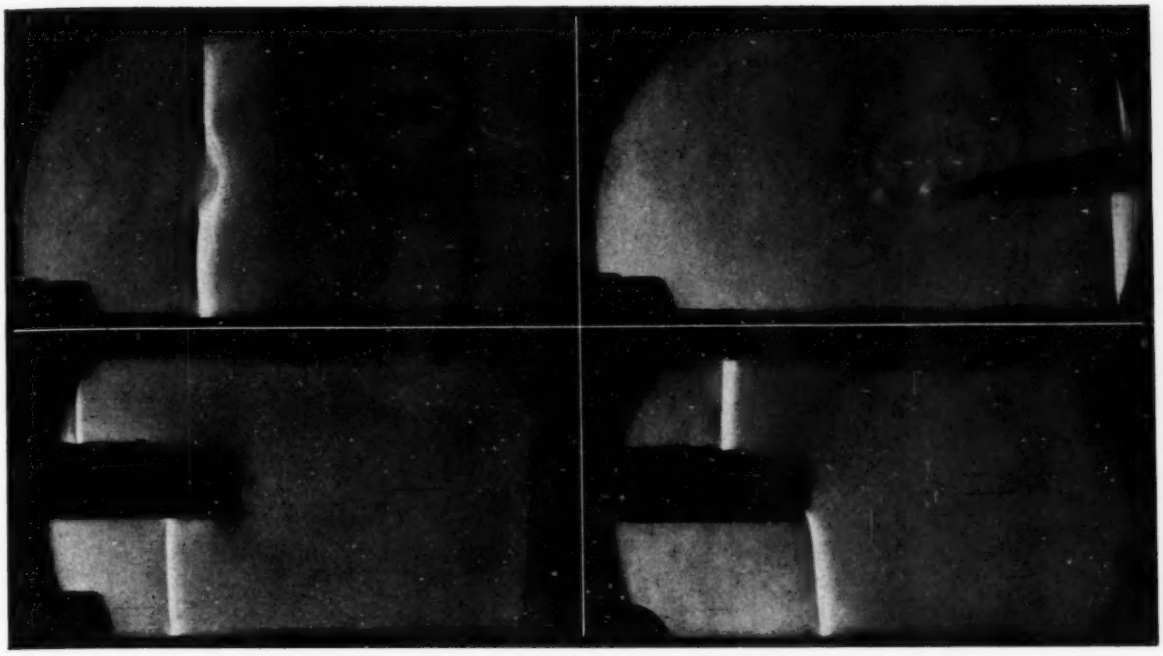

FIG. 18. Schlieren photographs of a shock traveling from left to right against subsonic flow in a channel containing an asymmetrical divider.

behind the rarefaction front is retarded by $u_2$ and by the reduced speed of sound.

Figure 14 shows the theoretical positions of the disturbances as functions of time. Interactions among the various disturbances occur and after the first cycle the flow becomes increasingly complex. The attenuation of the disturbances due to wall friction has been studied by Donaldson[13] and found to be very small in a tube of these proportions for any one cycle. The method of characteristics provides a tool for calculating these interactions and reflections. Neglecting friction and following the work of Guderley and others, Hess[14] has successfully applied the characteristics method to several much more difficult cases—for example, to the starting of flow in a variable cross-section supersonic nozzle when a diaphragm or quick-acting valve is opened at the throat.

Huber's tests were made with air, using an initial pressure ratio of 2.0. The internal cross section of the shock tube was 3×3 inches in size. The tube length varied from 56 to 104 in. the high pressure chamber being 32 in. long and the low pressure chamber being variable in length from 24 to 72 in. Figure 15 illustrates the pressure measuring crystal used. This is a commercial unit $\frac{5}{8}$ in. in outside diameter selected for its properties of high acoustic impedance, high sensitivity, and absence of cavity resonance. The crystal did not perform well when mounted in rubber, when a small air cavity and leakage were present, or when it was slightly misaligned.

The pressure traces produced by the crystal when mounted in each of two positions on the low pressure side of the diaphragm are presented in Fig. 16. In the upper diagram, the crystal was near the diaphragm and the trace shows the pressure rise due to the shock to take place over a measurable time increment. This result is caused primarily by failure of the diaphragm to burst instantaneously as a perfectly plane surface. In this connection, it is of interest to mention that of several materials tried for the diaphragm, the best was tracing paper—both because of its disintegration into many small pieces and because it had less stretch than the other materials. The number of thicknesses used was selected to match the pressure differential. Figure 16 also shows the reflected rarefaction zone and the slight rise in pressure due to reflection of the rarefaction from the temperature discontinuity. In general, the data are in reasonable agreement with the theoretical predictions.

The lower diagram of Fig. 16 was taken with the pick-up farther away from the diaphragm and with a shorter chamber. Here the shock is more nearly plane as would be expected at a greater distance from the initial burst because lagging disturbances have had time to catch up with the shock front. The small discontinuity in the theoretical curve at $t=5.2$ and 8.1 milliseconds is due to reflection of the shock from the temperature discontinuity at the contact surface. Again there is reasonable agreement with the theory.

[13] C. duP. Donaldson and R. D. Sullivan, "The effect of wall friction on the strength of shock waves in tubes and hydraulic jumps in channels," NACA TN 1942, September, 1949.

[14] R. V. Hess, "Study of unsteady flow disturbances of large and small amplitudes moving through supersonic or subsonic steady flows," NACA TN 1878, May, 1949.

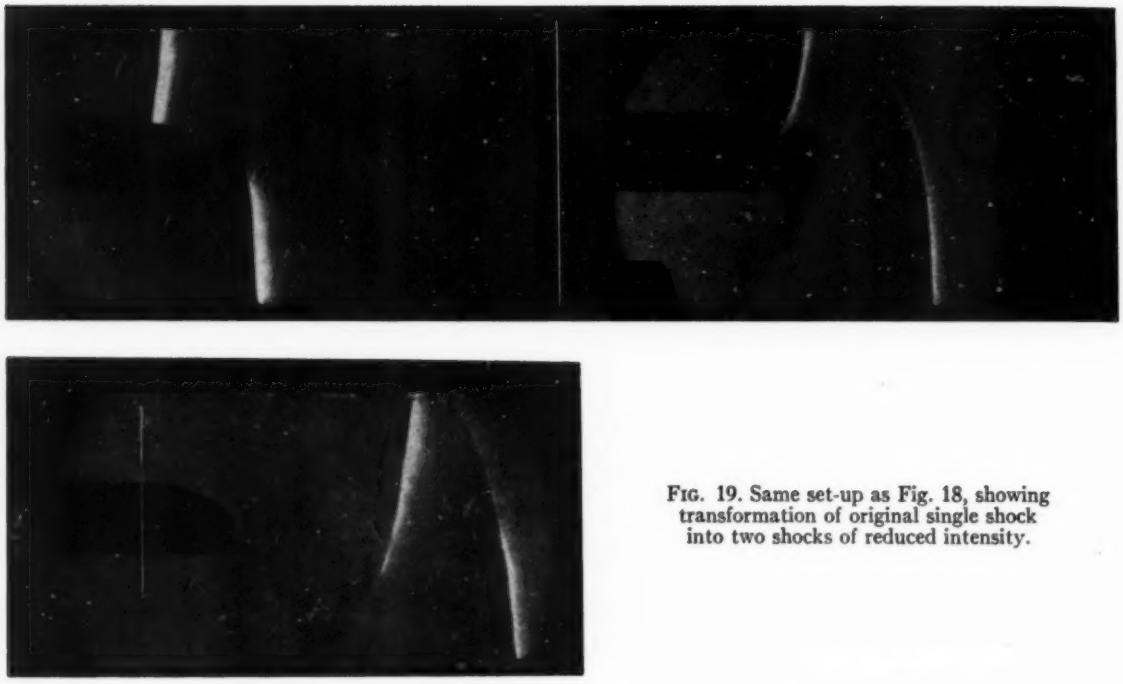

FIG. 19. Same set-up as Fig. 18, showing transformation of original single shock into two shocks of reduced intensity.

Schlieren photographs of the disturbances are shown on Fig. 17. The first picture, ($t=0.4\times10^{-3}$ sec.), taken just downstream of the ruptured diaphragm, shows the "shock" as a wide band. This explains why it did not appear as a discontinuity in the pressure trace. A few tube widths farther downstream, ($t=1.1\times10^{-3}$ sec.) the shock appears as a nearly plane discontinuity, although all of the reflections generated earlier have not yet caught up with it. The third picture, ($t=2.0\times10^{-3}$ sec.), shows the shock immediately after reflection from the end of the low pressure chamber. The oblique disturbances are believed to be reflections of the shock from the walls which were generated as a result of initial curvature of the reflected shock produced by deformation of the 11/16-in. thick end plate. The fourth picture ($t=2.7\times10^{-3}$ sec.) shows the reflected shock passing through the temperature discontinuity. This "discontinuity" is actually a turbulent band—in this case about one tube width in thickness. The finite thickness and turbulence are due mainly to irregularities introduced by the bursting of the diaphragm. Distortions of the shock in passage through this region are evident.

It is concluded from Huber's work that the only significant departures from the one-dimensional shock tube theory arise from the finite time and distortions associated with the rupturing of the diaphragm.

The final subject to be discussed briefly is related to the unsteady flow problem of supersonic diffusers. It is well known that the normal shock in supersonic diffusers oscillates in position due to pressure disturbances from the subsonic part of the diffuser itself or from the combustion chamber. The distance between the mean position of the shock and the throat of the diffuser must be increased as the amplitude of the oscillations increase. For maximum diffuser pressure recovery, the shock must be located as closely as possible to the diffuser throat and this requires therefore that the oscillations be minimized or, in the ideal case, eliminated.

A scheme proposed by Ferri for reducing the strength of the disturbances which generate the oscillations of the shock has been the subject of a preliminary investigation, results of which are illustrated in Figs. 18 and 19. These figures show schlieren photographs of a compressive disturbance (weak shock) traveling to the right against a subsonic flow ($M\approx0.2$) in a tube of square cross section. In the middle of the tube is an asymmetrically shaped two-dimensional body which splits the subsonic flow into two smaller channels of unequal area and velocity. The disturbance divides into two parts upon contacting this central body (upper right picture of Fig. 18). When the two shocks emerge into the channel at the forward end of the divider (lower pictures of Fig. 18) the upper shock lags behind the lower due to the greater retardation provided by the higher speed subsonic flow in the upper passage. Upon leaving the divider (upper pictures of Fig. 19) each shock tends to spread across the entire channel, forming a final configuration of two disturbances (lower picture of Fig. 19) each having about half of the intensity of the original shock. Of course, the rear shock will eventually overtake and coalesce with the leading shock if the duct is long enough. Numerous variations of this scheme suggest themselves. For example, a greater number of channels can be used to reduce further the strength of the initial disturbance or to produce any desired pulsation frequency. Considerable further theoretical and experimental research is required to explore the many possible applications of this principle.

# Contributed Original Research

## Modulation Conversion in a Wave Guide

PAUL S. ROGELL
*Hazeltine Electronics Corporation, Little Neck, New York*
(Received November 29, 1949)

Theory and design equations are presented for the conversion of a microwave, narrow-band f-m signal into very nearly a pure a-m signal within an ordinary wave guide of specified dimensions. Frequency relationships and guide dimensions are arranged so that the f-m side bands are shifted with respect to the carrier until they become a-m side bands at the guide output. A complex intelligence signal may be transmitted with negligible distortion if it is used to amplitude modulate an intermediate carrier which frequency modulates the microwave carrier.

IT is often desirable to utilize an amplitude-modulated signal at microwave frequencies. Since the generation of a microwave frequency-modulated signal is not difficult, the desired operation could be carried out if one possessed the means of converting a microwave f-m signal into an a-m signal. Such a conversion can be accomplished in an ordinary wave guide.

The basic principle employed is the fact that in a wave guide operated near cut-off the phase velocity of a single-frequency signal varies widely with the frequency of the signal. Down such a guide, the low frequency components of a signal travel faster than do the high frequency components. It is possible to adjust the position of the cut-off and the length of the guide so that the frequency components of an f-m wave at the input of the guide will rearrange themselves to form very nearly a pure a-m wave at the output.

The vectorial representation of a narrow band f-m wave, consisting of only a carrier and the first two side bands, is shown by Fig. 1a. It can be seen from the figure that as the carrier rotates, the two side bands add up so as to impart an alternating component to the speed of rotation of the carrier. In the figure, $\omega_c$ is the carrier angular frequency and $\omega_m$ is the angular frequency of a single-frequency modulating signal.

Suppose that the f-m signal of Fig. 1a be introduced into a wave guide operated near cut-off. Each of the three components of the signal will be changed in amplitude and phase upon arriving at the guide output. Let us arrange the parameters of the system so that the lower side band is shifted 450° and the upper side band 270°, each with respect to the carrier. Expressions for the relations that must hold among the parameters to achieve these phase shifts are developed in Appendix A. Also, let us assume that the side bands are equally attenuated. Actually, the resultant side bands are not quite equal, and the output contains a little phase modulation (see Appendix B).

Under the above conditions for phase and amplitude changes, the output signal may be represented by the vector diagram of Fig. 1b. The output is a pure a-m signal, since the two side bands add up so as to impart an alternating component to only the amplitude of the carrier.

It is generally desirable to use a complex wave, not a single frequency, as the transmitted information. To accomplish such a transmission, it would seem natural to merely allow $\omega_m$ to be variable. However, the phase shifts of the side bands with respect to the f-m carrier are intimately associated with the frequency separation of those side bands from the carrier. Varying $\omega_m$, therefore, would destroy the proper phase relations necessary to produce an a-m signal. The difficulty can be overcome by using the signal of frequency $\omega_m$ as an intermediate carrier that is amplitude modulated by the intelligence. In this case, the output signal is a microwave carrier amplitude modulated by an a-m intermediate carrier. The intelligence introduces a distortion term, but as long as the highest intelligence frequency is less than one-tenth the intermediate-carrier frequency, less than one percent distortion is introduced.

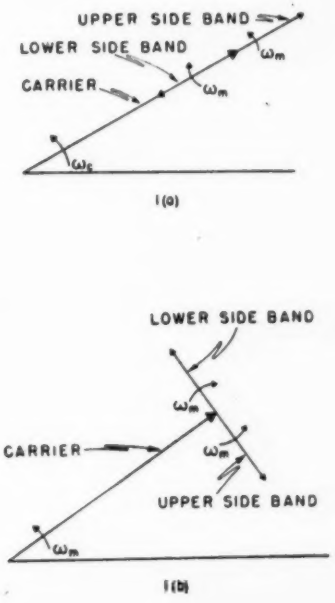


FIG. 1. Idealized vector diagrams for the f-m signal into the guide, and the a-m signal at the guide output.

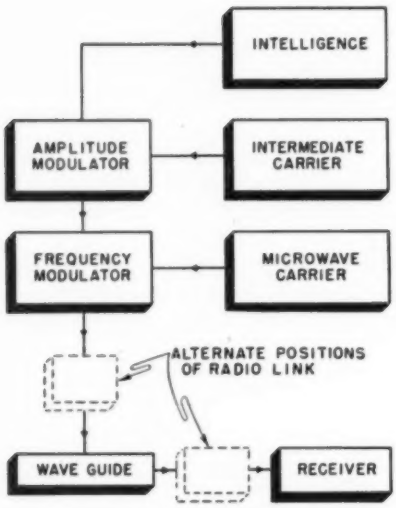


FIG. 2. Block diagram of the complete system.

The case of a variable intelligence frequency is analyzed in Appendix C.

The receiver used in the system could consist merely of two stages of crystal detection together with a suitable amount of amplification.

A simplified block diagram of the entire system is shown in Fig. 2. If the radio link were placed after the wave guide, then an a-m carrier would be transmitted, and a simple receiver could be employed. If the radio link were placed before the wave guide, then an f-m carrier would be transmitted, and the wave guide coupled to the crystals would act as a frequency-modulation detector.

Design equations for the wave-guide dimensions and for frequency relationships are developed in the Appendices. Either the guide output or the input should be variable in longitudinal position so as to secure exactly the desired length. As another design consideration, it would probably be necessary to use crystal stability when generating the intermediate and microwave carriers.

Suppose an amplitude-modulated signal is desired at a carrier frequency of 3000 mc. Let the wave guide be rectangular, carrying the $TE_{10}$ mode. Let the guide cut-off be 2960 mc, necessitating a transverse guide dimension of 5.06 cm. Then the design equations show that the intermediate-carrier frequency must be 33.2 mc, and the guide length must be 1.30 meters. The band width required would be 73.0 mc. Intelligence frequencies ranging from 0 to 3.3 mc would yield less than one percent amplitude distortion in the guide output. There would be a maximum frequency deviation at the guide output of 0.58 mc. This deviation is not large enough to affect the crystal detection in the receiver. The amplitude of the f-m side bands in the guide output relative to the a-m side bands would be 0.0091.

Under the above conditions, the guide output is nearly pure amplitude modulation, since the amplitude of the f-m side bands is less than one percent of the a-m side band amplitude, and there is less than one percent quadrature-component amplitude distortion.

## APPENDIX A

Let us investigate the relations that must exist among the system parameters if the side bands of the f-m carrier are to be shifted in phase by the proper amounts. The phase constant of a single-frequency wave in a guide may be expressed in terms of the frequency of the wave and the cut-off frequency of the guide.[1] We may write,

$$\beta_1=(\omega_c/c)\{[1+(\omega_m/\omega_c)]^2-(\omega_{co}/\omega_c)^2\}^{\frac{1}{2}}, \tag{1}$$

where $\beta_1$ is the phase constant of the upper side band, $\omega_{co}$ is the guide cut-off frequency, and $c$ is the speed of light. MKS units are used throughout.

Let $\delta$ be the difference in frequency between the lower side band and guide cut-off. That is,

$$\delta=\omega_c-\omega_{co}-\omega_m.$$

Neglecting terms of the order of $(\omega_m/\omega_c)^2$ compared to one, we may write,

$$(\omega_{co}/\omega_c)^2=[1-(\omega_m+\delta)/\omega_c]^2\approx 1-2[(\omega_m+\delta)/\omega_c],$$

and

$$[1+(\omega_m/\omega_c)]^2\approx 1+2\omega_m/\omega_c.$$

Substituting the approximate forms just derived into Eq. (1)

$$\beta_1\approx 1/c[2\omega_c(2\omega_m+\delta)]^{\frac{1}{2}}.$$

Similarly, it can be shown that

$$\beta_2\approx 1/c(2\omega_c\delta)^{\frac{1}{2}},$$
$$\beta_c\approx 1/c[2\omega_c(\omega_m+\delta)]^{\frac{1}{2}},$$

where $\beta_2$ and $\beta_c$ are the phase constants of the lower side band and the carrier respectively.

The ratio of the phase shift in the lower side band to the shift in the upper side band is

$$\frac{(\beta_c-\beta_2)l}{(\beta_1-\beta_c)l}\approx\frac{(\omega_m+\delta)^{\frac{1}{2}}-\delta^{\frac{1}{2}}}{(2\omega_m+\delta)^{\frac{1}{2}}-(\omega_m+\delta)^{\frac{1}{2}}}, \tag{2}$$

where $l$ is the length of the guide. This ratio varies from one to about 2.42 as $\omega_m$ varies from zero to $(\omega_c-\omega_{co})$. $5\pi/2$ and $3\pi/2$ were chosen as the smallest phase shifts that would accomplish the desired modulation conversion and still have a ratio between one and 2.42. Setting the right side of Eq. (2) equal to 5/3, and solving for $\omega_m$, we find

$$\omega_m=(240/49)\delta,$$

or

$$\omega_m=240/289(\omega_c-\omega_{co}). \tag{3}$$

Substituting the values for $\beta_c$, $\beta_2$, and $\omega_m$ into the equation for the phase shift of the lower side band,

$$l=5\pi/2(\beta_c-\beta_2),$$

we find

$$l=\frac{17\pi c}{4[2\omega_c(\omega_c-\omega_{co})]^{\frac{1}{2}}}. \tag{4}$$

The guide length and intermediate carrier frequency are determined from Eqs. (3) and (4) given the carrier and cut-off frequencies.

If $TE_{10}$ propagation is used in a rectangular guide, then the transverse guide dimension, $a$, is[2]

$$a=\pi c/\omega_{co}.$$

---

[1] See, for example, S. Ramo and J. R. Whinnery, *Fields and Waves in Modern Radio* (John Wiley and Sons, Inc., New York, 1944), p. 297.

[2] See reference 1, Table 9.04.

## APPENDIX B

This section considers the attenuation of the carrier and the first two side bands between guide input and output. The attenuation constant, $\alpha$, for a wave of angular frequency $\omega$, in a square guide propagating the $TE_{10}$ mode is[3]

$$\alpha=\frac{\omega_{co}}{\pi c}\left(\frac{\omega\epsilon}{2\sigma}\right)^{\frac{1}{2}}\frac{[1+2(\omega_{co}/\omega)^2]}{[1-(\omega_{co}/\omega)^2]^{\frac{1}{2}}},$$

where $\epsilon$ is the dielectric constant within the guide, and $\sigma$ is the conductivity of the guide walls.

The ratios of the output to input amplitudes for the carrier, the upper side band, and the lower side band will be $\exp(-\alpha_1 l)$, $\exp(-\alpha_2 l)$, and $\exp(-\alpha_3 l)$, respectively, where $\alpha_1$, $\alpha_2$, and $\alpha_3$ are the attenuation constants for waves of frequencies $\omega_c$, $\omega_c+\omega_m$, and $\omega_c-\omega_m$, respectively. The output a-m wave may be written,

$$e_{out}=AE_c\{\sin\omega_c t-(Bk/2)[\cos(\omega_c+\omega_m)t-D\cos(\omega_c-\omega_m)t]\}, \quad (5)$$

where $E_c$ is the input carrier amplitude, $k$ is the degree of modulation, and $A$, $B$ and $D$ are attenuation factors , that is,

$$A=\exp(-\alpha_1 l),$$
$$B=\exp[-(\alpha_2-\alpha_1)l],$$
$$D=\exp[-(\alpha_3-\alpha_2)l].$$

The constant $A$ would merely change the apparent carrier amplitude and the constant $B$ would change the apparent degree of modulation. Neither $A$ nor $B$ would influence the purity of the a-m output signal.

The constant $D$ is the relative amplitude of the side bands. Let us consider the two unequal side bands to be two equal side bands of amplitude $D$ plus a single side band of amplitude $1-D$. The maximum phase deviation of the output carrier would be $(1-D)/2$ radians, so the maximum frequency deviation would be $(1-D/2)\omega_m$. The amplitude of the first-order f-m side bands is proportional to $J_1[(1-D)(\omega_m/2)/\omega_m]$ or to $J_1[(1-D)/2]$, where $J_1$ is the Bessel function of first kind, first order. For small arguments,

$$J_1[(1-D)/2]\approx(1-D)/4$$

and the amplitude of the f-m side bands relative to the a-m side bands is $(1-D)/4D$. Using the values of the numerical example in the text, together with

$$\sigma_{copper}=5.80\times10^7$$
$$\epsilon=8.85\times10^{-12}$$

it is found that

$$D=0.965$$

The relative strength of the f-m side bands is 0.0091, and the maximum frequency deviation is 0.58 mc.

## APPENDIX C

Let $\omega_s$ be the variable frequency of an intelligence signal, and let this signal amplitude-modulate the intermediate carrier. The new amplitude of the intermediate carrier, $E_m'$, is

$$E_m'=E_m(1+M_s\cos\omega_s t)$$

where $E_m$ is the original intermediate-carrier amplitude, and $M_s$ is the degree of modulation by the intelligence. The instantaneous frequency of the f-m input, $\omega_i$, is now

$$\omega_i=\omega_c[1+M_mE_m(1+M_s\cos\omega_s t)\cos\omega_m t],$$

where $M_m$ is the degree of modulation by the intermediate carrier. The guide input, $e$, is

$$e=E_c\sin\left(\int_0^t\omega_i dt\right).$$

Using standard forms to integrate, and neglecting terms of order of magnitude $\omega_s^2$ compared to those of order of magnitude $\omega_m^2$, we have

$$e=E_c\sin\left\{\omega_c t+\frac{M_mE_m\omega_c}{\omega_m}\left[(1+M_s\cos\omega_s t)\sin\omega_m t-\frac{M_s\omega_s}{\omega_m}\sin\omega_s t\cos\omega_m t\right]\right\}. \quad (6)$$

The last term in Eq. (6) is a distortion term. Its amplitude relative to the amplitude of the desired signal is $\omega_s/\omega_m$, and it is in quadrature with the desired signal. Therefore, if $\omega_s/\omega_m$ never exceeds one-tenth, the distortion will be less than one percent.

The band width is

$$BW=2(\omega_m+\omega_{s_{max}})=2.2\omega_m,$$

where $\omega_{s_{max}}$ is the highest intelligence frequency. Substituting from Eq. (3),

$$BW=1.83(\omega_c-\omega_{co}). \quad (7)$$

Equation (7) is a design equation. Given the carrier frequency, cut-off may be chosen from considerations of band width, and the tolerable amount of f-m signal in the output (see Appendix B).

# Measurement of Self-Diffusion of Silver without Radioactive Tracers*

G. C. KUCZYNSKI
*Sylvania Electric Products, Inc., Bayside, New York*
(Received September 23, 1949)

A new method dispensing with the use of radioactive tracers has been developed for measurement of volume self-diffusion. The method is based upon the relationship of the rate of sintering of metallic wires to the coefficients of self-diffusion. The values of the self-diffusion coefficients for silver as measured by this method are in good agreement with those obtained by the radioactive tracers method.

SELF-DIFFUSION implies the diffusion of the atoms of a given substance into itself. Until recently, the detection of such a process was possible only by measurement of the rate of penetration of the radioactive isotope into another stable isotope of the same chemical element.

This method when first introduced by von Hevesy[1–3] was restricted to the study of diffusion of the naturally radioactive elements such as lead[4] and bismuth.[5] The discovery of artificial radioactivity removed this obstacle and allowed the determination of self-diffusion coefficients of copper, gold, silver and zinc using improved methods.[6,7]

In the previous work of this author,[8] the relationship of the radius $x$ of the interface between the sintered particles to the coefficient $D$ of volume self-diffusion was established.

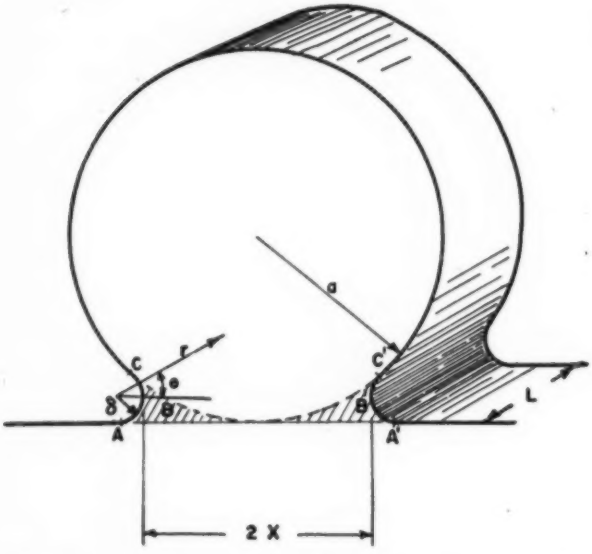


FIG. 1. Schematic representation of a wire bonded to a cylinder.

This relationship is as follows:

$$D=k/(40\gamma\delta^3)(T/t)(x^5/a^2), \tag{1}$$

where $k$ is Boltzmann's constant, $\gamma$ the surface energy of the metal $\delta$ the interatomic distance, $T$ the temperature of sintering on the Kelvin scale, $t$ time of sintering and $a$ the original radius of the particle. Work with small metallic particles is laborious and does not yield accurate results. The examination of the graphs contained in the above mentioned paper reveals a definite linear relationship between $(x^5/a^2)T/t$ and $1/T$. However, the spread of points is too large for accurate determination of the coefficient of diffusion. In his communication to the American Physical Society,[9] the author was able to report some of the diffusion coefficients of silver determined by a new method consisting of sintering of silver wires to cylindrical silver pieces. The detailed description of this method and results obtained is the subject of this paper. The new method allows to determine the self-diffusion of most metals without use of radioactive tracers.

## THEORETICAL CONSIDERATIONS

The wire in contact with the plate of the same metal forms a system which is not in equilibrium because its total surface free energy is not a minimum. During heating, the space between the wire and the plate

TABLE I. Sintering of 0.005-inch silver wires to silver cylinders.

| $T$°C | $t$ hrs. | $x\times10^{-4}$ cm | $a\times10^{-3}$ cm | $x/a$ | $D$ cm²/sec. | Atmosphere of heating |
|---|---|---|---|---|---|---|
| 900 | 1.0 | 14.1 | 6.00 | 0.235 | $7.0\times10^{-9}$ | air |
| | 2.0 | 15.2 | 5.85 | 0.260 | $5.4\times10^{-9}$ | air |
| | 4.0 | 18.3 | 5.85 | 0.313 | $6.9\times10^{-9}$ | air |
| 800 | 24.0 | 18.0 | 5.85 | 0.308 | $7.5\times10^{-10}$ | air |
| 700 | 4.0 | 8.2 | 5.85 | 0.140 | $8.9\times10^{-11}$ | air |
| | 5.0 | 8.9 | 5.85 | 0.150 | $1.2\times10^{-10}$ | hydrogen |
| | 6.0 | 9.0 | 5.85 | 0.154 | $1.1\times10^{-10}$ | air |
| | 16.0 | 10.6 | 5.85 | 0.180 | $9.2\times10^{-11}$ | hydrogen |
| | 48.0 | 14.6 | 6.20 | 0.240 | $8.5\times10^{-11}$ | argon |
| | 140.0 | 15.0 | 5.85 | 0.260 | $6.0\times10^{-11}$ | argon |
| 600 | 16.0 | 6.0 | 5.85 | 0.102 | $5.9\times10^{-12}$ | hydrogen |
| 460 | 64.0 | 3.8 | 5.85 | 0.065 | $8.0\times10^{-14}$ | hydrogen |

* This work was done on a research program sponsored by the AEC Contract AT-30-1-GEN-367.

[1] J. Groh and G. von Hevesy, Ann. d. Physik **63**, 85 (1920).
[2] G. von Hevesy and A. Obrutcheva, Nature **115**, 674 (1925).
[3] G. von Hevesy and W. Seith, Zeits. f. Physik **56**, 790 (1929).
[4] von Hevesy, Seith and Keil, Zeits. f. Physik **79**, 197 (1932).
[5] W. Seith, Zeits. f. Elektrochemie **39**, 538 (1933).
[6] Steigman, Shockley and Nix, Phys. Rev. **56**, 13 (1939).
[7] W. A. Johnson, Trans. A.I.M.M.E. **143**, 107 (1941).
[8] G. C. Kuczynski, "Self-Diffusion in Sintering of Metallic Particles," J. Inst. Metals, (February, 1949).
[9] G. C. Kuczynski, Phys. Rev. **75**, 1309 (1949).

gradually fills up forming a neck bounded by two cylindrical concave surfaces $ABC$ and $A'B'C$ in Fig. 1.

As in the case of sintering of the spherical metallic particles,[8] self-diffusion is responsible for the formation of this neck. If we assume the vacancy theory of diffusion, then the volume directly underneath the concave surfaces of the neck should have an excess concentration $\Delta C$ of holes over the equilibrium concentration $C_0$. This difference in concentration between the volume underneath the concave surface of the neck and the other parts of the system creates the diffusion gradient necessary for the flow of atoms into the neck area and thus promotes gradual filling up of the latter. The equation of flow can then be written as follows:

$$A\,|(\partial\Delta C/\partial r)_{r=\rho}|\,D'=dV/dt, \qquad (2)$$

where $A$ is the surface through which the vacancies enter the system, $V$ the filled volume between the wire and the plate indicated by shaded area in Fig. 1 $(\partial\Delta C/\partial r)_{r=\rho}$ the gradient of vacancy concentration on the surface of the radius of curvature $\rho$ (such as surface which contour is indicated in Fig. 1 by $ABC$ and $A'B'C$) and $D$ the coefficient of vacancy diffusion. The relationship between the $D'$ and $D$ the coefficient of atomic diffusion is $D'C_0=D$ where $C_0$ as before designates the equilibrium concentration of vacancies.

We shall first evaluate the excess hole concentration $\Delta C$. The free energy increase of the system, due to the dissolution of $n$ vacancies raising the concentration from $C_0$ to $C_0+\Delta C$ is $nkT\ln(C_0+\Delta C/C_0)$ or if $\Delta C$ is small $nkT(\Delta C/C_0)$. At the same time, there is the energy decrease due to the decrease of the pressure $\gamma/\rho$ over the neck area. This energy decrement is approximately $n\delta^3(\gamma/\rho)$ if the diameter of the vacancy is equal to the atomic diameter $\delta$. At equilibrium, these two energies have to be equal which results in the following expression for the increment of concentration under the neck area

$$\Delta C=(\delta^3\gamma/kT\rho)C_0. \qquad (3)$$

This excess concentration of holes causes the diffusion

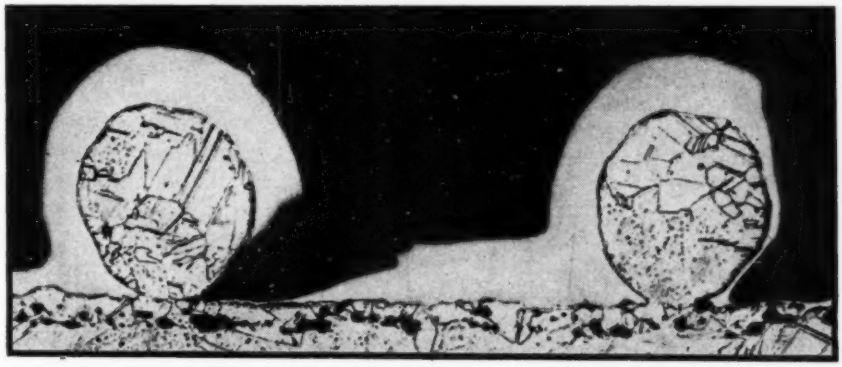

(a)

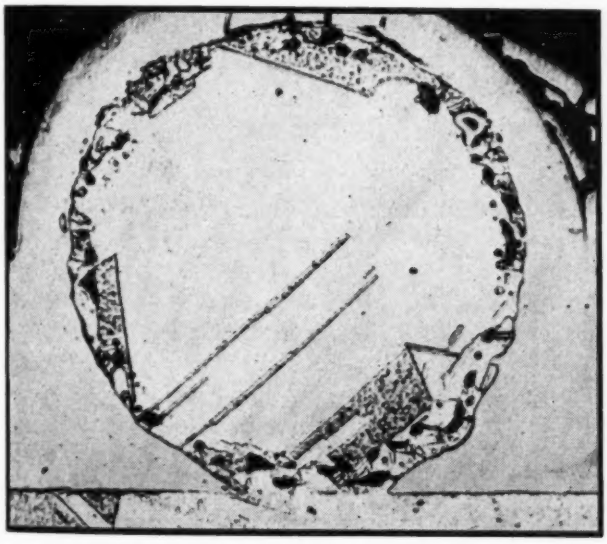

(b)

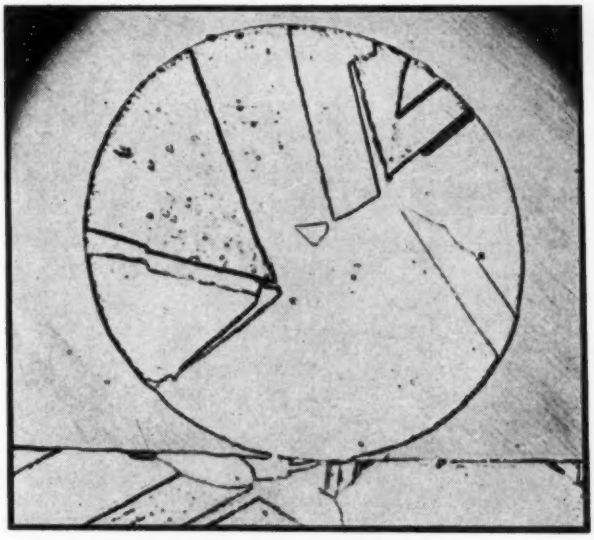

(c)

FIG. 2. (a) Cross section of silver wire sintered to silver cylinder at 800°C for 24 hours, magnified 200 times; (b) same sintered at 900°C for 1 hour, magnified 500 times; (c) same sintered at 700°C for 140 hours, magnified 500 times.

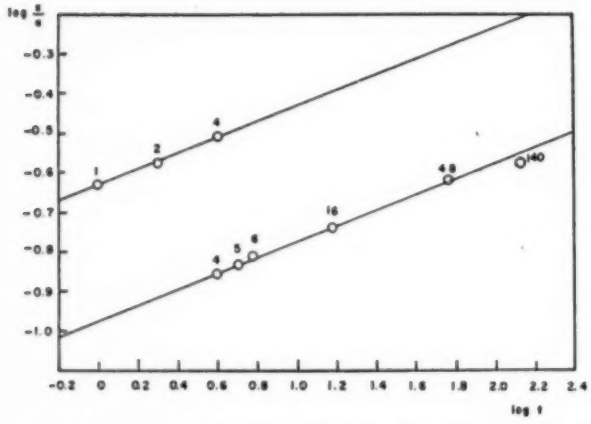


FIG. 3. Log$(x/a)$ *versus* log$t$ plots for silver wires bonded to silver cylinders. The inverse slope of these lines is approximately 5, proving that $x^5$ is proportional to the time of heating.

of atoms from the inner parts of the system to the neck. When the current is established $\partial C/\partial t=0$ and the concentration will be given by the solution of the Laplace equation

$$\nabla^2 C=0$$

this solution is a function of the radius $r$ drawn from the center of curvature 0 (Fig. 1) of the neck area and the angle $\theta$ of this radius with a direction perpendicular to the axis of the wire and parallel to the plate and also passing through the center of curvature. Obviously $\rho$ does not change along the length of the wire. Such a solution can be written in the form

$$C=\sum_{n/0}^{\infty}\frac{C_n\cos n\theta}{r^n},$$

or

$$\Delta C=\sum_{n/1}^{\infty}\frac{C_n\cos n\theta}{r^n}, \tag{4}$$

where

$$\Delta C=C-C_0.$$

Expression (4) should be approximately equal to (3) on the surface of the neck, where $r=\rho$, which implies that $|C_n|$ for $n>1$ are small and corresponding terms can be neglected in our approximation. We may accept, therefore, that

$$\Delta C\cong\delta^3\gamma C_0/kTr$$

and

$$(\partial\Delta C/\partial r)_{r=\rho}=-(\delta^3\gamma C_0/kT\rho^2). \tag{5}$$

Simple geometrical considerations based upon Fig. 1 lead to the following equations which are valid provided $x/a<\cdot 3$

$$\rho=(x^2/4a),\quad A=(\pi x^2 L/2a),\quad V=(x^3 L/2a),$$

where $L$ is the length of the sintered wire. Inserting these values into (5) and (2) and noting the $D'C_0=D$, we obtain

$$(80\pi/3)(\delta^3\gamma a^2/kTx^4)D=dx/dt,$$

and after integration

$$x^5/a^2=(80\pi/3)(\delta^3\gamma/kT)Dt. \tag{6}$$

Using this equation, we may express the coefficient of diffusion $D$ as a function of the readily measurable variables $x$, $a$, $T$ and $t$.

$$D=3/80\pi(kT/\delta^3\gamma t)x^5/a^2. \tag{7}$$

It has to be noted that in the above derivation, it was tacitly assumed that the contour of the neck $ABC$ in Fig. 1 is semicircular. If it were not so, then there would be a difference of concentration of vacancies proportional to the difference of the inverse radius of the smallest and largest radius of curvature and the diffusion current would tend to equalize the curvature. It is, therefore, reasonable to assume the contour to be circular.

## THE EXPERIMENTAL METHOD

As can be seen from the brief introduction, the determination of the coefficient of self-diffusion reduces itself to the sintering of a wire to a large block of the same metal and subsequent measurement of the width $2x$ of the interface formed. In order to demonstrate that in this case the mechanism of sintering is diffusion, the experimental test of Eq. (6) is necessary.

The experiments were performed on very pure silver metal. The sintering of the wire to a flat base was not successful because it was difficult to obtain good contact between the wire and the base. This problem was solved

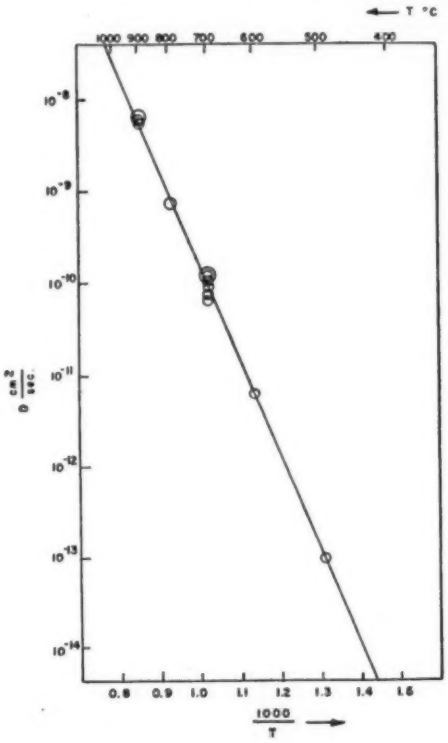


FIG. 4. Variation of volume self-diffusion coefficient of silver with temperature as determined from sintering experiments.

by winding the 0.005 in. diameter silver wire on a cylindrical piece of the same material of about $\frac{1}{4}$ in. diameter. This diameter was found large enough to allow to neglect the curvature of the cylinder and so consider it as approximately flat. Good care was taken to tighten the wire well on the cylinder without, however, introducing much plastic deformation in the interface. Specimens prepared in this manner were heated in hydrogen, air or argon at 900, 800, 700, 600 and 460°C for various periods of time, as indicated in Table I. After heating, the specimens were nickel plated in order to avoid loosening or deformation of the interfaces during the subsequent metallographic operations. Plated cylinders with wires sintered to them were then mounted in Bakelite and cut, in order to obtain a diametral cross section of the wire in contact with the base.

The results of the measurements of the diameter of the neck, sometimes show large scattering of values, due to more or less perfect contact along the wire. In order to assure maximum accuracy, a great number of readings were taken (more than twenty per temperature-time run) and the most probable diameter was determined from the frequency of occurrence curves.

The plane of the cut was not necessarily perpendicular to the axis of the wire and consequently the width of the interface $2x$ between the wire and the cylinder observed on the cross section was not the true one. This, however, was easily corrected as the apparent distortion of the interface and the known diameter of the wire are in the same proportion as the true interface width and the true wire diameter, known from micrometric measurements. The true width of the interface then was evaluated by multiplying its measured value by the ratio of the true diameter of the wire to its value as measured with the micrometer. Some examples of the polished sections prepared in the manner outlined above are shown in Fig. 2.

## RESULTS

Table I lists the half width values of the interface $x$, along with the radius of wire $a$, the $x/a$ ratio and the coefficient of self-diffusion $D$ calculated from Eq. (4). The last column contains details of the atmosphere used for each particular heat treatment. It is convenient to convert (6) into logarithmic relationship after dividing both sides by $a^3$

$$5\log\frac{x}{a}=\log t+\log\left(\frac{80\pi}{3}\frac{\delta^3\gamma D}{kTa^3}\right);$$

the last term is constant at a given temperature. By plotting $\log x/a$ *versus* $\log t$ one can obtain the exponent, which in the case of diffusion flow should be 5, by simple determination of the slope of the obtained straight line.

The $\log x/a/\log t$ plots at 900°C and 700°C are given in Fig. 3. The points fall on the straight lines whose inverse slopes are 5.0 and 5.1 respectively, indicating that the relationship $x^5\sim t$ holds, as should be expected when the diffusion flow is responsible for sintering. The fact that the points corresponding to the heat treatments in three different atmospheres fall on the same straight line, seems to indicate that in the case of silver bonding of wires or particles together is not affected by the surrounding atmosphere, as long as it is neutral. At 700°C, air can be considered neutral to silver.

Figure 4 represents the semilogarithmic plot of $\ln D$ *versus* $1000/T$. The experimental points fall very well on the straight line. The coefficient of self-diffusion of silver as determined from this graph is $D=0.9e^{-45,700/RT}$* and agrees very well with that obtained by W. A. Johnson[7] who used the radioactive isotope method for its determination. Johnson obtained $D=0.89e^{-45,900/RT}$. The value obtained from the experiments of sintering of silver spheres[8] was $D=0.60e^{-45,000/RT}$. As we can see all three values are in close agreement indicating that the wire method may well be used in the determination of the coefficients of self-diffusion of metals. Its greatest advantage is simplicity and great saving of time. In cases like aluminum where the radioactive isotopes are not available the wire method is the only one which permits determination of the self-diffusion coefficient.


## ACKNOWLEDGMENTS

The author wishes to express his gratitude to W. E. Kingston, Manager of Sylvania Metallurgical Laboratories, for his support of this project. He also wishes to thank H. Lipson of Sylvania Electric Products, Inc. for his aid in processing the specimens and Mrs. L. Roth for her skillful metallographic work.


* In the calculation of $D$ the value of surface energy for liquid silver, 1000 ergs/cm² was adopted, although it was expected that the surface energy for solid metal should be somewhat higher. However, the error introduced by this choice should not change the order of magnitude of the coefficient of diffusion.

# A Graphical Analysis of the Interference Patterns of an Elevated Ultra-High Frequency Antenna under Conditions of Atmospheric Stratification*

F. R. Abbott and C. J. Fisher
*U. S. Navy Electronics Laboratory, San Diego, California*
(Received September 6, 1949)

Analytical computation of the detailed lobe structure of an elevated meter or centimeter band antenna for a standard atmosphere is quite tedious. In case there are discontinuities in the gradient of refractive index the analysis becomes hopelessly involved.

This paper presents a straightforward method of graphical analysis for the optical region, equally applicable to a standard or stratified atmosphere.

## INTRODUCTION

A PICTORIAL presentation of the lobe structure of the low angle radiation pattern from an elevated microwave or v.h.f. antenna is usually constructed with a distorted scale. Horizontal distances may be compressed to a millionth while vertical dimensions are reduced to 1/10,000 or less. Thus elevation angles are greatly exaggerated.

It is advantageous to use such a distorted representation in the construction of ray diagrams. It is very significant that the path difference between intersecting rays under such a transformation is easily measureable and is directly reducible to the path difference of the corresponding rays at full scale.

Thus, if one is concerned with a centimeter or so path length difference between two rays intersecting at a distance of twenty miles, it becomes possible to construct the rays on a distorted scale drawing and measure the path difference on the drawing. The measured path difference multiplied by a constant factor gives the difference for the actual rays and the relative phase is thus determined.

Geometrical path differences on a drawing may be measured to a high degree of accuracy using an ordinary engineer's map measure, the rolling wheel of which has been graduated. It will be shown that the additional term included in the optical path difference may be determined by planimeter measurements of the area enclosed between the rays.

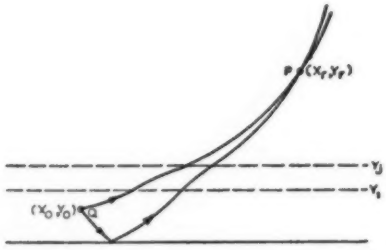


FIG. 1. Two optical paths for radiation proceeding from a source, $Q$, and traveling through an inversion layer between $Y_i$ and $Y_j$ to a point of intersection, $P$.

* M. E. Hall of the U. S. Navy Electronics Laboratory Antenna Range staff assisted in the preparation of the material for publication.

## THEORY

Consider radiation proceeding from a source at $Q$ to an arbitrary point, $P$, by two alternate optical paths. The second ray may have been occasioned by a reflection as indicated in Fig. 1 or by other means.

Formally, the optical path length of either ray is given by

$$S=\int_{X_0Y_0}^{X_rY_r} n\,dL, \tag{1}$$

in which $n$ is the refractive index and $dL$ is the element of geometrical path length which, in turn, is given by

$$dL=[1+(dY/dX)^2]^{\frac{1}{2}}dX \cong[1+\tfrac{1}{2}(dY/dX)^2-\tfrac{1}{8}(dY/dX)^4+\cdots]dX. \tag{2}$$

The third and all ensuing terms in the expression for $dL$ are very small for rays at low vertical angles and will henceforth be disregarded. The refractive index of the lower atmosphere, designated by $n$, is assumed to be dependent only on the elevation. It is further assumed that the vertical refractive index curve, $n=f(Y)$, may be replaced by a series of sections over which $dn/dY$ is constant. $n$ is expressible as

$$n=1+q(Y), \tag{3}$$

in which $q(Y)$ is a small fraction, generally 0.0004 or less for the case considered.[1] The radius of curvature of rays in a medium of slowly changing refractive index is given by[2]

$$1/R=(d/dY)\log n=(1/n)(dn/dY). \tag{4}$$

For values of $n$ very close to unity

$$1/R\cong(dn/dY). \tag{5}$$

The two rays in Fig. 1 thus proceed through three zones. In the lower zone the refractive index is increasing with increased altitude and since a ray bends into the denser medium, the curvature is upward. From elevations $Y_i$ to $Y_j$ the refractive index is decreasing and the

[1] I. Katz and J. M. Austin, "Qualitative survey of meteorological factors affecting microwave propagation," M.I.T. Radiation Lab. Report No. 488 (June 1, 1944).

[2] P. K. L. Drude, *The Theory of Optics* (Longmans, Green and Company, New York, 1902), p. 306.

curvature is downward. Above $Y_j$ the refractive index increases and the curvature is again upward.

Designate the quantities associated with the two rays by the subscripts $a$ and $b$, respectively. The path lengths from Eqs. (1)–(3) become

$$S_a \approx \int_{X_0}^{X_r} [1+q(Y)_a][1+\tfrac{1}{2}(dY/dX)_a^2]dX, \quad (6)$$

and

$$S_b \approx \int_{X_0}^{X_r} [1+q(Y)_b][1+\tfrac{1}{2}(dY/dX)_b^2]dX. \quad (7)$$

By neglecting terms of the order $\frac{1}{2}q(Y)(dY/dX)^2$ and higher, the optical path difference becomes

$$S_b-S_a \approx \int_{X_0}^{X_r} [q(Y)_b-q(Y)_a + \tfrac{1}{2}(dY/dX)_b^2-\tfrac{1}{2}(dY/dX)_a^2]dX. \quad (8)$$

Designating the vertical gradient of refractive index by $n'=dn/dy$, we have

$$q(Y)_b-q(Y)_a=n_b-n_a=\int_{Y_a}^{Y_b} n'dY,$$

and

$$S_b-S_a=\tfrac{1}{2}\int_{X_0}^{X_r} [(dY/dX)_b^2-(dY/dX)_a^2]dX + \int_{X_0}^{X_r}\int_{Y_a}^{Y_b} n'dYdX. \quad (9)$$

The first integral in Eq. (9) is simply the geometrical path length difference for the two rays and is expressible as $L_b-L_a$.

Since the gradient of refractive index, $n'$, is constant except for discontinuities at $Y=Y_i$ and $Y=Y_j$ the double integral is equivalent to the sum of the three area integrals, each multiplied by the value of $n'$ for the area concerned. This is expressible by $\sum_i n_i'A_i$ in which $A_i$ is the area characterized by a refractive index gradient $n_i'$ and bounded by the paths $a$ and $b$ and the elevation levels $Y_i$ and/or $Y_j$.

Thus, the optical path difference becomes

$$S_b-S_a=L_b-L_a+\sum_i n_i'A_i. \quad (10)$$

The construction of a ray diagram involves the reduction in dimensions expressed by

$$dy=CdY, \quad dx=DdX, \quad (11)$$

in which $C$ and $D$ assume values of the order of 1/10,000

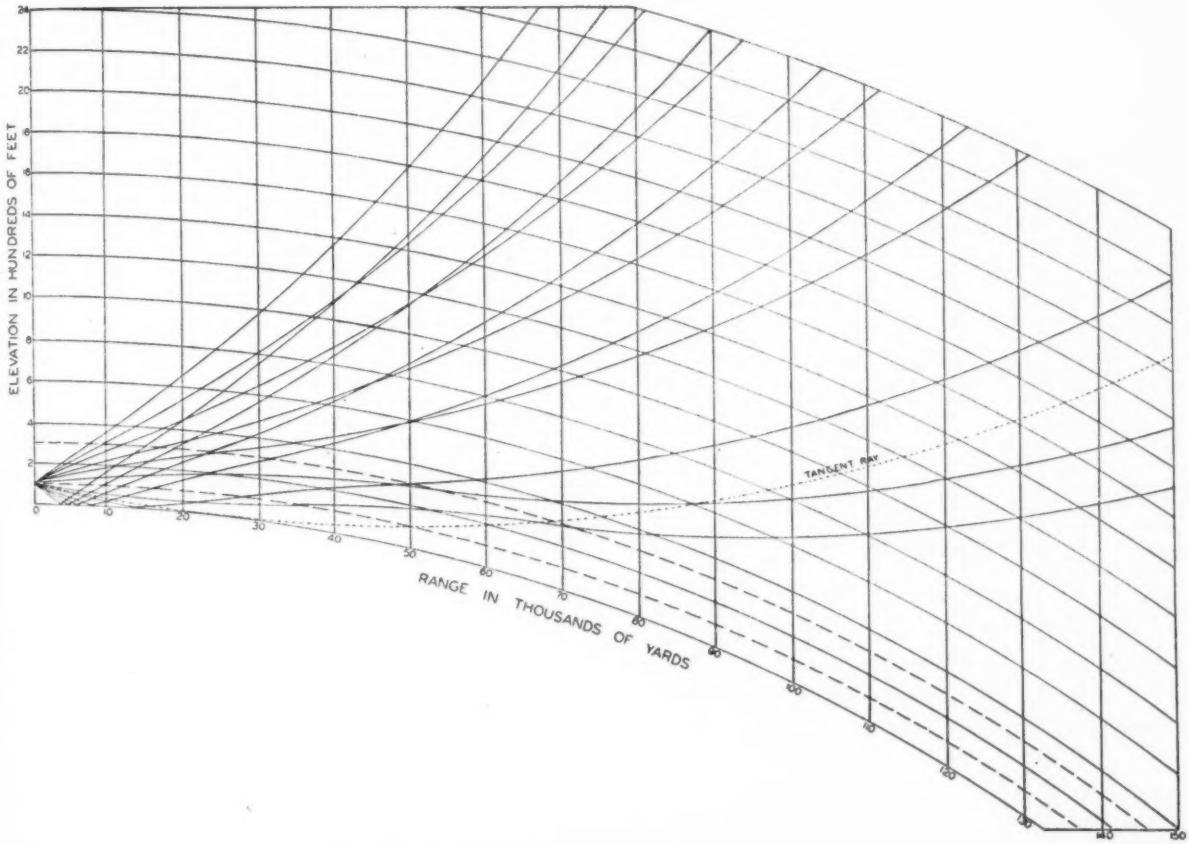


FIG. 2. Complete ray diagram.

and 1/1,000,000, respectively. In the scale coordinates Eq. (8) becomes

$$s_b - s_a = \frac{D}{2C^2}\int_{X_0}^{X_r}[(dy/dx)_b^2 - (dy/dx)_a^2]dx + \frac{1}{CD}\int_{X_0}^{X_r}\int_{Y_a}^{Y_b} n'dydx, \quad (12)$$

which like (9) is expressible as

$$s_b - s_a = D/C^2(l_b - l_a) + 1/CD\sum_i n_i'\alpha_i, \quad (13)$$

where $\alpha$ and $l$ are the reduced scale area and length symbols.

The radius of curvature of the rays on the reduced scale drawing is proportional to the radius of curvature of the actual rays. The proportionality factor is determined as follows:

From elementary calculus the radius of curvature of the actual rays is given by

$$R = \frac{[1+(dY/dX)^2]^{\frac{3}{2}}}{d^2Y/dX^2}.$$

For rays near grazing incidence $(dY/dX)^2$ is very small so that

$$1/R \approx d^2Y/dX^2. \quad (14)$$

The reduced scale radius, $r$, follows from the transformation of Eqs. (11) applied to (14) and is given by

$$1/r \approx C/D^2 d^2Y/dX^2. \quad (15)$$

By Eq. (5), Eq. (15) becomes

$$1/r \approx (C/D^2)n'. \quad (15a)$$

Introducing $r_i$, the scale radius of curvature of the rays, into Eq. (13) we have for the path difference

$$s_b - s_a = (D/C^2)[(l_b - l_a) + \sum_i \alpha_i/r_i]. \quad (16)$$

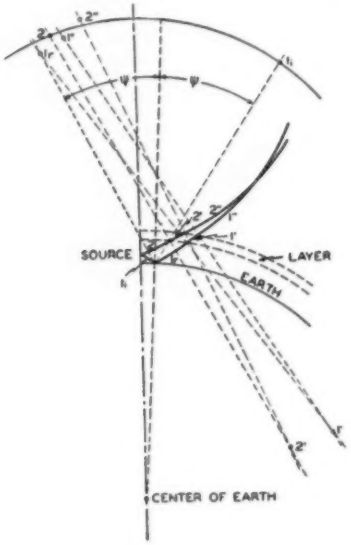


FIG. 3. Illustration of method of construction of a ray diagram.

As is shown in the Appendix the modification of the actual index of refraction curve does not alter the total path length difference of any pair of intersecting rays. It has been shown[3] that to construct a diagram in which the rays in regions of standard refraction are represented by straight lines requires the use of an effective earth's radius equal to 4/3 the actual radius of the earth. This defines the slope of a ray passing from the source through any point.

Since it is imperative to keep the angle of inclination of rays and the scaled earth surface small in order that the neglected terms of Eq. (2) do not introduce appreciable error, a curve of modified index has been selected that will minimize both. This curve is such that the resultant curvature of both the surface of the earth and the rays in regions of standard refraction is equal to half the curvature of the earth's surface relative to a ray in standard atmosphere obtained from the above relation. This gives a radius of curvature for both rays in the region of standard refraction and the surface of the earth equal to 8/3 the actual radius of the earth. Thus, from Eq. (15) the scaled earth radius equals $(D^2/C)R_e$, where $R_e$ is the modified radius of earth curvature and is equal to 8/3 actual earth radius.

In the actual construction of a ray diagram appropriate values of the scale factors, $C$ and $D$, are chosen and the earth's surface is drawn using the resulting value for the scaled earth radius as given above. The diagram shown in Fig. 2 was drawn on a chart 27×40 in. on which one inch vertical represents 150 ft. and one inch horizontal represents 2 miles. A layer of inversion of refractive index is indicated as being between the dashed lines. The transformation constants, $C$ and $D$, assume values of 1/1800 and 1/144,000, respectively and result in a scaled earth radius of 58 in.

## CONSTRUCTION OF RAY DIAGRAM

Using the location of the source of radiation as center, an arc of scaled earth radius is struck above the line representing the earth's surface. Equally spaced points along this arc provide centers of curvature for equally spaced rays emanating from the source. Consider a direct and reflected ray whose centers, for the sake of explanation of construction, shall be the arbitrary points, 2 and $1_i$, respectively, as shown in Fig. 3. When a direct ray, such as ray No. 2, is incident on the lower boundary of an inversion layer the curvature reverses in sign. The new center lies on an extension of the line passing through the center of curvature of the incident ray and the point of incidence. The radius of curvature of the ray while passing through the inversion layer is again defined by Eq. (15) and can be found from the modified index curve. This procedure is repeated when the ray meets the upper boundary of the layer and the new center is found on an extension of the second radius

[3] Schelleng, Burrows, and Ferrell, "Ultra-short-wave propagation," Proc. I.R.E. **21**, 427 (1933).

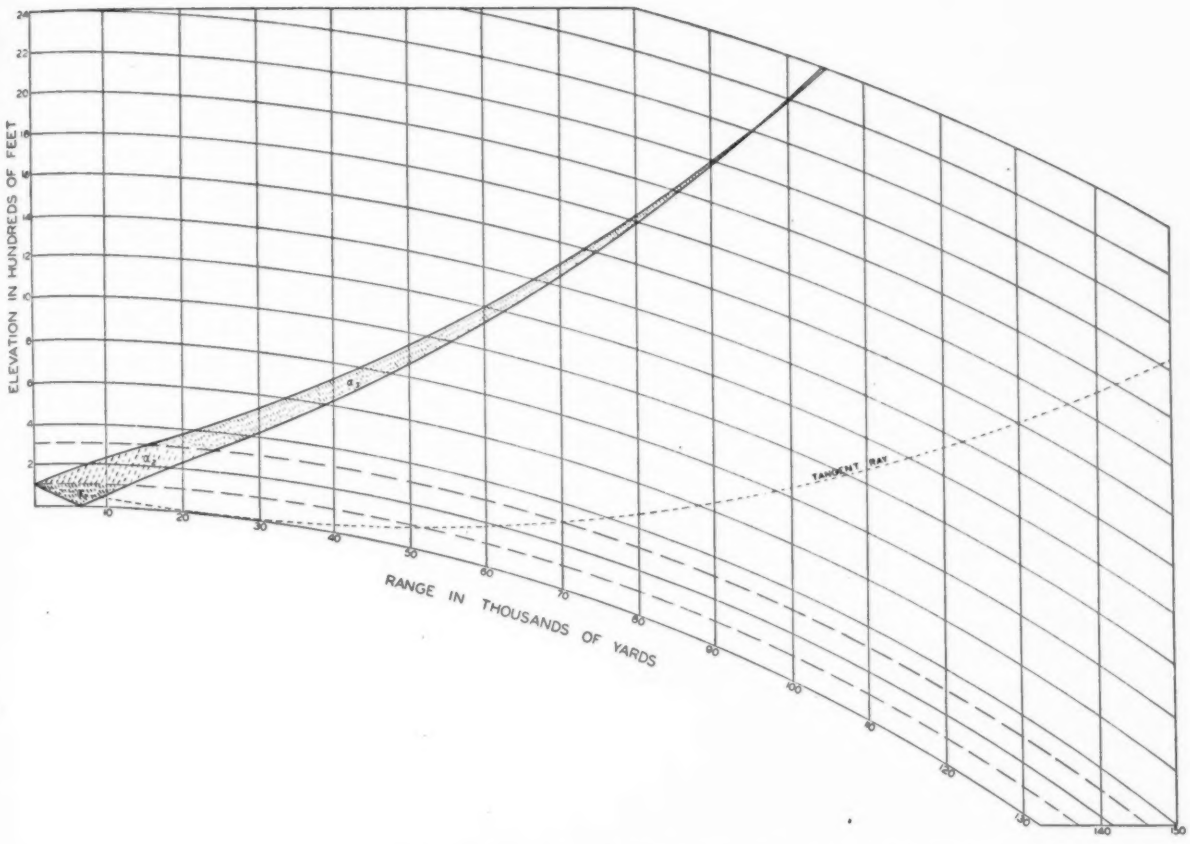


FIG. 4. Areas, $\alpha_i$, used in evaluating the resultant field, $E$, of Eq. (17) at any point of intersection.

passing through the point of incidence at the top of the layer. This is shown as line 2′2″ in Fig. 3.

In the case of a ray reflected from the earth's surface such as ray No. 1 in Fig. 3, an extension of the earth's radius is drawn through the point of reflection. Since the angle of reflection is equal to the angle of incidence, the center of curvature of the reflected ray is found on a line making an angle, $\psi$, with this extension of the earth's radius. The reflected ray from this point on is constructed exactly as the direct ray given above.

The areas, $\alpha_i$, of Eq. (16) bounded by the two rays and the levels of discontinuity in refractive index gradient shown in Fig. 4 are measured with a planimeter. The geometrical path difference is measured by running a map measure forward over one ray and backward along the alternate ray to the starting point. It should be remembered that terms of $\alpha_i/r_i$ are added algebraically and due regard should be given to change of sign of $r_i$ when the direction of curvature changes.

It is essential to select values of $C$ and $D$ such that the slope of the rays remains small. Otherwise the disregarded terms of Eq. (2) become excessively large.

The intensity of each component of the field normally decreases with distance in accordance with the inverse distance law of radiation fields. The two factors necessary to account for such variation are designated by $1/(d)^{\frac{1}{2}}$ and $1/(\delta)^{\frac{1}{2}}$ where $\delta$ is the distance between individual rays of the ray system at a distance, $d$, from the transmitter.

We then finally obtain the resultant field, $E$, at any point of intersection of two rays with reference to $E_0$, the field at some reference distance, $d_0$, in the form

$$\frac{E}{E_0}=\frac{1}{(d)^{\frac{1}{2}}}\left\{\frac{1}{(\delta_a)^{\frac{1}{2}}}+\frac{\rho}{(\delta_b)^{\frac{1}{2}}}\exp j\beta\left[\phi+\frac{D}{C^2}\left(l_b-l_a+\sum_i\frac{\alpha_i}{r_i}\right)\right]\right\}, \quad (17)$$

where $\beta=2\pi/\lambda$, $\delta_0$ is the ray spacing at distance $d_0$ from the source, usually taken as one meter, and the subscripts, $a$ and $b$, refer to the direct and reflected rays, respectively. Equation (17) is valid so long as $1/(\delta)^{\frac{1}{2}}$ is finite.

The phase shift, $\phi$, and the magnitude, $\rho$, are introduced to allow for phase rotation and change of intensity of the lower ray on reflection. In the case of horizontally polarized waves propagated over sea water, $\phi$ goes to $\lambda/2$, and $\rho$ becomes unity.

Figure 5 is a plot of the field pattern of a 3000-Mc source elevated 100 ft. above the surface of the earth. It was secured by evaluating Eq. (17) at all the points of intersection of rays on the corresponding ray diagram.

The foregoing method of analysis presents an unique

and simple procedure for computation of the radiation field in the optical zone, for an elevated very high frequency antenna in any type of stratified atmosphere. Good correlation has been obtained between the measured field in the optical zone under conditions of atmospheric stratification and the calculated field for the same condition.

A complete field analysis below the optical horizon must include diffracted, scattered and partially reflected components of radiation[4] none of which is considered in the above analysis.

A number of predicted low level coverage diagrams similar to Fig. 5 are available in reports WP-11, WP-14, and WP-15 of the U. S. Navy Radio and Sound Laboratory.[5] These include patterns of 200- and 3000-mcs sources for 13 types of non-linear atmospheric refractive index gradients.

## APPENDIX. PROOF OF THE INVARIANCE OF OPTICAL PATH DIFFERENCE TO THE CURVATURE IMPOSED ON SPACE BY THE USE OF A MODIFIED INDEX OF REFRACTION

There are a variety of forms that the modified index of refraction curve may take as is shown in Fig. 6. Each one lends more or less convenience to a given application. It would be well to ask what effect the modification of the gradient of the index of refraction has on the analysis presented.

The path difference for the two rays depicted in Fig. 1 is given by an expression of the form

$$S_b - S_a = (L_b - L_a) + \Sigma_i A_i/R_i,$$

where $L_b - L_a$ is the geometric path length difference and $A_i$ is the area bounded by the rays in the $i$ region. $R_i$ is the radius of curvature of the ray in the $i$ region.

For values of $n$ close to unity,

$$1/R \approx dn/dY \approx d^2Y/dX^2,$$

which leads to

$$S_b - S_a = (L_b - L_a) + \Sigma_i n' A_i. \tag{18}$$

From Eq. (8) we see that the geometric path length difference is expressible as

$$L_b - L_a = \tfrac{1}{2}\int [(dY/dX)_b^2 - (dY/dX)_a^2]dX$$

$$= \tfrac{1}{2}\int [(Y_b')^2 - (Y_a')^2]dX. \tag{19}$$

Let $z_a$ be the slope of the reflected ray at the point of reflection and $z_b$ be the slope of the direct ray at the point of reflection. Then

$$Y_a' = z_a - \int_0^X n_a' dX, \tag{20}$$

$$Y_b' = z_b - \int_0^X n_b' dX. \tag{20a}$$

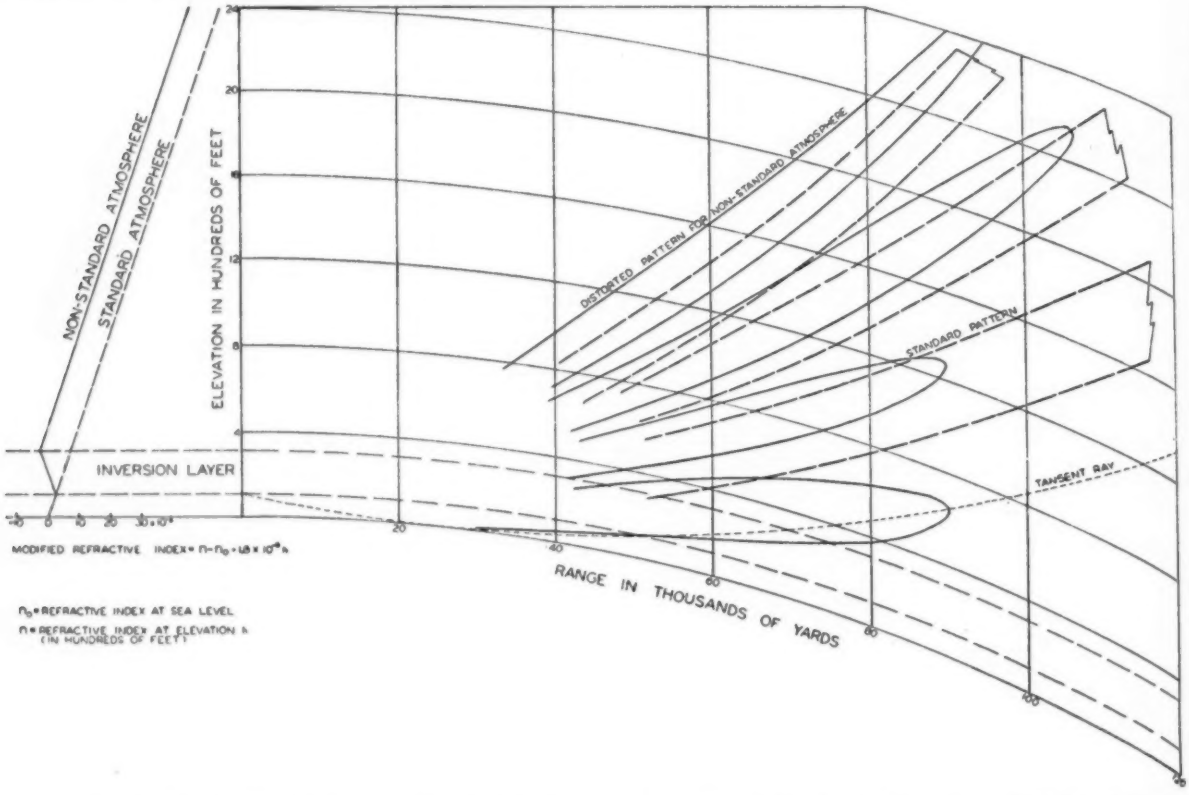
NON-STANDARD ATMOSPHERE
STANDARD ATMOSPHERE
ELEVATION IN HUNDREDS OF FEET
INVERSION LAYER
DISTORTED PATTERN FOR NON-STANDARD ATMOSPHERE
STANDARD PATTERN
TANGENT RAY
RANGE IN THOUSANDS OF YARDS
MODIFIED REFRACTIVE INDEX = n − n₀ + 1.8 × 10⁻⁶ h
n₀ = REFRACTIVE INDEX AT SEA LEVEL
n = REFRACTIVE INDEX AT ELEVATION h (IN HUNDREDS OF FEET)

FIG. 5. Plot of a field pattern showing low level coverage for a modified refractive index equal to $n - n_0 + 1.8 \times 10^{-6} h$, where $n_0$ is the refractive index at sea level and $n$ is the refractive index at elevation $h$. ($h$ is measured in hundreds of feet.)

[4] J. B. Smith and L. G. Trolese, "Propagation of radio waves in the lower troposphere," Proc. I.R.E. **35**, No. 11, 1198–1202 (November, 1947).

[5] U. S. N. R. and S. Lab. Report WP-11, "Procedure and charts for estimating low level coverage of shipboard 200 mcs radars under conditions of pronounced refraction" (April 10, 1944). U. S. N. R. and S. Lab. Report WP-14, "Predicted low level coverage of *S*-band radars as affected by weather" (November 1, 1944). U. S. N. R. and S. Lab. Report WP-15, "Predicted low level coverage of 200 mcs radars as affected by weather" (November 4, 1944).

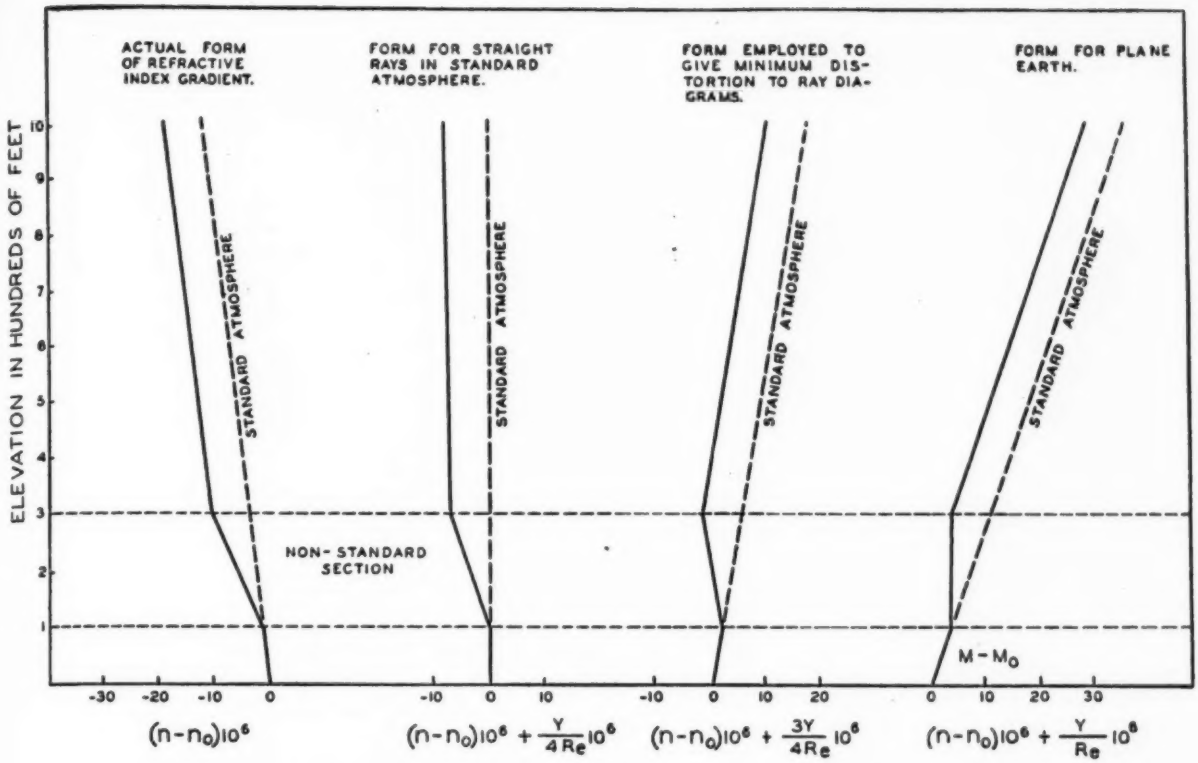
ACTUAL FORM OF REFRACTIVE INDEX GRADIENT.
FORM FOR STRAIGHT RAYS IN STANDARD ATMOSPHERE.
FORM EMPLOYED TO GIVE MINIMUM DISTORTION TO RAY DIAGRAMS.
FORM FOR PLANE EARTH.
ELEVATION IN HUNDREDS OF FEET
STANDARD ATMOSPHERE
NON-STANDARD SECTION
M - M0
(n-n0)10^6
(n-n0)10^6 + Y/4Re 10^6
(n-n0)10^6 + 3Y/4Re 10^6
(n-n0)10^6 + Y/Re 10^6

FIG. 6. Four useful types of representation of atmospheric refractive index gradient. All represent the same condition.

Let $n'$ be modified by an amount, $k$, and designate the new slopes by $U_a'$ and $U_b'$. It is seen from Fig. 6 that the factor, $k$, assumes values of $(Y/R_e)10^6$, $(Y/4R_e)10^6$ etc., where $Y$ is the elevation in hundreds of feet and $R_e$ is the radius of the earth.

$$U_a' = z_a - \int_0^X (n_a' + k)dX, \tag{21}$$

$$U_b' = z_b - \int^X (n_b' + k)dX. \tag{21a}$$

From (21) and (21a)

$$U_b' - U_a' = z_b - z_a - \int^X (n_b' - n_a')dX = Y_b' - Y_a', \tag{22}$$

$$U_b' + U_a' = z_b + z_a - \int_0^X (n_b' + n_a')dX - 2k\int_0^X dX = Y_b' + Y_a' - 2kX. \tag{23}$$

Hence,

$$(U_b')^2 - (U_a')^2 = (U_b' - U_a')(U_b' + U_a') = (Y_b')^2 - (Y_a')^2 - (Y_b' - Y_a')2kX. \tag{24}$$

Let $\Delta_g$ be the increment in geometric path length difference that results from modifying $n'$ by the factor $k$. From Eq. (19)

$$\Delta_g = \tfrac{1}{2}\left\{\int[(U_b')^2 - (U_a')^2]dX - \int[(Y_b')^2 - (Y_a')^2]dX\right\}. \tag{25}$$

By substituting (24) in (25) we see that

$$\Delta_g = -k\int_Q^P (Y_b' - Y_a')XdX. \tag{26}$$

Integrating Eq. (26) by parts and letting

$$u = X; \quad du = dX,$$

and

$$dv = (Y_b' - Y_a')dX; \quad v = Y_b - Y_a,$$

we see that

$$\Delta_g = -k\left[X(Y_b - Y_a)\Big|_Q^P - \int_Q^P (Y_b - Y_a)dX\right]. \tag{27}$$

In the first term, $Y_b - Y_a$ is equal to zero at the points $P$ and $Q$ since the rays cross and the difference in height is zero. The integral term represents the area, $A$, bounded by the two rays. Therefore, $\Delta_g = kA$.

From Eq. (18), the purely optical contribution to path difference is given by the term $\Sigma_i n_i' A_i$. By modifying the refractive index gradient by a factor, $k$, this term takes the form $\Sigma_i (n_i' + k)A_i$.

Let $\Delta_0$ be the variation in the purely optical component of the path length difference of two rays passing through media having refractive indices $n$ and $(n+k)$, respectively. Then

$$\Delta_0 = \Sigma_i n_i' A_i - \Sigma_i (n_i' + k)A_i = -\Sigma_i kA_i.$$

Since $\Sigma_i A_i$ represents the total area, $\Delta_0 = -kA$.

Thus, the total change in path length difference observed when $n$ is modified by a factor, $k$, is

$$\Delta_t = \Delta_g + \Delta_0 = kA - kA = 0.$$

It is important to note that the relative total path length difference is independent of the modification of the gradient of the index of refraction.

It is elementary to prove that the elevation and distance to the point of intersection of two rays is also independent of the choice of modified index.

# The Determination of the Impulsive Response of Variable Networks

LOTFI A. ZADEH
*Columbia University, New York, New York*
(Received November 21, 1949)

Starting with the differential equation relating the output and the input of a linear varying-parameter network, it is shown that the impulsive response of the system is related to a Green's function associated with the system through a linear operator which is the adjoint of the right-hand operator in the given differential equation. A perturbation procedure for the determination of the impulsive response of a slowly varying network is outlined. Use of the method is illustrated by a simple example involving a band width-modulated *RC* half-section.

## GENERAL THEORY

THE term *variable network* is commonly used to describe a network in which one or more element-values are dependent upon a combination of the three variables—time, input, and output. The variability of transmission characteristics of variable networks makes them ideally suited for many applications in the fields of communication and control. In practice, however, the use of variable networks has been, and still is, very limited mainly because of the lack of adequate means for their analysis, synthesis and mechanization.

The most basic problem in the theory of variable networks is that of analysis. In general, the analysis of a variable network in which the element-values are functionals of the input, output, and time, presents mathematical problems of a prohibitive degree of complexity—problems which for all practical purposes are unsolvable except through use of high speed automatic computers. There are, however, certain classes of variable networks which are amenable to purely analytical treatment. The most important of these is the class of so-called linear varying-parameter networks, that is, linear networks in which the element-values are functions of time only, and are independent of both the input and the output. Familiar examples of such networks are the amplitude and frequency modulators and—as a limiting case—the ordinary fixed linear networks. To simplify the terminology, the term *variable network* as used in this paper will refer to a linear varying-parameter network.

The behavior of a variable network may be described in several different ways—some of which are implicit and some explicit. Usually, the behavior is described *implicitly* by means of a differential equation relating the output of the network, $e_2(t)$, to the input $e_1(t)$. This equation is, in general, of the form

$$[a_n(t)p^n+\cdots+a_1(t)p+a_0(t)]e_2(t) = [b_m(t)p^m+\cdots+b_1(t)p+b_0(t)]e_1(t), \quad (1)$$

where $p=d/dt$ and the $a$'s and $b$'s are known functions of time. Equation (1), which is sometimes referred to as the *fundamental* equation of the system, may be written more compactly as

$$L(p;t)e_2(t)=K(p;t)e_1(t), \quad (2)$$

where $L(p;t)$ and $K(p;t)$ stand, respectively, for the left-hand and right-hand operators in Eq. (1). The input $e_1(t)$ is usually assumed to be zero for $t<0$, and the network itself is assumed to be unexcited, though not necessarily fixed, prior to $t=0$. Thus, the problem of the determination of the response to a specified input $e_1(t)$ reduces to the solution of the differential equation represented by Eq. (1), subject to homogeneous initial conditions at $t=0-$.

A commonly used form of *explicit* description of the behavior of a variable network is based on the notion of the *impulsive response* of the network. The impulsive response $W(t,\xi)$ is defined as the response of the system at $t=t$ to a unit impulse applied at $t=\xi$. In other words, $W(t,\xi)$ is the solution of the equation

$$L(p;t)W(t,\xi)=K(p;t)\delta(t-\xi), \quad (3)$$

where $\delta(t-\xi)$ represents a unit impulse at $t=\xi$. The salient property of $W(t,\xi)$ is that the response to any given input $e_1(t)$, may be expressed in terms of $W(t,\xi)$ and $e_1(t)$ through the superposition integral

$$e_2(t)=\int_{-\infty}^{\infty} W(t,\xi)e_1(\xi)d\xi. \quad (4)$$

Thus, when the behavior of a network is described by means of its impulsive response, the determination of the response of the network to any given input reduces to performing the relatively simple operation expressed by Eq. (4).

A more convenient form of explicit description of the behavior of a variable network is based on the notion of the *system function*[1] of the network. Briefly, the system function of a variable network is defined as a function $H(j\omega;t)$ such that $H(j\omega;t)e^{j\omega t}$ represents the steady-state response of the network to $e_1(t)=e^{j\omega t}$. In other words, the system function $H(j\omega;t)$ is the complex envelope of the response of the network to $e^{j\omega t}$. It is shown in [1] that $H(j\omega;t)$ is the steady-state solution of the differential equation

$$L(p+j\omega;t)H(j\omega;t)=K(j\omega;t), \quad (5)$$

and that $H(j\omega;t)$ and $W(t,\xi)$ are related to each other

[1] L. A. Zadeh, "Frequency analysis of variable networks," Proc. I.R.E. 38, 291–299 (1950).

by the relations:

$$H(j\omega;t)=\int_{-\infty}^{\infty}W(t,\xi)e^{-j\omega(t-\xi)}d\xi \tag{6}$$

and

$$W(t,\xi)=\frac{1}{2\pi}\int_{-\infty}^{\infty}H(j\omega;t)e^{j\omega(t-\xi)}d\omega. \tag{7}$$

The salient characteristic of $H(j\omega;t)$ is that the response to any given input $e_1(t)$ may be expressed in terms of $H(j\omega;t)$ and $e_1(t)$ through the relation

$$e_2(t)=\mathfrak{L}^{-1}\{H(s;t)E_1(s)\}, \tag{8}$$

where $E_1(s)$ is the Laplace transform of $e_1(t)$ and $\mathfrak{L}^{-1}$ represents the inverse Laplace transformation. In evaluating the inverse Laplace transform of $H(s;t)E_1(s)$, $t$ should be treated as if it were a constant parameter. Thus, when the behavior of a variable network is described by means of its system function $H(j\omega;t)$, the determination of the response of the network to any given input requires only the use of a standard table of Laplace transforms. This constitutes one of the advantages of describing the behavior of a variable network by its system function $H(j\omega;t)$ rather than by its impulsive response $W(t,\xi)$.

The central problem in the analysis of a variable network is that of obtaining an explicit description of the behavior of the network starting from an implicit description of the behavior. In other words, the problem is to determine either the impulsive response $W(t,\xi)$ or the system function $H(j\omega;t)$ from the knowledge of the fundamental equation of the system. In general, this problem cannot be solved exactly, so that in most cases it is necessary to use approximate methods for the determination of $W(t,\xi)$ or $H(j\omega;t)$. The problem of the determination of $H(j\omega;t)$ is treated in [1]. The problem to be considered in the following is that of the determination of $W(t,\xi)$ in the case of slowly varying networks. In such networks the coefficients $a_\nu(t)$ and $b_\mu(t)$ in Eq. (1) do not vary appreciably over the effective duration[2] of the impulsive response of the network. Most of the variable networks encountered in practice belong to this category.

## DETERMINATION OF $W(t,\xi)$

From the definition of the impulsive response of a variable network it follows that $W(t,\xi)$ is the solution of Eq. (3) subject to homogeneous initial conditions at $t=\xi-$. On the other hand, the commonly used Green's function $G(t,\xi)$, which is associated with Eq. (2), is in effect the impulsive response of a system whose fundamental equation is

$$L(p;t)e_2(t)=e_1(t). \tag{9}$$

Stated more precisely, $G(t,\xi)$ is the solution of the differential equation

$$L(p;t)G(t,\xi)=\delta(t-\xi), \tag{10}$$

subject to homogeneous initial conditions at $t=\xi-$, or equivalently, to the following conditions:

$$G^{(\lambda)}(t,\xi)_{t=\xi+}=0,\quad \lambda=0,1,2,\cdots,n-2,$$
$$G^{(n-1)}(t,\xi)_{t=\xi+}=\frac{1}{a_n(\xi)}, \tag{11}$$

at $t=\xi+$. In view of Eqs. (3) and (10) it is evident that $W(t,\xi)$ and $G(t,\xi)$ are closely related to each other. To obtain the form of this relation it is sufficient to apply the superposition integral to Eq. (9), treating $K(p;t)\delta(t-\xi)$ as the input to the system described by Eq. (9). Thus, we find

$$W(t,\xi)=\int_{-\infty}^{\infty}G(t,u)[K(p;u)\delta(u-\xi)]du, \tag{12}$$

where $u$ is the variable of integration and $p=d/du$. Making use of the identity

$$\int_{-\infty}^{\infty}f(u)p^k\delta(u-\xi)du\equiv(-1)^kf^{(k)}(\xi), \tag{13}$$

Eq. (12) reduces to the desired relation, namely,

$$W(t,\xi)=b_0(\xi)G(t,\xi)-\frac{\partial}{\partial\xi}[b_1(\xi)G(t,\xi)]$$
$$+\cdots+(-1)^m\frac{\partial^m}{\partial\xi^m}[b_m(\xi)G(t,\xi)]. \tag{14}$$

This relation may be expressed more compactly in the form

$$W(t,\xi)=K^*(p;\xi)G(t,\xi) \tag{15}$$

where $p$ should be interpreted as $d/d\xi$, and the operator $K^*(p;\xi)$ is the adjoint of $K(p;\xi)$.

Equation (15) shows that the problem of the determination of $W(t,\xi)$ may be reduced to the somewhat simpler problem of finding a Green's function satisfying the initial conditions expressed by Eq. (11). This, evidently, is equivalent to finding the impulsive response of the system described by Eq. (9).

In finding $G(t,\xi)$ we shall make use of the assumption that the operator $L(p;t)$ does not vary appreciably over the effective duration of $G(t,\xi)$. In general, Eq. (10) may be rewritten as

$$L(p;\xi)G(t,\xi)=\delta(t-\xi)+[L(p;\xi)-L(p;t)]G(t,\xi), \tag{16}$$

where the coefficients in $L(p;\xi)$ are the constants $a_\nu(\xi)$ and $b_\mu(\xi)$, which are the values of $a_\nu(t)$ and $b_\mu(t)$ at the instant of application of the unit impulse. Now since the network has been assumed to be a slowly varying one, $a_\nu(t)$ and $b_\mu(t)$ will not differ appreciably from $a_\nu(\xi)$ and

[2] The effective duration of a signal is, roughly speaking, the length of the interval outside of which the amplitude of the signal is small by comparison with its maximum value.

$b_n(\xi)$ over the effective duration of $G(t, \xi)$. Hence, the second term in the right-hand member of Eq. (16) may be regarded as a perturbation and accordingly a perturbation procedure[3] may be used for the determination of $G(t, \xi)$.

As the first step in the procedure, $G(t, \xi)$ is expressed in the form of a perturbation series

$$G(t, \xi)=G_1(t, \xi)+G_2(t, \xi)+G_3(t, \xi)+\cdots, \quad (17)$$

where $G_1(t, \xi)$ is the first approximation to $G(t, \xi)$, and $G_2(t, \xi)$, $G_3(t, \xi)$, etc., are the successive correction terms. Substituting this series into Eq. (16), it is found that Eq. (16) reduces to a set of iterative relations

$$L(p; \xi)G_1(t, \xi)=\delta(t-\xi), \quad (18)$$

$$L(p; \xi)G_{k+1}(t, \xi) =[L(p; \xi)-L(p; t)]G_k(t, \xi), \quad k=1, 2, \cdots, \quad (19)$$

which formally provide the solution of the problem.

The formal solution represented by Eqs. (18) and (19) may be simplified to a considerable extent, first, by making further use of the assumption that $L(p; t)$ is a slowly varying function of time, and second, by expressing Eqs. (18) and (19) in Laplace transform form. Thus, expanding the right-hand operator in Eq. (19) in a Taylor series around $t=\xi$ and neglecting all but the first, say, $N$ terms in this expansion and also in Eq. (17),[4] the iterative relation expressed by Eq. (19) assumes the following form:

$$-L(p; \xi)G_{k+1}(t, \xi)\cong\left[(t-\xi)\frac{\partial L(p; \xi)}{\partial \xi} +\frac{1}{2!}(t-\xi)^2\frac{\partial^2 L(p; \xi)}{\partial \xi^2} +\cdots+\frac{1}{N!}(t-\xi)^N\frac{\partial^N L(p; \xi)}{\partial \xi^N}\right]G_k(t, \xi). \quad (20)$$

Next, transforming both sides of Eq. (20) with respect to $t'=t-\xi$ and letting $F_k(s; \xi)$ (or simply $F_k$) represent the Laplace transform of $G_k(t, \xi)$, we obtain:

$$F_1=1/L(s; \xi) \quad (21)$$

and

$$F_{k+1}\cong F_1\left\{\frac{\partial}{\partial s}\left[F_k\frac{\partial L(s; \xi)}{\partial \xi}\right]+\cdots+\frac{(-1)^{N-1}}{N!} \times\frac{\partial^N}{\partial s^N}\left[F_k\frac{\partial^N L(s; \xi)}{\partial \xi^N}\right]\right\}, \quad k=1, 2, \cdots. \quad (22)$$

The above relations express essentially the solution of the problem. It will be noted that from these relations the terms $F_1$, $F_2$, $F_3$, etc. can be obtained in succession by using nothing more complicated than routine differentiation. Once $F_1$, $F_2$, $F_3$, etc. have been determined, the terms $G_1(t, \xi)$, $G_2(t, \xi)$, $\cdots$, $G_N(t, \xi)$, forming the $N$th order approximation to $G(t, \xi)$, can be found by using a table of Laplace transforms. And finally, the $N$th order approximation to $W(t, \xi)$ is obtained in the form

$$W(t, \xi)\cong W_1(t, \xi)+W_2(t, \xi)+\cdots+W_N(t, \xi), \quad (23)$$

by substituting the $N$th order approximation to $G(t, \xi)$ into Eq. (15). These, in brief, are the steps leading to the determination of $W(t, \xi)$.

In most practical cases Eq. (23) develops as a power series in a small parameter. Thus the questions of convergence and the accuracy of the obtained approximation to $W(t, \xi)$ can usually be resolved without significant difficulties. Actually, many if not most of the variable networks encountered in practice are such that the first two or three terms in Eq. (23) provide an adequate approximation to $W(t, \xi)$.

The use of the foregoing method is well illustrated by a simple example for which an exact solution can be obtained by classical methods. Consider a low pass *RC* half-section with a periodically varying band width. The behavior of such a network is described by the first-order differential equation

$$(p+1+\epsilon\cos\omega_0 t)e_2(t)=(1+\epsilon\cos\omega_0 t)e_1(t), \quad (24)$$

where

$$\epsilon=\frac{\text{amplitude of band width variation}}{\text{mean band width}},$$

$$\omega_0=\frac{\text{frequency of band width variation}}{\text{mean band width}},$$

$$t=\text{actual time}\times\text{mean band width}.$$

Using the standard method of solution of first-order equations, the impulsive response of the network is found to be

$$W(t, \xi)=(1+\epsilon\cos\omega_0\xi) \times\exp[-(t-\xi)-(\epsilon/\omega_0)(\sin\omega_0 t-\sin\omega_0\xi)]. \quad (25)$$

Using the approximate method, we find

$$F_1=\frac{1}{L(s; \xi)}=\frac{1}{s+1+\epsilon\cos\omega_0\xi} \quad (26)$$

and

$$F_2=\frac{\epsilon\omega_0\sin\omega_0\xi}{(s+1+\epsilon\cos\omega_0\xi)^3}, \quad (27)$$

from which

$$W(t, \xi)\cong(1+\epsilon\cos\omega_0\xi)[1+(\epsilon\omega_0/2)(t-\xi)^2\sin\omega_0\xi] \times\exp[-(t-\xi)(1+\epsilon\cos\omega_0\xi)]. \quad (28)$$

[3] The perturbation method used in the sequel is based on Schelkunoff's wave perturbation method, "Approximate solution of linear differential equations," Bell Sys. Tech. J. 27, 350–364 (1948).

[4] In some cases the number of terms conserved in the two expansions need not be the same.

It can easily be verified that Eq. (28) is in agreement with Eq. (25) up to the first-order terms in $\omega_0$. Thus, whenever the frequency of band width variation is reasonably small by comparison with the mean band width, Eq. (28) provides an adequate approximation to the impulsive response of the network. A higher order approximation may be obtained, if necessary, by continuing the iteration beyond $F_2$.

---

# An Extension of Wiener's Theory of Prediction*

LOTFI A. ZADEH AND JOHN R. RAGAZZINI
*Department of Electrical Engineering, Columbia University, New York, New York*
(Received November 14, 1949)

The theory of prediction described in this paper is essentially an extension of Wiener's theory. It differs from the latter in the following respects.

1. The signal (message) component of the given time series is assumed to consist of two parts, (a) a non-random function of time which is representable as a polynomial of degree not greater than a specified number $n$ and about which no information other than $n$ is available; and (b) a stationary random function of time which is described statistically by a given correlation function. (In Wiener's theory, the signal may not contain a non-random part except when such a part is a known function of time.)
2. The impulsive response of the predictor or, in other words, the weighting function used in the process of prediction is required to vanish outside of a specified time interval $0 \leq t \leq T$. (In Wiener's theory $T$ is assumed to be infinite.)

The theory developed in this paper is applicable to a broader and more practical class of problems than that covered in Wiener's theory. As in Wiener's theory, the determination of the optimum predictor reduces to the solution of an integral equation which, however, is a modified form of the Wiener-Hopf equation. A simple method of solution of the equation is developed. This method can also be applied with advantage to the solution of the particular case considered by Wiener. The use of the theory is illustrated by several examples of practical interest.

## I. INTRODUCTION

PREDICTION—in the broad sense of the term—consists essentially of estimating the values of some function of time on the basis of a time series which may or may not contain random errors. For instance, a typical problem in prediction is as follows. Given a time series $e_1(t)$ which is composed of a signal $s(t)$ and a random disturbance (noise) $N(t)$; provide an estimate of $s(t+\alpha)$, $\alpha$ being a positive constant, as a continuous function of time. More generally, the quantity to be estimated may be a functional of $s(t)$ such as $ds/dt$, $\int s dt$, etc. In forming such estimates the mathematical operations that may be employed are usually limited by practical considerations. Thus, in most cases the operator furnishing the estimate must be linear and fixed in addition to the obvious requirement of being physically realizable. The physical counterpart of such an operator is what is commonly known as a predictor or an estimator.

It is evident that a function of time cannot be predicted intelligently unless sufficient *a priori* information is available about both the function and the errors. The nature of such information, as well as the characteristics of the signal and noise, can assume a variety of forms. Of these the more common ones have been investigated in recent years with the result that for certain classes of time series it is now possible to design predictors which make optimum use of the *a priori* information concerning the signal and the noise. Thus, when the given time series is stationary and the correlation functions of the signal and noise are known, one can use Wiener's theory[1] to arrive at the specifications of the optimum predictor, that is, one minimizing the mean-square value of the prediction error. On the other hand, when, as is often the case in practice, the given time series is non-stationary, the available theories of prediction, notably Phillips and Weiss' theory,[2] do not lead to the best possible predictor except for a narrow class of time series. It is possible, however, to extend Wiener's theory in many different directions thereby making it applicable to a wider class of problems than is covered by either Wiener's or Phillips and Weiss' theories in their present forms. One such extension is discussed in this paper. A feature of the extension is that the signal (message) is assumed to consist of a stationary component superimposed on a non-random function of time which is known to be representable as a polynomial of degree less than or equal to a specified number $n$. It will also be shown that the general method developed for treating this problem can be applied with advantage to the solution of many cases of practical

* This work was performed in association with the Special Projects Department of The M. W. Kellogg Company for the Watson Laboratories of the Air Materiel Command.

[1] N. Wiener, "The extrapolation, interpolation, and smoothing of stationary time series," Report of the Services 19, Research Project DIC-6037, M.I.T. (February, 1942). Published in book form by John Wiley and Sons, Inc., New York (1949).

[2] R. S. Phillips and P. R. Weiss, "Theoretical calculation on best smoothing of position data for gunnery prediction," Report 532, Rad. Lab., M.I.T. (February, 1944).

interest as well as the particular case considered by Wiener.

## II. FORMULATION

Consider a given time series $e_1(t)$ which is the sum of a function $s(t)$ (signal) and a stationary random disturbance $N(t)$. Let $s^*(t)$ be the quantity to be estimated and let $s^*(t)$ be related to $s(t)$ through a given linear operator $K(p)$, i.e.,

$$s^*(t)=K(p)s(t). \tag{1}$$

$K(p)$ may be thought of as the system function of an *ideal predictor*, i.e., a predictor capable of perfect prediction in the absence of noise. In many cases, particularly those involving actual prediction, the operator $K(p)$ is not physically realizable so that the process of estimation cannot be carried out exactly even in the absence of random disturbances.

Frequently it will be convenient to use a different, though equivalent representation of Eq. (1), i.e.,

$$s^*(t)=\int_{-\infty}^{\infty} k(\tau)s(t-\tau)d\tau, \tag{2}$$

where $\tau$ is the variable of integration and $k(t)$ represents the impulsive response of the ideal predictor. $K(p)$ shall be referred to as the ideal prediction operator. As a matter of convenience, the more common of the many possible forms which $K(p)$ and $k(t)$ can assume are given in Table I.

Like all theories of prediction, the theory to be described applies only to a special class of time series. The time series to be considered in the work which follows will be assumed to consist of a signal $s(t)$ and noise $N(t)$, with the signal being composed of a random component $M(t)$ superposed upon a non-random function of time $P(t)$, i.e.,

$$s(t)=M(t)+P(t). \tag{3}$$

The assumptions made concerning the characteristics of $P(t)$, $M(t)$, and $N(t)$, are as follows:

(a) $P(t)$ is assumed to be representable as a polynomial in $t$ of degree not higher than a specified number $n$.

(b) $M(t)$ and $N(t)$ are stationary functions of time described respectively by their auto-correlation functions $\psi_M(\tau)$ and $\psi_N(\tau)$.

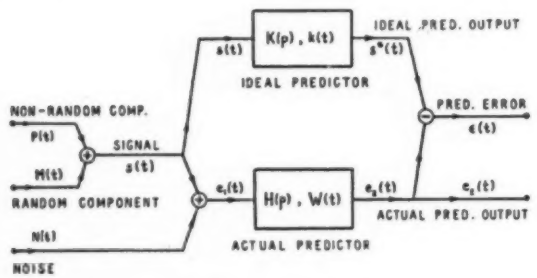


FIG. 1. Flow diagram of prediction process.

TABLE I. Common forms of the prediction operators $K(p)$ and $k(t)$.

| Relation between $s^*(t)$ and $s(t)$ | Significance of the quantity to be estimated | $K(p)$ | $k(t)$ |
|---|---|---|---|
| $s^*(t)=s(t)$ | Present value of $s(t)$ | $1$ | $\delta(t)$ |
| $s^*(t)=\dot{s}(t)$ | Present value $\dot{s}(t)$ | $p$ | $\delta^{(1)}(t)$ |
| $s^*(t)=\ddot{s}(t)$ | Present value of $\ddot{s}(t)$ | $p^2$ | $\delta^{(2)}(t)$ |
| $s^*(t)=s(t-\alpha)$ | Past or future value of $s(t)$ depending respectively on whether $\alpha$ is a positive or negative constant | $e^{-\alpha p}$ | $\delta(t-\alpha)$ |

*Note.*—$\delta(t)$ denotes a unit impulse at $t=0$, and $\delta^{(p)}(t)$ stands for the $p$th derivative of $\delta(t)$ with respect to $t$ (time).

(c) $M(t)$ and $N(t)$ have zero mean and are uncorrelated. This assumption is introduced only for the purpose of simplification and is not essential to the analysis. The condition expressed by (c) prevails in most practical cases.

Referring to Fig. 1, these inputs are shown being applied to the actual predictor whose system function is $H(p)$ and whose impulsive response is $W(t)$. The output of the predictor, $e_2(t)$, may be expressed in operational form

$$e_2(t)=H(p)e_1(t) \tag{4}$$

or, alternatively, in the form of a superposition integral

$$e_2(t)=\int_0^{\infty} W(\tau)e_1(t-\tau)d\tau. \tag{5}$$

An important characteristic of the actual predictor is the so-called prediction or estimation error $\epsilon$, which is defined as the difference between the output of the predictor and the quantity to be estimated, $s^*(t)$. Equation-wise this is:

$$\epsilon=e_2(t)-s^*(t). \tag{6}$$

If there were no noise and if $K(p)$ were physically realizable there would be no prediction error and $H(p)$ would be identical with $K(p)$. This, of course, is the trivial case of the prediction problem. In what follows it will be assumed that either because of the presence of noise or physical unrealizability of $K(p)$, or both, $H(p)$ cannot be the same as $K(p)$.

The available *a priori* information about $s(t)$ and $N(t)$ is assumed to consist of $n$, $\psi_M(\tau)$, and $\psi_N(\tau)$. The problem is to specify the system function or the impulsive response of a predictor that would minimize in a certain sense the prediction error $\epsilon=e_2(t)-s^*(t)$. By analogy with Wiener's theory it will be postulated that the optimum predictor is the one in which: (a) the ensemble mean of $\epsilon$ is equal to zero (for all values of $t$), and (b) the ensemble variance of $\epsilon$ is a minimum. Denoting the ensemble average by the symbol $\langle\ \rangle_{Av}$, these conditions read:

(a) $\langle\epsilon\rangle_{Av}=0$ or, equivalently, $\langle e_2(t)\rangle_{Av}\equiv\langle s^*(t)\rangle_{Av}$, (7)

(b) $\sigma^2=\langle\epsilon^2\rangle_{Av}=$ minimum, (8)

where $\sigma^2$, the ensemble variance of $\epsilon$, is equal to the mean-square value of the prediction error. In what follows, conditions (a) and (b) will be used as the basis for the determination of the optimum predictor.

## III. DETERMINATION OF THE IMPULSIVE RESPONSE OF THE OPTIMUM PREDICTOR

It will be recalled that the output of a predictor may be expressed in the form of a superposition integral

$$e_2(t)=\int_0^\infty W(\tau)e_1(t-\tau)d\tau \tag{9}$$

where $\tau$ is a dummy variable and $W(t)$ represents the impulse response of the predictor. In practice it is usually found necessary to restrict the duration of sampling of the input time series to a finite constant $T$, meaning in other words that $W(t)$ must be zero outside the interval $0\leq t\leq T$. To place this property in evidence Eq. (9) will be written in the following form:

$$e_2(t)=\int_0^T W(\tau)e_1(t-\tau)d\tau. \tag{10}$$

In the limiting case where the duration of sampling is infinite ($T\to\infty$) Eq. (10) becomes identical with Eq. (9).

By hypothesis,

$$e_1(t)=P(t)+M(t)+N(t). \tag{11}$$

Substituting Eq. (11) into Eq. (10) and making use of the identity

$$P(t-\tau)\equiv P(t)-\tau\dot{P}(t)+\frac{\tau^2}{2!}\ddot{P}(t)+\cdots+(-1)^n\frac{\tau^n}{n!}P^{(n)}(t), \tag{12}$$

it is found that $e_2(t)$ may be expressed as:

$$e_2(t)=\mu_0P(t)-\mu_1\dot{P}(t)+\frac{\mu_2}{2!}\ddot{P}(t)+\cdots+(-1)^n\frac{\mu_n}{n!}P^{(n)}(t)+\int_0^T W(\tau)M(t-\tau)d\tau+\int_0^T W(\tau)N(t-\tau)d\tau, \tag{13}$$

where $\mu_0$, $\mu_1$, $\mu_2$, etc., designate the moments of $W(t)$, i.e.,

$$\mu_\nu=\int_0^T \tau^\nu W(\tau)d\tau, \quad \nu=0, 1, 2, \cdots n. \tag{14}$$

Since $M(t)$ and $N(t)$ are stationary (with zero mean), it follows that the ensemble means of $e_2(t)$ and $s^*(t)$ depend only on the non-random component of the signal, i.e.,

$$\langle e_2(t)\rangle_{Av}=\int_0^T W(\tau)P(t-\tau)d\tau \tag{15}$$

or

$$\langle e_2(t)\rangle_{Av}=\mu_0P(t)-\mu_1\dot{P}(t)+\frac{\mu_2}{2!}\ddot{P}(t)+\cdots+(-1)^n\frac{\mu_n}{n!}P^{(n)}(t), \tag{16}$$

and

$$\langle s^*(t)\rangle_{Av}=\langle K(p)s(t)\rangle_{Av} \tag{17}$$

or

$$\langle s^*(t)\rangle_{Av}=K(p)P(t). \tag{18}$$

Comparing Eqs. (16) and (18), condition (a) is reduced to

$$K(p)P(t)\equiv\mu_0P(t)-\mu_1\dot{P}(t)+\frac{\mu_2}{2!}\ddot{P}(t)+\cdots+(-1)^n\frac{\mu_n}{n!}P^{(n)}(t). \tag{19}$$

Equation (19), being an identity, determines the values of $\mu_0$, $\mu_1$, $\cdots$, and $\mu_n$. In other words, *the ideal prediction operator $K(p)$ determines through Eq. (19) the first $n+1$ moments of the impulsive response of the optimum predictor.*

As an illustration of the foregoing statement consider a case where the quantity to be estimated is the derivative of $s(t)$, i.e., $s^*(t)=\dot{s}(t)$. For this case Eq. (19) reduces to

$$\dot{P}(t)\equiv\mu_0P(t)-\mu_1\dot{P}(t)+\frac{\mu_2}{2!}\ddot{P}(t)+\cdots+(-1)^n\frac{\mu_n}{n!}P^{(n)}(t), \tag{20}$$

and a term by term comparison of the left-hand and right-hand sides of Eq. (20) yields:

$$\begin{aligned}\mu_0&=\int_0^T W(\tau)d\tau=0\\ \mu_1&=\int_0^T \tau W(\tau)d\tau=-1\\ \mu_2&=\int_0^T \tau^2W(\tau)d\tau=0\\ &\cdots\\ \mu_n&=\int_0^T \tau^nW(\tau)d\tau=0.\end{aligned} \tag{21}$$

These, therefore, are the $n+1$ constraints which the impulsive response of a derivative estimating network must satisfy.

As the second example consider a case where $K(p)s(t)=s(t-\alpha)$, $\alpha$ being a positive or negative constant. For

this case Eq. (19) reads

$$P(t-\alpha)\equiv\mu_0 P(t)-\mu_1\dot{P}(t)+\frac{\mu_2}{2!}\ddot{P}(t)+\cdots+(-1)^n\frac{\mu_n}{n!}P^{(n)}(t). \quad (22)$$

Rewriting $P(t-\alpha)$ as

$$P(t-\alpha)\equiv P(t)-\alpha\dot{P}(t)+\frac{\alpha^2}{2!}\ddot{P}(t)+\cdots+(-1)^n\frac{\alpha^n}{n!}P^{(n)}(t), \quad (23)$$

and making in Eq. (22) a term-by-term comparison of the coefficients of $P(t)$, $\dot{P}(t)$, etc., it is easily found that:

$$\begin{aligned}\mu_0&=\int_0^T W(\tau)d\tau=1\\ \mu_1&=\int_0^T \tau W(\tau)d\tau=\alpha\\ &\cdots\\ \mu_n&=\int_0^T \tau^n W(\tau)d\tau=\alpha^n,\end{aligned} \quad (24)$$

which thus represent the constraints imposed upon $W(t)$ in case the quantity to be estimated is $s(t-\alpha)$.

The problem that remains to be solved is that of minimizing $\sigma^2$. For this purpose it will be necessary to develop an explicit expression for $\sigma^2$ in terms of $W(t)$ and the auto-correlation functions of the signal and noise. Assuming that condition (a) is satisfied, it follows from inspection of Eqs. (6), (13), and (19) that the prediction error is given by the expression

$$\epsilon=\int_0^T W(\tau)[M(t-\tau)+N(t-\tau)]d\tau-K(p)M(t) \quad (25)$$

or equivalently

$$\epsilon=\int_0^T W(\tau)[M(t-\tau)+N(t-\tau)]d\tau-\int_{-\infty}^{\infty}k(\tau)M(t-\tau)d\tau \quad (26)$$

where $k(t)$ is the impulsive response of the ideal predictor. The mean-square value of $\epsilon$ may be written as

$$\sigma^2=\langle\epsilon^2\rangle_{Av}=\lim_{L\to\infty}\frac{1}{L}\int_0^L \epsilon^2 dt \quad (27)$$

or

$$\sigma^2=\lim_{L\to\infty}\frac{1}{L}\int_0^L dt\left\{\int_0^T W(\tau)[M(t-\tau)+N(t-\tau)]d\tau-\int_{\infty}^{\infty}k(\tau)M(t-\tau)d\tau\right\}^2. \quad (28)$$

A typical term of Eq. (28) such as

$$\lim_{L\to\infty}\frac{1}{L}\int_0^L dt\left[\int_0^T W(\tau)M(t-\tau)d\tau\right]^2 \quad (29)$$

is expressible in the form of a triple integral

$$\int_0^T\int_0^T d\tau_1 d\tau_2 W(\tau_1)W(\tau_2)\times\lim_{L\to\infty}\frac{1}{L}\int_0^L M(t-\tau_1)M(t-\tau_2)dt \quad (30)$$

which in view of the definition of the auto-correlation function of $M(t)$, i.e.,

$$\psi_M(\tau)=\lim_{L\to\infty}\frac{1}{L}\int_0^L M(t)M(t-\tau)dt \quad (31)$$

may be written as

$$\int_0^T\int_0^T W(\tau_1)W(\tau_2)\psi_M(\tau_1-\tau_2)d\tau_1 d\tau_2. \quad (32)$$

Proceeding similarly in the case of other terms, Eq. (28) reduces finally to the following expression:

$$\begin{aligned}\sigma^2=&\int_0^T\int_0^T W(\tau_1)W(\tau_2)[\psi_M(\tau_1-\tau_2)\\ &+\psi_N(\tau_1-\tau_2)]d\tau_1 d\tau_2\\ &-2\int_{\infty}^{\infty}\int_0^T W(\tau_1)k(\tau_2)\psi_M(\tau_1-\tau_2)d\tau_1 d\tau_2\\ &+\int_{-\infty}^{\infty}\int_{-\infty}^{\infty}k(\tau_1)k(\tau_2)\psi_M(\tau_1-\tau_2)d\tau_1 d\tau_2\end{aligned} \quad (33)$$

where, to recapitulate: $\tau_1$, $\tau_2$ = dummy variables; $W(t)$ = impulsive response of the predictor; $\psi_M(\tau)$ = auto-correlation function of $M(t)$ [$M(t)$ is the stationary part of the input signal]; $\psi_N(\tau)$ = auto-correlation function of $N(t)$ [$N(t)$ is the input noise]; $k(t)$ = impulsive response of the ideal predictor.

Returning to the problem of minimization of $\sigma^2$ it will be noted first that the last term in Eq. (33) is independent of $W(t)$ and hence, insofar as minimization of $\sigma^2$ is concerned, need not be considered. Second, it will be recalled that $W(t)$ is subject to the $n+1$ constraints

expressed by Eq. (14); therefore, the problem of minimizing $\sigma^2$ with respect to the class of $W(t)$'s satisfying Eq. (14) reduces essentially to an isoperimetric problem in the calculus of variations. Following the standard approach to such problems, one is led to minimizing the following expression:

$$I=\sigma^2-2\lambda_0\mu_0-2\lambda_1\mu_1-\cdots-2\lambda_n\mu_n \tag{34}$$

or, more explicitly

$$I=\int_0^T W(\tau_1)d\tau_1\Big\{\int_0^T W(\tau_2)[\psi_M(\tau_1-\tau_2)+\psi_N(\tau_1-\tau_2)]d\tau_2-2\int_{-\infty}^{\infty}k(\tau_2)\psi_M(\tau_1-\tau_2)d\tau_2-2\lambda_0-2\lambda_1\tau_1-\cdots-2\lambda_n\tau_1^n\Big\} \tag{35}$$

where the constants $\lambda_0, \lambda_1, \cdots, \lambda_n$, are the Lagrangian multipliers. Proceeding in the usual manner, that is, setting the variation of $I$ equal to zero, it is easily found that $I$ and hence $\sigma^2$ is a minimum provided $W(t)$ satisfies the following integral equation:

$$\int_0^T W(\tau)[\psi_M(t-\tau)+\psi_N(t-\tau)]d\tau=\lambda_0+\lambda_1 t+\cdots+\lambda_n t^n+\int_{-\infty}^{\infty}k(\tau)\psi_M(t-\tau)d\tau,\quad 0\le t\le T. \tag{36}$$

This equation together with the $n+1$ constraints expressed by Eq. (14) provides the basis for the determination of the optimum predictor. It will be observed that in the particular case where $n=0$, $T=\infty$, and $k(t)=\delta(t+\alpha)$ [$\delta(t)$ standing, as usual, for a unit impulse at $t=0$], Eq. (36) reduces to

$$\int_0^{\infty} W(\tau)[\psi_M(t-\tau)+\psi_N(t-\tau)]d\tau=\psi_M(t+\alpha),\quad t>0 \tag{37}$$

which is essentially the integral equation of Wiener's theory. On the other hand, in the special case where $M(t)\equiv 0$, Eq. (36) reduces to

$$\int_0^T W(\tau)\psi_N(t-\tau)d\tau=\lambda_0+\lambda_1 t+\cdots+\lambda_n t^n,\quad 0\le t\le T \tag{38}$$

which is the integral equation of Phillips and Weiss' theory. Thus, the integral equations of Wiener's, and Phillips and Weiss' theories are special cases of Eq. (36).

## IV. SOLUTION OF THE INTEGRAL EQUATION

In the general case where $\psi_M(\tau)$ and $\psi_N(\tau)$ are prescribed but otherwise arbitrary auto-correlation functions, the complicated nature of the integral equation makes it appear that the solution of Eq. (36) is a formidable problem. In reality, the problem is not as difficult as it may seem, for by using a procedure to be described, the general case can be reduced to a special case which has a simple solution.

Preliminary to the discussion of this procedure it will be expedient to introduce the spectral densities of $M(t)$, $N(t)$, and $M(t)+N(t)$. Denoting these by $S_M(\omega^2)$, $S_N(\omega^2)$, and $S(\omega^2)$, respectively, and recalling that the spectral density of a function is the inverse Fourier transform of its auto-correlation function,[1] it follows that

$$S_M(\omega^2)=\int_{-\infty}^{\infty}\psi_M(\tau)e^{-j\omega\tau}d\tau \tag{39}$$

$$S_N(\omega^2)=\int_{-\infty}^{\infty}\psi_N(\tau)e^{-j\omega\tau}d\tau \tag{40}$$

and

$$S(\omega^2)=S_M(\omega^2)+S_N(\omega^2). \tag{41}$$

Now the spectral density function $S(\omega^2)$ may be factored[1] into the product of two conjugate factors

$$S(\omega^2)=G(j\omega)\cdot G(-j\omega) \tag{42}$$

such that both $G(j\omega)$ and $1/G(j\omega)$ are analytic in the right half of the $j\omega$-plane. Usually $S(\omega^2)$ is assumed to be a rational function of $\omega^2$ of the form

$$S(\omega^2)=[A(\omega^2)/B(\omega^2)], \tag{43}$$

where $A(\omega^2)$ and $B(\omega^2)$ are polynomials in $\omega^2$. For such cases the process of factorization is quite straightforward as can be seen from the following examples:

(a) $S(\omega^2)=\omega^2;\qquad G(j\omega)=j\omega.$

(b) $S(\omega^2)=\dfrac{1}{\omega^2+\omega_0^2};\quad G(j\omega)=\dfrac{1}{j\omega+\omega_0}.$

(c) $S(\omega^2)=\dfrac{\omega^2+a^2}{\omega^4+b^2\omega^2+c^4};$

$$G(j\omega)=\frac{j\omega+a}{(j\omega)^2+j\omega(b^2+2c^2)^{\frac{1}{2}}+c^2}.$$

To summarize, a rational spectral density function may be written as

$$S(\omega^2)=|G(p)|^2_{p=j\omega} \tag{44}$$

where $G(p)$ is of the form:

$$G(p)=\frac{Q(p)}{R(p)}=\frac{a_0+a_1p+\cdots+a_mp^m}{b_0+b_1p+\cdots+b_lp^l}, \tag{45}$$

and the polynomials $Q(p)$ and $R(p)$ do not have any zeros in the right half of the $p$-plane.

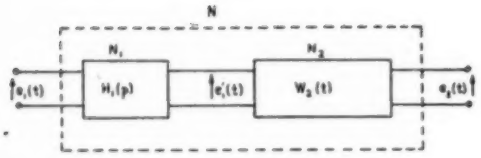


FIG. 2. Division of the predictor into the component networks $N_1$ and $N_2$.

The outline of the procedure used[3] for the solution of Eq. (36) can be best explained with reference to Fig. 2. The predictor $N$ is assumed to be composed of two networks $N_1$ and $N_2$. The function of $N_1$ is to suitably modify some of the characteristics of the input time series $e_1(t)$, while that of $N_2$ is to provide the desired prediction through operating on the time series $e_1'(t)$, which is the output of $N_1$. It will be seen later that it is possible to choose $N_1$ in such a manner that the determination of the impulsive response of $N_2$ becomes an easily solvable problem. Then, once $W_2(t)$ (the impulsive response of $N_2$) is determined, the impulsive response of $N$, $W(t)$, can easily be found from the relation

$$W(t)=H_1(p)W_2(t), \tag{46}$$

where $H_1(p)$ is the system function of $N_1$. The choice of $H_1(p)$ and the problem of determination of $W_2(t)$ are discussed in the sequel.

It is evident that the problem of determination of $W_2(t)$ is similar to that of the determination of $W(t)$, except that the characteristics of the input time series are different for the two problems. An inspection of the integral equation (36) shows that it can be solved rather easily when the input to the predictor consists of a polynomial in $t$ and a stationary component whose spectral density is a polynomial in $\omega^2$. Therefore, in order to make the determination of $W_2(t)$ a simple problem, it is necessary to provide $N_2$ with an input which has this property. It is not difficult to verify that such a condition will obtain if, and only if, the system function of $N_1$ is chosen to be

$$H_1(p)=R(p), \tag{47}$$

where $R(p)$ is the denominator of $G(p)$ [cf. Eq. (45)]. With this choice of $H_1(p)$ the input to $N_2$ will consist of a polynomial in $t$ of the same degree[4] as $P(t)$, and a stationary component $M'(t)+N'(t)$ whose spectral density is

$$S'(\omega^2)=|H_1(j\omega)|^2S(\omega^2) \tag{48}$$

or, in view of Eqs. (43), (44), and (47),

$$S'(\omega^2)=A(\omega^2), \tag{49}$$

where $A(\omega^2)$ is the numerator of $S(\omega^2)$. It will be noted that $A(\omega^2)$ is a polynomial of the form

$$A(\omega^2)=\gamma_0+\gamma_1\omega^2+\cdots+\gamma_m\omega^{2m}, \tag{50}$$

and correspondingly the auto-correlation function of $M'(t)+N'(t)$ is

$$\psi_{M'}(\tau)+\psi_{N'}(\tau)=\gamma_0\delta(\tau)-\gamma_1\delta^{(2)}(\tau)+\cdots+(-1)^m\gamma_m\delta^{(2m)}(\tau), \tag{51}$$

where $\delta^{(\nu)}(\tau)$ represents the impulse function of $\nu$th order [i.e., the $\nu$th derivative of the unit impulse function $\delta(\tau)$].

In addition to $\psi_{M'}(\tau)+\psi_{N'}(\tau)$, a number of other quantities associated with the input to $N_2$ enter the integral equation satisfied by $W_2(t)$. The significance of each of these quantities, as well as their expressions, are as follows:

(a) $S_{M'}(\omega^2)=$ spectral density of $M'(t)$
$$=S_M(\omega^2)|R(j\omega)|^2. \tag{52}$$

(b) $\psi_{M'}(\tau)=$ auto-correlation function of $M'(t)$
$$=\frac{1}{2\pi}\int_{-\infty}^{\infty}S_M(\omega^2)|R(j\omega)|^2e^{j\omega\tau}d\omega. \tag{53}$$

(c) $k'(t)=$ ideal impulsive response for $N_2$
$$=[1/R(p)]k(t). \tag{54}$$

In terms of these quantities the integral equation satisfied by $W_2(t)$ reads:

$$\int_0^{\infty}W_2(\tau)[\psi_{M'}(t-\tau)+\psi_{N'}(t-\tau)]d\tau=\lambda_0'+\lambda_1't+\cdots+\lambda_n't^n+\int_{-\infty}^{\infty}k'(\tau)\psi_{M'}(t-\tau)d\tau, \quad t\geq 0. \tag{55}$$

It will be noticed that in the case of $W_2(t)$ the upper limit of the integral is infinity, while in the case of $W(t)$ [cf. Eq. (36)] it is $T$. The explanation for this difference is that $W_2(t)$ need not vanish for $t>T$, even though $W(t)$ is required to do so. Thus in general, $W_2(t)$ will be piecewise analytic in the interval $0<t<\infty$ as is illustrated in Fig. 3. Denoting the parts of $W_2(t)$ extending over the intervals $0\leq t\leq T$ and $T<t<\infty$ by $U(t)$ and $V(t)$, respectively, the relation connecting $W(t)$ and $W_2(t)$ [cf. Eq. (46)] may be rewritten in the following form:

$$W(t)=R(p)U(t) \tag{56a}$$

and

$$0=R(p)V(t). \tag{56b}$$

These relations show that $W(t)$ is completely determined by the part of $W_2(t)$ which extends over the interval $0\leq t\leq T$; the form of $W_2(t)$ outside this interval is irrelevant to the determination of $W(t)$.

[3] The appendix of a report by Bode, Blackman, and Shannon, "Data smoothing and prediction in fire-control systems," Research and Development Board, Washington, D. C. (August, 1948), contains a brief exposition of a method which is similar in certain respects to the method described here.

[4] It is tacitly assumed that $R(p)$ does not have a zero at the origin or, in other words, that $S(\omega^2)$ does not have a pole at zero frequency.

Returning to the integral equation (55), it will be noted that the range of integration $0\leq\tau<\infty$ may be divided into two parts, $0\leq\tau\leq T$ and $T<\tau<\infty$, involving $U(t)$ and $V(t)$, respectively. Since $V(t)$ is determined by Eq. (56b) to within a finite number of constants, the integral equation in question degenerates into an integral equation involving only $U(t)$:

$$\int_0^T U(\tau)[\psi_M'(t-\tau)+\psi_N'(t-\tau)]d\tau=\lambda_0'+\lambda_1't+\cdots+\lambda_n't^n+\int_{-\infty}^{\infty}k'(\tau)\psi_M'(t-\tau)d\tau,\quad 0\leq t\leq T. \quad (57)$$

Upon substitution of Eqs. (52), (53), and (54), and performing minor simplifications, Eq. (57) reads

$$\int_0^T U(\tau)[\gamma_0\delta(t-\tau)-\gamma_1\delta^{(2)}(t-\tau)+\cdots+(-1)^m\gamma_m\delta^{(2m)}(t-\tau)]d\tau=\lambda_0'+\lambda_1't+\cdots+\lambda_n't^n+\frac{1}{2\pi}\int_{-\infty}^{\infty}S_M(\omega^2)K(j\omega)R(-j\omega)e^{j\omega t}d\omega. \quad (58)$$

Making use of the identity

$$\int_0^T U(\tau)\delta^{(2\nu)}(t-\tau)d\tau\equiv p^{2\nu}U(t), \quad (59)$$

Equation (58) may be rewritten as

$$[\gamma_0-\gamma_1p^2+\cdots+(-1)^m\gamma_mp^{2m}]U(t)=\lambda_0'+\lambda_1't+\cdots+\lambda_n't^n+\frac{1}{2\pi}\int_{-\infty}^{\infty}S_M(\omega^2)K(j\omega)R(-j\omega)e^{j\omega t}d\omega. \quad (60)$$

Since in this equation the left-hand side operator is simply $A(-p^2)$ [cf. Eq. (50)], the integral equation (57) finally reduces to the following differential equation:

$$A(-p^2)U(t)=\lambda_0'+\lambda_1't+\cdots+\lambda_n't^n+\frac{1}{2\pi}\int_{-\infty}^{\infty}S_M(\omega^2)K(j\omega)R(-j\omega)e^{j\omega t}d\omega. \quad (61)$$

The general solution of this equation is of the form:

$$U(t)=A_0'+A_1't+\cdots+A_n't^n+B_1'\exp(\alpha_1t)+B_2'\exp(\alpha_2t)+\cdots+B_{2m}'\exp(\alpha_{2m}t)+\frac{1}{2\pi}\int_{-\infty}^{\infty}\frac{S_M(\omega^2)}{A(\omega^2)}K(j\omega)R(-j\omega)e^{j\omega t}d\omega,\quad 0\leq t\leq T, \quad (62)$$

where $A_0'$, $A_1'$, $\cdots$, $A_n'$ and $B_1'$, $B_2'$, $\cdots$, $B_{2m}'$ are as yet undetermined constants, and $\alpha_1$, $\alpha_2$, $\cdots$, $\alpha_{2m}$ are the roots of the characteristic equation

$$A(-p^2)=0. \quad (63)$$

In brief, Eq. (62) provides an explicit expression for $U(t)$ involving $2m+n+1$ undetermined constants. Availability of such an expression reduces the problem of determination of $W(t)$ to a relatively routine matter which is discussed in the following section.

## V. DERIVATION OF AN EXPLICIT EXPRESSION FOR $W(t)$

Recalling that $W(t)$ is related to $U(t)$ through the operational relation

$$W(t)=R(p)U(t), \quad (56a)$$

and substituting $U(t)$ as given by Eq. (62) into Eq. (56a), it is readily found that in the most general case $W(t)$ is given by the following expression:

$$W(t)=[u(t)-u(t-T)]\left\{A_0+A_1t+\cdots+A_nt^n+B_1\exp(\alpha_1t)+\cdots+B_{2m}\exp(\alpha_{2m}t)+\frac{1}{2\pi}R(p)\int_{-\infty}^{\infty}\frac{S_M(\omega^2)}{A(\omega^2)}K(j\omega)R(-j\omega)e^{j\omega t}d\omega\right\}+C_1\delta(t)+\cdots+C_{l-m}\delta^{(l-m-1)}(t)+D_1\delta(t-T)+\cdots+D_{l-m}\delta^{(l-m-1)}(t-T) \quad (64)$$

where the $A$'s, $B$'s, $C$'s, and $D$'s are as yet undetermined constants, and the unit step functions $u(t)$ and $u(t-T)$ are used simply to indicate that $W(t)$ is zero outside the interval $0\leq t\leq T$. The impulse functions contained in the expression for $W(t)$ arise from operation by $R(p)$ on the discontinuities of $U(t)$ at $t=0$ and $t=T$. It will be observed that the order of these impulse functions does not exceed $l-m-1$, which is one-half the order of the zero of $S(\omega^2)$ at infinity minus one. This is due to the fact that the first $m-1$ derivatives of $U(t)$ vanish at $t=0$ and $t=T$. It is not difficult to verify that if this would not have been the case, the mean-square error at the output of $N_2$ would be infinite.

Having obtained the general expression for $W(t)$ in the form of Eq. (64), there remains the problem of determination of the $2l+n+1$ unknown constants. These can be found in the following manner:

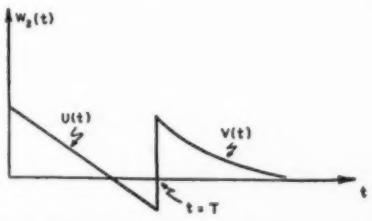


FIG. 3. Form of the impulsive response of $N_2$.

1. Substituting $W(t)$ as given by Eq. (64) into the integral equation (36) and requiring that the equation be satisfied identically, leads to $2l$ linear homogeneous equations in the $A$'s, $B$'s, $C$'s, and $D$'s.

2. Substituting $W(t)$ as given by Eq. (64) into the $n+1$ moment equations

$$\int_0^T \tau^\nu W(\tau)d\tau=\mu_\nu, \quad \nu=0, 1, 2, \cdots, n \tag{65}$$

yields other $n+1$ linear equations. These $n+1$ equations, together with the $2l$ equations obtained in (1), provide a system of $2l+n+1$ linear equations in the unknown constants. Solution of this system gives the values of the $A$'s, $B$'s, $C$'s, and $D$'s and thus completes the process of determination of $W(t)$.

It should be remarked that in some cases it is advantageous to deal with the system function $H(p)$ of the predictor, rather than with its impulsive response $W(t)$. In such cases one can use a transformed form of the integral equation (36) which is as follows:

$$\frac{1}{2\pi}\int_{-\infty}^{\infty} H(j\omega)S(\omega^2)e^{j\omega t}d\omega=\lambda_0+\lambda_1 t+\cdots+\lambda_n t^n + \frac{1}{2\pi}\int_{-\infty}^{\infty} S_M(\omega^2)K(j\omega)R(-j\omega)e^{j\omega t}d\omega. \tag{66}$$

Using Eq. (64), the solution of this equation may be written directly as

$$\begin{aligned} H(p)=&\int_0^T (A_0+A_1 t+\cdots+A_n t^n)e^{-pt}dt \\ &+\frac{B_1}{p+\alpha_1}+\frac{B_2}{p+\alpha_2}+\cdots+\frac{B_{2m}}{p+\alpha_{2m}} \\ &-\left\{\frac{B_1\exp(\alpha_1 T)}{p+\alpha_1}+\frac{B_2\exp(\alpha_2 T)}{p+\alpha_2}+\cdots\right. \\ &\left.+\frac{B_{2m}\exp(\alpha_{2m}T)}{p+\alpha_{2m}}\right\}e^{-pT}+\frac{1}{2\pi}R(p)\int_0^T dte^{-pt} \\ &\times\int_{-\infty}^{\infty}\frac{S_M(\omega^2)}{A(\omega^2)}K(j\omega)R(-j\omega)e^{j\omega t}d\omega \\ &+C_1+C_2 p+\cdots+C_{l-m}p^{l-m-1} \\ &+(D_1+\cdots+D_{l-m}p^{l-m-1})e^{-pT}. \end{aligned} \tag{67}$$

The undetermined constants involved in this expression are found in the same manner as in the case of $W(t)$, that is, $H(p)$ as given by Eq. (67) is substituted into the integral equation (66) and the resulting expression is treated as an identity. The $2l$ linear relations between $A_0, A_1, A_2, \cdots$, etc., which are obtained in this manner are adjoined to the $n+1$ relations resulting from Eq. (65); then the system of linear equations in the unknown constants is solved for $A_0, A_1, A_2, \cdots$, etc.

In order to facilitate application of the techniques described in the preceding sections, a summary of the procedure for the determination of $W(t)$ (or $H(p)$) is given in Section VI. Furthermore, actual use of the procedure is illustrated by a few practical examples at the end of the section.

## VI. SUMMARY OF THE PROCEDURE FOR DETERMINATION OF $W(t)$ AND $H(p)$

The complete expressions for $W(t)$ (the impulsive response of the optimum predictor) and $H(p)$ (the system function of the optimum predictor) are given by Eqs. (64) and (67). In order to avoid the necessity for reference to preceding sections, the meaning of all symbols appearing in these equations is given:

$u(t)$ = unit step function.
$T$ = duration of sampling (settling time).
$A_0, A_1, \cdots, A_n, B_1, B_2, \cdots, B_{2m}, C_1, C_2, \cdots, C_{l-m}, D_1, D_2, \cdots, D_{l-m}$ = undetermined constants.
$n$ = degree of the polynomial component of the input signal.
$S_M(\omega^2)$ = spectral density of $M(t)$[$M(t)$ is the stationary part of the input signal].
$S(\omega^2)$ = spectral density of $M(t)+N(t)$[$N(t)$ is the input noise].
$A(\omega^2)$ = numerator of $S(\omega^2)$.
$B(\omega^2)$ = denominator of $S(\omega^2)$.
$Q(j\omega)$ = a factor of $A(\omega^2)$ containing all the zeros in right half of the $j\omega$-plane.
$R(j\omega)$ = a factor of $B(\omega^2)$ containing all the zeros in the left half of the $j\omega$-plane.
$2l$ = degree of $B(\omega^2)$.
$2m$ = degree of $A(\omega^2)$.
$\alpha_1, \alpha_2, \cdots, \alpha_{2m}$ = roots of the characteristic equation $A(-p^2)=0$.
$\delta(t)$ = unit impulse function.
$\delta^{(\nu)}(t)$ = $\nu$th derivative of $\delta(t)$.

The undetermined constants occurring in the expression for $W(t)$ [and $H(p)$] can be found in the following manner.

1. $W(t)$ as given by Eq. (64) is substituted into the integral equation (36) and the resulting expression is treated as an identity. This gives $2l$ homogeneous linear equations in the unknown constants. Same equations can be obtained by substituting $H(p)$, as given by Eq. (67), into the integral equation (66).

2. $W(t)$ as given by Eq. (64) is substituted into the $n+1$ constraint equations

$$\int_0^T \tau^\nu W(\tau)d\tau=\mu_\nu, \quad \nu=0, 1, \cdots, n. \tag{14}$$

where the $\mu_\nu$ are determined by the choice of the prediction operator $K(p)$ [cf. Eq. (19)]. The resulting $n+1$ linear equations in the unknown constants are adjoined to the $2l$ equations obtained from (1). The set of $2l+n+1$ linear equations thus obtained is solved for the undetermined constants $A_0, A_1, \cdots, D_{l-m}$. This concludes the process of determining $W(t)$ [or $H(p)$].

## VII. ILLUSTRATIVE EXAMPLES

### Example 1. Wiener's Theory

Wiener's theory is, in the main, a study of the particular case in which $P(t)\equiv 0$, $T=\infty$ and $K(p)=e^{-ap}$. For this case Eq. (64) gives

$$W(t)=u(t)\left\{\frac{1}{2\pi}R(p)\times\int_{-\infty}^{\infty}\frac{S_M(\omega^2)}{A(\omega^2)}K(j\omega)R(-j\omega)e^{j\omega(t-\alpha)}d\omega+B_1\exp(\alpha_1 t)+\cdots+B_{2m}\exp(\alpha_{2m}t)\right\}. \quad (68)$$

The exponential terms appearing in Eq. (68) may be made to vanish through a slight rearrangement of the factors in the first term of Eq. (68). The resulting expression for $W(t)$ is the same as that obtained by using Wiener's theory, namely,

$$W(t)=u(t)\frac{1}{2\pi}\frac{R(p)}{Q(p)}\times\int_{-\infty}^{\infty}\frac{S_M(\omega^2)}{Q(-j\omega)}R(-j\omega)e^{j\omega(t-\alpha)}d\omega. \quad (69)$$

The rearrangement amounts, essentually, to choosing a particular solution of Eq. (61) which differs from the one chosen before by the exponential terms of Eq. (68). The same result may be achieved directly by choosing $H_1(p)$ [cf. Eq. (47)] as

$$H_1(p)=R(p)/Q(p).$$

With this choice of $H_1(p)$ [in place of the one expressed by Eq. (47)] the various quantities entering Eq. (55) become:

$$S'(\omega^2)=1,$$
$$\psi_M'(\tau)+\psi_N'(\tau)=\delta(\tau),$$
$$S_M'(\omega^2)=S_M(\omega^2)\,|R(j\omega)/Q(j\omega)|^2,$$
$$K'(j\omega)=K(j\omega)Q(j\omega)/R(j\omega),$$

and hence the integral equation (55) reduces to

$$W_2(t)=u(t)\frac{1}{2\pi}\int_{-\infty}^{\infty}\frac{S_M(\omega^2)}{Q(-j\omega)}K(j\omega)R(-j\omega)e^{j\omega t}d\omega; \quad (55a)$$

Eq. (69) then follows immediately from the relation connecting $W(t)$ and $W_2(t)$ [cf. Eq. (46)].

### Example 2

The assumptions made here are as follows:

1. $M(t)\equiv 0.$
2. $n=1.$
3. $\psi_N(\tau)=e^{-a|\tau|}; \quad S_N(\omega^2)=\dfrac{2a}{\omega^2+a^2}.$

The choice of the prediction operator is left open.

*Solution*

For this case $A(-p^2)=2a$, and hence $\alpha_1=\cdots=\alpha_{2m}=0$. Also, $l=1$, $M\equiv 0$; hence Eq. (64) gives

$$W(t)=A_0+A_1t+C_1\delta(t)+D_1\delta(t-T), \quad (70)$$

and

$$H(p)=\frac{A_0}{p}(1-e^{-pT})+\frac{A_1}{p}\left(\frac{1}{p}-\frac{e^{-pT}}{p}+Te^{-pT}\right)+C_1+D_1e^{-pT}. \quad (71)$$

Substituting $H(p)$ as given by Eq. (71) into the integral equation

$$\frac{1}{2\pi}\int_{-\infty}^{\infty}\frac{2a}{a^2-p^2}H(p)e^{pt}dp=\lambda_0+\lambda_1t, \quad 0\le t\le T, \quad (72)$$

and requiring that this equation be satisfied identically, leads to the following relations:

$$aA_0-A_1-a^2C_1=0, \quad (73)$$

$$aA_0+(aT+1)A_1-a^2D_1=0. \quad (74)$$

Furthermore, substituting $W(t)$ as given by Eq. (70) into the constraint equations

$$\int_0^T W(\tau)d\tau=\mu_0 \quad (75)$$

and

$$\int_0^T \tau W(\tau)d\tau=\mu_1, \quad (76)$$

yields

$$A_0T+A_1(T^2/2)+C_1+D_1=\mu_0, \quad (77)$$

and

$$A_0(T^2/2)+A_1(T^3/3)+D_1T=\mu_1. \quad (78)$$

The unknown constants $A_0$, $A_1$, $C_1$, and $D_1$ can be readily found from the solution of Eqs. (73), (74), (77), and (78). Thus,

$$A_0=\mu_0\frac{4a(a^2T^2+3aT+3)}{(a^2T^2+6aT+12)(aT+2)}-\mu_1\frac{6a^2}{a^2T^2+6aT+12}, \quad (79)$$

$$A_1=-\mu_0\frac{6a^2}{a^2T^2+6aT+12}+\mu_1\frac{12a^2}{T(a^2T^2+6aT+12)}, \quad (80)$$

$$C_1=\mu_0\frac{2(2a^2T^2+9aT+12)}{(a^2T^2+6aT+12)(aT+2)}-\mu_1\frac{6(aT+2)}{T(a^2T^2+6aT+12)}, \quad (81)$$

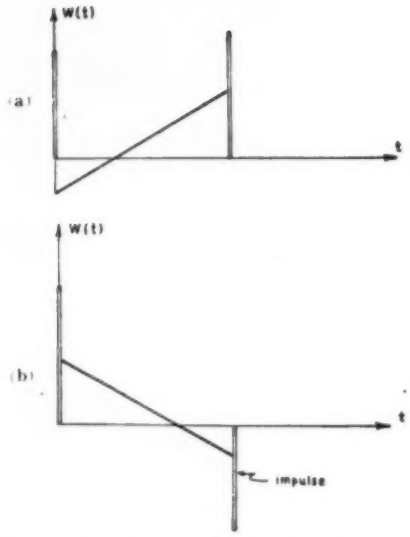


FIG. 4. Shapes of optimum weighting functions. (a) For the best value of $s(t)$. (b) For the best value of $s(t-\alpha)$ ($\alpha$-negative).

and

$$D_1=-\mu_0\frac{2aT(aT+3)}{(a^2T^2+6aT+12)(aT+2)}+\mu_1\frac{6(aT+2)}{T(a^2T^2+6aT+12)}. \quad (82)$$

Whenever the stationary part of the input signal is zero [i.e., $M(t)\equiv 0$], the mean-square value of the prediction error assumes the simple form

$$\sigma^2=\mu_0\lambda_0+\mu_1\lambda_1+\cdots+\mu_n\lambda_n, \quad (83)$$

which may be readily established by substituting Eq. (36) into the general expression for $\sigma^2$ [cf. Eq. (33)]. For the particular case under consideration Eq. (83) gives

$$\sigma^2=\mu_0{}^2\frac{8(a^2T^2+3aT+3)}{(a^2T^2+6aT+12)(aT+2)}+\mu_1{}^2\frac{24a}{T(a^2T^2+6aT+12)}-\mu_0\mu_1\frac{24a}{(a^2T^2+6aT+12)}. \quad (84)$$

The expressions given above are valid for any choice of the prediction operator. For the particular case in which the predictor is called upon to furnish the best possible estimate of the present value of $\dot{s}(t)$, the values of $\mu_0$ and $\mu_1$ are, respectively,

$$\mu_0=0,\quad \mu_1=-1 \quad [\text{cf. Eq. (21)}] \quad (85)$$

On the other hand, in the case of the estimation of $s(t+\alpha)$ (i.e., the value of $s(t)$ $\alpha$-seconds in the future)

$$\mu_0=1,\quad \mu_1=-\alpha \quad [\text{cf. Eq. (24)}] \quad (86)$$

The shapes of $W(t)$ for these two particular cases are illustrated in Fig. 4.

### Example 3

The case to be considered here is the same as that treated in Example 2, except that the auto-correlation function of $N(t)$ is assumed to be of the form

$$\psi_N(\tau)=e^{-a|\tau|}\cos\omega_0\tau, \quad (87)$$

with the associated spectral density function being

$$S_N(\omega^2)=\frac{2a(a^2+\omega_0{}^2+\omega^2)}{\omega^4+2(a^2-\omega_0{}^2)\omega^2+(a^2+\omega_0{}^2)^2}. \quad (88)$$

This form of spectral density function is of considerable practical importance since it provides a reasonably good approximation to many of the actual spectra encountered in practice.

*Solution*

By Eq. (64), the weighting function for this case is of the form

$$W(t)=A_0+A_1t+B_1e^{bt}+B_2e^{-bt}+C_1\delta(t)+D_1\delta(t-T),\quad 0\le t\le T, \quad (89)$$

where $b=(a^2+\omega_0{}^2)^{\frac{1}{2}}$. Substituting $W(t)$ as given by Eq. (89) into Eq. (36), and requiring that Eq. (36) be satisfied by $W(t)$ establishes four linear algebraic equations between the six constants $A_0$, $A_1$, $B_1$, $B_2$, $C_1$, $D_1$. These are:

$$\begin{aligned}
&-2ab^2A_0+2(a^2-\omega_0{}^2)A_1-b^3B_1+b^3B_2+C_1=0,\\
&2\omega_0{}^2b^2A_0-4a\omega_0{}^2A_1+b^3(b-a)B_1+b^3(b+a)B_2=0,\\
&-2ab^2A_0+2(\omega_0{}^2-a^2-aTb^2)A_1+\frac{e^{bT}}{2b}B_1-\frac{e^{-bT}}{2b}B_2+D_1=0,\\
&2\omega_0{}^2b^2A_0+2\omega_0{}^2(2a+b^2T)A_1+b^3(b+a)e^{bT}B_1+b^3(b-a)e^{-bT}B_2=0.
\end{aligned} \quad (90)$$

The constraints imposed by the prediction operator $K(p)$ are given by Eq. (14); they are:

$$\int_0^T W(\tau)d\tau=\mu_0, \quad (75)$$

and

$$\int_0^T \tau W(\tau)d\tau=\mu_1. \quad (76)$$

The requirement that $W(t)$ must satisfy Eqs. (75) and (76) leads to two additional linear equations. These are:

$$2bTA_0+bT^2A_1+2(e^{bT}-1)B_1-2(e^{-bT}-1)B_2 +2bC_1+2bD_1=\mu_0,$$

and

$$3b^2T^2A_0+2b^2T^3A_1+b[e^{bT}(bT-1)+1]B_1 -6[e^{-bT}(bT+1)-1]B_2+6b^2D_1=\mu_1. \quad (91)$$

The coefficients $A_0$, $A_1$, $B_1$, $B_2$, $C_1$, $D_1$ of Eq. (89) are the solutions of the six linear equations (90) and (91).

The expression for the mean-square value of the prediction error can be conveniently expressed in terms of $A_0$ and $A_1$. Thus, making use of Eq. (83) it is readily found that

$$\sigma^2=(2a/b^2)(\mu_0A_0+\mu_1A_1). \quad (92)$$

This completes essentially the solution of the problem.


### ACKNOWLEDGMENTS

The authors wish to thank Mr. H. T. Marcy of The M. W. Kellogg Company and Mr. H. Sherman of the Watson Laboratories, AMC, for their encouragement and support of this work.


---

# Potential Flow into Circumferential Openings in Drain Tubes*


DON KIRKHAM

*Iowa State College Agricultural Experiment Station, Department of Agronomy and Department of Physics, Ames, Iowa*



(Received December 22, 1949)



A theoretical analysis of the effect of the spaces between drain tube units as used in the artificial drainage of soil is given. The problem is one of potential flow; therefore, the results are applicable to heat flow, etc. The basic problem solved is that for axially symmetric flow from an external cylindrical boundary at constant potential to a series of equal, equally spaced openings at a lower potential, all located axially on, and comprising a part of, the otherwise impervious drain tube. The radii of the open sections and impermeable sections of the drain tube are equal. The basic problem is extended to obtain the solution to the practical problem—the seepage of ground water into drain tubes beneath a horizontal water table. The exact solution of the basic problem is not suitable for numerical work. Accordingly, approximate solutions of specified uncertainty are derived and are utilized for tabulation of numerical results. As an example, the analysis shows, in the case of 6 in. diameter drain tubes having 1 ft. long impermeable sections and buried 4 ft. deep in uniformly permeable soil, that increasing the openings from $\frac{1}{32}$ in. width to $\frac{1}{4}$ in. width will increase the flow 36 percent; while embedding the tubes in gravel, to make the $\frac{1}{32}$ in. openings of effectively infinite width, will increase the flow 180 percent.


IN the drainage of soil, for agricultural use, for foundations, roads, or for dams, excess ground water is generally removed by drain tubes installed two or more feet below the soil surface. These tubes consist, in most cases, of 1 ft. long sections of impervious pipe, either tile or cement, fitted together axially, except for a space left between individual units, to permit the water to enter. In practice the opening between the units is usually small. It may be less than 1/64 in. or, as much as $\frac{1}{4}$ in. But if the tubes are embedded in gravel, as is sometimes the case, the open space between the pipe units becomes effectively infinite. This is a consequence of the negligible loss of head which results when water seeps through gravel as compared with water seeping through soil. In this paper the effect of width of opening between the pipe units on drainage rate will be analyzed. As the problem is one of potential theory, the results will be applicable to other physical problems as flow of heat, electricity, etc.[1]

In the actual drainage problem the drain tubes are installed in a nearly horizontal position in the soil. Therefore if the soil is water-saturated to the surface of the ground, the soil surface is an equipotential plane, and the flow problem may be solved by the method of images.

## AXIAL FLOW

Before applying the method of images it is convenient to solve a simpler problem: that of axially symmetrical flow for the system indicated in Fig. 1. Here, because of symmetry, only a section $ABCD$ need be considered. This section is bounded by inner and outer cylindrical surfaces at $r=a$ and $r=b$; by a plane $z=0$, midway between an open space of width $2c$; and a plane $z=s$, $2s$ being the distance between centers of openings.

Taking $\phi$ as the potential function, $V_a$ as the constant potential over the openings of the drain tube, and $V_b$ the constant potential over the outer cylinder, the boundary conditions are—I: $\phi=V_a$, $r=a$, $0\leq z\leq c$; II: $\partial\phi/\partial r=0$, $r=a$, $c<z\leq s$; III: $\partial\phi/\partial z=0$, $z=s$; IV: $\phi=V_b$, $r=b$; V: $\partial\phi/\partial z=0$, $z=0$.

The exact solution of $\nabla^2\phi$ which satisfies the above conditions can be formulated. This exact solution, is not, however, tractable in calculations. Therefore, a simpler, approximate solution is sought. Simplification is looked for through substitution of approximately correct,


* Journal Paper No. 1728 of the Iowa Agricultural Experiment Station, Ames, Iowa. Project No. 998.


[1] M. Muskat, *The Flow of Homogeneous Fluids through Porous Media* (McGraw-Hill Book Company, Inc., New York, 1937, or J. W. Edwards, Inc., Ann Arbor, Michigan, 1946), p. 140.

homogeneous boundary conditions at $r=a$, for the accurate, mixed boundary conditions, I and II. Homogeneous boundary conditions at $r=a$ can be realized in two ways: (1) by using the exact condition, $\phi=V_a$ for $0<z<c$ and finding by trial a $\phi$ for $c<z<s$ such that over $c<z<s$, $\partial\phi/\partial r=0$; or (2), by using the exact condition

$$\partial\phi/\partial r=0, \quad c<z<s, \quad r=a \tag{1}$$

and finding by trial a $\partial\phi/\partial r$ such that

$$\partial\phi/\partial r=f(z, r, b, s, c)=f(z), \quad 0\leq z<c, \quad r=a, \tag{2}$$

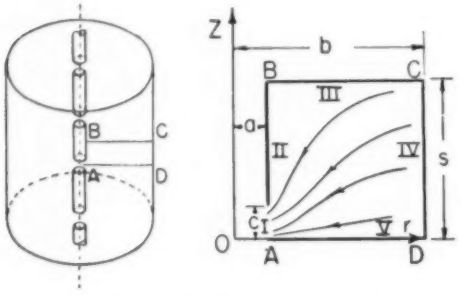


FIG. 1. Case of axially symmetric flow.

the $\phi$ in Eq. (2) satisfying simultaneously the relation

$$\phi=V_a, \quad 0\leq z<c, \quad r=a. \tag{3}$$

Because in practice one has $c\ll s$, with the consequence that $\partial\phi/\partial r$ is known exactly $(=0)$ over most of the boundary, it appears better to use the second method. Accordingly we attempt to satisfy Eqs. (1), (2) and (3).

As will appear, Eqs. (1) and (2) can, with the aid of Fourier series, be satisfied for an infinite number of values of $f(z)$. To satisfy, in addition, Eq. (3), however, there exists only one suitable value of $f(z)$, and to determine this value, by trial with accuracy, considerable labor would be required. A form of $f(z)$ which satisfies Eq. (3) for practical purposes can be determined by considering the two-dimensional case[2] into which Fig. 1 goes over when $a\to\infty$. Here with $b>s$, $s\gg c$, $y$ replacing $r$, $x$ replacing $z$, $z'=x'+iy'$, $i=(-1)^{\frac{1}{2}}$; one finds,[3] taking $w$ for the complex potential,

$$\frac{dw}{dz'}=\frac{A\cos\pi(x'+iy')/2s}{[\sin^2\pi c/2s-\sin^2\pi(x'+iy')/2s]^{\frac{1}{2}}},$$

where $A$ is a constant. Now, setting $y=0$, and observing that the $x$-component of $dw/dz'$ over the opening is zero, there results

$$\left[\frac{\partial\phi}{\partial y}\right]_{y=0}=\frac{A\cos\pi x'/2s}{(\sin^2\pi c/2s-\sin^2\pi x'/2s)^{\frac{1}{2}}}, \quad 0<x'<c,$$

or, in notation corresponding to Fig. 1,

$$\left[\frac{\partial\phi}{\partial r}\right]_{r=a}=\frac{A\cos\pi z/2s}{(\sin^2\pi c/2s-\sin^2\pi z/2s)^{\frac{1}{2}}}, \quad 0<z<c,$$

that is with $c$, and hence $z$, small compared to $s$,

$$\left[\frac{\partial\phi}{\partial r}\right]_{r=a}\simeq A'[1-(z/c)^2]^{-\frac{1}{2}}, \quad c\ll s, \quad 0<z<c, \tag{4}$$

where $A'$ is a constant $(A'=2sA/\pi c)$.

In order to evaluate the constant $A'$ there is available the expression for the flux $Q_1$ entering the tube between $z=0$ and $z=c$. This flux is

$$Q_1=2\pi aK\int_0^c \partial\phi/\partial r\Big|_{r=a}\,dz,$$

where $K$ is the soil permeability[4] (thermal conductivity in the heat problem, $\phi$ being then the temperature). Substituting Eq. (4) in the last expression and integrating, there results

$$Q_1=ac\pi^2A'K.$$

It is more convenient to consider the flow into unit length of drain tube including both the open and the impervious portions of surface. Let $Q$ be this flux. Then, $Q=Q_1/s=ac\pi^2A'K/s$; that is

$$A'=Qs/ac\pi^2K \tag{5}$$

and Eq. (4) becomes

$$[\partial\phi/\partial r]_{r=a}\simeq(Qs/ac\pi^2K)[1-(z/c)^2]^{-\frac{1}{2}}, \quad 0<z<c. \tag{6}$$

This expression, since we took $b>s$, does not involve $b$.

As has been indicated, the right-hand sides of Eqs. (2) and (6) require development in a Fourier series. A cosine series is needed. It is

$$[\partial\phi/\partial r]_{r=a}=\sum_{n=1}^{\infty}A_n\cos n\pi z/s+A_0/2, \quad 0<z<s,$$

where the coefficients are found in the usual way to have the values,

$$A_0/2=Q/2a\pi K, \tag{7}$$

$$A_n=(2Q/a\pi^2K)\sin^{-1}[(s/n\pi c)\sin n\pi c/s]. \tag{8}$$

If we now define $R_0(n\pi r/s)$ by

$$R_0(n\pi r/s)=\frac{K_0(n\pi b/s)I_0(n\pi r/s)-I_0(n\pi b/s)K_0(n\pi r/s)}{K_0(n\pi b/s)I_1(n\pi a/s)+I_0(n\pi b/s)K_1(n\pi a/s)}, \tag{9}$$

in which $I_0$ and $K_0$ are modified Bessel functions of the

[2] Two-dimensional boundary conditions in solving problems of axial symmetry have recently been applied by W. R. Smythe, Rev. Mod. Phys. **20**, 176 (1948).

[3] W. R. Smythe, *Static and Dynamic Electricity* (McGraw-Hill Book Company, Inc., New York, 1939), first edition, p. 89.

[4] Muskat (see reference 1, p. 294) uses the symbol $\bar{k}$ where we use $K$. $K$ is the quantity of water seeping through a unit length of soil of unit cross section when the difference in hydraulic head across the unit length is unity. Our $\phi$ has the physical significance of hydraulic head and is equivalent to Muskat's $\Phi/\bar{k}$.

first, and second kind and zero order; and $I_1$, of the first kind and first order; we can write down a function $\phi$ which satisfies $\nabla^2\phi=0$ and conditions (II), (III), (IV), and (V) exactly, and (I) approximately. It is

$$\phi=\sum_{n=1}^{\infty}\frac{A_n s}{n\pi}R_0\left(\frac{n\pi r}{s}\right)\cos\frac{n\pi z}{s}+\frac{A_0}{2}a\ln\frac{r}{b}+V_b, \quad (10)$$

where the $A_n$ and $A_0$ are given by Eqs. (7) and (8).

The right-hand side of Eq. (10) does not converge rapidly; nor has an analytic summation for it been found. Furthermore the flux values based on Eq. (10), as numerical calculations show, are not appreciably different for practical purposes, from the values resulting from a simpler expression obtained as follows.

## SIMPLIFIED APPROXIMATE SOLUTION OF SPECIFIED UNCERTAINTY

Let (instead of Eq. (4))

$$[\partial\phi/\partial r]_{r=a}=B', \quad 0<z<c; \quad (11)$$

then, as Eq. (5) was determined, one finds

$$B'=Qs/2ac\pi K.$$

Also, developing the right-hand side of Eqs. (1) and (11) into a Fourier cosine series in the interval $0<z<s$, there results

$$[\partial\phi/\partial r]_{r=a}=\sum_{n=1}^{\infty}B_n\cos\frac{n\pi z}{s}+\frac{B_0}{2},$$

where

$$B_0/2=cB'/s,$$
$$B_n=(2B'/n\pi)\sin n\pi c/s.$$

Instead of Eq. (10) we now have

$$\phi=\sum_{n=1}^{\infty}(B_n s/n\pi)R_0(n\pi r/s)\cos n\pi z/s + (B_0/2)a\ln r/b+V_b;$$

or, in terms of the flux $Q$,

$$\phi=\frac{Q}{2\pi K}\left[\ln\frac{r}{b}-\frac{2s^2}{ac\pi^2}S(r,z)\right]+V_b \quad (12)$$

where

$$S(r,z)=-\sum_{n=1}^{\infty}\frac{1}{n^2}\sin\frac{n\pi c}{s}R_0\left(\frac{n\pi r}{s}\right)\cos\frac{n\pi z}{s}. \quad (13)$$

In Eq. (12) $\phi(r,z)$ is given in terms of supposedly known values of $V_b$ and $Q$. If, however, $\phi(r,z)$ is known for some point $(r,z)$, the flux $Q$ may be considered as unknown and there results

$$Q=\frac{2\pi K[V_b-\phi(r,z)]}{\ln b/r+(2s^2/ac\pi^2)S(r,z)}. \quad (14)$$

We will now establish, referring to Fig. 2, lower and upper limits $Q_l$ and $Q_u$ for the flux. In the figure the line $EF$ represents the equipotential passing through the point $(r,z)=(a,c)$, the point $E$ being at higher potential than the point $A$. Now, since in the actual physical problem the potential along $AE$ does not increase but has the constant value $V_a$, identification of $V_a$ with $\phi(r,z)=\phi(a,0)$ in Eq. (12) establishes a lower limit $Q_l$ of flow.

Suppose now that $V_a$ is identified with the equipotential $EF$,[5] specified analytically by $\phi=\phi(a,c)$. Then, in order that the potential along $AE$ be constant, a section $AEF$ of soil must be removed. But with this soil removed the flow will be greater than if the potential $V_a$ were applied along $AE$ with no soil removed. Therefore, identification of $\phi(r,z)$ with $\phi(a,c)=V_a$ yields an upper limit of flow.

From the above considerations and Eqs. (13) and (14) we have then

$$Q_l=\frac{2\pi K(V_b-V_a)}{\ln b/a+(2s^2/ac\pi^2)S(a,0)}, \quad (15)$$

$$Q_u=\frac{2\pi K(V_b-V_a)}{\ln b/a+(2s^2/ac\pi^2)S(a,c)}; \quad (16)$$

and we define an average value of flux $Q_{av}$ by

$$Q_{av}=(Q_l+Q_u)/2, \quad (17)$$

a value which should not be far in error.

Although Eqs. (15) and (16) are correct lower and upper limits of the flow for all values of $a$, $b$, $c$, and $s$, the expressions may be simplified. This is true, because for

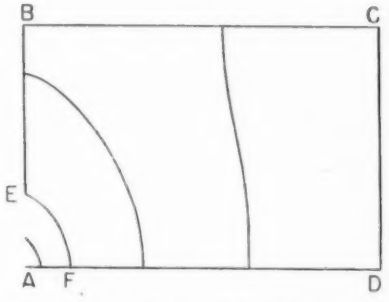


FIG. 2. Schematic equipotentials for the region $ABCD$ of Fig. 1 when the normal component of flux density across the stricture $AE$ is constant.

the range of values of $a$, $b$, and $s$ considered in the following, there is valid the approximation $R_0(n\pi a/s)=-K_0(n\pi a/s)/K_1(n\pi a/s)$ to better than 1 part in $10^8$. (The approximation $R_0(n\pi r/s)=-K_0(n\pi r/s)/K_1(n\pi a/s)$ is correct to better than 1 part in $10^5$, the worst case being for $n=1$ and $r=b$.) There results then, finally, for

[5] The distance $AF$ in Fig. 2 has been computed, using Eq. (10). For $2a=19.2/\pi\simeq 6$, $b=48$, $2c=4/15\simeq\frac{1}{4}$, $s=6$, it is $AF=0.075$, where, for a practical example all units may be taken as inches. It will be shown that $b=48$ in. corresponds to a depth of 24 in. for a horizontally installed drain tube.

numerical calculations

$$Q_l=\frac{2\pi K(V_b-V_a)}{\ln b/a+(2s^2/ac\pi^2)S_1}, \tag{18}$$

$$Q_u=\frac{2\pi K(V_b-V_a)}{\ln b/a+(2s^2/ac\pi^2)S_2}, \tag{19}$$

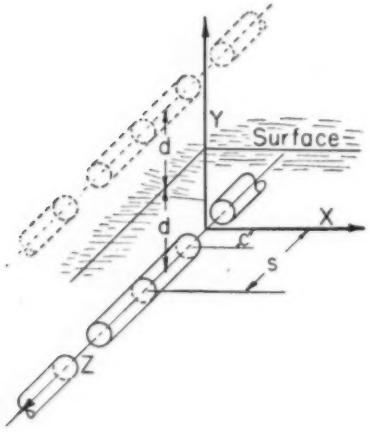


FIG. 3. Image case for a single drain tube. The semi-distance $c$ between impermeable units is indicated larger than is found in practice.

where

$$S_1=S(a,0)=\sum_{n=1}^{\infty}\frac{1}{n^2}\sin\frac{n\pi c}{s}\frac{K_0(n\pi a/s)}{K_1(n\pi a/s)}, \tag{20}$$

$$S_2=S(a,c)=\sum_{n=1}^{\infty}\frac{1}{2n^2}\sin\frac{2n\pi c}{s}\frac{K_0(n\pi a/s)}{K_1(n\pi a/s)}. \tag{21}$$

A commonly recommended size of drain tube for laterals (as distinguished from mains) is 5 in. inside diameter. Smaller diameters, sometimes as small as 2 in. have been used. Unit lengths are almost invariably 1 ft., and wall thickness about ½ in. In view of the above and in order to simplify computations the following values for geometrical quantities have been used: $a/s=0.8/\pi$ and $1.6/\pi$; $b/s=8$, 16 and 200; $c/s=1/1440$, $2/1440$, $\cdots$, $32/1440$. With $2s=1$ ft. the values of $a/s$ and $c/s$ correspond to $2a=3.06$ and 6.12 in., and $2c$ to approximately $1/128$, $1/64$, $\cdots$, ¼ in. The values chosen for $b/s$ correspond (with $2s=1$ ft.) to $b=4$, 8 and 100 ft.

Numerical results for $S_1$ and $S_2$ are presented in Table I. The values were computed from Eqs. (20) and (21) by summing term by term, from $n=1$ to $n=44$ and using Euler-McLaurin[6] summation formulas for $n=45$ to $\infty$, taking for $n\geq 45$, $K_0(n\pi a/s)/K_1(n\pi a/s)=1$. Taking the latter ratio = 1 accounts for the uncertainty in the last place of decimals in Table I. In preparing Table I the relation $S_2[(1/2)c/s]=(1/2)S_1(c/s)$ was useful. There is a similar relation for $Q_l$ and $Q_u$.

[6] Cf. E. T. Whittaker and G. Robinson, *The Calculus of Observations* (Blackie and Son, Limited, London, 1924), p. 135.

TABLE I. Values of $S_1$ and $S_2$, Eqs. (20) and (21).

| | $a/s=1.6/\pi$ | | $a/s=0.8/\pi$ | |
|---|---|---|---|---|
| $c/s$ | $S_1$ | $S_2$ | $S_1$ | $S_2$ |
| 32/1440 | 0.22912 (2)[a] | 0.18186 (1) | 0.21141 (4) | 0.16515 (1) |
| 16/1440 | 0.13849 (2) | 0.11455 (1) | 0.12942 (4) | 0.10572 (2) |
| 8/1440 | 0.08128 (4) | 0.06925 (1) | 0.07668 (9) | 0.06471 (2) |
| 4/1440 | 0.04666 (4) | 0.04066 (2) | 0.04434 (9) | 0.03834 (5) |
| 2/1440 | 0.02634 (4) | 0.02333 (2) | 0.02517 (6) | 0.02217 (4) |
| 1/1440 | 0.01468 (2) | 0.01317 (2) | 0.01405 (4) | 0.01259 (3) |

[a] Numbers in parentheses indicate uncertainty (±) in the fifth decimal place.

Table II presents values of $Q_l'$, $Q_M'$ and $Q_u'$, where,

$$\left.\begin{aligned} Q_l'&=Q_l/K(V_b-V_a),\\ Q_M'&=Q_M/K(V_b-V_a),\\ Q_u'&=Q_u/K(V_b-V_a).\end{aligned}\right\} \tag{22}$$

The uncertainty in $Q_M'$ is greatest, $51/570=8.95$ percent for the values $b/s=8$, $a/s=0.8/\pi$ and $c/s=32/1440$; and (except for $c/s=1$ when the uncertainty is zero) is least, $14/437=3.20$ percent for the values $b/s=200$, $a/s=1.6/\pi$, and $c/s=1/1440$. The uncertainty in $Q_M'$ increases with decreasing $a/s$ and $b/s$ and increasing $c/s$. The uncertainty 3.20 percent found for $c/s=1/1440$ is larger than was expected.

## IMAGE CASE: A SINGLE DRAIN TUBE

Figure 3 represents the image case. The drain tube is buried horizontally (nearly, in practice) at depth $d$ below a plane water table, here taken as the surface of

TABLE II. Values of $Q_l'$, $Q_M'$, and $Q_u'$.[a]

| | $a/s=1.6/\pi$ | | | $a/s=0.8/\pi$ | | |
|---|---|---|---|---|---|---|
| $c/s$ | $Q_l'$ | $Q_M'$ | $Q_u'$ | $Q_l'$ | $Q_M'$ | $Q_u'$ |
| | | | $b/s=8$ | | | |
| 1 | 2.281 | 2.281 | 2.281 | 1.823 | 1.823 | 1.823 |
| 32/1440 | 0.916 | 0.981 | 1.045 | 0.570 | 0.621 | 0.671 |
| 16/1440 | 0.815 | 0.865 | 0.916 | 0.494 | 0.532 | 0.570 |
| 8/1440 | 0.733 | 0.774 | 0.814 | 0.435 | 0.465 | 0.494 |
| 4/1440 | 0.666 | 0.699 | 0.732 | 0.389 | 0.412 | 0.435 |
| 2/1440 | 0.610 | 0.638 | 0.666 | 0.351 | 0.370 | 0.389 |
| 1/1440 | 0.563 | 0.586 | 0.610 | 0.321 | 0.336 | 0.352 |
| | | | $b/s=16$ | | | |
| 1 | 1.823 | 1.823 | 1.823 | 1.518 | 1.518 | 1.518 |
| 32/1440 | 0.832 | 0.885 | 0.937 | 0.537 | 0.581 | 0.625 |
| 16/1440 | 0.747 | 0.790 | 0.832 | 0.469 | 0.503 | 0.536 |
| 8/1440 | 0.678 | 0.713 | 0.747 | 0.415 | 0.442 | 0.469 |
| 4/1440 | 0.620 | 0.649 | 0.678 | 0.373 | 0.394 | 0.415 |
| 2/1440 | 0.572 | 0.596 | 0.620 | 0.338 | 0.356 | 0.373 |
| 1/1440 | 0.530 | 0.551 | 0.572 | 0.310 | 0.324 | 0.338 |
| | | | $b/s=200$ | | | |
| 1 | 1.052 | 1.052 | 1.052 | 0.943 | 0.943 | 0.943 |
| 32/1440 | 0.624 | 0.652 | 0.681 | 0.441 | 0.470 | 0.499 |
| 16/1440 | 0.573 | 0.599 | 0.624 | 0.394 | 0.418 | 0.441 |
| 8/1440 | 0.533 | 0.554 | 0.575 | 0.356 | 0.375 | 0.394 |
| 4/1440 | 0.496 | 0.515 | 0.533 | 0.324 | 0.340 | 0.356 |
| 2/1440 | 0.465 | 0.481 | 0.496 | 0.298 | 0.311 | 0.324 |
| 1/1440 | 0.437 | 0.451 | 0.465 | 0.276 | 0.287 | 0.298 |

[a] $Q_l'$, $Q_M'$ and $Q_u'$ are respectively a lower, an average, and an upper limit of flow for a unit length of a long drain tube of the type indicated in Fig. 1, the permeability of the conducting medium, and the difference in potential across the outer and inner flow boundaries (IV and I of Fig. 1), being unity. Cf. Eqs. (18), (19), and (22).

TABLE III. Relative flow into cracks between 1 ft. long[a] impervious drain tube units.

| Crack width inches | Depth of tube 2 ft. Diameter 6 in. | Depth of tube 2 ft. Diameter 3 in. | Depth of tube 4 ft. Diameter 6 in. | Depth of tube 4 ft. Diameter 3 in. |
|---|---|---|---|---|
| Flow into a completely open[b] drain tube taken as unity | | | | |
| 1/128 | 0.257 | 0.185 | 0.302 | 0.214 |
| 1/64 | 0.280 | 0.203 | 0.327 | 0.234 |
| 1/32 | 0.306 | 0.226 | 0.356 | 0.260 |
| 1/16 | 0.339 | 0.255 | 0.391 | 0.291 |
| 1/8 | 0.379 | 0.292 | 0.433 | 0.331 |
| 1/4 | 0.430 | 0.341 | 0.485 | 0.383 |
| Inf. | 1.000 | 1.000 | 1.000 | 1.000 |
| Flow into a crack 1/32 in. wide taken as unity | | | | |
| 1/32 | 1.000 | 1.000 | 1.000 | 1.000 |
| 1/16 | 1.100 | 1.128 | 1.099 | 1.116 |
| 1/8 | 1.238 | 1.290 | 1.216 | 1.272 |
| 1/4 | 1.405 | 1.508 | 1.361 | 1.432 |
| Inf. | 3.268 | 4.425 | 2.809 | 3.846 |

[a] Crack widths, tube diameters and length of tube units are nominal. The entries in the table correspond actually (see Fig. 3) to $s=6$ in. (not $s-c=6$ in.) to $2c=1/120$, $1/60$, $1/30$, etc. in. and to $2a=19.2/\pi=6.06$ in. and $2a=9.6/\pi=3.03$ in. Infinite crack width corresponds to $c/s=1$. The depths 2 and 4 ft. are correct.
[b] For practical purposes in soil drainage, a drain tube embedded in gravel

the soil. The soil is of uniform permeability $K$ and extends downward to great depth, the drain tube being the only exit for soil water. The fictitious image drain is distance $d$ above the soil surface. With the coordinate axes as shown, and referring to Eq. (12), the potential $\theta$ may be written down by inspection and is

$$\theta=\frac{F}{2\pi K}\left\{\ln\frac{(x^2+y^2)^{\frac{1}{2}}}{[x^2+(2d-y)^2]^{\frac{1}{2}}}+\frac{2s^2}{ac\pi^2}\sum_{n=1}^{\infty}G_n n^{-2}\sin n\pi c/s\cdot\cos n\pi z/s\right\}+V_d, \quad (23)$$

where

$$G_n=R_0\left[\frac{n\pi}{s}(x^2+y^2)^{\frac{1}{2}}\right]-R_0\left\{\frac{n\pi}{s}[x^2+(2d-y)^2]^{\frac{1}{2}}\right\},$$

and where $F$, now used instead of $Q$, is the flux per unit length of drain tube, including the open and closed parts, and $V_d$ is the hydraulic head at the surface of the soil.

We assume that the drain line is running full with zero back pressure or suction. Therefore, taking the axis of the drain tube as reference level for hydraulic head, the potential $V_w$ over the inside of the tube is $V_w=a$; also $V_d=d$ if the soil is water-saturated to the surface; and $V_d=d+t$, if in addition there is a surface layer of water of thickness $t$.

Let us consider Eq. (23) for the case that $c=s$, that is, for the case that the summation is zero. Then, taking $x=0$ and $y=a$, there results $F=2\pi K(V_d-V_w)/\ln(2d-a)/a$; and taking $x=0$ and $y=-a$, there results $F=2\pi K(V_d-V_w)/\ln(2d+a)/a$. One of these values is too high and one too low.[7] A value which more nearly equals the actual flux is $F=2\pi K(V_d-V_w)/\ln 2d/a$.[8] Similarly, a best value for $R_0$-terms at the surface of the drain tube is

$$R_0(n\pi a/s)-R_0(2n\pi d/s)=-[K_0(n\pi a/s)/K_1(n\pi a/s)-K_0(2n\pi d/s)/K_1(n\pi a/s)],$$

very nearly, $=-[K_0(n\pi a/s)/K_1(n\pi a/s)]$, very nearly (for practical values of $d$, $s$ and $a$). Therefore Eq. (23) may be written for the drain surface, upon solving for $F$,

$$F=2\pi K(V_d-V_w)\{\ln 2d/a+(2s^2/ac\pi^2)\sum_{n=1}^{\infty}n^{-2}\sin n\pi c/s\cdot\cos n\pi z/s\cdot K_0(n\pi a/s)/K_1(n\pi a/s)\}^{-1}.$$

Taking now, as was done in obtaining Eqs. (18) and (19), $z=0$ and then $z=c$, lower and upper limits, $F_l$ and $F_u$, for the flux are found to be

$$F_l=\frac{2\pi K(V_d-V_w)}{\ln 2d/a+(2s^2/ac\pi^2)S_1}, \quad (24)$$

$$F_u=\frac{2\pi K(V_d-V_w)}{\ln 2d/a+(2s^2/ac\pi^2)S_2}, \quad (25)$$

where $S_1$ and $S_2$ are given by Eqs. (20) and (21). Also, as in Eq. (17), we define

$$F_{av}=(F_l+F_u)/2; \quad (26)$$

and as in Eq. (22),

$$\left.\begin{aligned}F_l'&=F_l/K(V_d-V_w)\\F_{av}'&=Q_{av}/K(V_d-V_w)\\F_u'&=F_u/K(V_d-V_w)\end{aligned}\right\}. \quad (27)$$

Comparing Eqs. (18) and (19) with Eqs. (24) and (25), and Eq. (17) with Eq. (26), it is now apparent that Table II gives values of $F_l'$, $F_{hv}'$ and $F_u'$, if $b$ is taken

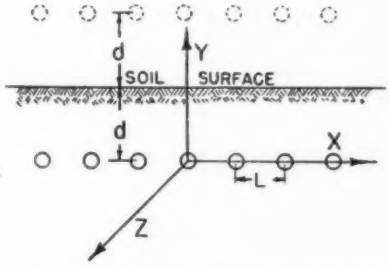


FIG. 4. A series of equally spaced drain tubes.

[7] The former value is too high, because the equipotential surface $\theta(0, a)$ lies outside the actual drain tube except at $(0, a)$; the latter, too small, because the equipotential $\theta(0, -a)$ lies inside the actual drain tube except at $(0, -a)$.
[8] The exact value (see reference 3, p. 77, Eq. 1) is $F=2\pi K(V_d-V_w)/\cosh^{-1}d/a$. The expression $\ln 2d/a$ approximates $\cosh^{-1}d/a$ to better than 1 part in 3400 for $d=4$ and $a=0.25$.

equal to $2d$, and if $F$'s are substituted for $Q$'s. With these considerations Table III has been prepared. The table brings out the fact that the width of opening between drain pipe units is an important factor in seepage calculations. For example, in a clay soil, where a crack width of $\frac{1}{4}$ in. may safely be used, flow to a 6 in. tube at 4 feet depth may be increased 36 percent over that achieved by putting the drain pipe units $\frac{1}{32}$ in. apart as is commonly done; while embedding the tubes in gravel may increase the flow 180 percent. In soils where gravel is not available and where wide drain tube openings might result in the entry of soil into the tubes, with possible clogging, screens could be placed over the openings. The soil would be stabilized by the time the screens deteriorate.

### IMAGE CASE: MULTIPLE DRAIN TUBES

For a series of drain tubes equally spaced at distance $L$ and at depth $d$ (Fig. 4), the potential is, comparing Eq. (23),

$$\theta=\frac{F}{2\pi K}\sum_{m=-\infty}^{\infty}\left[\frac{1}{2}\ln\frac{(x+mL)^2+y^2}{(x+mL)^2+(2d-y)^2}+T_m\right]+V_d, \quad (28)$$

where

$$T_m=\frac{2s^2}{ac\pi^2}\sum_{n=1}^{\infty}\frac{1}{n^2}\sin\frac{n\pi c}{s}\cos\frac{n\pi z}{s}\times\left(R_0\{(n\pi/s)[(x+mL)^2+y^2]^{\frac{1}{2}}\}-R_0\{(n\pi/s)[(x+mL)^2+(2d-y)^2]^{\frac{1}{2}}\}\right).$$

Now the first summation in Eq. (28) is[9]

$$(1/2)\ln(\cosh 2\pi y/L-\cos 2\pi x/L)/(\cosh 2\pi(2d-y)/L-\cos 2\pi x/L);$$

or putting $y=a$, $x=0$, it is

$$(1/2)\ln(\cosh 2\pi a/L-1)/[\cosh 2\pi(2d-a)/L-1]=\ln[(\sinh\pi a/L)/\sinh\pi(2d-a)/L].$$

The second summation in Eq. (28), when $y=a$ and $x=0$, reduces, since $d\gg s$, $L\gg s$, to the single summation $\sum_{n=1}^{\infty}{}'[-K_0(n\pi a/s)/K_1(n\pi a/s)]n^{-2}\sin n\pi c/s\cdot\cos n\pi z/s$, in which $(-K_0/K_1)$ has been written, as before, for $R_0$. Therefore, Eq. (28) yields, taking first $x=0$, $y=a$, $z=0$, and then $x=0$, $y=a$, $z=c$, lower and upper limits for the flux as follows.

$$F_l=\frac{2\pi K(V_d-V_w)}{\ln[(\sinh 2\pi d/L)/(\sinh\pi a/L)]+(2s^2/ac\pi^2)S_1}, \quad (29)$$

$$F_u=\frac{2\pi K(V_d-V_w)}{\ln[(\sinh 2\pi d/L)/(\sinh\pi a/L)]+(2s^2/ac\pi^2)S_2}, \quad (30)$$

where the $a$ in $\sinh\pi(2d-a)/L$ has been dropped for the same reason that the $a$ in $(2d-a)$ was dropped in obtaining Eqs. (24) and (25).

It is apparent, comparing Eqs. (18), (19); (24), (25); and (29), (30), that the same two correction terms $(2s^2/ac\pi^2)S_1$ and $(2s^2/ac\pi^2)S_2$ will apply in a number of drainage problems.[10,11] These terms, multiplied by $1/2\pi K$, represent upper and lower limits of a resistance term which, in order to compute the flux, must be added to the resistance of the medium when calculated for completely open drain tubes. Stated in another way, the loss in hydraulic head due to strictures in a drain tube of the type shown in Fig. 1, whether there is a single tube or a number of tubes in an installation, will not exceed $(Q/2\pi K)(2s^2/ac\pi^2)S_1$; nor be less than $(Q/2\pi K)(2s^2/ac\pi^2)S_2$, where $Q$ is the flow per unit length of tube.

[9] Compare Muskat, reference 1, p. 190.

[10] Don Kirkham, "Flow of ponded water into drain tubes in soil overlying an impervious layer," Trans. Amer. Geophys. Union **30**, 369–385, 1949.

[11] Y. Gustaffon, Untersuchungen Über die stromungsverhältnisse in gedräntem Boden, Acta. Agr. Suecana, Stockholm **2**, No. 1 (1946).

# Determination of Modified Index-of-Refraction over the Gulf of Mexico from Radio Data*

A. W. Straiton and A. H. LaGrone
*The University of Texas, Austin, Texas*
(Received November 21, 1949)

This paper presents the results of measurements of the signal strength and phase of 3.2-centimeter radio waves for a 26.5-mile path over the Gulf of Mexico under a variety of meteorological conditions. The radio data are used to determine the modified index-of-refraction as a function of height and the associated attenuation factor. The modified index-of-refraction curves are compared to those measured meteorologically.

## I. INTRODUCTION

THE strength of radio waves received through the troposphere is influenced by the distribution of the index-of-refraction with height. For this work a modified index-of-refraction, $M$,** is used to permit the use of a plane earth representation. Numerous papers have described the theory and measurements from which the radio signal strength may be determined from a known distribution of index with height.

Macfarlane[1] pointed out the possibility of reversing the process so as to obtain the index distribution with height from radio data. His method requires a knowledge of the height-gain curve and additional data from which the wave attenuation with distance may be determined.

Macfarlane's method may be extended[2] to use as known data the phase distribution with height as well as the signal strength distribution. This eliminates the necessity of additional information from which the attenuation may be determined. This modified method is used in this paper to obtain the low level index-of-refraction distribution on a 26.5-mile over-water path using a wave-length of 3.2 centimeters. These data, taken during June and July, 1949, are associated with a variety of meteorological conditions ranging from an almost standard atmosphere to very strong ducts.

## II. RADIO MEASUREMENTS

The radio path was over a section of the Gulf of Mexico adjacent to Bolivar Peninsula near Galveston, Texas as shown in Fig. 1. A 3.2-centimeter transmitter was located on a 50-foot tower on the mainland beach near High Island, Texas. A 2K39 Klystron supplied a continuous wave output of approximately 200 milliwatts. A picture of the transmitting tower is shown in Fig. 2.

Radio receivers were located on the northeast point of Galveston Island on two towers. The phase-difference equipment developed by the Electrical Engineering Research Laboratory of The University of Texas[3] was located on the elevator of a 60-foot tower with its base at 10 feet above mean sea level as shown in Fig. 3. This permitted measurements of the signal strength and phase difference from 15 to approximately 60 feet mean sea level. Three antennas were mounted on the elevator in a vertical line with a spacing of five feet between adjacent antennas. The signal strength was measured at the top and bottom antennas, and the phase difference was measured between the center and the two outside antennas. This permitted duplicate signal-strength and phase data over most of the height range obtained with the 60-foot tower. An auxiliary 16-foot tower with a movable elevator, as shown in Fig. 4, permitted measurement of signal strength from 2 to approximately 15 feet above the mean sea level. Horizontal polarization was used for the test.

## III. METEOROLOGICAL MEASUREMENTS

Meteorological stations were set up at two points along the radio path. One station was located at a lighthouse, Station $B$ in Fig. 1. Wet- and dry-bulb temperature soundings were made over a range of heights up to 60 feet, and wind speed and direction measurements were made at a height of about 70 feet.

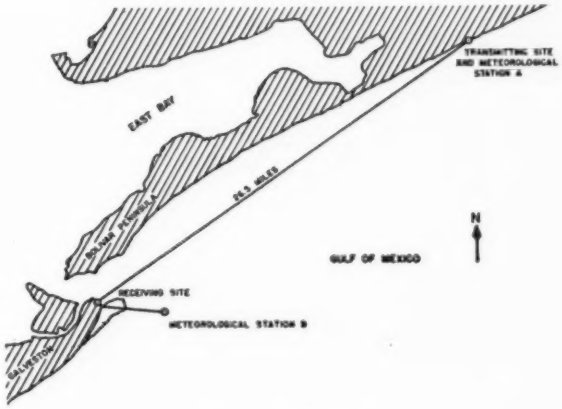


FIG. 1. Radio path.

* This work was sponsored by the ONR at The University of Texas under Contract N5ori-136, P.O.I.

** $M=(79/T)(P+4800e/T)+0.048h$, where $T$, $P$, $e$, and $h$ are temperature in degrees Kelvin, atmospheric pressure in millibars, vapor pressure in millibars, and height in feet. This permits the use of a plane earth representation. For the standard atmosphere, $dm/dh=0.036$ $M$ units per foot.

[1] G. G. Macfarlane, "A Method of Deducing the Refractive-Index Profile of a Stratified Atmosphere from Radio Observations," Meteorological Factors in Radio Wave Propagation; report of a conference of The Physical Society, London, 1948.

[2] A. W. Straiton, J. App. Phys. **20**, 228 (1949).

[3] F. E. Brooks, Jr. and C. W. Tolbert, "A Receiver for Measuring Angle-of-Arrival in a Complex Wave," Report No. 33, Electrical Engineering Research Laboratory, The University of Texas, 1949.

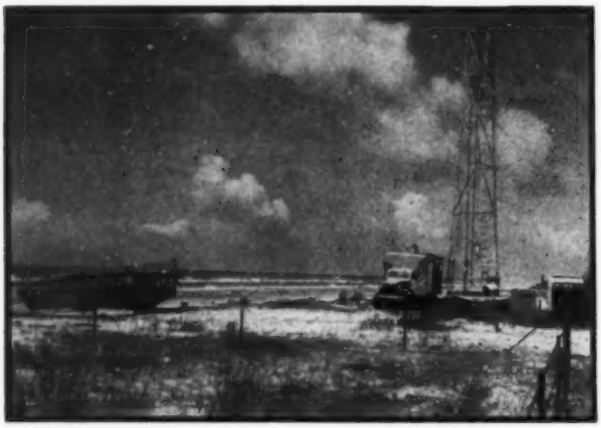

FIG. 2. Transmitting tower looking toward receiver.

The second meteorological station was on an oil drilling platform, Station $A$, approximately 50 feet off shore near the transmitter. Wet- and dry-bulb temperature measurements were made up to heights of 60 feet, and wind speed and direction were measured at the 10-foot platform level. A detailed description of the meteorological stations and the measurements is given elsewhere.[4] The meteorologically-measured modified index of refraction taken simultaneously with the radio data will be shown in this report for comparison with those determined from radio data.

## IV. THEORETICAL CONSIDERATIONS

For radio propagation well beyond the line of sight, the electrical field vector, $\psi$, may be expressed as the sum of a number of normal modes[5] as follows:

$$\psi = e^{i\omega t - i\pi/4}(2\pi/kr)^{\frac{1}{2}} \sum_m e^{-\gamma_m r} U_m(h_1) U_m(h), \qquad (1)$$

where $r$ is the distance around the earth's surface, $k$ is $2\pi$ divided by the wave-length, $\gamma_m$ is the propagation function for the $m$th mode, $U_m(h_1)$ and $U_m(h)$ are the height-gain function for the transmitter and receiver, respectively, for the $m$th mode.

For the distances and heights used in the measurement program, all modes higher than the first may usually be neglected.[6] The height-gain function is then given for the first mode by:

$$(d^2U_1/dh^2) + k^2[y(h) + \Lambda_1]U_1 = 0, \qquad (2)$$

where $\Lambda_1$ is characteristic value for the first mode.

## V. MACFARLANE'S EQUATION

Macfarlane[1] expressed Eq. (2) as follows: Let

$$U_1 = Ae^{i\phi} \quad \text{and} \quad \Lambda_1 = a + ib.$$

Then

$$k^2(y+a) = (\dot{\phi})^2 - d^2A/dh^2/A \qquad (3)$$

and

$$\dot{\phi} = \frac{-k^2 b \int_0^h A^2 dh}{A^2} \qquad (4)$$

where the dots indicate derivatives with respect to $h$.

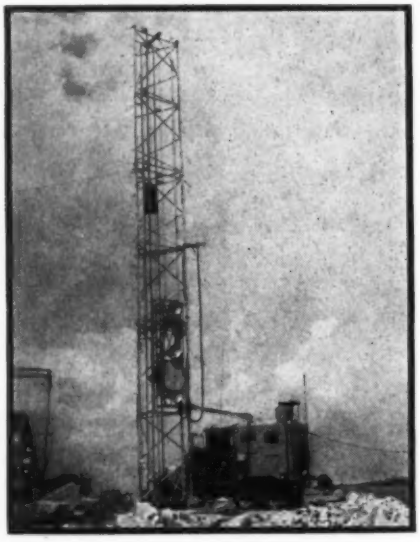

FIG. 3. Receiving tower with phase-difference equipment.

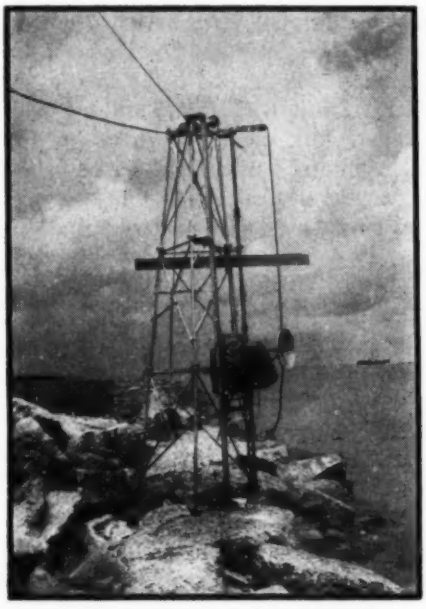

FIG. 4. Auxiliary tower for measurement of low level signal strengths.

[4] J. R. Gerhardt, "Summary of Meteorological Measurements Made for an Overwater Path near Galveston, Texas, during June and July, 1949," Report No. 36, Electrical Engineering Research Laboratory, The University of Texas, 1949.

[5] W. H. Furry, "Theory of Characteristic Functions in Problems of Anomalous Propagation," Report No. 680, Radiation Laboratory, Massachusetts Institute of Technology, 1945.

[6] H. W. Smith and A. W. Straiton, "Three Centimeter Radio Wave Propagation in a Surface Duct over The Gulf of Mexico," Report No. 26, Electrical Engineering Research Laboratory, The University of Texas, 1949.

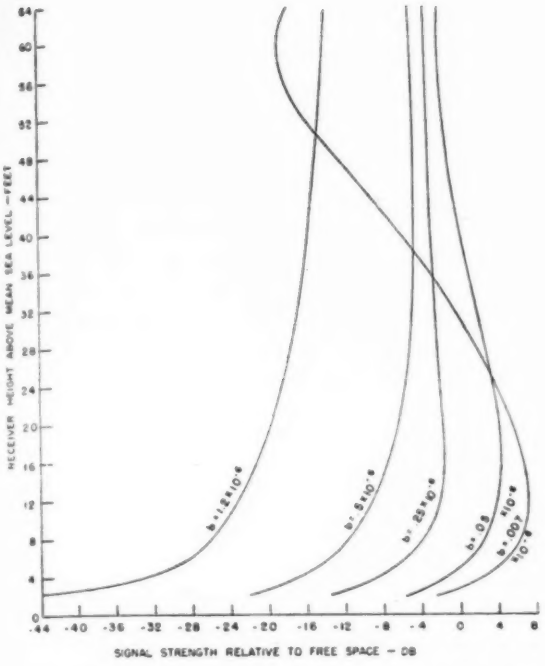


FIG. 5. Measured signal-strength curves on a db basis relative to free space.

Macfarlane replaced $\dot{\phi}$ in Eq. (3) by the right side of Eq. (4). Then, if the attenuation factor $b$ is known from measurements at other frequencies or distance, $(y+a)$ can be determined directly.

However, since the measurements made at the Electrical Engineering Research Laboratory were of $A$ and $\dot{\phi}$, $(y+a)$ can be determined directly from (3), and $b$ from (4).

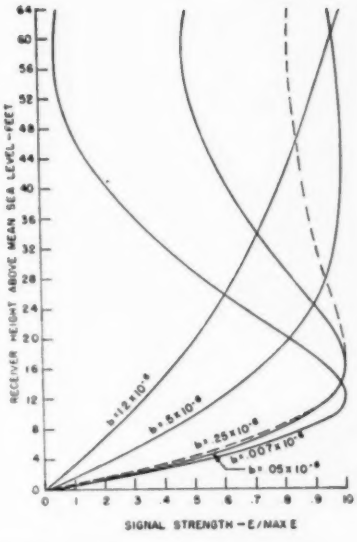


FIG. 6. Measured signal-strength curves relative to maximum signal in height interval.

## VI. PROCEDURE FOR FINDING $M$ CURVES

The procedure used was as follows:

1. The phase difference between the signals at the receivers and the signal strength at the receivers were obtained from the measurement charts. This provided the signal strength, $A$, and the phase difference, $\dot{\phi}$, both as a function of height.
2. The first derivative of $A$ with respect to $h$ was obtained graphically and plotted as a function of $h$. A smoothed first derivative was drawn and the original $A$ curve was modified in accordance with the smoothed first derivative curve.
3. The second derivative with respect to $h$, was found graphically and divided by $A$.
4. A smooth curve was drawn through the values of $\phi$ as a function of height.
5. The values of $(y+a)=[2(M-M_0)\times10^{-6}+a]$ were found from Eq. (3).
6. Curves of $\dot{\phi}$ for several assumed values of $b$ were plotted

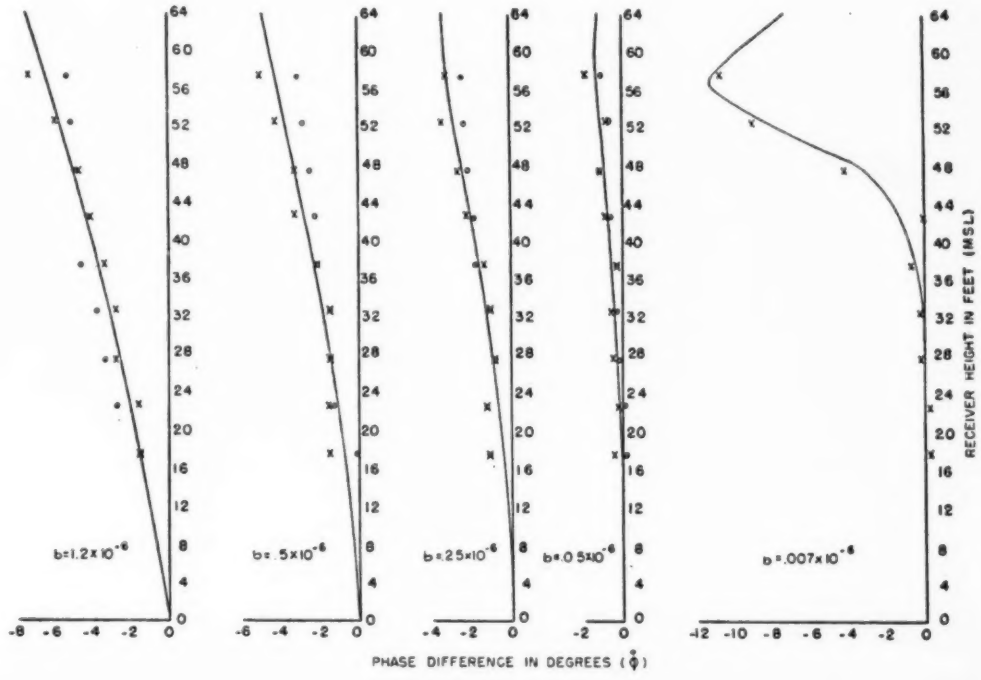


FIG. 7. Measured phase-difference curves.

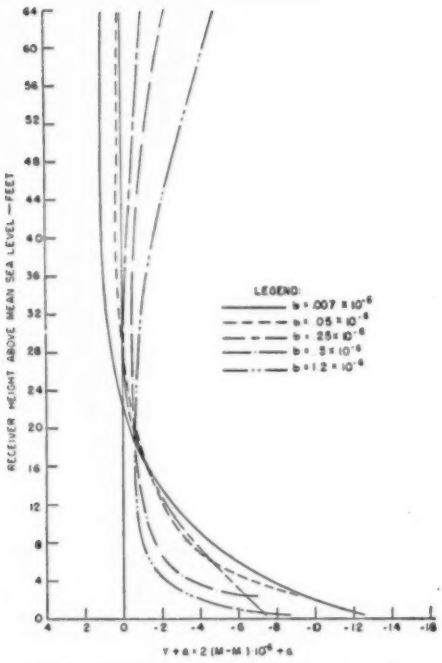


FIG. 8. $M$ curves determined from radio data.

from Eq. (4). When the measured values of $\phi$ were superimposed on these curves, the value of $b$ was chosen such that the measured curve coincided as nearly as possible with the one determined from the $A$ data.

## VII. HEIGHT-GAIN CURVES

In measuring the height-gain curves, data were taken in several ways. The receiver on the auxiliary 16-foot tower was moved up and down while its received signal was being recorded. The 16-foot tower receiver was then set at 15 feet and left there as a reference while the main receiver on the 60-foot tower was moved up continuously and down in five-foot steps. Since the signal was scintillating rapidly, averages of the various readings were taken to establish the height-gain curves shown. Fifty-two sets of such readings were taken and the height-gain or $A$ curves were drawn. Many of the $A$ curves were near duplicates and others were very similar. The entire group can be well represented by five samples which include the two extreme signals and three intermediate values. The signal strength-height curves for these five cases are shown on a db basis relative to free space in Fig. 5. The same curves are shown in Fig. 6 in terms of the field strength at a given height divided by the maximum field strength in the interval included. The curves representing the various examples are the ones which gave the smoothed first derivative curves. Seven intermediate values are added to increase to twelve the number used for the tabulation shown later.

TABLE I. Phase-integral condition.

| Number | Date | Time | $\int_0^{Z_0^1}(y+a+ib)dh$ | $\frac{1}{2}(\pi/k)$ |
|---|---|---|---|---|
| 1* | 7- 7-49 | 0530–0647 | $0.0346/-3°$ | 0.0394/0 |
| 2* | 7- 7-49 | 0815–0900 | $0.0362/-0.7°$ | 0.0394/0 |
| 3* | 6-30-49 | 0043–0105 | 0.0351 | 0.0394 |
| 4 | 6-29-49 | 0550–0621 | 0.0379 | 0.0394 |
| 5 | 7- 6-49 | 1130–1210 | 0.0373 | 0.0394 |
| 6 | 7- 6-49 | 1235–1300 | 0.0405 | 0.0394 |
| 7* | 6-29-49 | 1020–1059 | 0.0399 | 0.0394 |
| 8 | 6-27-49 | 1729–1815 | 0.0410 | 0.0394 |
| 9 | 6-28-49 | 0942–0957 | 0.0410 | 0.0394 |
| 10 | 6-27-49 | 1535–1555 | 0.0412 | 0.0394 |
| 11 | 6-28-49 | 0830–0900 | 0.0402 | 0.0394 |
| 12* | 6-27-49 | 1920–2001 | 0.0395 | 0.0394 |

* Cases shown in graphs.

## VIII. PHASE DIFFERENCE-HEIGHT CURVES

The phase-difference curves corresponding to the signal-strength curves shown in Figs. 5 and 6 are shown in Fig. 7. The points indicated are the values measured between the center and each of the two outside antennas for the five-foot interval runs. The lines shown are the values of $\phi$ determined from the corresponding signal-strength curves by Eq. (4). Because of the physical location of the receivers, it was not convenient to use a reference angle. The reference angles were then chosen so that $\phi$ would fulfill the boundary condition of being zero at zero height.

## IX. $M$ CURVES FROM RADIO DATA

The $A$ curves of Fig. 6 and the $\phi$ curves of Fig. 7 were used to determine $(y+a)$ from Eq. (3). The $M$ curves thus obtained for the five cases considered are shown in Fig. 8. The inability to separate $a$ from $2(M-M_0)$ is really no disadvantage. The reference value of index of refraction, $M_0$, is not of much significance and could, without harm, be increased or decreased. However, $(y+a)$ or $[2(M-M_0)\times10^{-6}+a]$ is the quantity that appears in the equations for the height-gain function given in reference 5. The degree to which $(y+a)$ goes negative is a measure of the amount of trapping and the points at which $(y+a)$ is zero are the "turning points," $Z_0^m$, of the W.K.B. approximation solution.

TABLE II. Attenuation factor.

| Number | From $M$ curves $b\times10^{-6}$ | From radio data $b\times10^{-6}$ | From radio data db/mile |
|---|---|---|---|
| 1* | 1.37 | 1.2 | 1.6 |
| 2* | 0.59 | 0.5 | 0.7 |
| 3* | 0.17 | 0.25 | 0.34 |
| 4 | 0.38 | 0.2 | 0.27 |
| 5 | 0.23 | 0.15 | 0.21 |
| 6 | 0.15 | 0.15 | 0.21 |
| 7* | 0.06 | 0.05 | 0.07 |
| 8 | 0.00 | 0.03 | 0.04 |
| 9 | 0.00 | 0.01 | 0.01 |
| 10 | 0.00 | 0.01 | 0.01 |
| 11 | 0.00 | 0.008 | 0.01 |
| 12* | 0.00 | 0.007 | 0.01 |

* Cases shown in graphs.

TABLE III. Positioning of $(y+a)$ curves.

| Number | $a$ From radio data | $a$ From shape of $M$ curve |
|---|---|---|
| 1* | −1.54 | −1.60 |
| 2* | −2.70 | −2.90 |
| 3* | −3.03 | −3.14 |
| 4 | −2.40 | −2.30 |
| 5 | −3.50 | −3.42 |
| 6 | −2.92 | −3.00 |
| 7* | −2.94 | −4.08 |
| 8 | −5.44 | −5.59 |
| 9 | −5.01 | −4.95 |
| 10 | −6.41 | −5.75 |
| 11 | −5.91 | −5.92 |
| 12* | −5.71 | −6.03 |

* Cases shown in graphs.

## X. CHECK OF PHASE-INTEGRAL CONDITION

From reference 5, the phase-integral condition is known to be

$$\int_0^{z_0'} (y+a+ib)^{\frac{1}{2}}dz=\frac{(m-\frac{1}{4})\pi}{k}=\frac{3\pi}{4k}. \qquad (5)$$

For the cases when $(y+a)$ becomes zero, $(ib)$ may be neglected and the integral evaluated numerically from the measured data as the area beneath the portion of the $(y+a)$ curve below the first turning point. For the case when $(y+a)$ did not become zero, the curve was approximated by a linear-exponential expression and a complex turning point established. With this turning point, the integral of Eq. (5) may be evaluated. The value of the phase integral of Eq. (5) for twelve cases is compared with the theoretical value in Table I.

TABLE IV. Free-space values.

| Number | db below arbitrary reference: From transmitter and receiver gain | From shape of $(y+a)$ curve | Deviation** db | Attenuation factor $b\times10^{-6}$ |
|---|---|---|---|---|
| 1* | 33.5 | 29.5 | 4.1 | 1.2 |
| 2* | 33.5 | 37.5 | − 4.0 | 0.5 |
| 3* | 33.5 | 42.5 | − 5.9 | 0.25 |
| 4 | 33.5 | 37.7 | − 4.2 | 0.2 |
| 5 | 33.5 | 44.9 | −11.4 | 0.15 |
| 6 | 33.5 | 36.6 | − 3.1 | 0.15 |
| 7* | 33.5 | 43.1 | − 9.6 | 0.05 |
| 8 | 33.5 | 41.5 | − 8.0 | 0.03 |
| 9 | 33.5 | 42.3 | − 8.8 | 0.01 |
| 10 | 33.5 | 42.7 | − 9.2 | 0.01 |
| 11 | 33.5 | 43.0 | − 9.5 | 0.008 |
| 12* | 33.5 | 43.7 | −10.2 | 0.007 |

* Cases shown in graphs.
** Minus indicates measured signa less than theoretical.

From Table I it is seen that the phase-integral condition is approximately satisfied.

## XI. DETERMINATION OF WAVE ATTENUATION

As discussed in Section V, the wave-attenuation factor $b$ may be determined from Eq. (4) by use of radio data. This attenuation is relative to the inverse square root relationship, and may be converted to decibels per mile as shown in Table II.

The attenuation factors may also be determined from the shape of the $M$ curves which were obtained from radio data. The procedure used was to express the $M$ curves from radio data in the form of a linear-exponential; and from the charts given by Pekeris and Ament,[7] values of $b$ were obtained. A comparison of these values of $b$ with those determined by Eq. (4) is also shown in

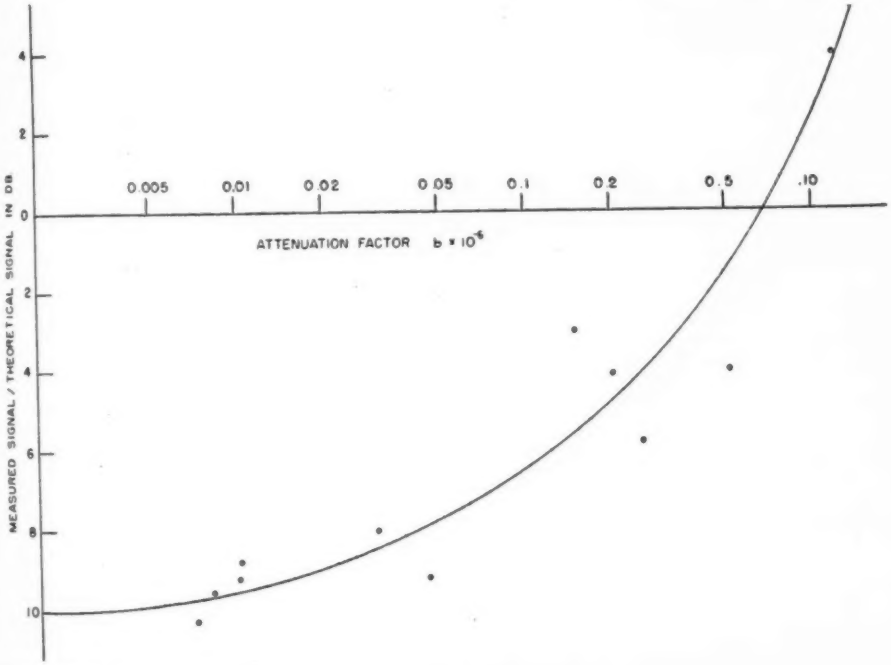


FIG. 9. Comparison of $M$ curves from radio data with meteorological data.

[7] C. L. Pekeris and W. S. Ament, Phil. Mag. **38**, 801–823 (1947).

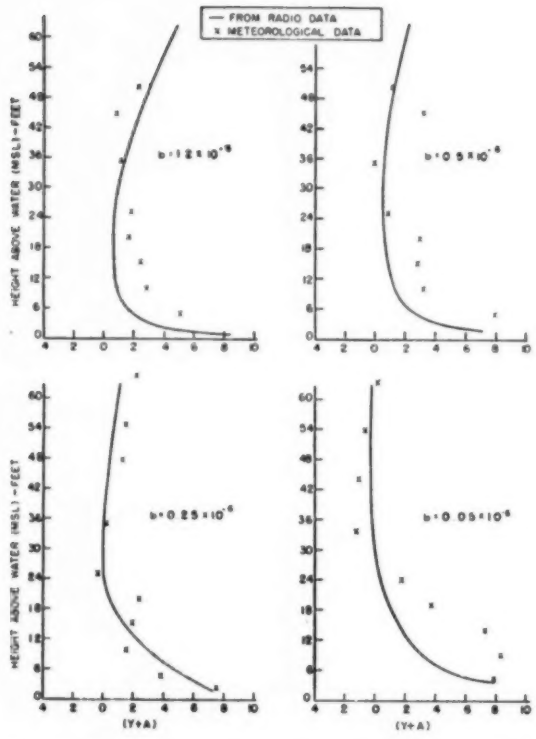


FIG. 10. Relationship between measured and theoretical signal strength.

Table II. The values of $b$ obtained from the charts for cases 8 through 12 are shown as zero, since the scale of the charts was such that the values could not be distinguished from zero. There would, of course, be some attenuation, and the value obtained from radio data is thought to be fairly accurate.

## XII. CHECK OF POSITIONING OF $M$ CURVES

The form of linear exponential used by Pekeris and Ament[7] was

$$M-M_0=(0.036h+ge^{-ch}).$$

Then $(y+a)$ will be given by

$$(y+a)=[2(M-M_0)\cdot 10^{-6}+a]$$
$$=[(0.072h+2ge^{-ch})\cdot 10^{-6}+a].$$

The values of $g$, $c$, and $a$ necessary to fit the linear exponential to $M$ curves were determined. However, the value of $a$ depends on $g$ and $c$ and may be determined from them by reference 7. In other words, a given shape of $M$ curve must have a certain positioning with respect to the $(y+a)$ axis. Since the positioning is known from the measured data, a comparison may be made between the measured and theoretical position of the $(y+a)$ curve. Such a comparison is shown in Table III.

## XIII. CHECK OF ABSOLUTE SIGNAL STRENGTH

The calculation of $M$ curves from radio data requires a knowledge of the relative and not the absolute signal strengths. However, from the shape of the $M$ curves determined from radio data, the signal strength relative to the free-space value may be determined. Using the measured signal strength, a theoretical value for the free-space signal was found for each case by the method of reference 5. Since the gains of the transmitting and receiving system were known as well as the power of the transmitter, a free-space value was established directly. The two values of the free-space signal are compared in Table IV.

From Table IV, it is noticed that the deviation between the theoretical and measured free-space signal strength is a function of the attenuation factor. This relationship is shown graphically in Fig. 9. For strong ducts in which the attenuation factor is low, the measured signal is considerably weaker than the theoretical value. However, for weaker ducts the measured signal strength approaches the theoretical value. It is thought that this deviation may be due to scattering by discontinuities in the atmosphere. For strong ducts, more signal is lost by scattering inside of the duct than is gained from scattering outside of the duct. However, when the signal is weak, the contribution from scattering outside of the duct is significant.

## XIV. COMPARISON WITH METEOROLOGICALLY MEASURED $M$ CURVES

As stated in Section III, meteorological data were taken at sites near both ends of the radio path. From the data taken at these sites simultaneously with the radio data, modified index-of-refraction distributions were obtained. For these curves, the measurements made at a given height at the two ends were averaged to obtain the value for that height. The $M$ curves determined from radio data are compared with meteorological data in Fig. 10. From this figure, it is seen that general agreement exists between the $M$ curves determined from radio data and meteorological data. However, it is noted that the meteorologically measured points are badly scattered. It is felt that it is difficult to determine the average $M$ curve over a distance from the measurements at a single site since the meteorological parameters were fluctuating considerably. It seems, therefore, that the $M$ curves may be obtained with a higher degree of accuracy from the radio data than from temperature and humidity measurements.

## XV. CONCLUSIONS

It appears from this paper that for the conditions of the experiment, the modified index-of-refraction values as a function of height may be satisfactorily determined from signal-strength and phase-difference measurements. However, for very short distances, the method will fail since a single mode will not account for the signal distributions. For greater distances or very weak signals, the method may fail when an appreciable part of the signal is the result of scattering from elevated discontinuities in the index of refraction.

# The Effective Permeability of an Array of Thin Conducting Disks

GERALD ESTRIN*
*University of Wisconsin, Madison, Wisconsin*
(Received December 5, 1949)

A three-dimensional array of thin conducting disks has found special application as an artificial refracting medium at microwave frequencies. Treatment of these refractive properties at oblique incidence requires specification of the dielectric and permeability coefficients of the medium.

When an alternating magnetic field is parallel to the disk faces, the field is undisturbed and the relative permeability coefficient is unity. When the alternating magnetic field is normal to the disk faces, circulating currents are induced on them. The boundary value problem of determining the current distribution on a single perfectly conducting disk is carried out in detail for the case where the disk diameter is small compared to the wave-length. This current distribution is found to be representable by a magnetic dipole. If the disks in an array are far enough apart to neglect interaction, a simple summation of the dipole moments shows the array to have a diamagnetic susceptibility in the direction normal to the disk faces.

Combining this result with an expression for the dielectric coefficient, which was developed earlier by Kock, the constants of the anisotropic array are completely specified.

## INTRODUCTION

THE first part of this paper evaluates the steady state circulating current distribution induced in a thin conducting disk by a perpendicular time varying magnetic field whose wave-length is large compared to the disk diameter. The disk is treated as the limiting case of an oblate spheroid. The use of oblate spheroidal coordinates and the definition of a scalar potential function, $V=rE_\varphi$, lead to a Legendre Polynomial solution outside a conducting spheroid and to a general power series solution inside. Imposition of boundary conditions at the surface and far from the obstacle provides a simple relation for the surface current density distribution in the limit of a perfectly conducting disk.

In Part II, a magnetic dipole equivalent to the surface current distribution on the disk, is evaluated by integration of ring-shaped elements. For the case of a three-dimensional array in which the packing of the disks is small enough to neglect interaction, the dipole moment per unit volume leads to an expression for the magnetic susceptibility. The composite medium is observed to be diamagnetic in the direction normal to the disk faces and non-magnetic in directions parallel to them. There is a simple relation between the magnetic and electric susceptibilities of this array. Knowledge of the disk radius and the number per unit volume completely specifies the component constituitive equations which are necessary to determine the effect of the composite medium on an obliquely incident electromagnetic wave. The constituitive coefficients are calculated for two cases; one typical of microwave lens design and the other of a prism constructed at the University of Wisconsin.

## PART I

As illustrated in Fig. 1, a conducting oblate spheroid is placed in a time varying magnetic field which is parallel to the axis of rotation of the spheroid. The applied field is given by $\bar{H}=\bar{\imath}H_a=\bar{H}_0\exp(-j\omega t)$. The diameter of the conducting body is assumed small compared to the wave-length and Maxwell's field equations for steady state become:

$$\nabla\times\bar{E}-j\omega\mu\bar{H}=0, \tag{1a}$$

$$\nabla\times\bar{H}-\sigma\bar{E}=0. \tag{1b}$$

Oblate spheroidal coordinates[1,2] provide a natural system for dealing with this problem. Using the notation defined in Appendix I, the component field equations separate into two independent sets. The set that must be solved in this case is given by:

$$\partial/\partial\eta(h_3E_\varphi)-j\omega\mu h_2h_3H_\xi=0, \tag{2a}$$

$$\partial/\partial\xi(h_3E_\varphi)+j\omega\mu h_1h_3H_\eta=0, \tag{2b}$$

$$\partial/\partial\xi(h_2H_\eta)-\partial/\partial\eta(h_1H_\xi)-\sigma h_1h_2E_\varphi=0. \tag{2c}$$

When the field equations in (1) are uncoupled they give

$$\nabla\times\nabla\times\bar{E}=j\omega\sigma\mu\bar{E}. \tag{3}$$

Since there is only a $\varphi$ component of $\bar{E}$, (3) yields

$$\frac{\partial}{\partial\xi}\left[\frac{h_2}{h_1h_3}\frac{\partial}{\partial\xi}(h_3E_\varphi)\right]+\frac{\partial}{\partial\eta}\left[\frac{h_1}{h_2h_3}\frac{\partial}{\partial\eta}(h_3E_\varphi)\right]=-j\omega\sigma\mu h_1h_2E_\varphi. \tag{4}$$

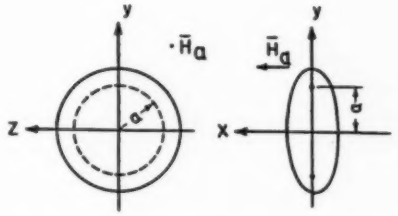


FIG. 1.

* RCA Research Fellow, Electrical Engineering Department.

[1] W. R. Smythe, *Static and Dynamic Electricity* (McGraw-Hill Book Company, Inc., New York, 1939).
[2] J. A. Stratton, *Electromagnetic Theory* (McGraw-Hill Book Company, Inc., New York, 1941).

If a potential function, $V \equiv rE_\varphi$, is now defined and substituted in (2) and (4), the following set of equations results.

$$H_\xi = \frac{-j}{\mu\omega h_2 h_3}\frac{\partial V}{\partial \eta}, \tag{5a}$$

$$H_\eta = \frac{j}{\mu\omega h_1 h_3}\frac{\partial V}{\partial \xi}, \tag{5b}$$

$$\frac{\partial}{\partial \xi}\left[\frac{h_2}{h_1 h_3}\frac{\partial V}{\partial \xi}\right]+\frac{\partial}{\partial \eta}\left[\frac{h_1}{h_2 h_3}\frac{\partial V}{\partial \eta}\right]+j\omega\sigma\mu\frac{h_1 h_2}{h_3}V=0. \tag{5c}$$

Separation of variables in (5c) is carried out in Appendix II yielding identical differential equations in the independent variables, $\eta$ and $(j\xi)$ of the form,

$$(1-x^2)\partial^2 y/\partial x^2+(k^2x^2+D)y=0, \tag{6}$$

where $k^2=ja^2\omega\sigma\mu$ and $a$ is defined in Appendix I.

Outside the conducting spheroid, $k^2=0$. Appendix III shows that with $D=l(l+1)$, Eq. (6) is then satisfied by a solution containing Legendre Polynomials of the first and second kind.

$$y=(1-x^2)d/dx[P_l(x)+Q_l(x)]. \tag{7}$$

Hence a set of solutions is obtained for the potential function, $V$, in the region outside the conducting spheroid.

$$V_0=\sum_{l=0}^{\infty} j(1-\eta^2)(1+\xi^2)\left[A_l\frac{d}{d\eta}P_l(\eta)+B_l\frac{d}{d\eta}Q_l(\eta)\right]\times\left[C_l\frac{d}{d\xi}P_l(j\xi)+D_l\frac{d}{d\xi}Q_l(j\xi)\right]. \tag{8}$$

The set of solutions, (8), must now be restricted by imposing the physical conditions of the problem.

(a) The field vectors are bounded. Therefore $V_0$ must be bounded for finite values of the coordinates. Since $Q_l(\pm 1)$ is unbounded, $B_l\equiv 0$ for all $l$.

(b) $H_\xi^2+H_\eta^2$ must reduce to the external field $H_a^2$ when $\xi\to\infty$. As shown in Appendix IV, this condition requires that

$$V_0\underset{\xi\to\infty}{\longrightarrow} j\omega\mu a^2(1-\eta^2)(1+\xi^2)H_a/2.$$

Since

$$Q_l(j\xi)\underset{\xi\to\infty}{\longrightarrow}0 \quad \text{and} \quad P_l(j\xi)\underset{\xi\to\infty}{\longrightarrow}\infty,$$

$$\sum_{l=0}^{\infty}\left[A_l\frac{d}{d\eta}P_l(\eta)\right]\left[C_l\frac{d}{d\xi}P_l(j\xi)\right]$$

may enter into the solution only as a constant. Hence $C_l\equiv 0$ for $l>1$.

(c) Symmetry considerations demand that $V(\xi,+|\eta|)=V(\xi,-|\eta|)$. Hence the solution may contain only even powers of $\eta$ and $A_l\equiv 0$ for $l=2n$, where $n=0, 1, 2, \cdots$.

Thus the solution for $V$ outside the spheroid reduces to

$$V_0=(1-\eta^2)(1+\xi^2)\left[\frac{j\omega\mu a^2}{2}H_a+\sum_{n=0}^{\infty}F_{2n+1}\frac{d}{d\eta}P_{2n+1}(\eta)\frac{d}{d\xi}Q_{2n+1}(j\xi)\right]. \tag{9}$$

Inside the conducting spheroid, the differential equation to be solved is of the form,

$$(1-x^2)d^2y/dx^2+[l(l+1)+k^2x^2]y=0. \tag{10}$$

A series solution in positive powers of $x$ results in the recursion formula,

$$C_{s+2}=\frac{s(s+1)-l(l+1)}{(s+2)(s+1)}C_s-\frac{k^2}{(s+2)(s+1)}C_{s-2}. \tag{11}$$

The continuity of $V$ at the surface requires that the solution contain only even powers of the independent variable. Hence

$$V_i=\sum_{n=0}^{\infty}G_{2n+1}\sum_s C_{2s}\eta^{2s}\sum_p C_{2p}(j\xi)^{2p}, \tag{12}$$

where the coefficients of (12) and (9) must be matched at the surface.[3]

## CURRENT DISTRIBUTION ON A PERFECTLY CONDUCTING DISK

For a perfectly conducting spheroid, $V_i=0$. $V$ must be continuous at the surface, $\xi=\xi_0$, for arbitrary values of $\eta$. This requires that

$$-j\mu\omega a^2 H_a/2=\left[\sum_{n=0}^{\infty}F_{2n+1}\frac{d}{d\eta}P_{2n+1}(\eta)\frac{d}{d\xi}Q_{2n+1}(j\xi)\right]_{\xi=\xi_0}. \tag{13}$$

This relation can hold only for $n=0$. Hence $F_{2n+1}\equiv 0$ for $n\neq 0$ giving

$$-j\mu\omega a^2 H_a/2=F_1[\cot^{-1}\xi-\xi/(1+\xi^2)]_{\xi=\xi_0}. \tag{14}$$

The spheroid reduces to a thin disk as $\xi\to 0$. In that case (14) yields $F_1=-j\mu\omega a^2 H_a/\pi$ and

$$V_0=j(1-\eta^2)(1+\xi^2)\omega\mu a^2 H_a\times\{1-2/\pi[\cot^{-1}\xi-\xi/(1+\xi^2)]\}/2. \tag{15}$$

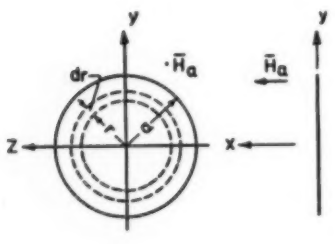


FIG. 2.

[3] Extensive treatment of this type of solution is given by R. C. Maclaurin, Trans. Camb. Phil. Soc. 17, 41–108 (1899).

The surface current density distribution is evaluated from the discontinuity in the tangential component of $\bar{H}$ at the double layer obtained when $\xi \to 0$. Using the relation (5b), the surface current density, $i_\varphi$, is

$$i_\varphi = 2[H_\eta|_{\xi=0}] = \frac{2j}{\mu\omega h_1 h_3}\frac{\partial V_0}{\partial \xi}\bigg|_{\xi=0}. \tag{16}$$

When the values of the metric coefficients are substituted, (16) reduces to

$$-i_\varphi = [4a(1-\eta^2)H_a/\pi\eta r]_{\xi=0}. \tag{17}$$

However $(1-\eta^2)/\eta \xrightarrow[\xi\to 0]{} r^2/a(a^2-r^2)^{\frac{1}{2}}$, resulting in the final simple expression,[4]

$$-i_\varphi = 4H_a r/\pi(a^2-r^2)^{\frac{1}{2}}. \tag{18}$$

## PART II

The circulating current, $I$, flowing in the ring element of Fig. 2 is given by

$$I = i_\varphi dr = -4H_a r dr/\pi(a^2-r^2)^{\frac{1}{2}}. \tag{19}$$

The effect of this circulating current may be represented by an elementary magnetic dipole, defined by

$$dm = \pi r^2 I = -4H_a r^3 dr(a^2-r^2)^{-\frac{1}{2}}. \tag{20}$$

Integration over the face of the disk [Dwight 323.01] then provides an expression for a magnetic dipole equivalent to the entire current distribution.

$$m = -(8/3)a^3 H_a. \tag{21}$$

A three dimensional array of thin conducting disks is illustrated in Fig. 3. If the number of disks per unit volume is small enough to neglect interaction between them, the magnetization of the composite medium is given simply by

$$M = Nm. \tag{22}$$

$N$ is the number of disks per unit volume and $m$ is given by (21). Since the ratio of the magnetization, $M$, to the applied field, $H_a$, is defined as the magnetic susceptibility $x_m$,

$$x_m = M/H_a = -8Na^3/3. \tag{23}$$

The negative susceptibility of (23) is a characteristic of diamagnetic media. The relative permeability is then evaluated from the relation,

$$k_m = 1 + x_m = 1 - 8Na^3/3. \tag{24}$$

The positive definite form of the expression for the energy stored in the magnetic field does not permit $k_m$ to be negative. This limitation is implicit in the assumption that $N$ is small.

Up to this point the obvious anisotropy of the composite medium has not been mentioned. For the cartesian coordinates shown in Fig. 3, (24) holds for an applied magnetic field in the $x$ direction, normal to the disk faces. In directions parallel to the disk faces, the thin disks do not disturb the applied field and $k_{my} = k_{mz} = 1$. Thus the constituitive equations for the magnetic vectors take the form,

$$\begin{bmatrix} B_x \\ B_y \\ B_z \end{bmatrix} = \mu_0 \begin{bmatrix} 1-8Na^3/3 & 0 & 0 \\ 0 & 1 & 0 \\ 0 & 0 & 1 \end{bmatrix} \begin{bmatrix} H_x \\ H_y \\ H_z \end{bmatrix}. \tag{25}$$

The electric susceptibility, $x_e$, for this type of array has previously been evaluated for the case of an external electric field parallel to the disk faces,[5] yielding

$$x_e = 16Na^3/3. \tag{26}$$

When the anisotropy is considered, the constituitive equations for the electric vectors become

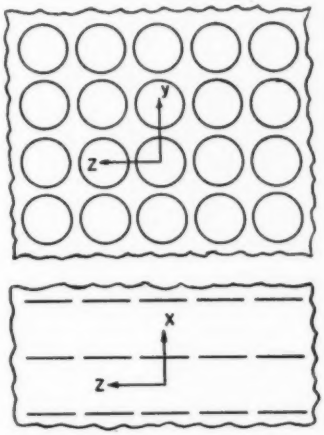

FIG. 3.

$$\begin{bmatrix} D_x \\ D_y \\ D_z \end{bmatrix} = \epsilon_0 \begin{bmatrix} 1 & 0 & 0 \\ 0 & 1+16Na^3/3 & 0 \\ 0 & 0 & 1+16Na^3/3 \end{bmatrix} \begin{bmatrix} E_x \\ E_y \\ E_z \end{bmatrix}. \tag{27}$$

The relations in (25) and (27) now completely specify the characteristics of the composite medium, which was originally developed for use in focusing microwaves. Past analyses of this medium have assumed normal incidence of a plane wave, thereby neglecting the anisotropic characteristics. These results now permit extension to the case of oblique incidence.

A typical value for the relative dielectric constant in arrays designed for microwave lenses is $k_e = 2.25$. The constituitive equations for this case then become:

$$\begin{bmatrix} D_x \\ D_y \\ D_z \end{bmatrix} = \epsilon_0 \begin{bmatrix} 1 & 0 & 0 \\ 0 & 2.25 & 0 \\ 0 & 0 & 2.25 \end{bmatrix} \begin{bmatrix} E_x \\ E_y \\ E_z \end{bmatrix}. \tag{28a}$$

$$\begin{bmatrix} B_x \\ B_y \\ B_z \end{bmatrix} = \mu_0 \begin{bmatrix} 0.375 & 0 & 0 \\ 0 & 1 & 0 \\ 0 & 0 & 1 \end{bmatrix} \begin{bmatrix} H_x \\ H_y \\ H_z \end{bmatrix}. \tag{28b}$$

An experimental prism, constructed at the University of

[4] This result differs by a factor of 2 from that reported by M. Marc Jouguet in an abstract in Comptes Rendus **216**, 523 April, 1943. The discrepancy is apparently due to his neglect of the double layer of surface current on the disk.

[5] W. E. Kock, "Metallic delay lenses," Bell Sys. Tech. J. **27**, 58 (January, 1948).

Wisconsin displays the following characteristics:

$$\begin{bmatrix} D_x \\ D_y \\ D_z \end{bmatrix} = \epsilon_0 \begin{bmatrix} 1 & 0 & 0 \\ 0 & 1.21 & 0 \\ 0 & 0 & 1.21 \end{bmatrix} \begin{bmatrix} E_x \\ E_y \\ E_z \end{bmatrix}. \tag{29a}$$

$$\begin{bmatrix} B_x \\ B_y \\ B_z \end{bmatrix} = \mu_0 \begin{bmatrix} 0.895 & 0 & 0 \\ 0 & 1 & 0 \\ 0 & 0 & 1 \end{bmatrix} \begin{bmatrix} H_x \\ H_y \\ H_z \end{bmatrix}. \tag{29b}$$


## ACKNOWLEDGMENT

The author would like to acknowledge the support given to this research project by the Radio Corporation of America since July, 1949 and by the Wisconsin Alumni Research Foundation from February, 1948 to June, 1949. In addition the author is indebted to the guidance of Professor V. C. Rideout of the University of Wisconsin Electrical Engineering Department.


## APPENDIX I

Oblate spheroidal coordinates are defined by the following relations:

$$y = r\cos\varphi; \quad z = r\sin\varphi, \tag{1a}$$

$$\frac{x^2}{a^2\xi^2} + \frac{r^2}{a^2(1+\xi^2)} = 1 \quad (0 \leq \xi \leq \infty), \tag{1b}$$

$$\frac{x^2}{-a^2\eta^2} + \frac{r^2}{a^2(1-\eta^2)} = 1 \quad (-1 \leq \eta \leq +1), \tag{1c}$$

$\xi$ = constant describes a family of confocal oblate spheroids where (2a) is the distance between the foci in any plane through the $x$-axis. $\eta$ = constant describes a family of confocal hyperboloids of one sheet, orthogonal to the spheroids. $\varphi$ measures the azimuth angle in the meridian plane.

An element of arc length in this system is given by:

$$\begin{aligned} (ds)^2 &= h_1^2(d\xi)^2 + h_2^2(d\eta)^2 + h_3^2(d\varphi)^2, \\ h_1 &= a(\xi^2+\eta^2)^{\frac{1}{2}}(1+\xi^2)^{-\frac{1}{2}}, \\ h_2 &= a(\xi^2+\eta^2)^{\frac{1}{2}}(1-\eta^2)^{-\frac{1}{2}}, \\ h_3 &= r = a[(1+\xi^2)(1-\eta^2)]^{\frac{1}{2}}. \end{aligned} \tag{2}$$

If the field vectors have no $\varphi$ dependence, the component field equations are given by (2) of Part I along with the following:

$$\partial(h_3H_\varphi)/\partial\eta - h_2h_3\sigma E_\xi = 0, \tag{3a}$$

$$\partial(h_3H_\varphi)/\partial\xi + h_1h_3\sigma E_\eta = 0, \tag{3b}$$

$$\partial(h_2E_\eta)/\partial\xi - \partial(h_1E_\xi)/\partial\eta - j\omega\mu h_1h_2H_\varphi = 0. \tag{3c}$$

## APPENDIX II

In (5c) of Part I, substitution of the metric coefficients gives

$$\frac{\partial}{\partial\xi}\left(\frac{1}{a(1-\eta^2)}\frac{\partial V}{\partial\xi}\right) + \frac{\partial}{\partial\eta}\left(\frac{1}{a(1+\xi^2)}\frac{\partial V}{\partial\eta}\right) + j\omega\sigma\mu a\left(\frac{\xi^2+\eta^2}{(1+\xi^2)(1-\eta^2)}\right)V = 0. \tag{1}$$

Let $V = V_1(\xi)V_2(\eta)$ and multiply through by $a(1-\eta^2)(1+\xi^2)/V_1V_2$.

$$\frac{(1+\xi^2)}{V_1}\frac{d^2V_1}{d\xi^2} + \frac{(1-\eta^2)}{V_2}\frac{d^2V_2}{d\eta^2} + ja^2\omega\mu\sigma(\xi^2+\eta^2) = 0. \tag{2}$$

Introducing the separation constant $D$, and making the substitutions, $\xi' = j\xi$ and $k^2 = j\omega\sigma\mu a^2$ gives

$$(1-\eta^2)d^2V_2/d\eta^2 + (k^2\eta^2+D)V_2 = 0, \tag{3a}$$

$$(1-\xi'^2)d^2V_1/d\xi'^2 + (k^2\xi'^2+D)V_1 = 0. \tag{3b}$$

## APPENDIX III

Outside the spheroid,

$$(1-x^2)d^2y/dx^2 + Dy = 0. \tag{1}$$

Consider the equation satisfied by the Legendre Polynomials, $P_l(x)$.

$$(1-x^2)d^2y/dx^2 - 2xdy/dx + l(l+1)y = 0. \tag{2}$$

Differentiate (2) with respect to $x$ and substitute $y = P_l(x)$.

$$(1-x^2)d^2/dx^2[d/dxP_l(x)] - 4xd/dx[d/dxP_l(x)] + [l(l+1)-2][d/dxP_l(x)] = 0. \tag{3}$$

Try the solution $d[P_l(x)]/dx = (1-x^2)^{-r}y$ in (3) and multiply through by $(1-x^2)^r$. This results in

$$(1-x^2)d^2y/dx^2 + 4x(r-1)dy/dx + \{(1-x^2)^{-1}[4x^2r(r-1)] + l(l+1) + 2(r-1)\}y = 0. \tag{4}$$

Let $r = 1$ in (4) giving

$$(1-x^2)d^2y/dx^2 + l(l+1) = 0. \tag{5}$$

Hence $y = (1-x^2)d[P_l(x)]/dx$ is a solution of (1).

A similar procedure shows that $y = (1-x^2)d[Q_l(x)]/dx$ is also a solution.

## APPENDIX IV

From (5a, 5b) of Part I and the relation $\partial V/\partial\eta = (\partial V/\partial r)(\partial r/\partial\eta)$,

$$[H_\xi^2 + H_\eta^2] = -1/\omega^2\mu^2r^2[1/h_2^2(\partial r/\partial\eta)^2 + 1/h_1^2(\partial r/\partial\xi)^2](\partial V/\partial r)^2. \tag{1}$$

Introducing the expressions for the metric coefficients given in Appendix I, (1) reduces to

$$[H_\xi^2 + H_\eta^2] = -1/\omega^2\mu^2r^2(\partial V/\partial r)^2. \tag{2}$$

Hence[6]

$$\partial V/\partial r \underset{\xi\to\infty}{\longrightarrow} j\omega\mu rH_a$$

resulting in

$$V_0 \underset{\xi\to\infty}{\longrightarrow} j\omega\mu r^2H_a/2 = j\omega\mu a^2(1-\eta^2)(1+\xi^2)H_a/2. \tag{3}$$

[6] Physical consideration of the final direction of induced current demands the positive root.

# Stress Analysis for Compressible Viscoelastic Materials

W. T. READ, JR.
*Bell Telephone Laboratories, Murray Hill, New Jersey*
(Received January 11, 1950)

Mathematical methods of stress analysis are presented for linear, compressible, viscoelastic, or anelastic, materials such as metals at high temperatures or high polymers with small strains. For such materials stress, strain and their time derivatives of all orders are related by linear equations with coefficients which are material constants. Fourier integral methods are used to show that static elasticity solutions can be used to determine the time dependent stresses in viscoelastic bodies with any form of boundary conditions.

If stress and double refraction and their time derivatives are also linearly related, the standard photoelastic techniques can be used to determine the directions and difference in magnitude of the time dependent principal stresses, even though the principal stress axes do not coincide with the polarizing axes and both vary with time. When viscoelastic models are used in photoelastic studies, the time variation of the stress distribution in the model represents a first approximation to the dependence of the stress in the elastic prototype on Poisson's ratio.

## INTRODUCTION

MANY efforts have been made to extend the standard methods of stress analysis to non-elastic materials. One approach has been to consider the general linear solid, defined as a material in which the stress-strain behavior can be represented by linear relations involving not only stress and strain but also their time derivatives of all orders. An elastic material represents the special case of a linear material in which the time derivatives can be neglected for the range of frequencies involved. Phenomena which are linear but time dependent have been called "viscoelastic" in the case of high polymers[1] and "anelastic" in the case of metals.[2] It has been shown that both the solutions of problems in elasticity and the standard photoelastic techniques can be applied to a linear incompressible solid when the forces and displacements given on the boundary vary uniformly with time and slowly enough that inertial effects can be neglected.[3,4] The present paper extends these results to the general, compressible, linear solid with any form of boundary conditions. The analysis makes use of the standard Fourier integral and operator methods. For simplicity the derivation considers only isotropic materials, but the results are readily generalized to the anisotropic case.

## 1. STRESS-STRAIN RELATIONS

In this section we show by use of Fourier integral methods that the time dependent stress-strain relations for the general linear solid can be transformed to static relations between the Fourier transforms of stress and strain, these relations having the same form as the elastic stress-strain relations except that the elastic constants are complex functions of frequency, readily determined from a simple tension test. We shall follow the conventional engineering notation, using $\sigma$'s and $\epsilon$'s for normal components of stress and strain respectively and $\tau$'s and $\gamma$'s for shearing components.

The most general linear isotropic stress-strain relations can be expressed in terms of three linear differential operators $H$, $K$ and $L$ by

$$H(\partial)/(\partial t)\sigma_x = K(\partial)/(\partial t)e + 2L(\partial)/(\partial t)\epsilon_x, \quad (1.1)$$

$$H(\partial)/(\partial t)\tau_{xy} = L(\partial)/(\partial t)\gamma_{xy} \quad (1.2)$$

where $e=\epsilon_x+\epsilon_y+\epsilon_z$ with four similar relations obtain by rotating subscripts. The operators have the form

$$H(\partial)/(\partial t) = H_0 + H_1(\partial/\partial t) + H_2(\partial^2)/(\partial t^2)\cdots H_n(\partial^n)/(\partial t^n)\cdots \quad (1.3)$$

the coefficients being constants of the material. By operating on (1.1) and (1.2) with $[1/H(\partial)/(\partial t)]$, the relations involve only two linear integro-differential operators and have the same form as in the elastic case, the two operators replacing the two independent elastic constants $\lambda$ and $G$.

The number of terms in the operators required to adequately represent the stress-strain relation depends on the material. In general an infinite number will be required for an exact representation. It is customary to represent the solid by a mechanical model consisting of springs and dashpots having constants which determine the constants in the stress-strain relations. However, when many derivatives are required in the stress-strain relations, it is not practical to determine the operators. In the general case a more practical approach is to determine two complex elastic constants $G(i\omega)$ and $\lambda(i\omega)$ which are functions of frequency $\omega$ and may be determined from a simple experiment and used to express the stress-strain relations in the following way: We represent the time dependence of $\tau_{xy}=\tau_{xy}(t)$ by a Fourier integral

$$\tau_{xy}(t) = \int_{-\infty}^{\infty} \bar{\tau}_{xy}(\omega) e^{i\omega t} d\omega, \quad (1.4)$$

[1] T. Alfrey, *Mechanical Behavior of High Polymers* (Interscience Publishers, Inc., New York, 1948).
[2] C. Zener, *Elasticity and Anelasticity of Metals* (University of Chicago Press, Chicago, 1948).
[3] T. Alfrey, "Non-Homogeneous Stress in Viscoelastic Media," Quart. J. App. Math. **II**, 113 (1944).
[4] R. D. Mindlin, "A mathematical theory of photo-viscoelasticity," J. App. Phys. **20**, 206 (1949).

where

$$\bar{\tau}_{xy}(\omega)=\frac{1}{2\pi}\int_{-\infty}^{\infty}\tau_{xy}(t)e^{-i\omega t}dt \tag{1.5}$$

is the Fourier transform of $\tau_{xy}(t)$. Expressing $\gamma_{xy}$ also as a Fourier integral, substituting into (1.2), and considering that the relation must hold for all values of time, we have

$$\bar{\tau}_{xy}(\omega)=G(i\omega)\bar{\gamma}_{xy}(\omega), \tag{1.6}$$

where $\bar{\gamma}_{xy}(\omega)$ is the Fourier transform of $\gamma_{xy}(t)$, and the complex modulus

$$G(i\omega)=\frac{L(\partial)/(\partial t)e^{i\omega t}}{H(\partial)/(\partial t)e^{i\omega t}}=\frac{L(i\omega)}{H(i\omega)}. \tag{1.7}$$

Defining another complex modulus,

$$\lambda(i\omega)=[K(i\omega)]/[H(i\omega)], \tag{1.8}$$

the relation (1.1) is transformed to

$$\bar{\sigma}_x(\omega)=\lambda(i\omega)\bar{e}(\omega)+2G(i\omega)\bar{e}_x(\omega), \tag{1.9}$$

where as before the bars denote Fourier transforms. Thus the time dependent stress-strain relations (1.1) and (1.2) are replaced by static relations between the Fourier transforms of stress and strain. The stress-strain relations can also be stated in terms of the complex Young's modulus and Poisson's ratio $E(i\omega)$ and $\nu(i\omega)$, which are related to $\lambda(i\omega)$ and $G(i\omega)$ by the same relations as in the elastic case. For an experimental determination of the two complex elastic constants, it is convenient to perform a simple tension test in which the tension $\sigma_x(t)$ varies with time in any convenient manner. By measuring the strain $e_x(t)$ along, and $e_y(t)$ at right angles to the tension, and taking the Fourier transforms of the three known functions of time, we can calculate

$$E(i\omega)=[\bar{\sigma}_x(\omega)]/[\bar{e}_x(\omega)]$$

and

$$\nu(i\omega)=-[\bar{e}_y(\omega)]/[\bar{e}_x(\omega)]. \tag{1.10}$$

For an anisotropic material the same results hold except that additional complex elastic constants are required.

## 2. DIFFERENTIAL EQUATIONS AND BOUNDARY CONDITIONS

The differential equations to be satisfied are the compatibility equations for the strains and the equilibrium equations, which involve the stresses, body forces and inertial terms. Whether we formulate the problem in terms of stress or displacement, we obtain equations which are the same as in the elastic case except that the elastic constants $\lambda$ and $G$ are replaced by the corresponding operators

$$\frac{K(\partial)/(\partial t)}{H(\partial)/(\partial t)} \quad \text{and} \quad \frac{L(\partial)/(\partial t)}{H(\partial)/(\partial t)}.$$

These equations can be treated in the same way as the stress-strain relations, all quantities including the body forces being expressed as Fourier integrals. This gives equations for the Fourier transforms which are the same as the static elasticity equations except that the elastic constants are replaced by the complex functions of frequency $\lambda(i\omega)$ and $G(i\omega)$. The boundary conditions on the Fourier transforms are the Fourier transforms of the actual time dependent boundary conditions. Thus every stress analysis problem involving the general linear solid can be reduced to a static elasticity problem and the extensive known solutions of elasticity used. When the Fourier transforms have been obtained, by substituting complex elastic constants and boundary values into the elasticity solution, the actual time dependent solution is obtained from the Fourier transforms, using relations of the form (1.4).

## 3. SPECIAL CASES AND APPROXIMATIONS

In this section we assume that inertial effects and body forces can be neglected, and that the boundary conditions vary uniformly with time. Let the time dependence of the applied forces and displacements be given by an arbitrary function $F(t)$. If the static elasticity solution for $F(t)=\text{constant}=\text{unity}$ is $S_e[x, y, z, \lambda, G]$, then the solution for the general linear solid is

$$S(x, y, z, t)$$

$$=\int_{-\infty}^{\infty}\bar{F}(\omega)S_e[x, y, z, \lambda(i\omega), G(i\omega)]e^{i\omega t}d\omega, \tag{3.1}$$

where

$$\bar{F}(\omega)=\int_{-\infty}^{\infty}F(t)e^{-i\omega t}dt \tag{3.2}$$

is the Fourier transform of $F(t)$, and $S$ may be any component of stress, strain or displacement. When $S_e[x, y, z, \lambda, G]$ is a rational algebraic function of $\lambda$ and $G$, Eq. (3.1) can be transformed to the operator equation

$$S(x, y, z, t)$$

$$=S_e\left[x, y, z, \frac{L(\partial)/(\partial t)}{H(\partial)/(\partial t)}, \frac{K(\partial)/(\partial t)}{H(\partial)/(\partial t)}\right]F(t). \tag{3.3}$$

Thus in problems of this type, which include the greater part of practical cases, the procedure is to replace the elastic constants in the elasticity solution for $F(t)=1$ by the corresponding operators. The elasticity solution in operator form acting on the actual $F(t)$ then gives the time dependent solution for the general linear solid. Since the operators are rational algebraic functions of $\partial/\partial t$, the solution can be expressed as a sum of partial fractions of the form

$$\frac{1}{\beta+(\partial/\partial t)}F(t)=e^{-\beta t}\int_{-\infty}^{t}e^{\beta t'}F(t')dt'. \tag{3.4}$$

In cases where the operators are known this is frequently the most practical method of solution.

When the elasticity solution involves only the ratio of elastic moduli, conveniently expressed by the dimensionless quantity $\nu$, special methods and simple approximate procedures can be used. For example, if loads are suddenly applied and held constant, the initial state of stress will be the same as that in an elastic body with Poisson's ratio equal to the Poisson's ratio of the instantaneous elastic response. Then, if the loads are held constant until a steady state is reached, the state of stress approaches that in an elastic body having the Poisson's ratio characteristic of the steady state. This suggests that a general linear solid is equivalent to an elastic solid with a time variable Poisson's ratio. To show that this is true to a first approximation, we expand the static elasticity solution $S_e[x, y, z, \nu]$, for $F(t)=1$, in a Taylor's series about some average value of $\nu$. Then, using a relation of the form (3.1) and neglecting second and higher order terms in the Taylor's series, we find

$$S[x, y, z, t]=S_e[x, y, z, \nu(t)]F(t), \tag{3.5}$$

where $\nu(t)$ is determined in terms of $F(t)$ by a simple tension test in which the strain $e_x$ in the direction of tension is $F(t)$, and $\nu(t)=-e_y(t)/F(t)$, $e_y(t)$ being measured at right angles to the tension. Equation (3.5) gives a first approximation to the time variation of the solution, and is exact in the special case where $\nu(t)$ = constant. The incompressible case is a special case of this special case, and corresponds to $\nu(t)=\frac{1}{2}$.

Another simple case occurs in problems of plane strain where the boundary conditions are on stress and there is no resultant force on an internal boundary; then the elasticity solution for the stress distribution is independent of the elastic constants, and the stress distribution in the general case is $F(t)$ times the static elasticity solution.

## 4. OPTICAL METHODS

In this section we consider transparent materials in which the stress-optical relations are of the same form as the stress-strain relations, and can be expressed by linear differential equations with constant coefficients. Although operator methods are used in the derivation, the parallel Fourier integral treatment is evident. It is shown that the standard techniques used in photoelasticity can be employed to determine the directions of the secondary principal axes of stress in the plane of the wave front and the secondary principal stress difference. No restrictions on the boundary conditions are involved.

The stress optical effect involves the relation between the stress and velocity tensors, the latter being simply related to the dielectric constant tensor.* We let $V_{xx}$, $V_{xy}$, $\cdots V_{zz}$ be the components of the velocity tensor. Since this tensor is symmetric, it can be represented by an ellipsoid, called the velocity ellipsoid, which provides a graphic means of describing the polarizing axes and wave velocities for plane polarized light. If the $xy$ plane is the plane of the wave front, then the polarizing axes are the axes of the ellipse formed by the trace of the ellipsoid in the $xy$ plane and the wave velocities, $V_1$ and $V_2$, are inversely proportional to the squares of the major and minor axes of the ellipse. The standard photoelastic techniques give the difference $V_1-V_2$ and the angle $\varphi$ between the polarizing axes and the fixed $x$ and $y$ axes. The difference $V_{xx}-V_{yy}$ is given by the tensor relation

$$V_{xx}-V_{yy}=(V_1-V_2)\cos 2\varphi, \tag{4.1}$$

where all quantities vary with both time and position in the specimen.

For an isotropic viscoelastic material the most general linear differential equations for the time dependence of the stress-optical effect give

$$X(\sigma_x-\sigma_y)=Y(V_{xx}-V_{yy}), \tag{4.2}$$

where $X$ and $Y$ are linear differential operators which may have any number of terms. Combining (4.1) and (4.2) gives

$$\sigma_x-\sigma_y=\frac{Y}{X}(V_1-V_2)\cos 2\varphi, \tag{4.3}$$

from which the stress difference $\sigma_x-\sigma_y$ can be calculated as a function of time for all points, where $V_1-V_2$ and $\varphi$ have been measured.

The choice of the fixed axes $x$ and $y$ is arbitrary. The stress difference $\sigma_x'-\sigma_y'$ referred to axes $x'$ and $y'$ at an angle $\theta$ to the $x$ and $y$ axes is given by (4.3) with $\varphi$ replaced by $\varphi-\theta$. Maximizing this with respect to $\theta$ gives the secondary principal stress difference in the plane of the wave front, the value of $\theta$ giving the direction of the secondary principal axes. Thus, as in photoelasticity, the optical measurements give the directions and difference in magnitude of the secondary principal stresses. In the general viscoelastic case the principal axes of stress are not parallel to the polarizing axes.

In the special cases of Section 3 where the state of stress is known to be the same as the stress in an elastic body, (4.3) takes the simple form

$$\sigma_1-\sigma_2=K(t)(V_1-V_2), \tag{4.4}$$

where

$$K(t)=\frac{1}{F(t)}\frac{Y}{X}F(t)$$

and $\sigma_1$ and $\sigma_2$ are the secondary principal stresses and

* The principal axes of the velocity tensor coincide with the principal axes of the dielectric constant tensor and the principal velocities are inversely proportional to the square roots of the principal dielectric constants: G. Joos, *Theoretical Physics* (G. E. Stechert and Company, New York, 1934), p. 349.

act in the directions of the polarizing axes. A simple tension experiment gives $K(t)$.

When viscoelastic materials are used for models in optical stress studies, and the Poisson's ratio has been measured for the instantaneous elastic deformation under constant load and also for the final steady state deformation, then the photoelastic analysis gives the stress distribution in the elastic prototype for two values of Poisson's ratio. As was discussed in the last section, the intermediate stress distributions are the first approximations to the stresses in an elastic prototype with a time variable Poisson's ratio. The viscoelastic model therefore gives information about the dependence of the stress distribution on Poisson's ratio.

# Electrolytic-Tank Measurements for Microwave Metallic Delay-Lens Media*

SEYMOUR B. COHN
*Sperry Gyroscope Company, Great Neck, New York*
(Received December 15, 1949)

In this paper it is shown how the low frequency index of refraction of a metallic delay-lens medium may be calculated from electrolytic-tank measurements on individual metallic elements of the medium. The proximity between adjacent elements is taken exactly into account for low frequencies. The test apparatus is described, and measured results are presented for three kinds of delay-lens structures.

## I. INTRODUCTION

IT has been shown by W. E. Kock that an array of discrete metallic obstacles in free space (Fig. 1) has an index of refraction greater than unity, and hence is a suitable lens medium for microwaves.[1] In his article Kock gives approximate index-of-refraction formulas, surface-shape relations, and practical methods of construction.

Kock's analysis for thin-strip and thin-circular-disk obstacles assumes the dimensions of the obstacles to be small compared to their spacings. Because of this assumption, substantial errors exist in practical delay-lens media for which rather close spacings are required in order to obtain a reasonably high index of refraction. In the case of the metallic-strip structure, the writer has presented accurate theoretical relations and graphs for the index of refraction and image admittance with proximity between the strips and the effect of frequency taken into account.[2] For other obstacle shapes an exact theoretical solution appears to be exceedingly difficult, and therefore experimental methods of acquiring index-of-refraction data are necessary. One possible method calls for direct index-of-refraction measurements in the microwave range on delay-medium samples. Another method, which is described in this paper, utilizes indirect measurement of the capacitance of individual obstacles with the aid of an electrolytic-tank analogy. Since promixity is taken fully into account, the index of refraction computed with the electrolytic-tank analogy is exact if the wave-length is much greater than the size and spacing of the obstacles.

The writer has shown how the problem of a metal-strip delay-lens medium may be reduced to that of a parallel-plane transmission line containing uniformly spaced obstacles, and has given formulas by which the parameters of the medium may be calculated from the equivalent circuit of the transmission line.[2] The same

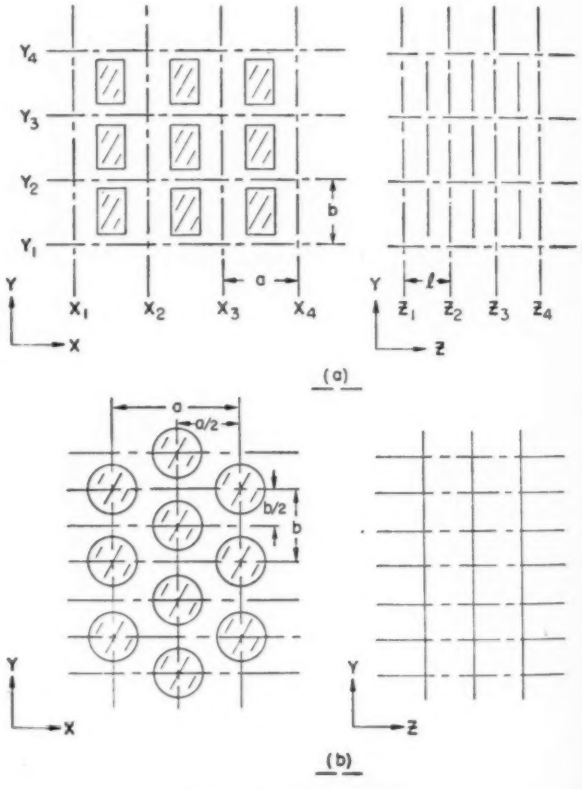


FIG. 1. Delay-lens media.

* The experimental work described in this paper has been performed as a part of a program of research under Contract No. W36-0.39-sc-38250 for the Evans Signal Laboratory, U. S. Army Signal Corps.

[1] W. E. Kock, "Metallic delay lenses," Bell Sys. Tech. J. **27**, 58 (1948).

[2] S. B. Cohn, "Analysis of the metallic-strip delay structure for microwave lenses," J. App. Phys. **20**, 257 (1949).

reduction may be made with many other kinds of delay-lens media (for example, those of Fig. 1) and the same formulas apply. The purpose of the electrolytic-tank measurements is to provide quantitative values of the shunt capacitance introduced by each obstacle in the equivalent circuit.

## II. THE EQUIVALENT CIRCUIT

The procedure by which an equivalent transmission line may be obtained for the two configurations of Fig. 1 will now be explained. Assume a plane wave in

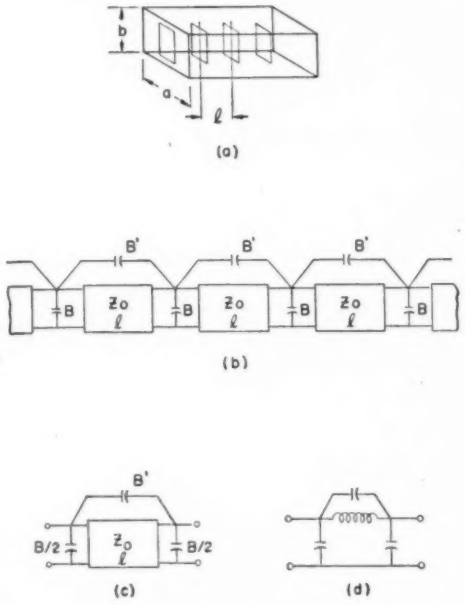


FIG. 2. Equivalent circuit of obstacles in a parallel-plane line.

the medium traveling in the $z$ direction with the average electrical polarization in the $y$ direction. Then with no disturbance to the electromagnetic field, thin "electric" walls may be inserted horizontally in planes $y_1$, $y_2$, $y_3\cdots$ and thin "magnetic" walls vertically in planes $x_1$, $x_2$, $x_3\cdots$ (an electric wall is a conducting sheet, while a magnetic wall is a hypothetical surface on which only tangential-electric and normal-magnetic field components can exist. Such a surface does not occur in nature, but is a useful tool for theoretical analysis). In this way a single channel through the medium such as that in Fig. 2a has been isolated. Since the top and bottom surfaces are conductors while the sides are nonconductors, the channel is in reality a parallel-plane transmission line shunted at uniform spacings by capacitive metallic obstacles. The wave velocity and the normalized image impedance of the transmission line is the same as that of the corresponding lens medium.

For the hexagonal distribution shown in Fig. 1b, the same procedure applies for obtaining the equivalent transmission line. Note that electric and magnetic planes may be passed through the center of each circular obstacle without altering the field, and hence a parallel-plane line having the cross-sectional dimensions $a/2$ and $b/2$ may be used.

The equivalent circuit for the basic transmission line of the metal-strip delay medium has been found in reference 2 to be that of Fig. 2b. The shunt capacitive susceptances represent the shunting effect of the obstacles in the transmission line, while the bridging capacitive susceptances $B'$ represent a proximity effect between adjacent obstacles in the line. Proximity effects between nonadjacent obstacles are neglected, since they are not believed to be of appreciable magnitude in delay-media computations. A second effect of proximity is a reduction in the magnitude of $B$. Experience with the metal-strip medium has shown that $B'$ is negligible when the obstacle spacing $l$ is large enough to make $B$ constant. This condition occurs for $l/b$ greater than approximately 0.75.

The boxes in Fig. 2b represent sections of transmission line of length $l$ and characteristic impedance $Z_0$. A single section of the line is shown in Fig. 2c. When the Pi equivalent circuit of the length $l$ of uniform line is substituted for the box and combined with the obstacle susceptances, one obtains the circuit shown in Fig. 2d, which may be recognized as an $m$-derived low pass filter section. Consequently, the delay lens may be expected to transmit waves freely up to a definite cut-off frequency and to have an opaque band above that. For lens applications only the band below this cut-off frequency is useful, and all discussion in this paper will be limited to this range. Even within this range, however, the capacitances and inductances of the equivalent circuit are not constants, but vary somewhat with frequency.

Note in Fig. 2d that the bridging susceptance $B'$ is shunted by an inductive element. At low frequencies $B'$ is almost zero while the inductive susceptance is very large, and therefore it may be seen that $B'$ can have no effect on the low frequency behavior of the delay medium. Consequently, the electrolytic-tank method can give precise values of the index of refraction at low frequencies even though it is incapable of measuring $B'$.

The formulas for the index of refraction and image

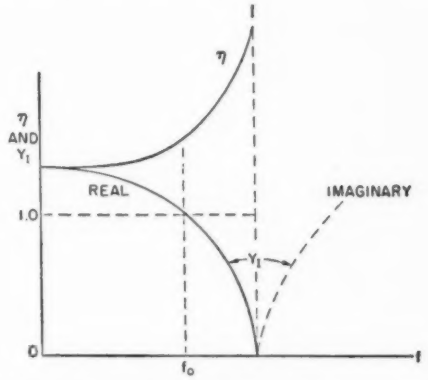


FIG. 3. Index of refraction and image admittance of a delay lens.

| SPACE-TANK ANALOGUE (MKS UNITS) | |
|---|---|
| SPACE | TANK |
| E | E |
| V | V |
| D | i |
| $Q=\int D\cdot ds$ | $I=\int i\cdot ds$ |
| $C=Q/V$ | $G=I/V$ |

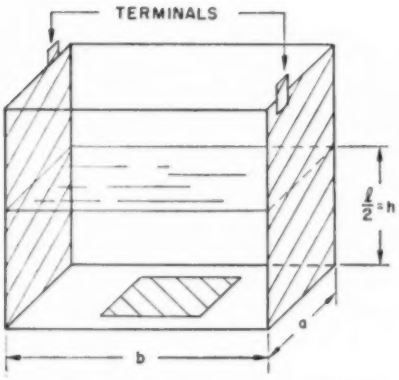


FIG. 4. Electrolytic analog for one obstacle.

admittance for the case of $B'$ negligible are:[2]

$$\eta=\frac{\lambda}{2\pi l}\cos^{-1}\left(\cos\frac{2\pi l}{\lambda}-\frac{B}{2Y_0}\sin\frac{2\pi l}{\lambda}\right), \tag{1}$$

$$y_I=\frac{Y_I}{Y_0}=\left[1+(B/Y_0)\cot\frac{2\pi l}{\lambda}-(B/2Y_0)^2\right]^{\frac{1}{2}}, \tag{2}$$

where $\eta$ is the index of refraction, $\lambda$ the wave-length in free space, $Y_0$ the characteristic admittance of the parallel-plane transmission line, $Y_I$ the image admittance of the line loaded by the obstacles, $y_I$ the normalized image admittance, and $l$ the spacing shown in Fig. 1. Equations (1) and (2) are correct only for a plane wave traveling normal to the obstacle planes. The surfaces of the lens should therefore be shaped in a given application so as to obtain this condition inside the lens. For this purpose, the index of refraction given by Eq. (1) may be correctly used with Snell's law of refraction. This was done by Kock in deriving his lens-surface formula for a "pencil-beam" lens.[1]

Figure 3 shows a sketch of $\eta$ and $y_I$. Note that at low frequencies these functions are essentially constant and equal to each other. At higher frequencies $\eta$ bends upward and $y_I$ downward. When $B'$ is neglected they bend less sharply than when it is taken into account. The limiting value of $\eta$ and $y_I$ at zero frequency is given by

$$\eta_0=y_{I0}=(1+B\lambda/2\pi lY_0)^{\frac{1}{2}}. \tag{3}$$

Since the construction and test of microwave delay-lens models are difficult and expensive, a static method of obtaining the lens parameters is desirable, even though it is accurate only at a low enough frequency or for a large enough $l/b$ ratio so that $B'$ is negligible. Direct measurements on a single obstacle are impossible in free space, since the necessary magnetic-wall boundary conditions are physically nonrealizable. Such measurements are feasible in an electrolytic tank, however, as will be apparent from the following discussion.

## III. PRINCIPLE OF THE ELECTROLYTIC-TANK METHOD

If a static potential is impressed between two conductors, the electric field lines will follow the same paths whether the conductors are immersed in free space or in a conducting solution. In Fig. 4 the analogy between various free-space quantities and electrolytic-tank quantities is brought out. The electric field and the potential in space are analogous to the same quantities in the tank, the displacement flux $D=\epsilon E$ in space is analogous to the current density $i=\sigma E$ in the tank, the charge on a conducting surface in space is analogous to the total current flowing through the surface in the tank, and the capacitance between two surfaces in space is analogous to the conductance between surfaces in the tank. In addition, an electric wall in space is the analog of a conducting wall in the tank, while a magnetic wall in space is the analog of a non-conducting wall in the tank. The latter point is of extreme importance, since it shows that the boundary conditions for the equivalent transmission line may be correctly simulated in the tank, thus permitting a precise low frequency determination of the delay-medium parameters with proximity taken completely into account.

It will now be shown that it is only necessary to make measurements on a length $l/2$ of the transmission line in order to determine $B$ correctly. Consider a static potential impressed between the top and bottom surfaces of the line of Fig. 2a. Then without disturbing

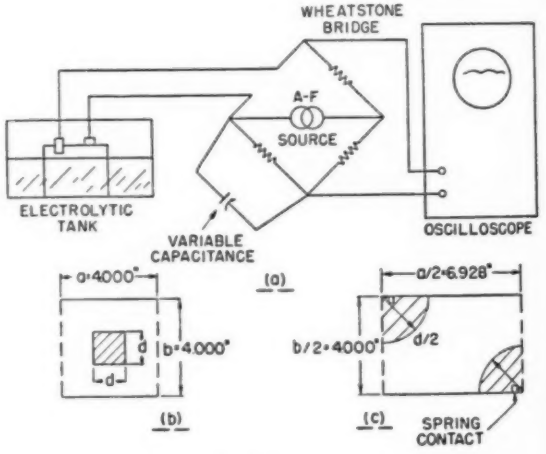


FIG. 5. Test equipment.

the electric field, magnetic walls may be inserted across the line in the obstacle planes and also halfway between the obstacles. The cell in Fig. 4 shows the electrolytic analog of the space between two magnetic walls. The obstacle and the two vertical walls of length $a$ are conductors. The two vertical walls of length $b$, the surface of the solution, and the bottom of the cell (except for the obstacle) are all non-conductors, simulating the magnetic walls of their free-space counterparts. In order to determine the capacitance of the obstacle, the conductance between the metallic sides

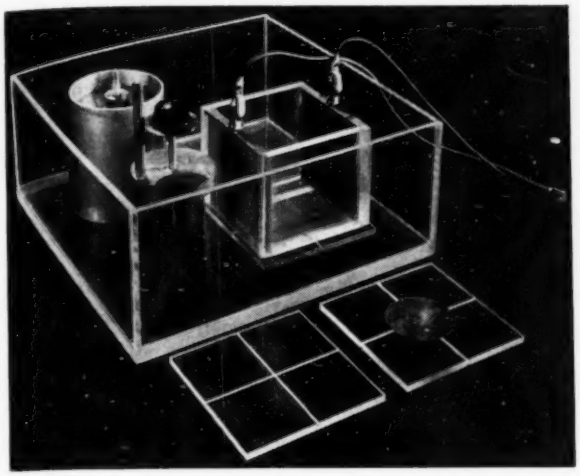

FIG. 6. Photograph of electrolytic-tank apparatus.

of the cell is measured with and without the obstacle present. The apparatus and techniques of the test will now be described.

## IV. THE APPARATUS

Figure 5 shows a block diagram of the test equipment. The cell conductance is measured by means of a Wheatstone bridge. The arms of the bridge consist of precision decade resistance boxes having a range of 1 to 111,110 ohms in one-ohm steps. The signal source operates at 1000 cycles and has a balanced ungrounded output. The detector is a high gain oscilloscope. the variable capacitance across one of the bridge arms serves to balance out stray circuit capacitances and a small series reactance which occurs at the contact between electrolyte and metal. The sensitivity of the circuit is such that a change in a bridge arm of one part in five thousand is easily discernible.

Rhodium plating is used on all conducting surfaces in contact with the liquid, since rhodium is highly inactive chemically and electrolytically. The electrolyte is a dilute solution of potassium chloride in distilled water. The concentration was chosen so that measured resistances would lie in the range of about 1500 to 9000 ohms. These resistances are too low for stray shunt capacitances to cause significant error and too high for circuit resistance and inductance to affect the accuracy.

A photograph of the tank apparatus appears in Fig. 6. The tank is made of Lucite and has internal dimensions of 12×12×5 in. The cell, which has dimensions of 4×4×3 in., has four vertical Lucite walls and no top or bottom. One opposite pair of walls is rhodium plated on the inside, and terminals connect to each of these surfaces. The obstacles are cut from thin copper sheets 0.0015 in. thick and are rhodium plated and cemented onto Lucite plates. Grooves are cut in the Lucite on the opposite side so that the plates will flatten readily with pressure when in use. The coaxial cylinders shown in the photograph are used to calibrate the conductivity of the solution. Although it is theoretically possible to obtain this calibration with the cell with the obstacle removed, it has been found that small but not negligible leakage currents escape from the interior of the cell through the cracks between the cell and the bottom plate, thus adding an unknown but constant conductance to the readings with and without the obstacle in place. The coaxial cylinders are by nature self-shielding, and leakage currents cannot exist. Hence, they may be expected to provide an accurate conductivity calibration. A depth gauge is also visible in Fig. 6. By means of this, the height of the electrolyte may be measured to an accuracy of about 0.002 in.

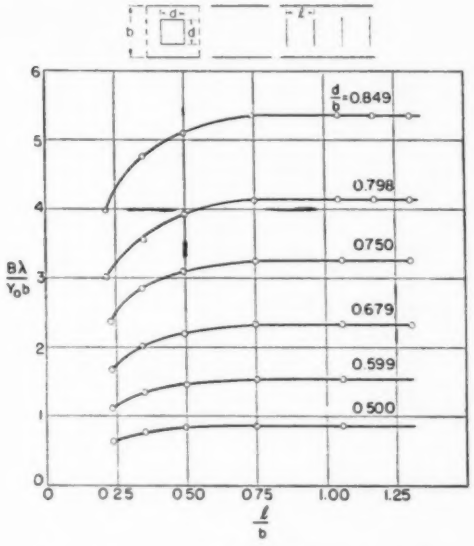


FIG. 7. Susceptance of thin square obstacles.

In performing a test, resistance measurements are made on the coaxial cylinders and on the cell with and without an obstacle in position. For the measurements without the obstacle, a blank Lucite plate having the same thickness as the obstacle plate is used in order to maintain a constant solution height. The susceptance of the obstacle may then be calculated from the following formula which is derived in the Appendix.

$$\frac{B\lambda}{Y_0 b}=\frac{4\pi h}{a}\left(\frac{376.6}{Z_{0\,\mathrm{coax}}}\right)\frac{R_3(R_2-R_1)}{R_1R_2}, \tag{4}$$

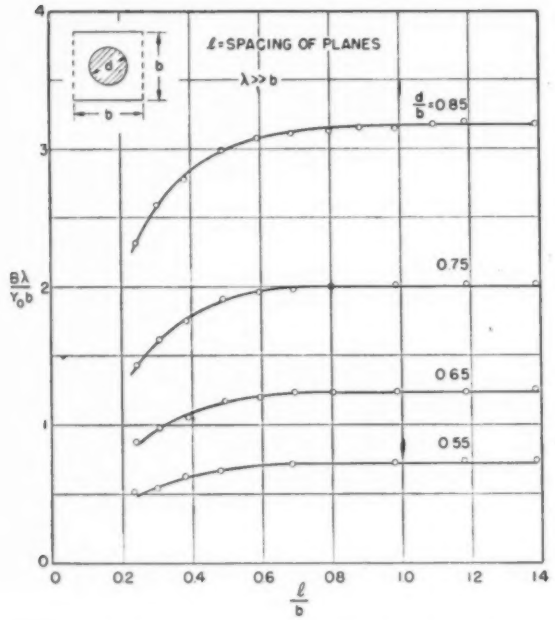


FIG. 8. Susceptance of thin circular obstacles, square distribution.

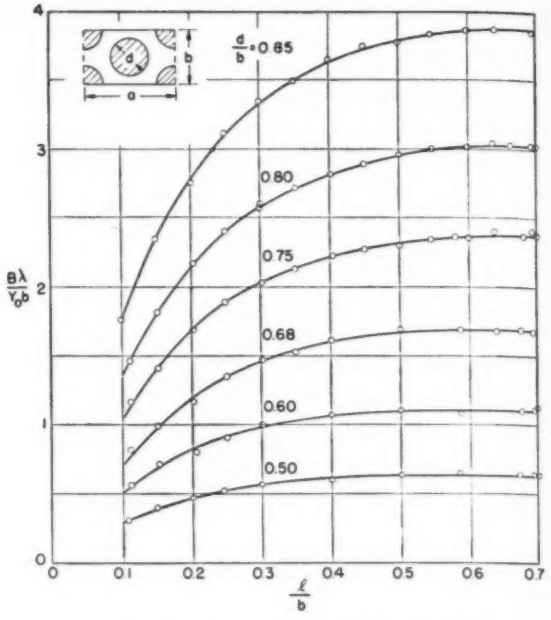


FIG. 9. Susceptance of thin circular obstacles, hexagonal distribution.

where $B$=shunt susceptance of obstacle ($=\omega C$); $Y_0 = 1/Z_0$=characteristic admittance of parallel-plane line ($=a/376.6b$); $\lambda$=wave-length; $b$=distance between metal plates of line; $a$=width of metal plates; $h$=height of water ($=l/2$); $Z_{0\,\text{coax}}$=characteristic impedance of coaxial cylinders ($=60\ln r_2/r_1$); $R_3$=resistance of coaxial cylinders; $R_2$=resistance of cell without obstacle; $R_1$=resistance of cell with obstacle.

Three kinds of configurations were measured, square obstacles having square distribution (Fig. 1a), circular obstacles having square distribution, and circular obstacles having hexagonal distribution (Fig. 1b). A top view of the cell for the first two is shown in Fig. 5b (with a square obstacle in place). A top view of the cell for the hexagonal distribution is shown in Fig. 5c. In this case it is necessary to have a low resistance contact between each obstacle quadrant and the adjacent conducting wall. This is obtained by means of a small leaf spring soldered to the wall. Since the spring is small and in a region of negligible current flow, its presence causes no appreciable error.

## V. EXPERIMENTAL DATA

The measured shunt-susceptance data for the three configurations are shown in Figs. 7–9. Also, a table of values taken from accurately drawn curves plotted from the data is given in the Appendix. Notice that for $l/b$ greater than approximately 0.75 the obstacle susceptances are independent of $l$. In practical delay media, however, it is generally necessary to have $l/b$ less than 0.75 in order to have a large enough index of refraction, and hence the non-constant portions of the graphs are the most useful. The data of Figs. 7, 8, and 9 are valid only if $\lambda \gg b$, since for shorter wave-lengths the obstacle susceptance does not have the frequency dependence of a constant capacitance. Some experimental r-f data now available indicate that the frequency error is very small if $b/\lambda \leq 0.25$.

The following theoretical formula gives the low frequency susceptance in a parallel-plane line of one or more thin circular disks having a diameter much smaller than the spacings to surrounding walls and having $l/b > 0.75$.

$$B/Y_0 = 4\pi n d^3/3\lambda ab. \tag{5}$$

This formula may be derived very easily from a relation given by W. E. Kock for the average dielectric constant of a medium containing a uniform distribution of circular disks (Eq. (22), reference 1). The symbol $n$ in Eq. (5) is the total number of obstacles in a cross section of the equivalent transmission line of sides $a$ and $b$. It is equal to one for the square distribution and two for the hexagonal distribution. Equation (5) is plotted in Fig. 10 along with the experimental data for circular disks ($l/b > 0.75$). The agreement between experiment and simple theory is very good for $d/b$ less than 0.5. This result checks the experimental method and also shows that Kock's low frequency formula for index of refraction is accurate provided that $d/b$ is less than 0.5 and $l/b$ greater than 0.75.

Another check between experiment and theory was obtained with a metal-strip obstacle which extended the full width of the cell and which had a ratio of 0.6 between the width of the strip and the spacing of the conducting plates. In this case the measured data are within one percent of the exact formula.

In Figs. 11–13 are plotted low frequency index-of-refraction curves calculated by Eq. (3) from the ex-

perimental curves of Figs. 7, 8, and 9. Notice that for given obstacle spacings the square obstacles have the highest index of refraction, the circular obstacles with hexagonal distribution the next highest, and the circular obstacles with square distribution the least. Consequently, the first two structures are likely to be more useful than the third.

The curves of Figs. 11–13 are accurate for $b/\lambda$ up to approximately 0.1. For $b/\lambda$ up to approximately 0.2, Eq. (1) may be used. For larger $b/\lambda$ it is necessary to take account of $B'$, which cannot be determined directly by any static method. The writer believes that a judicious estimate of $B'$ may be made based on the measurements of $B$, but a discussion of this possibility will be postponed, since experimental verification is thus far lacking.

Although the measurements on the hexagonal distribution were made with the incident electric field parallel to the $y$ axis (Fig. 1b), the index of refraction of a normally incident wave is the same for any polarization. This statement is obvious from the fact that three polarizations of a normal wave exist for which the field distributions are identical (except for 120 degree rotations), and that a normal wave of any other polarization may be represented by the sum of components polarized on two of these three axes. In a similar manner, it may be seen that the index of refraction of the square distributions is independent of the polarization of a normally incident wave. In addition, the normalized susceptance $B'/Y_0'$ of the hexagonal distribution for the electric field parallel to the $x$ axis is identical to $B/Y_0$ computed from Fig. 9 for the $y$ axis polarization, and the normal susceptance of the square distributions for polarizations of $\pm 45$ degrees from the $x$ or $y$ axis is identical to $B/Y_0$ computed from Figs. 7 and 8.

The writer wishes to thank his colleagues, H. L. Busching, R. Reisley, and R. C. MacVeety, who assisted in perfecting the measurement apparatus and techniques and in taking the data.

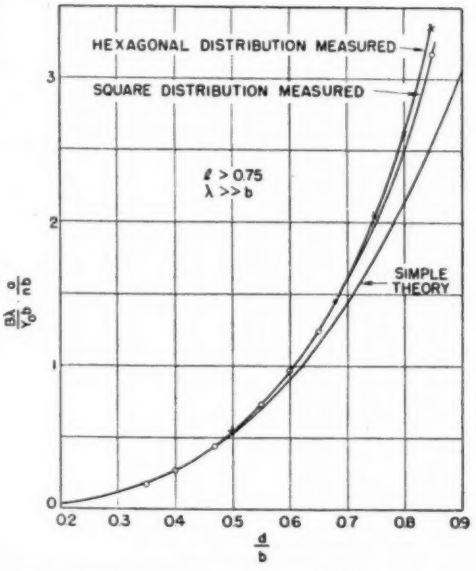


FIG. 10. Susceptance of thin circular obstacles.

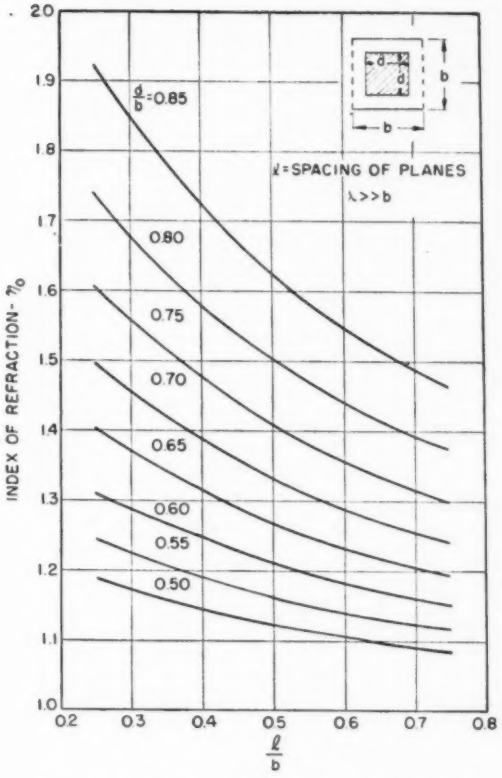


FIG. 11. Index of refraction of square obstacles.

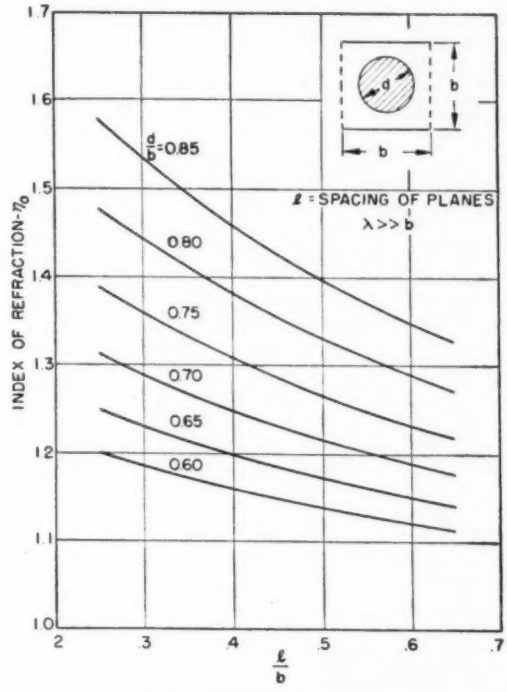


FIG. 12. Index of refraction of circular obstacles, square distribution.

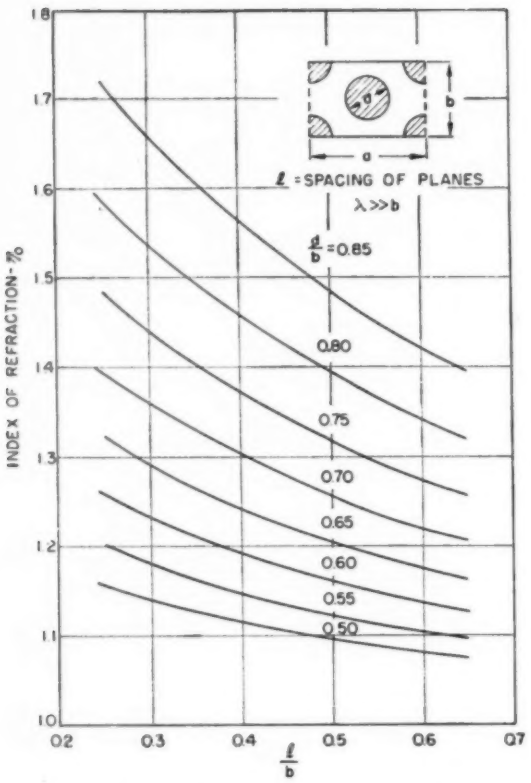


FIG. 13. Index of refraction of circular obstacles, hexagonal distribution.

## APPENDIX I

### 1. Derivation of Eq. (4)

Let the capacitance introduced by the obstacle be $C_{obst}$ and that of the coaxial line $C_{coax}$. The corresponding conductances in the tank are $G_{obst}$ and $G_{coax}$. Because of the analogy between capacitance and conductance

$$C_{obst}/C_{coax}=G_{obst}/G_{coax}.$$

The capacitance of the coaxial line is

$$C_{coax}=h/cZ_{0\,coax}\text{ farads},$$

where $c$ is the velocity of propagation in free space. The conductances are obtained from the measured resistances by

$$G_{coax}=1/R_3$$
$$G_{obst}=1/R_1-1/R_2=(R_2-R_1)/(R_1R_2).$$

In the described test method, the obstacle is cemented on a flat plate, and hence only half of the total obstacle capacitance $C$ is measured. Therefore

$$C=2\left[\frac{h}{cZ_{0\,coax}}\right]\frac{R_3(R_2-R_1)}{R_1R_2}.$$

When this is combined with $B=\omega C=2\pi cC/\lambda$ and $Y_0=a/376.6b$ one obtains Eq. (4).

### 2. Values of $B\lambda/Y_0b$

(a) Square obstacles.

| $d/b$ | $l/b=0.25$ | $l/b=0.35$ | $l/b=0.50$ | $l/b=0.65$ | $l/b\geq 0.75$ |
|---|---|---|---|---|---|
| 0.50 | 0.648 | 0.768 | 0.830 | 0.855 | 0.859 |
| 0.60 | 1.16 | 1.35 | 1.475 | 1.54 | 1.56 |
| 0.70 | 1.95 | 2.25 | 2.45 | 2.53 | 2.57 |
| 0.75 | 2.48 | 2.87 | 3.11 | 3.21 | 3.25 |
| 0.80 | 3.18 | 3.62 | 3.97 | 4.13 | 4.18 |
| 0.85 | 4.25 | 4.78 | 5.15 | 5.32 | 5.37 |

(b) Circular obstacles, square distribution.

| $d/b$ | $l/b=0.25$ | $l/b=0.35$ | $l/b=0.5$ | $l/b=0.65$ | $l/b\geq 0.8$ |
|---|---|---|---|---|---|
| 0.60 | 0.68 | 0.81 | 0.93 | 0.97 | 0.98 |
| 0.70 | 1.13 | 1.34 | 1.51 | 1.58 | 1.60 |
| 0.75 | 1.45 | 1.71 | 1.91 | 1.98 | 2.01 |
| 0.80 | 1.85 | 2.17 | 2.40 | 2.50 | 2.54 |
| 0.85 | 2.35 | 2.72 | 3.00 | 3.11 | 3.17 |

(c) Circular obstacles, hexagonal distribution.

| $d/b$ | $l/b=0.25$ | $l/b=0.35$ | $l/b=0.5$ | $l/b\geq 0.65$ |
|---|---|---|---|---|
| 0.50 | 0.525 | 0.595 | 0.630 | 0.635 |
| 0.60 | 0.915 | 1.025 | 1.095 | 1.100 |
| 0.70 | 1.48 | 1.69 | 1.82 | 1.86 |
| 0.75 | 1.89 | 2.13 | 2.31 | 2.38 |
| 0.80 | 2.39 | 2.71 | 2.96 | 3.03 |
| 0.85 | 3.09 | 3.50 | 3.78 | 3.87 |

# The Role of Cathode Temperature in the Glow Discharge

HAROLD JACOBS AND JACK MARTIN
*Signal Corps Engineering Laboratories, Fort Monmouth, New Jersey*
(Received March 24, 1950)

Experiments were conducted to study the role of the temperature of oxide-coated cathodes in the glow discharge of argon, neon, and mixtures of neon and argon, and mercury vapor and argon.

It was found that for tubes without mercury present, in the region of cathode temperature between 300°K and 750°K: (1) The sparking potential falls with increasing cathode temperature. (2) The regulation voltage rises with increasing cathode temperature. For argon and mercury vapor, the regulation voltage falls with increasing cathode temperature. The action here is attributed to metastable states of inert gas. (3) The current density in the glow discharge decreases with increasing cathode temperature. This, too, is attributed to the action of metastable states. (4) The minimum sustaining current in a glow discharge is found to decrease with increasing cathode temperature and rise with increasing pressure. (5) The current density in the glow discharge varies roughly linearly with pressure, or at a slightly higher rate, in contrast with the space-charge derivations which claim a variation with pressure squared. (6) The regulation voltage tends to rise very slightly at lower pressures.

## I. INTRODUCTION

COLD cathode behavior in the glow discharge region has received more interest in recent years due to its applications to electronic devices such as thyratrons, voltage regulators, lighting tubes, and switching devices. In the utilization of a glow tube in an electronic circuit a considerable amount of fundamental information must be integrated. For instance, variations of the cathode fall in potential is one type of problem which must be appreciated in designing a voltage regulator. The sparking potential values and relative stability of sparking potentials is important in switching devices and some thyratron control circuits. In the design of glow tubes, the current densities are of importance in order to calculate wattage dissipations at the cathode.

In reference to the stability of electrical performance of glow tubes, there is little or no fundamental information concerning the materials being used in modern tube fabrication techniques such as tubes with oxide-coated and inert gases. There is some general information, however, which is of interest and use in discussing these matters. For instance, the cathode fall in potential has been found to be related to the chemistry of the cathode surface. Bär[1] has shown that a lower work function will generally indicate a lower cathode fall in potential, for a given gas. Loeb[2] points out some early work in which analytic expressions were derived for current density in a glow discharge and cathode fall in potential.

In all of these calculations and in the derivations of most other investigators, the physical processes occurring in the glow are described as follows.

The mechanism of liberation of electrons from the cathode by positive ions or excited atoms is supposed to occur primarily in three ways. (a) Liberation of electrons by positive ion bombardment. (The exact mechanism is not yet understood.) (b) The freeing of electrons by photons produced in the gas. (c) Electron emission due to the effects of metastable atoms releasing energy to the cathode surface.

The electrons liberated from the cathode will, when accelerated, collide with the gas causing ionization and metastable states. These will, in turn, produce more electrons at the cathode. Most of these gas excitation processes are assumed to occur in the region of the cathode glow. For glow tubes where the current density is low and adequate anode area available, the cathode fall in potential is nearly equal to the total voltage across the tube.

In almost all of the reported experimental work with glow discharges and cathode effects, the tubes studied utilized metallic cathodes. In addition, for the case of these metallic surfaces, temperature changes were generally not regarded as important, until the higher temperatures were reached.[3]

## II. STATEMENT OF THE PROBLEM

The purpose of the investigation was to describe the action of the glow discharge for the case of an oxide-

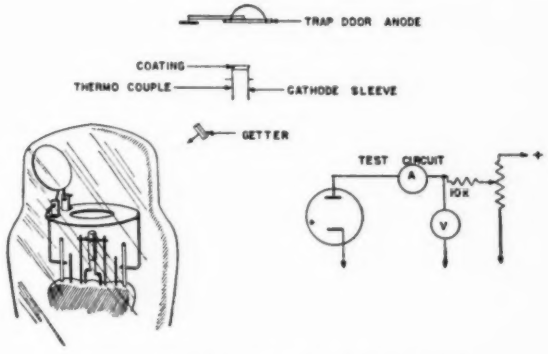


FIG. 1. Experimental tube and test circuit.

[1] Bär, Geiger, and Scheel, *Handbuch der Physik* (1927), Vol. 14, p. 203.
[2] L. B. Loeb, *Fundamental Processes and Electric Discharges in Gases* (John Wiley and Sons, Inc., New York, 1939), pp. 580–585.
[3] See reference 2, p. 607.

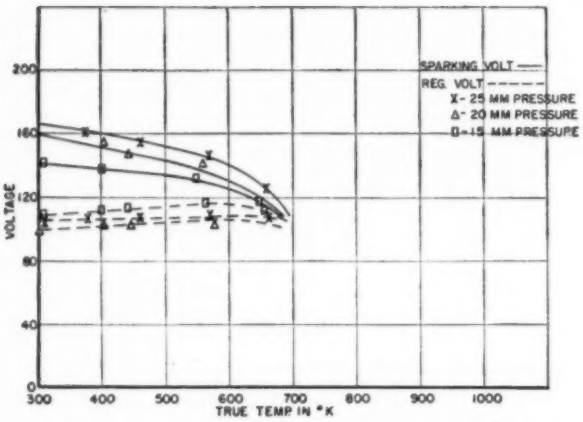


FIG. 2. Sparking potentials and regulation voltages as a function of temperature for neon gas and (BaSrCa)O cathodes.

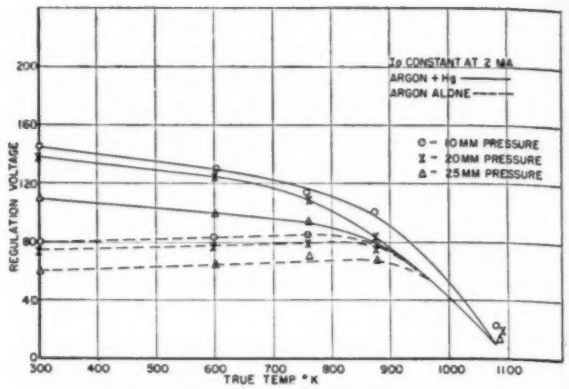


FIG. 3. Regulation voltages as a function of temperature for argon and argon contaminated with mercury.

coated cathode and an inert gas. Specifically, the following factors were studied as a function of cathode temperature and gas pressure: (a) sparking potential, (b) tube voltage drop, (c) current density, and (d) minimum current necessary to sustain a glow discharge. It was hoped, in this manner, that some of the causes of variations of the electrical characteristics in a glow discharge would be revealed.

## III. EXPERIMENTAL TECHNIQUE

Tubes were constructed as in Fig. 1; the test circuit is sketched next to the design of the tube.

All tubes were constructed with trap-door anodes. The purpose here was to provide uncontaminated anodes and to facilitate cathode temperature measurements. During exhaust, when the cathode was activated, the trap was in an upright position. After cathode activation, the trap door was dropped and processing continued.

It is to be noted that all temperatures were measured on the cathode base metal. Thus the cathode surface was estimated to be from 0 to 50 degrees cooler than the temperature of the base metal. For the experiments to be described, extreme exactness of temperature measurement at the cathode surface was not required.

The following procedure was established for testing. After aging, the sparking potential was measured and the temperature of the base metal recorded. By means of adjusting the power supply voltage the glow was brought so that it just covered the cathode surface, and did not flow down the sides of the cylinder. The area was taken as the area of the cathode, the current was measured and the current density calculated. The normal glow voltage was recorded by taking the fall in potential across the tube at this point. It was noted that the tube drop changed very little by varying the area of cathode covered by the glow discharge. After the normal glow tube drop was recorded, the current was decreased in the tube until the glow was extinguished. This was a rather abrupt point. Sometimes a sudden surge of current appeared as the glow was extinguished. The meaning here is not clear. Generally the current was decreased to the microampere region before it was extinguished. The minimum current refers to the lowest current that could be drawn before the glow became non-self-sustaining. The pressure of each tube was also recorded.

## IV. DATA AND DISCUSSION CONCERNING SPARKING POTENTIALS AND REGULATION VOLTAGES

For each tube, a determination was made of sparking potentials, and regulation voltage, as a function of the temperature of the base metal. Some sample curves are to be found in Figs. 2 and 3. It is of interest to note that as the cathode temperature increases, the sparking potential decreases. This is to be expected to some extent. However, for argon, as the cathode temperature increases, from 300°K to about 750°K the regulation voltage does not fall, but, in fact, tends to show a slight rise. The general tendency or rising regulation voltage with rising cathode temperature was noted for all the tubes with the (BaSrCa)O cathodes and pure argon gas. Actually 19 tubes with this combination were tested and all showed the same tendency. Tubes made with neon gas and argon-neon mixture behaved similarly.

A question arises as to why the regulation voltage increased as the cathode temperature went from 300°K to about 750°K. By the accepted concepts, as the cathode becomes more efficient, liberating more electrons, the necessary ionization of the gas for a self-sustained discharge should be produced by a lower

TABLE I. Sparking potentials in argon.

| Pressure times distance | Barium metal cathode (300°K) | (BaSrCa)O cathode (300°K) | (BaSrCa)O cathode (500°K) |
|---|---|---|---|
| 1.0 mm×cm | 92 volts | 95 volts | 90 volts |
| 1.5 | 100 | 109 | 99 |
| 2.0 | 111 | 120 | 110 |
| 2.5 | 121 | 134 | 120 |
| 3.0 | 128 | 144 | 126 |

TABLE II. Minimum sustaining currents for oxide cathodes and argon gas.

| Minimum sustaining current in ma at room temperature | Minimum sustaining current in ma at 500°K, cathode temperature | Pressure in mm of mercury |
|---|---|---|
| 0.08 | 0.06 | 5 |
| 0.22 | 0.11 | 10 |
| 0.37 | 0.16 | 15 |
| 0.48 | 0.20 | 20 |
| 0.62 | 0.25 | 25 |
| 0.75 | 0.29 | 30 |

field. Yet, experimentally this was not the case. One might suspect further that electron liberation just prior to the spark has a different mechanism from electron liberation due to the glow, since in the glow there is an increase in the number of metastables and photons close to the cathodes.

Another experiment was then performed where tubes were made up with argon gas and (BaSrCa)O cathodes, but this time a droplet of mercury was added prior to exhaust. After exhaust a portion of the mercury was still present as a droplet. During testing it was apparent that the presence of mercury vapor at room temperature had changed the characteristics of the tubes markedly, in the color of the glow, in the electrical properties, and in the cathode activity. During testing it was noted that the Hg greatly deactivated the (BaSrCa)O. Sometimes, as a cold cathode, the spark and glow would occur from the nickel instead of the cathode. Sometimes, only a part of the cathode was covered by the glow. In the following data only those tubes were used in which the glow was on the oxide-coated cathode surface. It was found, for mercury contaminated tubes, that as cathode temperature was increased, the regulation voltage decreased. This effect was in contrast to pure argon or neon where with increasing temperature the regulation voltage increased. As a matter of side interest the regulation voltage was higher for the argon and Hg tubes. The actual data are shown in Fig. 3.

The experiment with Hg vapor indicated the marked effect of Hg vapor in changing the glow characteristics. But more than this, it offers a possible explanation for the rather anomalous behavior of the regulation voltage in pure argon. In the glow discharge the liberation of electrons is aided not only by positive ions striking the surface but largely by photons and metastables. The effects of metastable atoms is greater in the glow than in the conditions leading to the spark. As the cathode in a glow discharge is heated, one might expect the gas in the cathode vicinity to have an increased kinetic energy. It seems reasonable to expect that a metastable atom can lose its energy by collision with a neutral atom, with the excess energy given off by the kinetic energy of the particles involved. If the kinetic energy of the gas particle is increased, one might expect the metastables to be decreased, thus the process of liberation of electrons from the cathode would be less efficient and a higher field would be necessary to maintain the discharge. One might expect that for pure argon the regulation voltage would rise with cathode temperature until the temperature rose enough to emit sufficient electrons for the tube to go into an externally sustained arc. The presence of the mercury in argon would effectively reduce the metastable argon atoms by ionization of the mercury. Without the metastables being present, the regulation voltage should drop with increasing cathode temperature and this is what has been observed.

Another point of interest is the determination of sparking potentials and regulation voltages at various pressures. For the case of (BaSrCa)O cathodes, it was found that the curves for sparking potential *versus* pressure×distance were very similar to those determined with barium metal cathodes in the same gas[4] (Table I).

It has been found, experimentally, that the regulation voltage, at constant temperatures, changes very slightly with pressure. In some cases, there is a slight increase of regulation voltage at reduced pressures.

## V. CURRENT DENSITY AND MINIMUM SUSTAINING CURRENT

The current density in a glow discharge has been studied theoretically and the following equation[5] is most often quoted to describe it:

$$_n = 5.92\times10^{-14}\frac{AB^2(k_+p)(1+\gamma)}{\log(1+1/\gamma)}p^2\frac{\text{amp}}{\text{cm}^2}. \qquad (1)$$

In the experiments performed, current density measurements were made with respect to pressure and cathode temperature. The current density was actually found to decrease with increasing temperature up to about 700°K. Above this temperature the current density would start to rise very rapidly. The data reveals

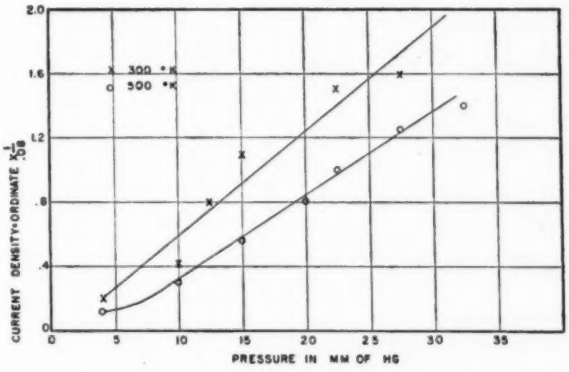


FIG. 4. Current density and pressure for argon-filled tubes and (BaSrCa)O cathodes. (Legend to the left of the figure should read: current density = ordinate × 1/0.08 ma/cm².)

[4] H. Jacobs and A. P. LaRocque, J. App. Phys. **18**, 199–203 (1947).

[5] See reference 2, p. 584.

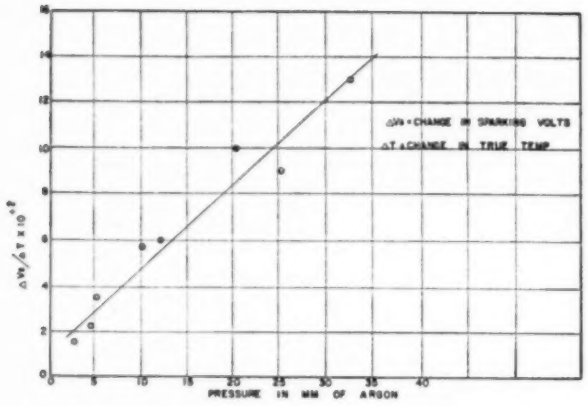


FIG. 5. The role of pressure on the change of sparking potential with respect to temperature (volts/°K) for argon gas and (BaSrCa)O cathodes.

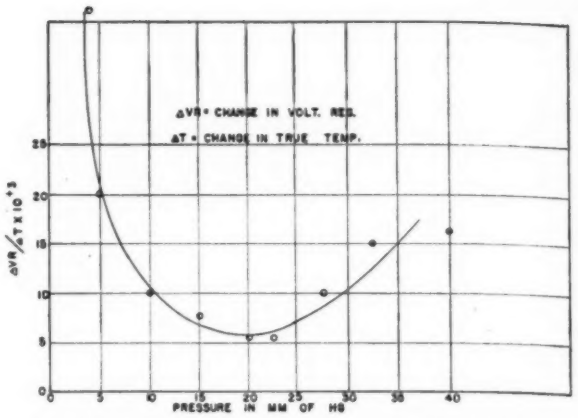


FIG. 6. The role of pressure on the change of regulation voltages with respect to temperature (volts/°K), for argon gas and (BaSrCa)O cathodes.

that as the cathode rises in temperature, the regulation voltage rises and the current density diminishes, until the region of the arc is approached, where the voltage drops rapidly and the current density rises rapidly.

Referring to Eq. (1) again, which was derived on space-charge considerations of positive ions, as $p^2$ increases, $j_s$ should increase. In Fig. 4 we find the current density *vs.* pressure at 300°K temperature and at 500°K, for argon. This indicates two factors. (a) Current density decreases with increasing temperatures in this range. (b) Current density is almost a linear function of pressure. (For the mixtures of neon and argon, the current density was found to increase at a slightly higher rate as the pressure was increased.)

At the same period of measurement the minimum sustaining current was measured and found to decrease with increasing temperature (Table II).

## VI. FURTHER CONSIDERATIONS

Upon study, the experiments with uncontaminated tubes indicated rather definite relationships between the change in sparking potential with respect to cathode temperature, $dV_s/dT$, and pressure. The change in regulation voltage with respect to pressure, $dV_R/dT$, was also found to be a function of pressure. As indicated in Fig. 5, $dV_s/dT$ was found to be a constant as the pressure was increased.[6] Similarly (see Fig. 6) $dV_R/dT$ was found to be a function of pressure—although not a constant.

The question then arises as to whether or not these experiments can give us a physical insight as to the mechanism in the spark. For instance, it has not been shown in what manner $\gamma$, the second Townsend coefficient, varies with cathode temperature for these particular cases. From Fig. 5, we can set up the following relation:

$$-dV_s/dT=Cp, \tag{2}$$

$dV_s$=change in sparking potential (volts), $dT$=change in cathode temperature (°K), $C$=constant, $p$=pressure in mm of mercury.

Using the Townsend criterion for sparking, Eq. (3) can be shown to be the equation for sparking.[7]

$$V_s=\frac{Bpd}{\ln[Apd/\ln(1/\gamma)]}, \tag{3}$$

where $V_s$=sparking potential, $p$=pressure, $d$=distance, $\gamma$=largely secondary emission on positive ion bombardment. This quantity, in addition, contains electrons liberated by photons and metastables. $A$ and $B$=empirical constants.

Integrating Eq. (2),

$$-V_s=CpT+V_0. \tag{4}$$

$V_0$ is the extrapolated hypothetical sparking potential near 0°K for a given pressure and distance. We are now in a position to discuss the manner in which $\gamma$ varies with cathode temperature. Substitute Eq. (3) in Eq. (4):

$$-\frac{Bpd}{\ln[Apd/\ln(1/\gamma)]}=CpT+V_0. \tag{5}$$

The following factors are assumed constant: $B$, $p$, $d$, $A$, $C$, and $V_0$. $\gamma$ is the remaining factor varying with $T$.

$$T=-\frac{Bpd}{Cp\ln[Apd/\ln(1/\gamma)]}+\frac{V_0}{Cp}. \tag{6}$$

$T$ varies as $K\{1/\ln[\ln(1/\gamma)]\}$, $K$=constant; $\ln[\ln(1/\gamma)]$ varies as $K/T$.

We can conclude: $\exp(e^{1/T})$ varies as $1/\gamma$ times a constant, for sparking.

Now let us refer to Fig. 6 which shows the increase of regulation voltage per change in cathode temperature as a function of pressure. We notice that at about 20

[6] $\Delta V_s/\Delta T$ is a negative quantity in Fig. 5.

[7] J. D. Cobine, *Gaseous Conductors* (McGraw-Hill Book Company, Inc., New York, 1941), p. 163.

mm, $dV_R/dT$ is a minimum. The behavior here is not readily explained at the present time.[8]

## VII. CONCLUSIONS

It was found that for experimental glow discharge tubes without mercury contaminations, and in the cathode temperature regions of from 300°K to 750°K, using oxide cathodes and inert gases:

1. The sparking potentials fall with increasing cathode temperatures.
2. The regulation voltage rises slightly with increasing cathode temperature. (For mercury vapor and argon, the regulation voltage falls with increasing cathode temperature.)
3. The current density decreases with increasing cathode temperature. This takes place concurrently with the increase in regulation voltage.
4. The minimum sustaining current in a glow discharge decreases with increasing cathode temperature, and rises with increasing pressure.
5. For the case of argon, the current density in the glow discharge varies roughly linearly with pressure in contrast with the space charge derivations which predict a variation with pressure squared. For the case of the neon, argon mixtures, the rate of increase in current density is not quite linear but slightly greater.
6. The decrease in sparking potential with respect to temperature diminished linearly with lower pressures. The change of regulation voltage with respect to temperature is related to pressure, but not in any simple manner.

[8] T. Jurrianse, Philips Res. Rep. **1**, 407 (1946). For the case of neon gas and a molybdenum cathode, it was found that $dV_R/dT$ was a negative quantity.


## VIII. ACKNOWLEDGMENT

We wish to thank Mr. K. M. McLaughlin and the Radio Corporation of America Development Group at Harrison, New Jersey, for their suggestions in the tube design and for the construction of the experimental tubes.


# The Emission of Radiation from Diatomic Gases. I. Approximate Calculations*


S. S. PENNER

*Jet Propulsion Laboratory, California Institute of Technology, Pasadena, California*



(Received February 6, 1950)



An approximate method for estimating radiant heat transfer from gaseous emitters is proposed. An average absorption coefficient is used for the effective width of an entire vibration-rotation band. The procedure for determining an average absorption coefficient in terms of the integrated absorption is justified, approximately, for very small optical densities and also for large total pressures where the spectral half-width is no longer small compared with the rotational spacing. Because of these limitations it is to be expected that the procedure proposed here will be particularly useful only in estimating gaseous emissivities for emitters in high-pressure combustion chambers. A preliminary compilation is given of the theoretical results which are necessary for making rapid estimates of the emissivities, over a wide temperature range, for CO, HI, HBr, HCl, and HF.


## I. INTRODUCTION

PROBLEMS concerned with the emission of radiant energy from an assembly of gaseous emitters which are in thermal equilibrium have formed the subject for theoretical and experimental investigations by two essentially distinct groups.

The members of one group, the theoretical physicists, have attacked the fundamental atomistic problem in an effort to evolve relations, based on quantum-mechanical considerations, which permit a rigorous solution of the problem, at least in principle. The basic relations between the various factors contributing to radiant heat transfer are correlated by the well-known relations between the coefficients of induced and spontaneous emission and induced absorption developed by Einstein in 1917.[1] Theoretical efforts to derive relations for the Einstein coefficients from first principles have culminated in Dirac's treatment of the interaction of radiation and matter, numerical application of which to specific problems usually involves formidable computational difficulties. Excellent reviews from the fundamental point of view of the work of Dirac, Born, Slater, and others have been given by Fermi[2] and Breit.[3] The subject of the interaction of radiation and matter is still far from solved, as is evidenced by intensive current activity in this field.[4]

Contributors of the second group involved in the calculation of intensities of radiation come from the ranks of the applied scientists and engineers who have contented themselves with a phenomenological description of the intensities of radiation emitted from gaseous bodies of various shapes, sizes, and compositions and who have based their predictions primarily upon empirically determined parameters such as effective over-all emissivities for pure gases and gaseous mixtures as functions of pressure, temperature, and path length. Although this approach has involved only


* This paper presents the results of one phase of research carried out at the Jet Propulsion Laboratory, California Institute of Technology, under Contract No. W-04-200-ORD-455, sponsored by the U. S. Army Ordnance Department.


[1] A. Einstein, Physik. Zeits. **18**, 121 (1917).

[2] E. Fermi, Rev. Mod. Phys. **4**, 87 (1932).

[3] G. Breit, Rev. Mod. Phys. **4**, 504 (1932).

[4] See, for example, V. F. Weisskopf, Rev. Mod. Phys. **21**, 305 (1949), and references cited in this article.

limited application of the fundamental relations determining the intensity of radiant energy emitted, it has nevertheless been developed to the point where reasonable predictions can be made for practical applications.[5]

It is apparent that use of the results of the theoretical physicists will suggest the most desirable lines of attack along which practical methods for the calculation of radiant heat transfer should be evolved. Accordingly, we shall devote our attention in this paper and in succeeding articles on radiant heat transfer to utilizing some of the established results relating to the calculation of radiant energy emitted from pure gases. For the present we shall content ourselves with developing and applying a simple and rather crude method for estimating gaseous emissivities by assigning an average absorption coefficient to an entire vibration-rotation band. Before proceeding with the presentation of details of this development, it appears desirable to review briefly the essential steps in estimating the intensity of radiation emitted from heated gases.

A gas emits radiation as the result of electronic, vibrational, and rotational transitions from excited energy levels to lower energy levels. The emitted radiant energy corresponding to these transitions is distributed over a wide wave-length region. Only the transitions corresponding to the infra-red vibration-rotation bands make an important contribution to the total radiant heat transfer at the temperatures of interest in connection with studies on combustion chambers. The total radiant intensity emitted from a given quantity of gas is obtained by summing the radiant intensities corresponding to each of the individual energy transitions. A calculation of this type requires knowledge of the following factors: 1. The number of molecules present in each of the various energy levels must be known. If thermal equilibrium obtains, this distribution can be calculated from quantum statistics. If thermal equilibrium does not exist, as may well be the case in a region of active combustion, then the equilibrium assumption and hence the numerical results derived from it are obviously invalid. 2. The transition probabilities for each of the possible energy transitions must be determined. Transition probabilities can be calculated with satisfactory precision for isolated quantum-mechanical systems such as vibrating-rotating diatomic molecules. At elevated temperatures and pressures, however, the various radiating systems may be perturbed as the result of interactions with neighboring molecules. These perturbations are neglected in the present calculations. 3. The frequencies corresponding to each of the energy transitions enter into the quantitative expressions for the radiant intensities. These frequencies can usually be determined with a high degree of precision from available spectroscopic data. 4. The spectral line shape must be known as a function of pressure and temperature. It can be calculated with relative ease if the familiar Lorentz collision formula is valid, and with some difficulty when it is not valid. In the present approximation, calculations of radiant heat transfer will be carried out without explicit allowance for line shape by introducing the restriction that the total pressure is sufficiently high to provide extensive overlapping of individual rotational lines.

## II. BASIC RELATIONS BETWEEN INTEGRATED ABSORPTION, EINSTEIN COEFFICIENTS, AND RADIANT INTENSITIES

An energy transition from a lower energy level $j$ to an upper energy level $i$ (or conversely) is accompanied by the absorption (or emission) of radiation of frequencies close to the frequency $\nu_{ij}$ given by the familiar quantum relation $\nu_{ij}=\Delta E_{ij}/h$ where $\Delta E_{ij}$ is the energy difference between the two levels under consideration, and $h$ is Planck's constant. Let $\rho(\nu_{ij})$ represent the volume density of radiant energy emitted by a blackbody in the frequency interval between $\nu_{ij}$ and $\nu_{ij}+d\nu_{ij}$. The integrated absorption $\int P_{\nu_{ij}}d\nu_{ij}$ is related to the Einstein coefficients of induced absorption and induced emission by the well-known relation[6]

$$\int P_{\nu_{ij}}d\nu_{ij}\simeq N_jB_{j\to i}h\nu_{ij}/c-N_iB_{i\to j}h\nu_{ij}/c$$
$$=N_iA_{i\to j}h\nu_{ij}/c\rho(\nu_{ij}), \quad (1)$$

where $N_j$=number of molecules per unit volume in quantum state $j$, $N_i$=number of molecules per unit volume in quantum state $i$, $B_{j\to i}$=Einstein coefficient of induced absorption, $B_{i\to j}$=Einstein coefficient of induced emission, $A_{i\to j}$=Einstein coefficient of spontaneous emission, and $c$=velocity of light. The symbol $P_{\nu_{ij}}$ indicates that the absorption coefficient with which we are concerned arises as the result of an energy transition between the levels $i$ and $j$. The integration in Eq. (1) may be performed over all frequencies $-\infty<\nu_{ij}<+\infty$ if we adopt the convention of calling frequencies smaller than $\nu_{ij}$ negative and frequencies larger than $\nu_{ij}$ positive.

Treatments of intensities of emission and absorption involving the Einstein coefficients are derived under conditions of thermal equilibrium.[1,6,7] Nevertheless it is customary to assume[8] that energy transitions from the upper level $i$ to the lower level $j$ occur at the net rate,

$$N_i[A_{i\to j}+B_{i\to j}\rho'(\nu_{ij})]-N_jB_{j\to i}\rho'(\nu_{ij}), \quad (2)$$

even if thermal equilibrium does not exist. Here $\rho'(\nu_{ij})$

[5] H. C. Hottel, "Radiant heat transfer," in W. H. McAdam's *Heat Transmission* (McGraw-Hill Book Company, Inc., New York, 1942); M. Jakob, *Heat Transfer* (John Wiley and Sons, Inc., New York, 1949).

[6] R. C. Tolman, Phys. Rev. **23**, 693 (1924); E. C. Kemble, Phys. Rev. **25**, 1 (1925).

[7] L. Pauling and E. B. Wilson, Jr., *Introduction to Quantum Mechanics* (McGraw-Hill Book Company, Inc., New York, 1935), p. 299.

[8] E. C. Kemble, *Fundamental Principles of Quantum Mechanics* (McGraw-Hill Book Company, Inc., New York, 1937), p. 450.

is the external energy density of radiation passing through the system under discussion.

An expression of the type given in Eq. (2) is not particularly useful for calculations of the net radiant intensity emitted. Instead we require a differential expression which can be obtained by considering the change of energy resulting from the passage of radiant energy through a radiating and absorbing system of emitters and receivers. If the incident radiant intensity (not necessarily the intensity of radiation emitted by a blackbody) is denoted as $I(\nu)$, the following differential equation results

$$dI(\nu)=P_\nu[c\rho(\nu)-I(\nu)]dX.$$

Here it is assumed that the fraction of radiant energy absorbed is proportional to the incident intensity of radiation (with the proportionality constant set equal to the spectral absorption coefficient $P_\nu$) and that the net change in radiant energy is proportional to the change in optical density $dX$ through the system of emitters and absorbers. Integration leads directly to the well-known relation

$$I(\nu)=c\rho(\nu)[1-\exp(-P_\nu X)] \qquad (3)$$

for the radiant energy emitted per unit area of surface by gaseous emitters distributed uniformly through a radiation path length of optical density $X$.

Equation (3) cannot be applied to practical calculations unless the dependence of $P_\nu$ on $\nu$ is known, a problem which requires detailed consideration of spectral line shape and its dependence on pressure, temperature, etc.[9,10] If Lorentz broadening obtains, $P_\nu$ is related to the integrated absorption by the dispersion formula

$$P_\nu=\frac{\delta}{\pi}\frac{\int P_{\nu ij}d\nu_{ij}}{(\nu-\nu_{ij})^2+\delta^2}, \qquad (4)$$

where $\delta$ represents the spectral half-width. If individual rotational lines are sufficiently broadened to cause overlapping of lines, then the spectral absorption coefficient, for collision-broadened lines, is given by a sum of terms of the type shown in Eq. (4). Therefore, in this particular case, the intensity of radiation $I(\nu)$ can be calculated provided the half-widths $\delta$ and the integrated absorption $\int P_{\nu ij}d\nu_{ij}$ are known for each transition. The half-width $\delta$ can be determined, for example, from the dependence of absorption on pressure[11] by utilizing the theoretical analysis of Elsasser.[12,13]

TABLE I. Effective band width of the fundamental of CO as a function of temperature.

| $T$ °K | $j_{max}$ | $\nu_{max}$ cm$^{-1}$ | $\nu_{min}$ cm$^{-1}$ | $\Delta\nu_{n\to n+1}$ cm$^{-1}$ |
|---|---|---|---|---|
| 300 | 28 | 2235 | 2021 | 214 |
| 500 | 36 | 2256 | 1982 | 274 |
| 1000 | 50 | 2287 | 1908 | 379 |
| 1500 | 62 | 2306 | 1841 | 465 |
| 2000 | 72 | 2317 | 1782 | 535 |
| 2500 | 80 | 2322 | 1732 | 590 |
| 3000 | 86 | 2325 | 1694 | 630 |

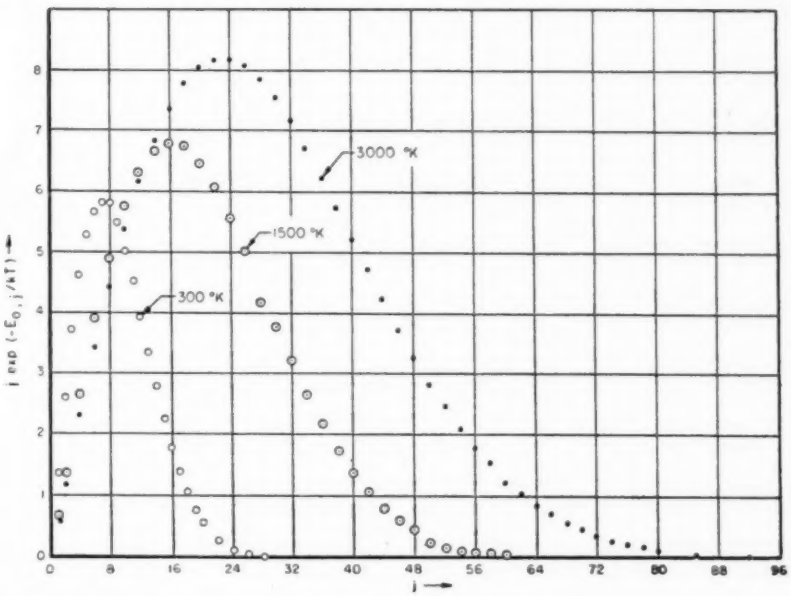


FIG. 1. Representative plots of $j\exp(-E_{0,j}/kT)$ *vs.* $j$ for carbon monoxide (different scales are used for the ordinate at different temperatures).

[9] H. Margenau and W. W. Watson, Rev. Mod. Phys. **8**, 22 (1936); H. M. Foley, Phys. Rev. **69**, 616 (1946).
[10] J. H. Van Vleck and V. F. Weisskopf, Rev. Mod. Phys. **17**, 227 (1945); P. W. Anderson, Phys. Rev. **76**, 647 (1949); E. Lindholm, Dissertation, Uppsala (1942).
[11] M. Summerfield and J. Strong, Phys. Rev. **59**, 217 (1941); A. M. Thorndike, J. Chem. Phys. **16**, 211 (1948).
[12] W. M. Elsasser, Phys. Rev. **54**, 126 (1938); Astrophys. J. **87**, 497 (1938).
[13] W. M. Elsasser, Harvard Meteorological Studies No. 6, 1942. The theoretical treatment of Elsasser has recently been generalized to arbitrarily spaced rotational lines of arbitrary intensity distribution [see F. Matossi, R. Mayer, and E. Rauscher, Phys. Rev. **76**, 760 (1949)].

The dependence of $\delta$ on pressure and temperature can be calculated, approximately, for collision-broadened lines.[9,10] Individual values for integrated absorption for rotational transitions can be calculated if the integrated absorption for a vibration-rotation band has been determined experimentally. Calculations for diatomic molecules involve the use of theoretical results obtained by Oppenheimer[14] and applied by Dennison.[15] Similar calculations are also possible for the simpler polyatomic molecules.

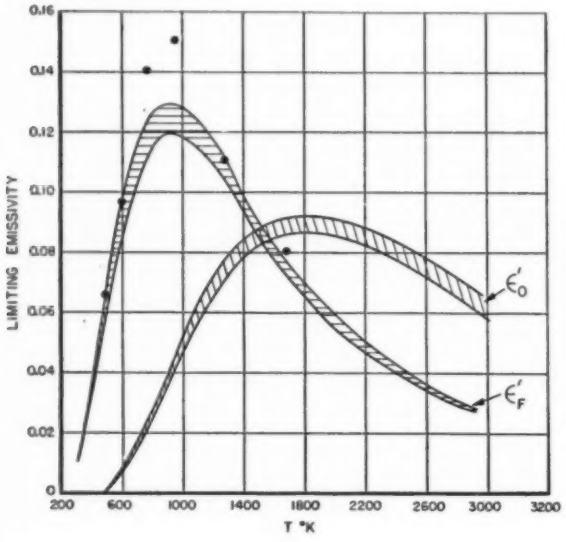


FIG. 2. Limiting emissivity of CO as a function of temperature. Experimental data for $pl=5$ ft-atmos. (cf. reference 19): ●

| $T$ °K | $j_{max}$ (upper curve) | $j_{max}$ (lower curve) |
|---|---|---|
| 300 | 30 | 28 |
| 500 | 38 | 36 |
| 1000 | 54 | 50 |
| 1500 | 66 | 62 |
| 2000 | 76 | 72 |
| 2500 | 86 | 80 |
| 3000 | 92 | 86 |

## III. A METHOD FOR THE APPROXIMATE CALCULATION OF THE INTENSITY OF RADIATION EMITTED FROM GASES WHICH ARE IN THERMAL EQUILIBRIUM

In this section we shall consider drastic simplifications of methods for making radiant heat-transfer calculations for gases.

### A. A Method for Estimating an Upper Limit for the Emission of Radiant Energy from Pure Gases and Gaseous Mixtures

An upper limit is obtained for the total radiant energy $\int_{n\to n'} I_\nu d\nu$ emitted for frequencies corresponding to the vibrational transition from $n$ to $n'$ if we set

$$\int_{n\to n'} I_\nu d\nu = c\int_{\Delta\nu_{n\to n'}} \rho(\nu)d\nu, \qquad (5)$$

where $\Delta\nu_{n\to n'}$ designates an appropriate band width for the vibration-rotation band under consideration. The total radiant energy emitted over all emission bands is evidently obtained by summing the contributions for all possible vibrational transitions, i.e., The maximum

$$I_T = \sum_{n,\,n'}\int_{n\to n'} I_\nu d\nu = c\sum_{n,\,n'}\int_{\Delta\nu_{n\to n'}} \rho(\nu)d\nu. \qquad (6)$$

value of the effective emissivity $\epsilon'_{max}$ is defined by the relation

$$\epsilon'_{max} = \left\{\sum_{n,\,n'}\int_{\Delta\nu_{n\to n'}} \rho(\nu)d\nu\right\} \Big/ \int_0^\infty \rho(\nu)d\nu. \qquad (7)$$

The calculation of an upper limit for the emissivity is seen to require an independent estimate of band widths $\Delta\nu_{n\to n'}$. It is to be expected that a suitable method for the calculation of $\Delta\nu_{n\to n'}$ will lead to theoretical upper limits for the emissivities which are in agreement with the experimentally observed limits approached by given emitters as the optical density is increased. The method suggested here for the calculation of effective band width approximately fulfills this requirement.[16] The principal factor determining the dependence of integrated absorption on rotational quantum number is of the form

$$j\exp(-E_{n,j}/kT) \quad \text{or} \quad j\exp(-E_{n,j-1}/kT),$$

where $E_{n,j}$ represents the energy of the $n$th vibrational and $j$th rotational level, $k$ is the Boltzmann constant, and $T$ represents the absolute temperature. These facts suggest that the band width $\Delta\nu_{n\to n'}$ be set equal to the frequency interval for which the factors $j\exp(-E_{n,j}/kT)$ or $j\exp(-E_{n,j-1}/kT)$ have values in excess of $10^{-3}$ of their maxima at a given temperature. This definition of $\Delta\nu_{n\to n'}$ is admittedly arbitrary. However, the exponential terms decrease so rapidly with increasing values of $j$ that a different definition, such as setting $\Delta\nu_{n\to n'}$ equal to the frequency interval in which $j\exp(-E_{n,j}/kT)$ or $j\exp(-E_{n,j-1}/kT)$ have values in excess of $10^{-2}$ or $10^{-4}$ of their respective max-

TABLE II. Effective band width of the first overtone of CO as a function of temperature.

| $T$ °K | $j_{max}$ | $\nu'_{max}$ cm$^{-1}$ | $\nu'_{min}$ cm$^{-1}$ | $\Delta\nu_{n\to n+2}$ cm$^{-1}$ |
|---|---|---|---|---|
| 300 | 28 | 4337 | 4124 | 213 |
| 500 | 36 | 4349 | 4078 | 271 |
| 1000 | 50 | 4357 | 3981 | 376 |
| 1500 | 62 | 4357 | 3890 | 467 |
| 2000 | 72 | 4357 | 3808 | 549 |
| 2500 | 80 | 4357 | 3737 | 620 |
| 3000 | 86 | 4357 | 3682 | 675 |

[14] J. R. Oppenheimer, Proc. Camb. Phil. Soc. **23**, 327 (1926).
[15] D. M. Dennison, Phys. Rev. **31**, 503 (1928).

[16] The utility of an empirically determined effective band width seems to be supported by absorption measurements performed by the author and D. Weber. The "effective band width" of the CO fundamental at room temperature was found to increase only about 20 percent when the pressure of absorbing gas was increased from 5 mm to 200 p.s.i. at constant total pressure.

ima, would lead to substantially the same results as the definition of band width adopted for the present application. It should be noted that the definition of effective band width given here leads to similar results for all transitions of the form $n \rightarrow n+1$ provided the anharmonicities are not excessive. Estimates of overtone intensities indicate that the effective band widths of the overtones correspond, approximately, to the same limiting values for the rotational quantum numbers $j$ as for the fundamental

The foregoing considerations lead to a straightforward method for estimating effective band widths. The application of this method is described here for carbon monoxide.

In Fig. 1 a plot is shown of $j \exp(-E_{0,j}/kT)$ for carbon monoxide as a function of $j$ for representative values of the temperature. Similar plots have been prepared for each of the following temperatures: 300, 500, 1000, 1500, 2000, 2500, and 3000°K. Reference to Fig. 1 shows that for all values of $j$ up to about $j_{\max}=28$ the integrated absorption is larger than $10^{-3}$ of its maximum value at 300°K. Similar results are obtained at other temperatures. It follows from the preceding discussion that $\Delta\nu_{0\rightarrow 1} \simeq \Delta\nu_{1\rightarrow 2} \simeq \Delta\nu_{2\rightarrow 3} \simeq \cdots =$ effective band width of the fundamental $=\nu_{\max}-\nu_{\min}$, where $\nu_{\max}$ and $\nu_{\min}$ are given, respectively, by the approximate relations

$$\nu_{\max} \simeq \frac{E(1, j_{\max}) - E(0, j_{\max}-1)}{h} \tag{8}$$

$$\nu_{\min} \simeq \frac{E(1, j_{\max}-1) - E(0, j_{\max})}{h}. \tag{8a}$$

Band widths have been calculated for the fundamental vibration-rotation band of carbon monoxide from available spectroscopic data[17] by the use of this method. The results are summarized in Table I.[18]

For sufficiently large values of $j$ a band head should be obtained beyond which the calculated maximum cutoff frequency should decrease with increasing values of $j_{\max}$. This phenomenon is observed for smaller $j$-values in the case of the first overtone of CO (see below). When a band head does occur, the cut-off frequency should evidently be chosen to coincide with the extreme frequency value corresponding to the band head rather than to a frequency calculated from either Eq. (8) or Eq. (8a).

In accord with the preceding discussion we set $\Delta\nu_{0\rightarrow 2} \simeq \Delta\nu_{1\rightarrow 3} \simeq \cdots =$ effective band width of the first overtone $=\nu'_{\max}-\nu'_{\min}$ where

$$\nu'_{\max} \simeq \frac{E(2, j_{\max}) - E(0, j_{\max}-1)}{h} \tag{9}$$

$$\nu'_{\min} \simeq \frac{E(2, j_{\max}-1) - E(0, j_{\max})}{h}. \tag{9a}$$

As explained in the preceding paragraph, Eq. (9) or Eq. (9a) should not be used if a band head is observed for $j$ values which are smaller than the appropriate values of $j_{\max}$. Relevant band width calculations for the first overtone of CO are summarized in Table II.

Since the integrated absorption of the second overtone of CO is very small compared with that of the fundamental and since, furthermore, the intensity of radiation emitted by a blackbody at temperatures below about 2000°K is relatively small in the frequency region in which the second overtone emission band is found, the contributions of the second overtone to radiant heat transfer will not become important until relatively high temperatures and large optical densities have been reached. These contributions may be included in radiant heat-transfer calculations by following the procedure outlined above for calculations on the fundamental and the first overtone.

If only the fundamental and the first overtone make significant contributions to the intensity of radiation emitted from a given gas, then Eq. (7) reduces to the relation

$$\epsilon'_{\max} = \frac{\sum_n \int_{\Delta\nu_{n\rightarrow n+1}} \rho(\nu)d\nu}{\int_0^\infty \rho(\nu)d\nu} + \frac{\sum_n \int_{\Delta\nu_{n\rightarrow n+2}} \rho(\nu)d\nu}{\int_0^\infty \rho(\nu)d\nu} = \epsilon_F' + \epsilon_0'. \tag{10}$$

The ratios $\epsilon_F'$ and $\epsilon_0'$ occurring on the right-hand side of Eq. (10) have been evaluated by using the effective band widths summarized in Tables I and II. These ratios have also been calculated for effective band widths determined by making a somewhat different choice for $j_{\max}$ at each temperature. The results of these calculations are plotted in Fig. 2. Reference to Fig. 2 indicates that the contribution to the radiant intensity emitted from the fundamental $\epsilon_F'$ shows a maximum value near 900°K. The fraction of the total radiant energy contributed by the first overtone $\epsilon_0'$ reaches a maximum value at temperatures in the neighborhood of 2000°K. At still higher temperatures contributions from upper harmonics will become important.

[17] H. Sponer, Molekülspektren (Verlag Julius Springer, Berlin, 1935); J. E. Mayer and M. G. Mayer, *Statistical Mechanics* (John Wiley and Sons, Inc., New York, 1940), pp. 468–469; for more recent spectroscopic data on CO, see G. Herzberg and K. N. Rao, J. Chem. Phys. **17**, 1099 (1949).

[18] Band widths and corresponding emissivities have also been calculated for values of $j_{\max}$ somewhat different from those listed in Table I. The effect of the choice of $j_{\max}$, within reasonable limits, on the calculated emissivity was found to be small and is illustrated in Fig. 2.

According to the present procedure, the upper limit for the theoretical emissivity $\epsilon'_{max}$ is obtained by adding the contributions from the fundamental $\epsilon_F'$ and the first overtone $\epsilon_0'$ according to Eq. (10). It should be noted, however, that there is a certain inconsistency inherent in the use of a curve corresponding to the sum of the emissivity contributions from the fundamental and the first harmonic. Thus the integrated overtone absorption coefficient for a given rotational line is very small ($\sim 10^{-2}$ for CO) compared with the corresponding absorption coefficient of a rotational line of the fundamental. Therefore, the overtone will not act as a blackbody absorber or emitter until the optical density is exceedingly large. But for optical densities sufficiently large to make the overtone act as a blackbody, the intensity of radiation from the fundamental, which makes an appreciable contribution to the total radiant heat transfer, may be appreciable even for frequencies outside the range of the calculated band widths. Hence when the overtone acts as a blackbody, the fundamental must have an emissivity greater than the emissivity shown in Fig. 2.

Remarks similar to those made for radiant heat transfer from the first overtone apply to radiant heat transfer from upper harmonics.

TABLE III. Effective band width of the fundamental of HI as a function of temperature.

| $T$ °K | $j_{max}$ | $\nu_{max}$ cm$^{-1}$ | $\nu_{min}$ cm$^{-1}$ | $\Delta\nu_{n\to n+1}$ cm$^{-1}$ |
|---|---|---|---|---|
| 300 | 16 | 2387 | 1988 | 399 |
| 500 | 22 | 2420 | 1880 | 540 |
| 1000 | 31 | 2439 | 1703 | 736 |
| 1500 | 37 | 2439 | 1577 | 862 |
| 2000 | 46 | 2439 | 1379 | 1060 |
| 2500 | 49 | 2439 | 1311 | 1128 |
| 3000 | 54 | 2439 | 1196 | 1243 |

TABLE IV. Effective band width of the first overtone of HI as a function of temperature.

| $T$ °K | $j_{max}$ | $\nu'_{max}$ cm$^{-1}$ | $\nu'_{min}$ cm$^{-1}$ | $\Delta\nu_{n\to n+2}$ cm$^{-1}$ |
|---|---|---|---|---|
| 300 | 16 | 4513 | 4119 | 394 |
| 500 | 22 | 4514 | 3974 | 540 |
| 1000 | 31 | 4514 | 3720 | 794 |
| 1500 | 37 | 4514 | 3528 | 986 |
| 2000 | 46 | 4514 | 3208 | 1306 |
| 2500 | 49 | 4514 | 3093 | 1421 |
| 3000 | 54 | 4514 | 2894 | 1620 |

TABLE V. Effective band width of the fundamental of HBr as a function of temperature.

| $T$ °K | $j_{max}$ | $\nu_{max}$ cm$^{-1}$ | $\nu_{min}$ cm$^{-1}$ | $\Delta\nu_{n\to n+1}$ cm$^{-1}$ |
|---|---|---|---|---|
| 300 | 15 | 2755 | 2261 | 494 |
| 500 | 19 | 2785 | 2167 | 618 |
| 1000 | 27 | 2813 | 1964 | 849 |
| 1500 | 33 | 2814 | 1801 | 1013 |
| 2000 | 41 | 2814 | 1575 | 1239 |
| 2500 | 43 | 2814 | 1517 | 1297 |
| 3000 | 47 | 2814 | 1400 | 1414 |

The preceding considerations lead to the conclusion that for moderate values of the optical density it is to be expected that observed emissivity values will tend to approach and then slightly exceed the emissivity corresponding to the emission of radiant energy from the fundamental, with the fundamental acting as a blackbody emitter. This qualitative conclusion is borne out by experimental data of the emissivity of carbon monoxide measured by Hottel and Ullrich,[5,19] which are also shown in Fig. 2. The experimental data for an optical density corresponding to 5 ft.×atmos. are seen to follow the calculated blackbody emissivity curve of the fundamental with reasonable accuracy. In view of the approximations involved in the present calculations, the agreement between theory and experiment must be considered to be satisfactory.

In concluding this discussion it appears desirable to point out that the method for estimating upper limits for the emissivities described here lends itself readily to calculations on polyatomic molecules.

### B. A Method for Estimating Emissivities of Pure Gases

A more realistic estimate of the emissivity of pure gases than is provided by Eq. (10) is obtained by using an appropriate average absorption coefficient for each of the vibration-rotation bands. In this case Eq. (10) should be replaced by the following relation for the emissivity $\epsilon'$:

$$\epsilon' = [1-\exp(-\bar{k}_F pl)]\frac{\sum_n \int_{\Delta\nu_{n\to n+1}} \rho(\nu)d\nu}{\int_0^\infty \rho(\nu)d\nu} + [1-\exp(-\bar{k}_{F.O.} pl)]\frac{\sum_n \int_{\Delta\nu_{n\to n+2}} \rho(\nu)d\nu}{\int_0^\infty \rho(\nu)d\nu} + [1-\exp(-\bar{k}_{S.O.} pl)]\frac{\sum_n \int_{\Delta\nu_{n\to n+3}} \rho(\nu)d\nu}{\int_0^\infty \rho(\nu)d\nu} + \cdots, \quad (11)$$

where $\bar{k}_F$ = average absorption coefficient for fundamental vibration-rotation band, $\bar{k}_{F.O.}$ = average absorption coefficient for first overtone, $\bar{k}_{S.O.}$ = average absorption coefficient for second overtone, $p$ = partial pressure of absorber, and $l$ = optical path length. If only the contributions to the total radiant heat transfer from the fundamental and from the first overtone are

[19] W. Ullrich, Thesis, Massachusetts Institute of Technology, Cambridge (1935).

of importance, it is evidently sufficient to use the first two terms on the right-hand side of Eq. (11). Numerical evaluation of $\epsilon'$ is facilitated by the use of the blackbody intensity ratios over the effective band widths, i.e., $\epsilon_F'$ and $\epsilon_0'$, of the type presented in Fig. 2. The problem at hand therefore reduces to the evaluation of average absorption coefficients.

Before attempting to determine the numerical value of an average absorption coefficient it is appropriate to inquire about the existence of a coefficient of this type for an entire vibration-rotation band. A detailed consideration of this problem has indicated that for moderate values of the optical density $pl$ an average absorption coefficient of the order of one-half the maximum absorption coefficient obtained with low spectral resolution should be observed provided $P_\nu$ can be represented as a linear function of $\nu$.[20] The physical significance of a relation of the form, $\bar{k}=\frac{1}{2}P'_{\max}$ where $P'_{\max}$ is the maximum absorption coefficient observed under low resolution, is dubious. Of more obvious significance would be a relation between $\bar{k}$ and the integrated absorption of a given vibration-rotation band. A relation of this type can be derived by proceeding in the manner described next.

From Eq. (3) we obtain, for example, for the entire fundamental vibration-rotation band of a diatomic molecule with $P$ and $R$ branches but no $Q$ branch, the relation

$$\sum_n \sum_j \int_{\substack{n\to n+1\\ \Delta j=\pm 1}} I_\nu d\nu = c \sum_n \sum_j \int_{\substack{\Delta\nu_{n\to n+1}\\ \Delta j=\pm 1}} \rho(\nu)[1-\exp(-P_\nu pl)]d\nu \quad (12)$$

where $P_\nu$ is given by Eq. (4) for collision-broadened lines. The subscript $n\to n+1$ indicates the type of vibrational transition, whereas the subscript $\Delta j=\pm 1$ identifies the rotational transitions. If the vibration-rotation band is sufficiently narrow, we may replace $\rho(\nu)$ by an average value over the effective band width $\Delta\nu_{n\to n+1}$. Denoting the product of (a) this constant value of $\rho(\nu)$, (b) the effective band width, and (c) the velocity of light by $I_F^0$, and denoting the intensity sum over the band branches on the left-hand side of Eq. (12) by $I_F$, we obtain the relation

$$\frac{I_F}{I_F^0}=\frac{1}{\Delta\nu_{n\to n+1}}\sum_n\sum_j\int_{\Delta\nu_{n\to n+1}}[1-\exp(-P_\nu pl)]d\nu. \quad (13)$$

For sufficiently small values of the optical density $P_\nu pl \ll 1$ for all values of $\nu$. In this case we may expand the exponential in Eq. (13), retaining only the first two terms, and obtain the result

$$\frac{I_F}{I_F^0}=\frac{pl}{\Delta\nu_{n\to n+1}}\sum_n\sum_j\left(\int_{\substack{n\to n+1\\ j\to j-1}}P_\nu d\nu+\int_{\substack{n\to n+1\\ j-1\to j}}P_\nu d\nu\right) \quad (14)$$

[20] Compare A. Schack, Zeits. der techn. Physik **5**, 267 (1924).

TABLE VI. Effective band width of the first overtone of HBr as a function of temperature.

| $T$ °K | $j_{\max}$ | $\nu'_{\max}$ cm$^{-1}$ | $\nu'_{\min}$ cm$^{-1}$ | $\Delta\nu_{n\to n+2}$ cm$^{-1}$ |
|---|---|---|---|---|
| 300 | 15 | 5172 | 4685 | 487 |
| 500 | 19 | 5173 | 4559 | 614 |
| 1000 | 27 | 5173 | 4270 | 903 |
| 1500 | 33 | 5173 | 4024 | 1149 |
| 2000 | 41 | 5173 | 3658 | 1515 |
| 2500 | 43 | 5173 | 3561 | 1612 |
| 3000 | 47 | 5173 | 3359 | 1814 |

TABLE VII. Effective band width of the fundamental of HCl as a function of temperature.

| $T$ °K | $j_{\max}$ | $\nu_{\max}$ cm$^{-1}$ | $\nu_{\min}$ cm$^{-1}$ | $\Delta\nu_{n\to n+1}$ cm$^{-1}$ |
|---|---|---|---|---|
| 300 | 13 | 3088 | 2553 | 535 |
| 500 | 17 | 3129 | 2438 | 691 |
| 1000 | 24 | 3166 | 2221 | 945 |
| 1500 | 31 | 3168 | 1990 | 1178 |
| 2000 | 35 | 3168 | 1854 | 1314 |
| 2500 | 37 | 3168 | 1784 | 1384 |
| 3000 | 45 | 3168 | 1503 | 1665 |

TABLE VIII. Effective band width of the first overtone of HCl as a function of temperature.

| $T$ °K | $j_{\max}$ | $\nu'_{\max}$ cm$^{-1}$ | $\nu'_{\min}$ cm$^{-1}$ | $\Delta\nu_{n\to n+2}$ cm$^{-1}$ |
|---|---|---|---|---|
| 300 | 13 | 5831 | 5304 | 527 |
| 500 | 17 | 5835 | 5152 | 683 |
| 1000 | 24 | 5835 | 4851 | 984 |
| 1500 | 31 | 5835 | 4500 | 1335 |
| 2000 | 35 | 5835 | 4282 | 1553 |
| 2500 | 37 | 5835 | 4168 | 1667 |
| 3000 | 45 | 5835 | 3685 | 2150 |

The double sum in Eq. (14) evidently represents the integrated absorption over the fundamental vibration-rotation band. Relations similar to Eq. (14) can be derived for harmonic vibration-rotation bands.

By comparing Eq. (11) with Eq. (14) we obtain the following relations for the average absorption coefficients for sufficiently small values of the optical density:

$$\bar{k}_F=\frac{1}{\Delta\nu_{n\to n+1}}\sum_n\sum_j\left(\int_{\substack{n\to n+1\\ j\to j-1}}P_\nu d\nu+\int_{\substack{n\to n+1\\ j-1\to j}}P_\nu d\nu\right)=\frac{\alpha_{01}}{\Delta\nu_{n\to n+1}} \quad (15)$$

$$\bar{k}_{F.O.}=\frac{1}{\Delta\nu_{n\to n+2}}\sum_n\sum_j\left(\int_{\substack{n\to n+2\\ j\to j-1}}P_\nu d\nu+\int_{\substack{n\to n+2\\ j-1\to j}}P_\nu d\nu\right)=\frac{\alpha_{02}}{\Delta\nu_{n\to n+2}} \quad (16)$$

etc., where $\alpha_{01}$ and $\alpha_{02}$ represent the integrated absorp-

TABLE IX. Effective band width of the fundamental of HF as a function of temperature.

| $T$ °K | $j_{max}$ | $\nu_{max}$ cm$^{-1}$ | $\nu_{min}$ cm$^{-1}$ | $\Delta\nu_{n\to n+1}$ cm$^{-1}$ |
|---|---|---|---|---|
| 500 | 12 | 4305 | 3343 | 962 |
| 1000 | 16 | 4359 | 3110 | 1249 |
| 1500 | 20 | 4374 | 2866 | 1508 |
| 2000 | 23 | 4374 | 2678 | 1696 |
| 2500 | 27 | 4374 | 2423 | 1951 |
| 3000 | 29 | 4374 | 2295 | 2079 |
| 3500 | 31 | 4374 | 2167 | 2207 |
| 4000 | 33 | 4374 | 2040 | 2334 |
| 4500 | 36 | 4374 | 1851 | 2523 |
| 5000 | 39 | 4374 | 1666 | 2708 |

TABLE X. Effective band width of the first overtone of HF as a function of temperature.

| $T$ °K | $j_{max}$ | $\nu'_{max}$ cm$^{-1}$ | $\nu'_{min}$ cm$^{-1}$ | $\Delta\nu_{n\to n+1}$ cm$^{-1}$ |
|---|---|---|---|---|
| 500 | 12 | 7938 | 6995 | 943 |
| 1000 | 16 | 7938 | 6676 | 1262 |
| 1500 | 20 | 7938 | 6320 | 1618 |
| 2000 | 23 | 7938 | 6032 | 1906 |
| 2500 | 27 | 7938 | 5621 | 2317 |
| 3000 | 29 | 7938 | 5405 | 2533 |
| 3500 | 31 | 7938 | 5183 | 2755 |
| 4000 | 33 | 7938 | 4955 | 2983 |
| 4500 | 36 | 7938 | 4603 | 3335 |
| 5000 | 39 | 7938 | 4241 | 3697 |

tion over the fundamental and the first overtone, respectively.

The validity of Eqs. (15) and (16) has been demonstrated only under the very restrictive condition that $P_\nu pl \ll 1$ for all $\nu$. This result will not be of any particular practical significance. Fortunately, however, it can be shown that Eqs. (15) and (16) also represent reasonable approximations when the total pressure is sufficiently high. This result can be obtained by utilizing Elsasser's theoretical treatment for equally intense and equally spaced rotational lines.[12,13] Elsasser has shown that for this idealized rotational distribution the fraction of radiation absorbed as the result of a given transition is

$$\frac{I}{I_0}=1-\exp\left[\frac{1}{d}\int P_{\nu ij}d\nu_{ij}\tanh\left(\frac{2\pi\delta}{d}\right)pl\right] \qquad (17)$$

where $d$ represents the spacing between rotational lines. For equally intense and equally spaced rotational lines, to which Elsasser's treatment applies, the following identity must be valid

$$(1/d)\int P_{\nu ij}d\nu_{ij}=\alpha_{01}/\Delta\nu_{n\to n+1}. \qquad (18)$$

From Eqs. (17) and (18) it may evidently be inferred that relations of the form of Eqs. (15) and (16) apply for the average absorption coefficients provided $\delta$ is sufficiently large compared to $d$, a result which will obtain for large total pressures. In fact, as was first pointed out by Elsasser,[13] an absorption coefficient equal to the ratio of integrated absorption to line spacing represents a good approximation provided the ratio of half-width to line spacing is greater than or equal to $1/\pi$. Equations (15) and (16) exemplify this result as applied to an entire vibration-rotation band. We therefore arrive at the important conclusion that average absorption coefficients, as given in Eqs. (15) and (16) represent a crude but approximately justifiable result for sufficiently large total pressures. The condition $\delta/d\geq 1/\pi$ will be fulfilled for many molecules at pressures in excess of a few hundred pounds per square inch. Thus the present results are seen to be immediately applicable to liquid-fuel and solid-fuel rocket motors operating at pressures of a few hundred to several thousand pounds per square inch provided line broadening is still accounted for by the dispersion formula. For the present purposes the assumption of collision broadening and, therefore, of the approximate validity of Eqs. (15) and (16) for approximate heat-transfer calculations at elevated pressures will be made.[21]

The principal practical value of relations of the form of Eqs. (15) and (16) is the result of the fact that the integrated absorption is approximately independent of temperature and pressure for a given number of emitters or absorbers. Therefore the temperature dependence of the average absorption coefficient can be calculated as soon as the effective band width is known. In this connection it may be of interest to note that the present method of calculation is, to some extent, self-compensating as far as errors introduced by a poor estimate of band width are concerned. Thus a small value of $\Delta\nu$ will be partly compensated by a large value of $\bar{k}$.

The total integrated absorption (neglecting anharmonicities) corresponding to a transition from the $(n-1)$th to the $n$th vibrational energy level is determined by the following approximate relation[15]

$$\alpha_{01}=\frac{\pi\epsilon_F^2 N_T n\exp(-E_{n-1}/kT)}{3\mu c\sum_n^\infty \exp(-E_{n-1}/kT)}[1-\exp(-h\nu_0/kT)]$$

where $\epsilon_F$ represents the effective charge, $N_T$ is the total number of absorbing (or emitting) molecules per unit volume per unit pressure, $\mu$ is the reduced mass, and $\nu_0$ is the frequency of the band center. Since, approximately

$$\frac{\exp(-E_{n-1}/kT)}{\sum_{n=1}^\infty \exp(-E_{n-1}/kT)}=\frac{\exp[-(n-1)h\nu_0/kT]}{\sum_{n=1}^\infty \exp[-(n-1)h\nu_0/kT]}$$

[21] Unpublished absorption measurements on the fundamental of CO at pressures up to 800 p.s.i. and at room temperature have led to experimental results which are described by Eq. (4). Details concerning this work will be published elsewhere.

it follows that

$$\alpha_{01}=\pi\epsilon_F^2 N_T/3\mu c. \tag{19}$$

Relations similar to Eq. (19) can be derived readily for diatomic molecules with $Q$ branch and also for polyatomic molecules.[22] Equation (15) may be written, in terms of the effective charge, as follows:

$$\bar{k}_F=\frac{N_T\pi\epsilon_F^2}{3\mu c}\frac{1}{\Delta\nu_{n\to n+1}}. \tag{20}$$

Since $N_T$ varies inversely as the temperature, i.e., for an ideal gas

$$N_T=\frac{7.34\times10^{21}}{T}\ \text{molecules/cc}\times\text{atmos}. \tag{21}$$

it follows that

$$\frac{\bar{k}_F(T_1)}{\bar{k}_F(T_2)}=\frac{T_2}{T_1}\frac{\Delta\nu_{n\to n+1}(T_2)}{\Delta\nu_{n\to n+1}(T_1)}, \tag{22}$$

$$\frac{\bar{k}_{F.O.}(T_1)}{\bar{k}_{F.O.}(T_2)}=\frac{T_2}{T_1}\frac{\Delta\nu_{n\to n+2}(T_2)}{\Delta\nu_{n\to n+2}(T_1)}, \tag{23}$$

etc. Thus the average absorption coefficient at any desired temperature can be estimated from available room temperature measurements by the use of Eqs. (22) and (23).

### C. Critique of the Approximate Method for Emissivity Calculations

The principal virtue of the suggested procedure for emissivity calculations is the result of the fact that semiquantitative information regarding gaseous emissivities at elevated total pressures can be obtained by very simple calculations without requiring more than highly approximate values for the integrated absorption. Thus the integrated absorption for the fundamental vibration-rotation bands is generally so high that for total pressures of several hundred p.s.i. or more the fundamental will act practically as a blackbody at relatively low partial pressures of absorber. At elevated temperatures somewhat larger partial pressures of absorber will be required because of an increase in the effective band width with temperature. As the result of rapid saturation for absorption and emission from the fundamental, calculated emissivities tend to be relatively insensitive to the numerical values of the average absorption coeficients, at least as far as emission from the fundamental is concerned. The contributions from the first overtone to radiant heat transfer do not become important until very high partial pressures of absorber and relatively high temperatures have been reached.

Although emissivity calculations are relatively insensitive to the numerical values of the average absorption coefficient, they depend strongly on the numerical value of the effective band width. It is indeed

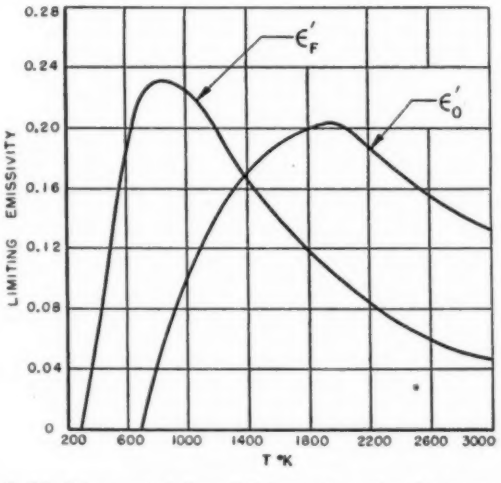


FIG. 3. Limiting emissivity of HI as a function of temperature.

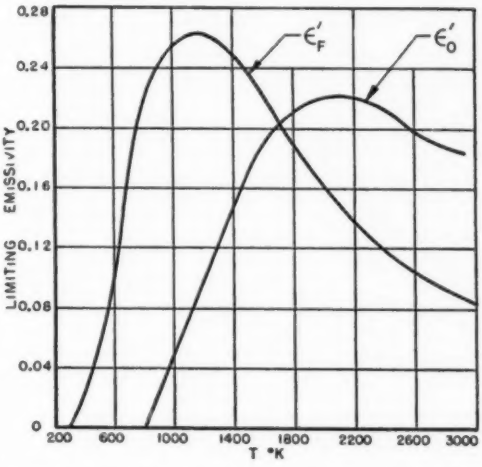


FIG. 4. Limiting emissivity of HBr as a function of temperature.

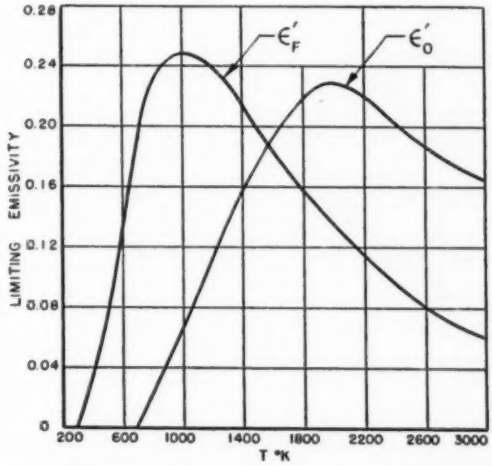


FIG. 5. Limiting emissivity of HCl as a function of temperature.

[22] M. W. Wolkenstein, J. Phys. USSR **5**, 185 (1941); A. M. Thorndike, A. J. Wells, and E. B. Wilson, Jr., J. Chem. Phys. **15**, 157 (1947); A. M. Thorndike, J. Chem. Phys. **15**, 868 (1947).

fortunate that the effective band width does not vary rapidly with the pressure of absorbing gas.[16] This conclusion follows most obviously from an examination of the term $\exp(-P_e pl)$. The exponent is seen to be proportional to the optical density $(pl)$ but changes with rotational quantum number as $j\exp(-E_{o,j}/kT)$. Since the effective band width is relatively insensitive to optical density, we are justified in concluding that curves of the limiting emissivity as a function of temperature for the fundamental vibration-rotation band, of the type shown in Fig. 2 for CO, represent a valuable indication of the semiquantitative variation of emissivity with temperature over a wide range of partial pressures of absorber at elevated total pressure and constant path length. As the partial pressure of the absorber is increased, the expected emissivity will exceed the limiting emissivity of the fundamental by roughly the amount contributed by the second term on the right-hand side of Eq. (11).

## IV. APPLICATION TO DIATOMIC MOLECULES

The spectral emissivity for a number of diatomic gases can be determined, approximately, from available experimental data on integrated absorption by utilizing the method for calculating emissivities outlined in Section III-B. It should be noted that approximate heat-transfer calculations by the method proposed in this report will, in general, become less accurate as the rotational spacing increases. For example, emissivity calculations for HF (rotational spacing $\simeq 40$ $cm^{-1}$) will be considerably less reliable than for CO (rotational spacing $\simeq 4$ $cm^{-1}$) at a pressure of a few hundred pounds per square inch, because of inadequate overlapping of the rotational lines of HF. Since considerable uncertainty exists regarding the numerical value of the integrated absorption and of the corresponding effective charge, we shall present here only a tentative compilation of experimental data without extensive emissivity calculations. More reliable values for the integrated absorption should become available as the result of current measurements on diatomic molecules.[23]

### A. Effective Band Widths for Diatomic Molecules at Different Temperatures

The results of effective band width calculations for CO have been presented in Tables I and II. Similar data for HI, HBr, HCl, and HF are given in Tables III to X.

It is a simple matter to calculate the ratios

$$\epsilon_F' = \left\{ \sum_n \int_{\Delta\nu_{n\to n+1}} \rho(\nu)d\nu \right\} \Big/ \int_0^\infty \rho(\nu)d\nu$$

and

$$\epsilon_0' = \left\{ \sum_n \int_{\Delta\nu_{n\to n+2}} \rho(\nu)d\nu \right\} \Big/ \int_0^\infty \rho(\nu)d\nu$$

by use of the effective band widths listed in Tables I to X. The results of these calculations for CO have been plotted in Fig. 2 and were discussed earlier in this paper. Limiting emissivities for the hydrogen halides obtained in this manner are shown in Figs. 3 to 6.

### B. Effective Charges of Diatomic Molecules

The integrated absorption for the fundamental and the first overtone of CO was measured by a novel indirect method by Matheson in 1932.[24] He reported the values

$\alpha_{01} = 1.182\times10^{13}$ (cm-atmos.)$^{-1}$ sec.$^{-1}$ at 300°K,
$\alpha_{02} = 1.54\times10^{11}$ (cm-atmos.)$^{-1}$ sec.$^{-1}$ at 300°K.

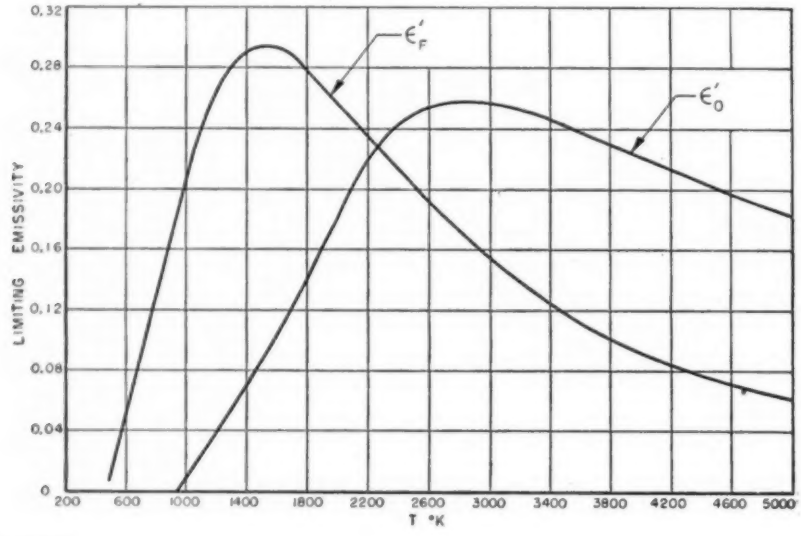


FIG. 6. Limiting emissivity of HF as a function of temperature.

[23] S. S. Penner and D. Weber (to be published).
[24] L. A. Matheson, Phys. Rev. **40**, 813 (1932).

From the value of $\alpha_{01}$ it is seen that the effective charge of CO is $\epsilon_F = 3.9 \times 10^{-10}$ e.s.u.

The effective charges $\epsilon_F$ for three of the hydrogen halides have been determined by Bartholomé.[25] This work has been criticized by Kemble[26] because of lack of adequate spectral resolution used in making absorption measurements. In this connection it should also be noted that the value for the integrated absorption of HCl reported by Bartholomé is considerably smaller than the corresponding value observed by Bourgin some years earlier,[27] which was later shown to be in agreement with the value of the effective charge calculated from infrared dispersion measurements.[28]

For HI, HBr, and HCl Bartholomé[25] reported effective charges of $0.033e$, $0.075e$, and $0.086e$, respectively, where $e$ is the charge of an electron. In order to estimate $\epsilon_F$ for HF, it was decided to extrapolate the values for the other hydrogen halides by plotting $\epsilon_F/e$ as a function of the electric moment $\mu'$ divided by the normal interatomic distance $r_0$ of the hydrogen halides.[29] The electric moment $\mu'$ for monomeric HF has been reported as $1.91 \times 10^{-18}$ e.s.u.[30] A plot of $\epsilon_F/e$ as a function of $\mu'/r_0$ was found to lead to the result $\epsilon_F \simeq 0.11e$ for HF. According to the measurements of Bourgin[27] and Rollefson and Rollefson[28] it appears likely that these values for the effective charges are too small. As an approximate correction, multiplication by the factor (1/0.42) of all the effective charge values of the hydrogen halides is suggested. The correction factor (1/0.42) represents the ratio of the effective charge of HCl reported by Rollefson and Rollefson[28] to the effective charge of HCl observed by Bartholomé.[25]

Reliable experimental values of the integrated absorption for the first overtone for the hydrogen halides are not available. For this reason it is suggested to calculate $\bar{k}_0$ directly by use of a theoretical relation derived by Rosenthal[31] which can be shown to lead to the relation

$$\frac{k_0}{\bar{k}_F} = \frac{x_e(1-5x_e)}{(1-3x_e)^2}, \tag{24}$$

where $x_e$ is the anharmonicity constant for the molecule under discussion. Equation (24) gives a lower limit for the average absorption coefficient $\bar{k}_0$ since the derivation of this relation includes only contributions to the intensity of the first overtone resulting from the first term in the expansion of the electric moment in terms of internuclear distance. The calculated lower limit for the intensity of the overtones represents a reasonably good approximation to the true intensity in some cases. This assertion has been verified for HCl by comparison with measured intensity ratios.[31] The ratio $x_e(1-5x_e)/(1-3x_e)^2$ is seen to be somewhat smaller than the integrated intensity ratio of overtone to fundamental for CO, using Matheson's data.[24]

### C. Application to Emissivity Calculations

The results listed in Tables I to X, together with the quantitative absorption measurements summarized in Section IV-B, provide the data necessary for approximate emissivity calculations at elevated total pressures. Because of the uncertainty in the quantitative absorption measurements, we shall not present extensive emissivity tables at this time but rather illustrate the method of calculation by a representative example.

It is desired to determine the emissivity of HF at 3000°K when the gas is uniformly distributed through a radiation path length $l$ of 10 cm and the partial pressure of undissociation HF is 15 atm.[32] The total pressure is 25 atm.

From the data given in Section IV-B the average absorption coefficients are found to be $\bar{k}_F = 2.41 \times 10^{-3} \times (1/0.42)^2 = 13.7 \times 10^{-3}$ (cm×atmos.)$^{-1}$ and $\bar{k}_0 = 4.64 \times 10^{-5} \times (1/0.42)^2 = 26.3 \times 10^{-5}$ (cm×atmos.)$^{-1}$, respectively. Using the limiting emissivity plots of Fig. 6 we find for the upper limits of the emissivities of the fundamental and the first overtone the values 0.155 and 0.256, respectively. Hence the emissivity $\epsilon'$ is

$$\epsilon' = [1-\exp(-13.7\times10^{-3}\times15\times10)]0.155 + [1-\exp(-26.3\times10^{-5}\times15\times10)]\times0.256 = 0.144.$$

The author takes pleasure in expressing his appreciation for many stimulating discussions to Dr. Martin Summerfield, who initiated the program of the calculation of gaseous emissivities from spectroscopic data. The numerical calculations were performed by the computing group of the Jet Propulsion Laboratory under the supervision of Mrs. Macie Roberts.

[25] E. Bartholomé, Zeits. f. Physik **B23**, 131 (1933).
[26] E. C. Kemble, J. Chem. Phys. **3**, 316 (1935).
[27] D. G. Bourgin, Phys. Rev. **29**, 794 (1927).
[28] R. Rollefson and A. H. Rollefson, Phys. Rev. **48**, 779 (1935).
[29] This extrapolation of observed values of $\epsilon_F$ for HCl, HBr, and HI to yield the effective charge $\epsilon_F$ for HF is based on the relation $\epsilon_F = (d\mu'/dr)_{r=r_0} \simeq 3\mu'/r_0$ which, although apparently not valid for the hydrogen halides, may give a reasonable relation for the change of $\epsilon_F$ with $\mu'/r_0$. The effective charge of HF will be measured in the near future. The effect of association of HF on emissivity has been neglected since association would not be expected to be of importance at elevated temperatures.
[30] N. B. Hannay and C. P. Smyth, J. Am. Chem. Soc. **68**, 171 (1946).
[31] J. E. Rosenthal, Proc. Nat. Acad. Sci. **21**, 281 (1935).
[32] It should be noted that $p$ always refers to the partial pressure of the undissociated emitter since the atomic species H, C, O, I, Br, Cl, and F do not radiate in the infra-red and therefore do not make an appreciable contribution to radiant heat transfer at temperatures below about 5000°K.

# X-Ray Measurement of Long Range Order in β-Brass*

D. Chipman and B. E. Warren
*Massachusetts Institute of Technology, Cambridge, Massachusetts*
(Received February 6, 1950)

The long range order in β-Brass has been determined by measuring the integrated intensity of the (100) superstructure reflection from a single crystal held at various temperatures. With a single crystal, and CuKα-radiation obtained by a balanced Ni-Co filter, there is ample intensity for measurement with a Geiger counter spectrometer. The measured long range order parameter $S$ is in satisfactory agreement with the theoretical predictions.

## I. INTRODUCTION

THE β-Brass phase exists at about the composition CuZn. There is a critical temperature of approximately 465°C, above which the structure is disordered body-centered cubic, and below which it is an ordered CsCl structure. In a perfectly ordered $AB$ structure, the $A$ atoms are at α-sites and the $B$ atoms at β-sites. In a structure with partial long range order, if $r_\alpha$ represents the fraction of α sites rightly occupied by an $A$ atom, the Bragg and Williams[1] long range order parameter is given by $S=2r_\alpha-1$. For perfect order $S=1.0$ and for complete disorder $S=0.0$. For an $AB$ structure with partial long range order, the structure factor is given by

$$F=[f_B r_\beta+f_A(1-r_\beta)]+[f_A r_\alpha+f_B(1-r_\alpha)] \times\exp[\pi i(h+k+l)].$$

For the superstructure reflections $h+k+l=$ odd

$$F=(f_B-f_A)(2r_\alpha-1)=(f_B-f_A)S. \qquad (1)$$

The integrated intensity is proportional to $F^2$, and hence a measurement of the integrated intensity of a superstructure reflection gives directly the square of the long range order parameter.

Since $(f_{Zn}-f_{Cu})$ is small, superstructure lines on a powder pattern of β-Brass are extremely weak. The difference in scattering factors has been increased by the use of ZnKα-radiation[2] and it can be further enhanced by the use of crystal monochromated CuKβ-radiation. However, by using a single crystal of β-Brass, the (100) reflection is strong enough to be readily measured. In general, with crystal monochromated radiation there will be a half-λ from the continuous spectrum reflected from (200) of the sample and superimposed on the (100) peak. This can be eliminated by using (111) of fluorite as the monochromator. We have used CuKα-radiation with a balanced Ni-Co filter and the tube run at 15 kv constant potential. This eliminated half-λ-difficulties and gave ample intensity for the measurements.

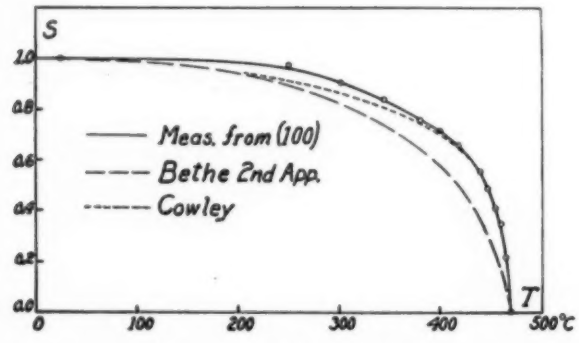


FIG. 1. Measured values of the long range order parameter for β-Brass compared with theoretical values.

## II. MEASUREMENT OF LONG RANGE ORDER IN β-BRASS

The single crystal of β-Brass was cut parallel to a (100) face and polished and etched. It was mounted in a small furnace provided with a Ni foil window for the primary and diffracted beams. A slow stream of nitrogen was used to prevent oxidation. The temperature was measured by a thermocouple fastened to the back of the crystal. The crystal was mounted at the center of a Geiger counter spectrometer. With a wide counter slit and fixed position of the counter, rocking curves were made plotting intensity as a function of crystal angle.

The long range order at room temperature was measured by comparing the integrated intensities of (100) β-Brass and (600) NaCl.

$$A_{CuZn}\left[\frac{F^2(L\cdot P)e^{-2M}}{\mu v_a^2}\right]_{NaCl} = A_{NaCl}\left[\frac{F^2(L\cdot P)e^{-2M}}{\mu v_a^2}\right]_{CuZn}, \qquad (2)$$

where $A$ is the measured rocking curve area, $F$ is the structure factor, $(L.P.)$ is the Lorentz-polarization factor, $e^{-2M}$ is the temperature factor, $\mu$ is the linear absorption factor, and $v_a$ is the unit cell volume. The Hönl correction[3] was applied to the scattering factors. From (2) we obtain $F$ for β-Brass in absolute units, and using (1) we get directly the long-range order parameter $S$. The value obtained was $S=1.08$. This value has been interpreted as meaning that within the

* Research sponsored by the ONR under Contract N5-ori-07832.
[1] W. L. Bragg and E. J. Williams, Proc. Roy. Soc. **145**, 699 (1934).
[2] F. W. Jones and C. Sykes, Proc. Roy. Soc. **161**, 440 (1937).
[3] R. W. James, *The Optical Principles of the Diffraction of X-Rays* (G. Bell and Sons, London, 1948), p. 608.

experimental error the long range order in $\beta$-Brass at room temperature is essentially perfect.

To measure long range order as a function of temperature, the crystal of $\beta$-Brass was held at a series of temperatures up to and above $T_c=465°C$. A rocking curve was made at each temperature. The rocking curve areas, corrected for a temperature factor $e^{-2M}$, are proportional to $S^2$. Normalizing the areas to make $S=1.00$ at room temperature, the values of $S$ shown in Fig. 1 were obtained. The measured values of $S$ are compared with the theoretical curves of Bethe[4] and Cowley.[5] The Cowley curve is a plot of the equation

$$\ln(1+S^2/1-S^2)=2S^2(T_c/T), \tag{3}$$

using $T_c=738°K$. There is qualitative agreement with either curve. The quantitative agreement with the Cowley curve is probably within the experimental error.

## III. ANTIPHASE DOMAINS IN β-BRASS

If antiphase domains in an ordered structure are small enough, they show up by a broadening of the superstructure lines. Although antiphase domains are to be expected in ordered $Cu_3Au$, the structure of ordered CuZn is such that they are not to be expected. However, it was thought worth while making a set of line breadth measurements to test the point. The counter slit was made very narrow and the counter set at a series of positions to plot out the diffraction peak. At each position of the counter, the crystal was turned at constant velocity through the reflecting range, and the total count recorded. The peak breadth obtained in this way is independent of any mosaic structure in the crystal.

Two samples were prepared; one cooled from above $T_c$ to room temperature in five hours, and the other quenched from 500°C into brine. Both samples were then polished and etched, and peaks plotted out for the (100) reflection. Within experimental error the two breadths were the same—about 11 min. in $2\theta$. Although a measurement of the breadth of the (100) peak is not a sensitive test for antiphase domains, the results indicate that there is no prominent antiphase structure in $\beta$-Brass.

## IV. EFFECT OF ANTIPHASE DOMAINS ON THE INTEGRATED INTENSITY OF A SUPERSTRUCTURE LINE

It is important in the determination of the long range order parameter that the integrated intensity of a superstructure reflection is independent of the existence of antiphase domains.

Imagine the ordered crystal to be divided into blocks $N_1a_1$, $N_2a_2$, $N_3a_3$, where $N_1$, $N_2$, $N_3$ are numbers of the order 10–20. Cells within a block are numbered $m_1m_2m_3$ and the blocks are numbered $n_1n_2n_3$. To allow for any system of antiphase domains or displacements within the crystal we assign an arbitrary phase $\varphi_{n_1n_2n_3}$ to the amplitude from each block. The amplitude of diffracted radiation from the crystal is then

$$\begin{aligned}\text{Amp}=F\sum_m \exp[(2\pi i/\lambda)(s-s_0)\cdot(m_1a_1+m_2a_2+m_3a_3)]\\ \times\sum_n \exp[i\varphi_n]\exp[(2\pi i/\lambda)(s-s_0)\\ \cdot(n_1N_1a_1+n_2N_2a_2+n_3N_3a_3)],\end{aligned}$$

where $F$ is the structure factor per cell and $s$, $s_0$ are unit vectors giving the directions of the diffracted and primary beams. Let

$$s-s_0=\lambda(h_1b_1+h_2b_2+h_3b_3),$$

where $b_1b_2b_3$ are the reciprocal vectors and $h_1h_2h_3$ are continuous variables. The intensity from the crystal is then

$$\begin{aligned}I(h_1h_2h_3)=F^2\sum_m\sum_{m'}\exp[2\pi i\{h_1(m_1-m_1')\\ +h_2(m_2-m_2')+h_3(m_3-m_3')\}]\\ \times\{N_B+\sum_{\substack{n\ n'\\ n\neq n'}}\sum'\exp[i(\varphi_n-\varphi_{n'})]\\ \times\exp[2\pi i\{h_1N_1(n_1-n_1')+h_2N_2(n_2-n_2')\\ +h_3N_3(n_3-n_3')\}]\}\end{aligned} \tag{4}$$

where $N_B$ is the number of blocks in the crystal.

The measured integrated intensity of a reflection is proportional to an integral of the interference function throughout a sufficient region in reciprocal space about the point *hkl* to include everything contributing to the *hkl* reflection.

$$P=K\int\int\int I(h_1h_2h_3)dh_1dh_2dh_3. \tag{5}$$

Substituting (4) in (5) and considering a term $n\neq n'$

$$\begin{aligned}\int_{h-\frac{1}{2}}^{h+\frac{1}{2}}\exp[2\pi ih_1\{(m_1-m_1')+N_1(n_1-n_1')\}]dh_1\\ =\exp[2\pi ih\{(m_1-m_1')+N_1(n_1-n_1')\}]\\ \times\frac{\sin\pi\{(m_1-m_1')+N_1(n_1-n_1')\}}{\pi\{(m_1-m_1')+N_1(n_1-n_1')\}}.\end{aligned}$$

The integrals are zero for all terms where $n\neq n'$ and

$$\begin{aligned}P=KF^2N_B\int\int\int\sum_m\sum_{m'}\exp[2\pi i\{h_1(m_1-m_1')\\ +h_2(m_2-m_2')+h_3(m_3-m_3')\}]dh_1dh_2dh_3.\end{aligned}$$

The measured integrated intensity is the number of blocks $N_B$ times the integrated intensity from each block and independent of the arbitrary phases $\varphi_n$. Hence a measurement of the long range order parameter $S$ from the integrated intensity of a superstructure reflection is independent of whether or not antiphase domains exist in the ordered structure.

[4] H. Bethe, Proc. Roy. Soc. **150**, 552 (1935).
[5] J. M. Cowley, Phys. Rev. **77**, 667–675 (1950).

# The Resolving Power of an X-Ray Microscope

EDWARD PRINCE*
*General Electric Research Laboratory*
(Received February 10, 1950)

A formula for determining the resolving power of an x-ray microscope built according to the design suggested by Kirkpatrick and Baez is derived, and an estimate of that resolving power given. The optimum resolving power is such as to resolve points separated by a distance of the order of 2000A.

## INTRODUCTION

PAUL Kirkpatrick and A. V. Baez[1] have described a method of forming optical images with x-rays, making use of the total reflection at grazing incidence. The x-rays are reflected from two cylindrical mirrors in such a way that one mirror brings all horizontal lines to a focus, and the other brings all vertical lines to a focus. On the basis of diffraction theory, Kirkpatrick and Baez set the limit of resolution of such a system at about 70A, assuming perfect geometrical focusing and unit magnification. Since perfect focusing with mirrors is a condition which may be achieved only for infinitesimally small objects, these assumptions are not directly applicable to the analysis of an actual x-ray microscope built according to this design, and it is, therefore, desirable to make an estimate of the optimum conditions in a practical instrument, taking into consideration both the geometrical and the diffraction effects at the same time.

## MATHEMATICAL ANALYSIS

In order to evaluate the combined effects of geometrical aberration and diffraction, let us first derive an applicable formula for each in turn. The effect of diffraction can be determined easily from the usual

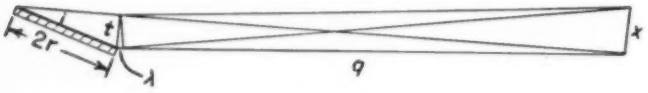


FIG. 1.

formula (see Fig. 1):

$$x=(\lambda q)/t \tag{1}$$

where $x$ is the separation of two resolved spots in the image; $t$ is the width of the aperture; $q$ is the distance from the aperture to the image; and $\lambda$ is the wavelength. Let $y$ be the resolution, $p$ the distance from the object to the aperture, and $2r$ the width of the mirror. The resolution is then:

$$y=(xp)/q \quad \text{or} \quad y=(\lambda p)/t. \tag{2}$$

If $i$ is the critical glancing angle, and is small, so that $\sin i=i$, then the resolution due to diffraction is given by:

$$t=2ri, \quad y=(\lambda p/2ri). \tag{3}$$

It is now necessary to find an expression for the resolution in terms of the geometrical aberrations. This is difficult, because it is dependent on the distribution of intensity around the focus, but the distance by which the extreme ray misses the focus gives a sufficient condition which probably does not differ from the necessary condition by more than a factor of 2 or 3. Kirkpatrick and Baez evaluate this quantity for a circular section:

$$y=\tfrac{3}{2}(r^2/R) \tag{4}$$

where $R$ is the radius of curvature and $R\gg r$. A minimum value of $y$ may be obtained by equating expressions 3 and 4, giving:

$$\frac{\lambda p}{2ri}=\frac{3r^2}{2R}, \quad r=\left(\frac{\lambda pR}{3i}\right)^{\frac{1}{3}} \tag{5}$$

or

$$y=\left(\frac{3\lambda^2 p^2}{8Ri^2}\right)^{\frac{1}{3}}. \tag{6}$$

## CONCLUSION

If $p=10$ cm $R=20$ m and $i$ is the value used by Kirkpatrick and Baez, $i=7\times10^5\lambda$, then $y$ is equal to about 3400A. By the use of different curves and with skillful operation, it is probable that this figure can be reduced by a factor of 2, and possibly by as much as a factor of 4, but it is highly doubtful that the limit can be reduced much more than that in a practical instrument with reasonable magnification. This makes the x-ray microscope potentially an instrument with resolution between that of the ordinary optical microscope and that of the electron microscope, with an advantage of high penetrating power.

The author wishes to express his thanks to Dr. David Harker and Miss C. M. Lucht, of the General Electric Research Laboratory, who suggested this investigation.

* Present address: Cavendish Laboratory, Cambridge University, Cambridge, England.

[1] P. Kirkpatrick and A. V. Baez, J. Opt. Soc. **38**, 766 (1948).

# Metallic Evaporation and the Diameter of Tobacco Mosaic Virus with the Electron Microscope*

H. KAHLER AND B. J. LLOYD, JR.
*National Cancer Institute, Bethesda, Maryland*
(Received March 13, 1950)

Tobacco mosaic virus has been used as a known test object for the intercomparison of several methods of small particle measurements, all involving metallic evaporation. Various characteristics of these methods, which determine their accuracy, were investigated. Measurement of groups and the derivation of a mean size therefrom is primarily limited in accuracy only by the exactness of juxtaposition of the successive particles in the group. The measurement of the images of single particles is subject to the relatively large error associated with the uncertainty in the relationship between the true particle edge and the image of the edge which has received a coating of metal. The measurement of shadow lengths reduces this error by the factor $2\tan\alpha/2$. A symmetrical shadow method is described which reduces the error of substrate tilt, and is insensitive to amount of metal deposited. An average over the four best methods gave a value 150.0±3.6A agreeing closely with the x-ray determination.

## INTRODUCTION

ONE of the most important problems in electron microscopy is the measurement of the size of small particles. The percentage errors which arise in such measurements obviously should increase as the size of the particle diminishes down to the resolving power of the instrument. The object of the present investigation was to intercompare several methods of measurement in regards to general accuracy and reliability. Tobacco mosaic virus, TMV, is one of the few small objects which have been extensively studied for size (diameter) and its use as a test object would appear to be satisfactory for the present study. The methods studied all involved the evaporation of metallic films upon the specimen; it was, therefore, necessary to make some supplemental studies upon the relation of metal film to TMV particle.

While this study was under way an inter-laboratory comparison of a much larger particle (polystyrene latex Dow No. 580) was initiated by Gerould[1] following the work of Williams and Backus. Agreement to ±2 percent was obtained by 12 out of 16 laboratories for the mean of the particle size, the value reported by us being 2600±65A, which was within 0.4 percent of the inter-laboratory mean. In certain phases of our work this material was therefore used for determination of magnification power.

## METHOD

The preparation of TMV was put on Formvar films (the Formvar having been cleared of large aggregates by a one hour centrifugation at 20,000×$g$). The different arrangements of components in the vacuum evaporator is illustrated in Fig. 1. Single filament evaporation takes place with the filament at $Y_1$, and double evaporation with filaments at $Y_1$ and $Y_2$. The angle $\alpha$, of evaporation, is 90 degrees with the filament at the position $Y$ (vertical evaporation). When the long axis of the TMV is in the direction $OX$, it is parallel to the evaporation beams from $Y_1$ and $Y_2$, and when in the direction $OZ$ it is perpendicular to the evaporation beam.

The electron microscope was used without an objective aperture. The microscope calibration was done with a 20,000 line/inch diffraction grating replica, coated with chromium, and in some cases with polystyrene latex (Dow No. 580). Low magnification photos (×8000) were made with the unbiased gun and large angle of illumination while high resolving power photos at ×23,000 were taken with the biased gun, compensated objective and an additional fine focusing potentiometer.

### Method I. Group Measurement

It is possible to obtain the metal coated specimen in the form of a horizontal linear array of particles or monomolecular film,[2] which is in some respects a one-dimensional crystal. Measurement across a number of the particles, excluding the extremes of the array, gives

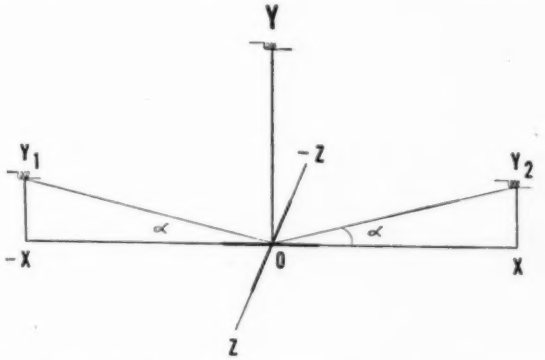


FIG. 1. Sketch of set-up in vacuum evaporator. Filaments at $Y_1$ for single evaporation, at $Y_1$ and $Y_2$ for double evaporation and at $Y$ for vertical evaporation. Long axis of TMV in direction $OX$, evaporation parallel to axis; TMV in direction $OZ$, evaporation perpendicular to TMV axis.

* This paper, in part, was presented at the Toronto meeting of the Electron Microscope Society of America, September 11, 1948.

[1] C. H. Gerould, J. App. Phys. **21**, 71 (1950); **21**, 183 (1950).

[2] R. C. Williams and R. W. G. Wyckoff, Science **101**, 594 (1945).

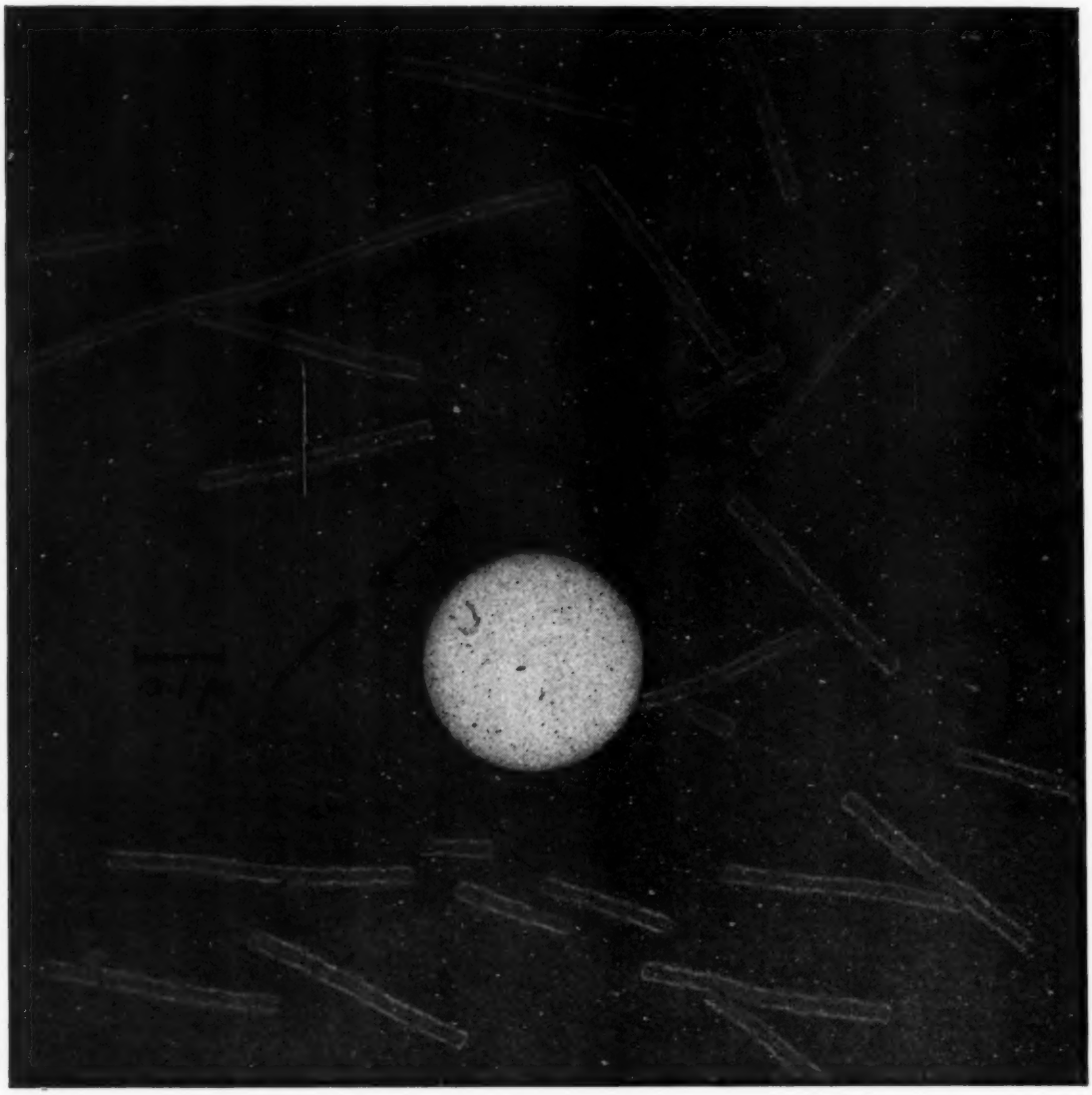

FIG. 2. Light Cr double evaporation 1.5 mg at angle 2 cm to 10 cm each filament. Circle in center of photograph is polystyrene latex, diameter 2600A (unshadowed), which is underfocused as shown by diffraction ring; compensated objective, biased gun. Arrows indicate direction of chromium evaporation beams. Print of positive.

an average particle spacing which is independent of the metal coating and boundary diffraction effects. The chief uncertainty in this procedure is in the unknown juxtaposition of consecutive particles. It was shown by Bernal and Fankuchen[3] that the minimum particle spacing in a TMV gel was 175A, with a hexagonal close packed two-dimensional lattice. When this gel was air dried to a hexagonal crystal the spacing shrank to 152A decreasing to 150A upon vacuum drying over $P_2O_5$ with a high degree of uniformity in size. These authors postulated a water shell on the particles about 10A thick, preventing a closer approach than 175A as long as any free water was present. From this it may be concluded that TMV particles deposited from the aqueous film onto the Formvar screen have a minimum spacing of 175A while still in the wet state. For such a system as the dried monomolecular TMV on the Formvar substrate, the x-ray data gives no direct evidence as to the final packing dimension, though it could be argued that the spacing should be somewhere between 150 and 175A.

*Experimentally*,[4] a value of 152 without an estimate of deviation has been reported, and a value 130±6A was assigned to a related cucumber virus where the 6A refers to deviation between group means $\sigma_M$ rather than individual variation. We have found that the mean for different groups of 8 to 20 TMV particles range in size from 152 to 160A with a standard deviation $\sigma_M$ between groups of 3A and a mean of 155A. The variation in packing and measurement of individual particles

[3] J. C. Bernal and I. Fankuchen, J. Gen. Physiol. **25**, III (1941).

[4] C. A. Knight and G. Oster, Arch. Biochem. **15**, 289 (1947).

$\sigma$ deduced from groups of 10 would obviously be larger as $\sigma=(n-1)^{\frac{1}{2}}\sigma_M=9$A where $n$ is the number of particles per group. From this it would appear that those groups of particles which have the smallest spacing or are packed the closest give nearest to the x-ray measurement for a completely desiccated particle. It also indicates that desiccation on the screen is accompanied by a shrinkage of the group spacing from 175A to a value close to 150A.

A variation of this procedure namely a replication of crystal surfaces should give an even closer correspondence with Bernal and Fankuchen's results.

It appears that the group method gives a mean value whose error is only slightly larger than the usual calibration errors of the electron microscope.

### Method II. Direct Measurement on Doubly Coated Particles

This method consists in evaporating a thin coating of metal, from two oppositely placed filaments, upon opposite edges of the particles, and measuring the distance across the highly magnified image of particles having their long axis perpendicular (*OZ*) Fig. 1 to the metal beam direction.

For the direct measurement of particle diameter, the electron microscope was fitted with a compensated objective to reduce astigmatism[5] and to increase resolving power (estimated to be 20A).

Using the double coating method it was found possible to decrease the amount of evaporated chromium to the point where shadows were scarcely visible but contrast of the particle edges was sufficient for measurements, (Fig. 2). In this photo the apparent widening of the particles is evident as the particles approach a perpendicular direction to the evaporation beam. This widening is more rapid than would be expected on the basis of the amount of metal deposited on the particle. Actually, the particles parallel to the evaporation beams are narrower than the calculated value. In Fig. 3 there is shown a focal series for two particles, one a long aggregated virus rod nearly perpendicular to the direction of the evaporation beams (arrows) and a shorter rod nearly parallel to the beam direction. Figure 3 is reproduced as a print of a negative since previous authors have used such prints in discussing diffraction patterns. As an aid to the estimation of the in-focus position, the diffraction fringes on a polystyrene latex sphere placed on the screen after shadowing were noted (Fig. 2). The magnitude of the out-of-focus position was estimated from the data obtained for displacement of the specimen *versus* objective lens currents after the method of Hillier and Ramberg.[5]

This series is characterized by two minima (black) near each edge of the rods for the overfocused positions and a single minimum near the edge for the underfocused images. The measurement across the diameter

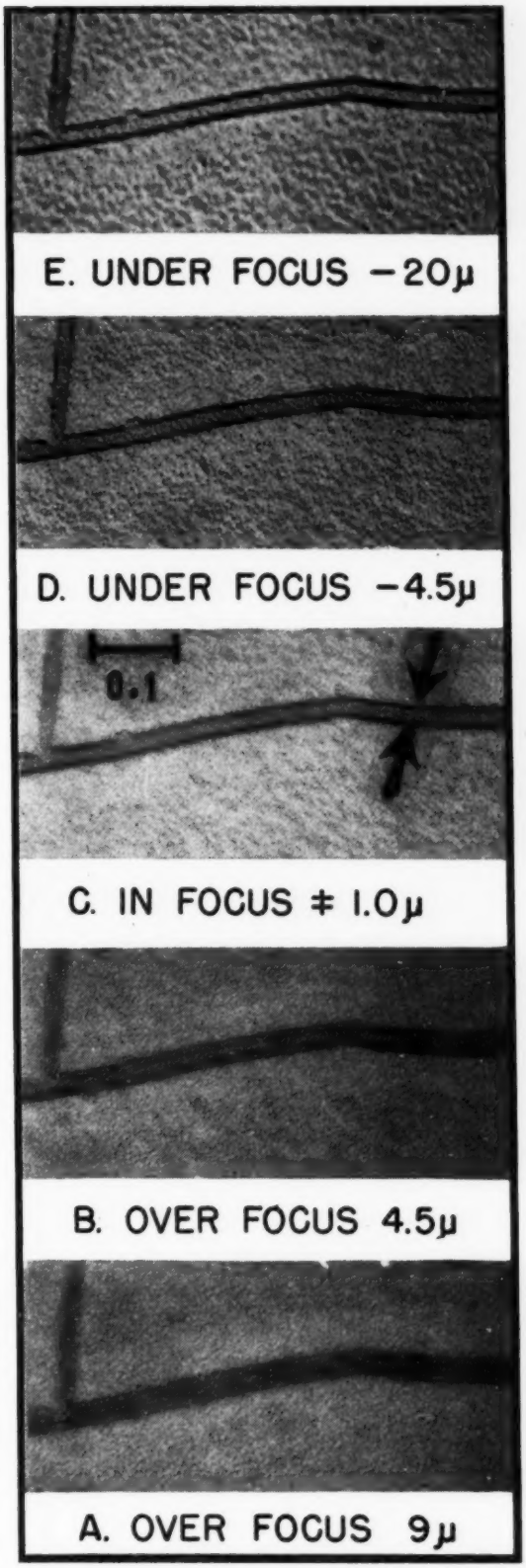


FIG. 3. Focal series of TMV double coated with 2×5.5 mg Cr tan$\alpha$=2/12 biased gun, compensated objective. In-focus position estimated with aid of diffraction pattern of polystyrene latex spheres added to the specimen screen after shadowing (not shown). Direction of evaporation beam shown by arrows. Print of negative.

[5] J. Hillier and E. G. Ramberg, J. App. Phys. **18**, 48 (1947).

of the particles between fringe centers in the three upper pictures ($c, d, e$) is approximately the same (to within $\pm 10$A); in the lower pictures ($a, b$) a similar value is obtained when the measurement is made between the mid-point, (maximum), of each pair of fringes. Thus, over a focal range of $29\mu$, an invariant measurement (to within $\pm 10$A) is obtained between selected points of the edge fringes.

The diffraction minima of the metallic coating cannot be exactly defined in position with respect to the original uncoated particle edge. Part of this uncertainty lies in the variable difference between effective thickness of the metal and its calculated thickness. When a light coating of chromium is deposited on the particle edges in a perpendicular direction, the intensity minima of the slightly underfocused images lie between the middle of the coating and the outer coating edge.

A series of measurements showed that the distance between fringe minima was $10 \pm 20$A larger than the calculated distance between the centers of the metallic coatings.

For other positions of the TMV such as long axis parallel to the evaporation beam the disposition of metal is no longer principally upon the extreme edges so that frequently the images are too narrow. The same holds for vertical evaporation (filament at $Y$ Fig. 1).

### Method III. A Combination of I and II

A light symmetrical coating is deposited as in method II, producing intensity minima near the edge of the particles. Then two particles lying side by side are compared with a single particle close by and parallel in order to eliminate the edge error. For the single particle the measured distance between fringe centers reduced by the magnification factor is,

$$X_1 = D + 2e$$

where $e$ is the amount by which the fringe deviates from the true edge, $D$ is the true diameter.

For the double particle,

$$X_2 = 2D + 2e$$

from which

$$X_2 - X_1 = D.$$

The value obtained by this procedure was $152 \pm 11$A.

The chief precautions to be observed are equality of shadowing and, as in method II, the use of high magnifications.

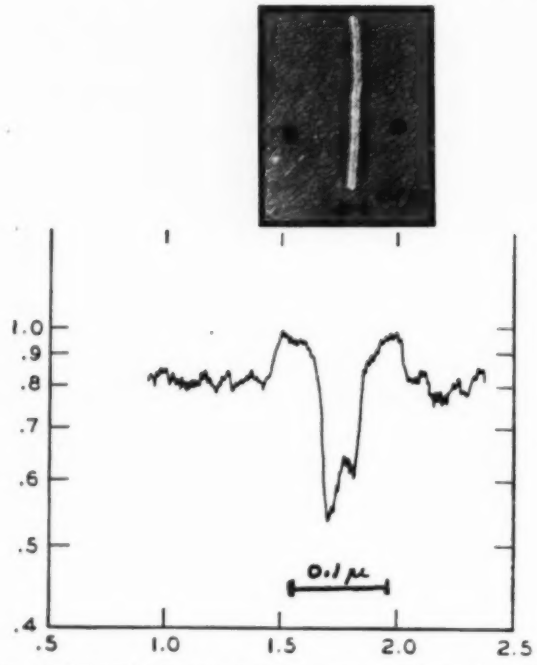


FIG. 4. Microphotometer tracing across a photo of a double shadowed virus particle. Two shadow beams of chromium were unequal, resulting in unequal metallic coatings. Print of a positive. Non-biased gun, low power original.

### Method IV. Direct Measurement Following Single Metallic Coating

Coatings of gold of a series of thicknesses were deposited on the TMV by evaporation from a single filament at an angle of 10 degrees. The measurement was made across the particle. This method has all the faults of the double coating method (II) and in addition, the more serious error which asymmetry introduced into the measurement giving values too erratic to quote.

### Method V. Double Shadows

The set-up for the production of double shadows is identical with that of the double coating procedure (II), with evaporation sources at $Y_1$, $Y_2$. The only difference is in the employment of a larger amount of metal to be evaporated.

A microphotometer tracing (courtesy of W. C. White of these laboratories) of a photograph of a heavily shadowed particle is shown in Fig. 4. In this experiment, more metal was incident on the particle in one direction than in the opposite direction resulting in unequal shadows and a displacement of the central line. Figure 5 illustrates the case where the two metal beams are nearly equal.

One of the sources of error in the single shadow method (VI) described in a following section, is variation in shadow length due to unknown local tilting of the substratum.[6,7] In the double shadow method, this error is considerably diminished, since a tilt in the substrate results in a shortening of one shadow and a lengthening of the other shadow, the two errors partially compensating.

Thus, if the shadowing beam in the evaporator makes an angle $\alpha$ with the horizontal and the substrate is tipped at an angle $\beta$ with the horizontal, $2X$ being the length of the total shadow on the horizontal plane, the length of the shadow on the tilted plane is

$$B_1 + B_2 = X\left[\frac{\sin\alpha}{\sin(\alpha+\beta)} + \frac{\sin\alpha}{\sin(\alpha-\beta)}\right],$$

[6] F. W. Boswell, British J. Exp. Path. **28**, 253 (1947).
[7] R. C. Williams and R. C. Backus, J. App. Phys. **20**, 98 (1949).

where $B_1$ is the short shadow, $B_2$ the long shadow. For $\alpha=10°$ and $\beta=3°$, $B_1$ is 77 percent of $X$, $B_2$ is 142 percent of $X$ while the sum or double shadow length is 110 percent of $2X$.

It is obvious that a simple inspection of a double shadowed photograph will given an estimate of the flatness and angle of the substratum. Such photographs yield fairly consistent values for the particle height

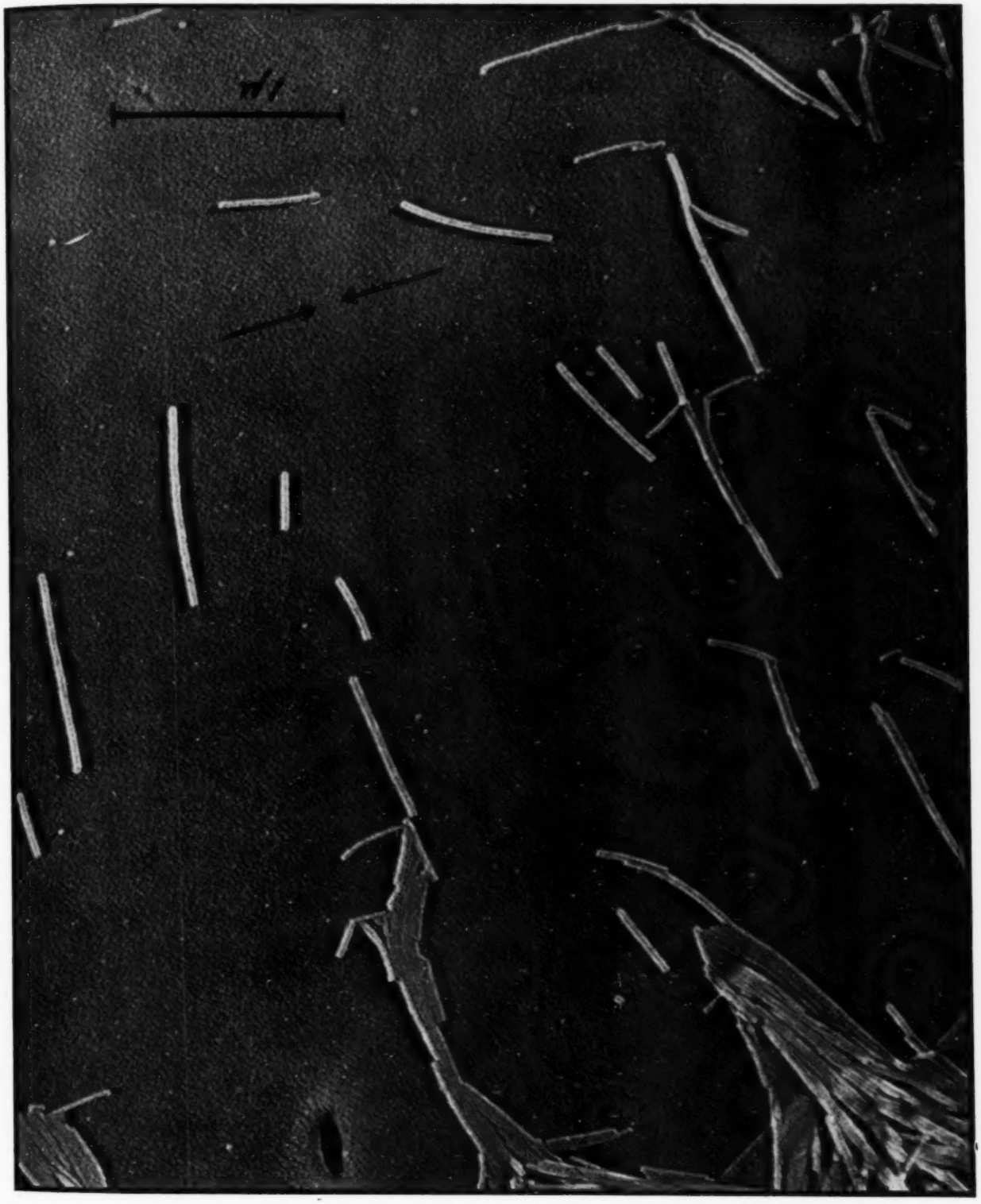

FIG. 5. Heavy Cr double shadows, 7.2 mg Cr at an angle of 2 cm to 8 cm in each evaporation filament, unbiased gun, uncompensated objective. Arrows indicate direction of chromium evaporation beams. Print of a positive.

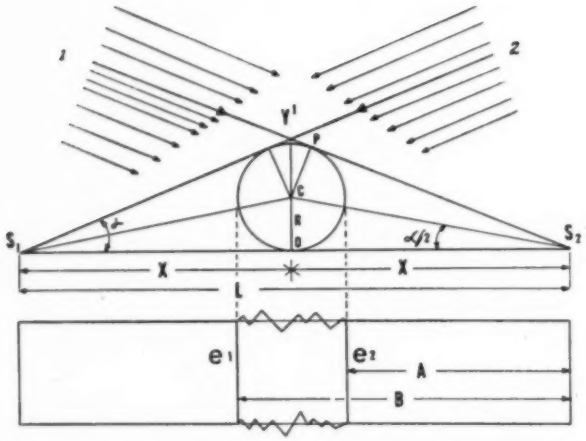


FIG. 6. Diagram of shadowing detail. Single evaporation from filament at 1, shadow measured $A$ or $B$. Double evaporation from 1 and 2, double shadow length is $L$.

from $2R=L/M\tan\alpha/2$ where $R$ is the radius of the particle, $L$ is the double shadow length, $M$ the magnification, $\alpha$ is the angle of evaporation. In all shadow methods the use of $2\tan\alpha/2$ instead of $\tan\alpha$ as is ordinarily done is preferable since from Fig. 6 $X\tan\alpha$ gives $OY'$ whereas $2X\tan\alpha/2$ gives $2R$. The error in using $\tan\alpha$ instead of $2\tan\alpha/2$ for 10° is 1 percent, for 20° is 3 percent, for 30° is 8 percent and for 40° is 15 percent. The increase in the length of shadow due to accumulated metal on the top of the particle will be partially compensated by a shortening of the shadow due to an accumulation of metal on the backbround.

The double shadow method has the disadvantage of a low shadow contrast the metal thickness outside the shadow being twice that inside. In order to obtain the maximum shadow contrast, lower magnifications (8000–10,000) have been more satisfactory than photographs taken at 20–25,000 times.

The Formvar screens for these measurements were precoated with a thin layer of evaporated aluminum in order to prevent any sinking of the particles into the Formvar. Then TMV was put on the aluminum surface. In the evaporator the filaments were straight tungsten wires arranged horizontally with Au and Al[8] in the weight ratio 3.5/1 wrapped around the wires. This was done to obtain an accurate measurement of the evaporation angle. Latex No. 580 was then added to the screens for calibration of magnification. Measurements of the photographs of these specimens gave a value of 145,8±8.2A. This is within the expected errors in magnification and determination of exact shadow boundary.

[8] *International Critical Tables*, Vol. II, p. 402.

This method is therefore comparable in accuracy to group method I and method II.

### Method VI. Single Shadows

Evaporation of metal from filament $I$, Fig. 6, gives a cast shadow[9] from which the diameter, $2R$, of the particle may be estimated either by measurement of distances $A$ or $B$. Since $R=X\tan\alpha/2$, $X=A+R$ and $X=B-R$ by substitution

$$2R=\frac{2A}{M}\frac{\tan\alpha/2}{(I-\tan\alpha/2)}$$

and

$$2R=\frac{2B}{M}\frac{\tan\alpha/2}{(I+\tan\alpha/2)},$$

where $M$ is the magnification. The errors made in estimating $A$ and $B$ are reduced to about 0.2 because of the trigonometric factor with a shadowing angle of 10°. The length $B$ requires a correction for metal thickness at $e_1$; because of the comparatively heavy coatings required by shadowing methods a large fraction of the image appears opaque. The only recourse is to measure to the outer limit of the image and to subtract the full metal thickness to obtain $B$. It may be noted that the circle of confusion errors at the extremities of the $B$ measurement tend to cancel out while for the $A$ measurement they are additive.

The procedure which gave the most consistent results was the use of a system of 3 slits interposed between a line filament and the specimen screens 20 cm away in the evaporator in order to define the angle of evaporation, utilizing gold and the low intensity microscope gun. Measurements on 24 views gave for the $A$ measurement 147.6±13A and for the $B$ measurement 152.2 corrected to 146.2±14A. Despite the insignificant difference between these 2 values, the $B$ measurement seems from other series of tests to be the more reliable of the two.

It may be remarked that the single shadow method gives a hybrid measurement, the shadow region corresponding to height and the remainder of the measurement across the particle being width.

### SUMMARY OF MEASUREMENTS

An average taken over the better methods should reduce the methodical error. The mean of method (I) 155A, (III) 152A, (V) 146A, (VI) 147A, is 150.0±3.6A. This agrees with the mean value obtained by the x-ray method.

[9] H. O. Müller, Kolloid Zeits. 99, 6 (1942).

# The Apparent Size of Objects as Observed in the Electron Microscope*

STANLEY F. KERN AND RAYMOND A. KERN
*Lilly Research Laboratories, Eli Lilly and Company, Indianapolis, Indiana*
(Received March 24, 1950)

The image formed in the electron microscope of shadowed polystyrene latex spheres is larger than the image of unshadowed spheres. This increase in image size and probable causes are discussed. Implications of this phenomena on the study of viruses and other biological specimens are mentioned.

## INTRODUCTION

IN our studies with the electron microscope it has been felt that there is a real difference in the image size of small objects depending upon whether they are shadowed or unshadowed. This difference has been thought by some workers to be accounted for by the increased contrast resulting from the deposition of the metal, together with the actual amount of metal deposited. This has not been a satisfying explanation.

After Williams and Backus[1] announced the remarkable uniformity of particle size of the small spheres in Dow Latex No. 580 *G*, Lot No. 3584, some of this material was obtained to use as a rapid internal check of magnification of the electron microscope. A few preliminary experiments indicated that the size of the image of the latex particle is different for shadowed and unshadowed specimens. Since these particles are remarkably uniform for a given method of sample preparation, it was felt that a study of size changes resulting from shadowing could be undertaken using the styrene particles as a standard specimen.

## EXPERIMENTAL

### Effect of Electron Bombardment

Since the proposed experiments were to involve exposing a specimen to the electron beam for a time longer than usual, and since it is well known that a specimen grows when bombarded,[2–4] it was necessary to ascertain the extent of growth of the Dow Latex particles under conditions of bombardment. In these experiments an early model *B*, RCA electron microscope with an unbiased gun, operating at 60 kv accelerating potential was used. For observation of the specimen a beam current of 250 microamperes was employed with a spot 7 to 10 microns in width, and 15 to 20 microns in length. The findings are summarized as follows:

1. Near the wire of the supporting screen bombardment of the specimen resulted in a rapid growth of the particle. Bombardment for eighteen minutes caused the diameter of the unshadowed balls to increase 570A u. while the shadowed balls had increased 320A u. This may or may not be a significant difference.

2. When observations are confined to the center of the opening the beam does not hit the wire of the supporting screen. Under these conditions bombardment for eighteen minutes resulted in a growth of the particles of about 80 A.° u. In eight minutes no size change could be measured. To more closely approximate the conditions to be expected in later experiments where repeated exposures were to be made, thirty exposures of one unshadowed field were made. No measurable change in size was found until the twenty-fifth exposure. It was concluded, therefore, that ten to fifteen exposures of a field could be made without danger of a measurable particle growth due to electron bombardment, if the field chosen was in the center of an opening.

### Effect of Shadowing

In these studies a mixture of platinum and palladium was used as the shadowing metal. Fifteen milligrams of platinum and five milligrams of palladium were evaporated from a 20-mil tungsten filament placed 8.5 cm from the specimen. In all cases except where indicated

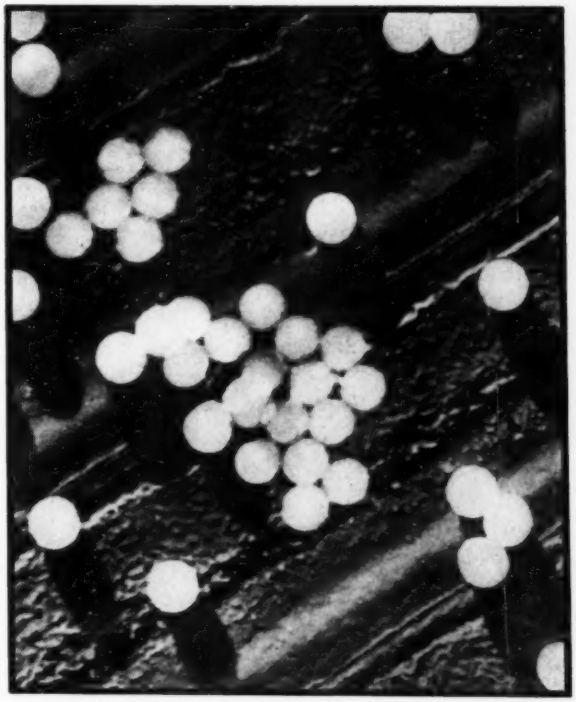

FIG. 1. Shadowed and unshadowed latex particles on the replica of a diffraction grating. 27,000×.

* Presented at the Washington Meeting of the Electron Microscope Society of America October 6–8, 1949.

[1] R. C. Williams and R. C. Backus, J. App. Phys. **20**, 224 (1949).
[2] J.H.L. Watson, J. App. Phys. **18**, 153 (1947) and **19**, 110 (1948).
[3] J. Hillier, J. App. Phys. **19**, 226 (1948).
[4] V. E. Cosslett, J. App. Phys. **18**, 844 (1947).

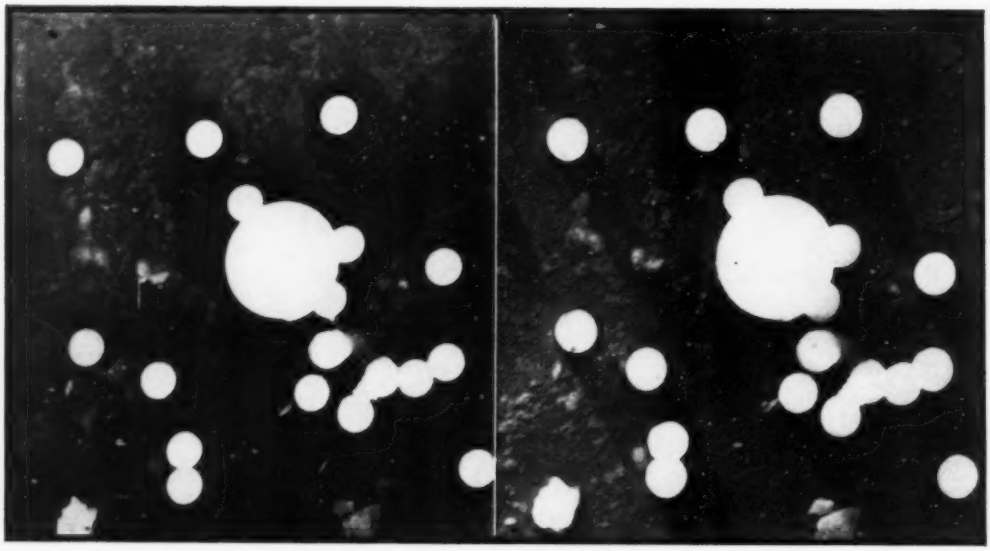

(a) (b)

FIG. 2. (a) Latex particles before shadowing. (b) Same field after shadowing. 21,700×.

the angle of shadowing was 10°. A new filament was used for each experiment. The filament with shadowing metal in place was weighed before and after shadowing. The weight loss of the filament and metal was less than the combined weight of the platinum and palladium. It can be safely estimated, therefore, that a layer of metal 10A u. or less was deposited on a flat portion of the field.

Figure 1 is an electron micrograph showing shadowed and unshadowed polystyrene spheres in the same field. A small drop of the latex was allowed to dry on a replica of a diffraction grating and the sample shadowed. Then a second drop of latex was applied to the screen and allowed to dry. The shadowed balls are easily differentiated from the unshadowed balls and their size difference measured. The unshadowed balls measure 2590A u. ±50A u., whereas the shadowed balls measured 2840A u. ±50A u.

To determine the change of diameter on an individual sphere, micrographs were made of the same field before and after shadowing, Fig. 2. Again the size of the average sphere before shadowing was 2590A u. and after shadowing was 2840A u.

Measurements were made on only those particles which were not in contact with another particle. All measurements on shadowed spheres were made perpendicular to the direction of the shadow.

## DISCUSSION

These results show that the image size changes when the specimen is shadowed and that the amount of change is relatively constant. At this time no definite explanation for the observed facts is offered. However, the following have suggested themselves.

One possible explanation is the deposition of extraneous materials during shadowing and electron bombardment. This possibility appears to be ruled out by our

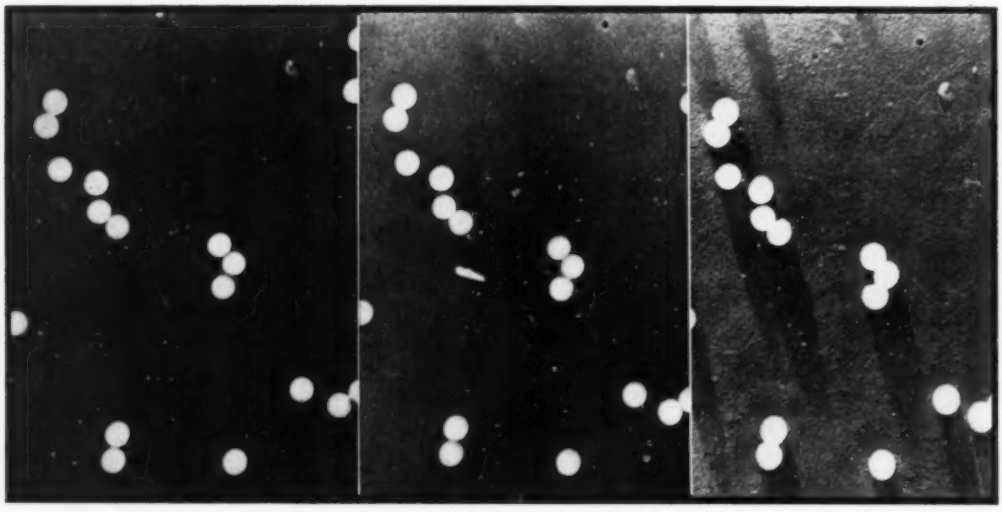

(a) (b) (c)

FIG. 3. (a) Unshadowed latex particles; (b) Same field vertically shadowed; (c) Same field after oblique shadowing. 14,250×.

studies on the effect of electron bombardment on the size of the polystyrene spheres, and, secondly, by the fact that shadowing at a vertical angle does not cause a comparable change in particle size. This experiment will be discussed later. The sharp image obtained also indicates that this is not an over-all deposition of a scattering material.

A second possibility which was considered was the effect of contrast differences resulting from the shadowing. It was felt that possibly the addition of the highly absorbing metal film would materially affect the position of greatest contrast at the edge of the image and would, as a consequence, change its apparent size. Consideration of such a phenomenon shows that this effect could not account for any such large change in particle size.

A third possibility which presents itself is the possibility that a charge differential exists between the polystyrene sphere and its surroundings. If the spherical particle is charged negatively with respect to its surroundings, the potential gradient around the particle would constitute a negative electron lens acting on those electrons passing through and near the particle. Such a lens action would result in the size of the image of the sphere being smaller than would be expected if the sphere were not charged.

Shadowing the specimen at a low angle with a conducting film of platinum-palladium provides an electrical contact which substantially eliminates any charge differential between the particle and its surroundings. This reduces or eliminates the lens effect. The resulting image would be larger.

If this is correct, vertical shadowing of the spheres in such a way that no electrical contact is made between the metal cap on the sphere and the metal deposited on the film should result in no decrease of the charge on the particles, and the image size should be that of unshadowed particles. Figure 3 shows three electron micrographs of the same field—Fig. 3a before shadowing, Fig. 3b after vertical shadowing, and Fig. 3c after oblique shadowing. A just measurable increase in the size of the spheres was found for the vertical shadowed balls. This could be accounted for in that the amount of metal deposited on the ball and film in vertical shadowing was much greater than for oblique shadowing. The obliquely shadowed spheres in Fig. 3c are larger than the unshadowed and vertically shadowed spheres.

It appears that this experiment substantiates the charge theory; and it has been observed, also, that there is a difference in the position of the Fresnel diffraction lines on the shadowed and unshadowed side of a polystyrene sphere for any given setting of the objective lens current. This can be interpreted to mean that the shadowed side and the unshadowed side of the sphere are not brought simultaneously into the best focus.

Close observation of fields having spheres lying partially within the shadows of other spheres (see Fig. 3c) reveals that the portion of the sphere within the shadow of another sphere, and hence not shadowed, has a smaller radius of curvature than the adjoining portion which is shadowed. The sharpness of this effect leads one to believe that whatever the ultimate basic cause of these observations it must be well defined and intimately related to the presence or absence of a continuous film of metal.

FIG. 4. *Streptomyces Griseus* Phage. The size differences between the shadowed and unshadowed phage are more than can be accounted for by the added platinum-palladium. 33,750×.

In spite of these findings it is still possible to use the spheres as a rapid check on calibration as well as for an internal standard of magnification calibration, if one first ascertains the image size to be expected for the condition under which the spheres are used.

The question arises whether objects other than polystyrene latex particles are also subject to this phenomenon. In Fig. 4 is shown one of the phages of *Streptomyces Griseus*. A few are within the shadow of the conidium; and therefore they are not shadowed. Others are outside the shadows and are themselves shadowed. The shadowed bodies are obviously much larger than the unshadowed. This is an indication that the same electron optical condition demonstrated for the polystyrene latex particles also affects the image size of these phage particles. If the present qualitative interpretation of these observations is correct, it is anticipated that this inherent error in apparent size of unshadowed objects in the electron microscope may be very generally encountered.


## ACKNOWLEDGMENT

The authors wish to acknowledge the criticisms and suggestions made by Dr. W. W. Davis during the progress of this work.

# The Current-Hysteresis of the Electrolytic Aluminum-Oxide Rectifier

A. J. Dekker and Helen M. A. Urquhart
*Physics Department, University of British Columbia, Vancouver, British Columbia, Canada**
(Received January 3, 1950)

A hysteresis in the rectification of the contact aluminum-aluminum oxide-electrolytic solution was found by Dekker and van Geel. In the present paper, measurements of the current-voltage characteristics between 1 and 2000 cycles are described. A tentative explanation of the hysteresis is given in terms of a pre-breakdown phenomenon.

## I. INTRODUCTION

When, in a solution of ammonium-borate, an aluminum plate is used as anode and an inert counterelectrode as cathode, the current, for constant applied voltage, decreases with time until only a small current remains flowing.[1] During the decrease of the current an oxide layer is formed on the aluminum. The final thickness of the layer is approximately proportional to the applied voltage (formation voltage) and amounts to about 0.1 micron per 100 volts.[2] During the formation process the current is carried almost completely by ions migrating under the influence of the high electric field in the layer[3] ($10^6-10^7$ volts per cm). The small "leak-current" observed after the formation process has ceased is probably caused by electrons flowing from the solution through the oxide into the aluminum.[2] Because of the high capacity per unit area of these layers, they find application in electrolytic condensers. The so-called "porous-layers" will not be discussed in this paper.[4]

It is well known that the system aluminum-aluminum oxide-electrolyte exhibits rectifying properties: the currents are very small for the aluminum positive (below the formation voltage, of course) with respect to the solution, while for opposite polarity they may be very large. It may be noted in passing that zirconium and tantalium show similar properties. The relation between current and voltage of the system is treated in this paper. In particular the behavior of the rectifier when a.c. voltages are applied will be discussed.

The d.c. current-voltage characteristics have been the subject of many previous investigations.[5] However, the origin of the observed time-effects discussed in Section II below, is not completely understood. Investigations of the a.c. characteristics, mainly at 50 cycles, were started by Dekker and van Geel.[6] These authors found a large hysteresis loop in the forward current (aluminum negative). In the present paper the a.c. characteristics for frequencies ranging from 1–2000 cycles per second will be discussed.

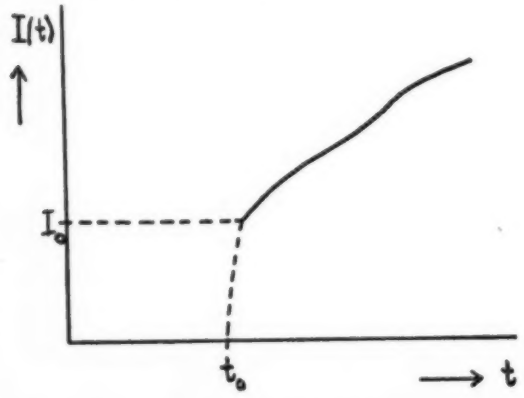


Fig. 1. The current I of an electrolytic rectifier as a function of time, for a d.c. voltage applied in the forward direction at a time $t=t_0$.

## II. D.C. CURRENT-VOLTAGE CHARACTERISTICS

Since the d.c. current-voltage characteristics have a bearing on the behavior of the electrolytic rectifier for a.c. voltages, they will be briefly reviewed. It will be assumed that only voltages below the formation voltage are applied to the rectifier, so that no further oxidation takes place.

Suppose that at time $t=t_0$ a constant voltage $V$ is applied in the forward direction (Al negative). The forward current generated by $V$ is not constant but varies with time (Fig. 1). The current reaches a certain "instantaneous" value $I_0$ by the time a meter responds (approx. one sec.) and then increases slowly but erratically with time. Because no saturation value of the current is reached over a period of several hours, it is possible that during this time chemical changes occur in the layers that lower their resistance. This change of resistance will be referred to as the after effect. What happens between $t=t_0$ and the time when the meter responds will be discussed below (Section VI). The "instantaneous" value $I_0$ introduced above is determined not only by $V$ but also by the "history" of the

* This research was carried out with the aid of a grant from the Defense Research Board at the University of British Columbia. The authors are much indebted to this institution for allowing them to publish this work.

[1] W. Ch. van Geel, Zeits. f. Physik **69**, 765 (1931).

[2] W. Ch. van Geel and H. Emmens, Zeits. f. Physik **87**, 220 (1933).

[3] E. J. W. Verwey, Physica **2**, 1059 (1935).

[4] See W. Ch. van Geel and H. Emmens, Physica **1**, 45 (1934); S. Anderson, J. App. Phys. **15**, 477 (1944); A. J. Dekker and W. Ch. van Geel, Philips Res. Rep. **2**, 313 (1947).

[5] See for instance W. Ch. van Geel, reference 1; A. Günther-schulze and H. Betz, Zeits. f. Elektrochemie **37**, 727 (1931); R. Störmer, Zeits. f. Tech. Physik **16**, 508 (1935).

[6] This research was carried out at the Philips Research Laboratories, Eindhoven, Holland.

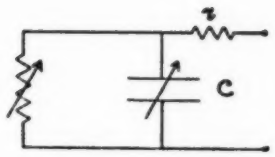


FIG. 2. Equivalent circuit of a rectifier.

rectifier. In general, voltages applied in the forward direction before $t=t_0$ tend to increase the "instantaneous" value, while voltages in the reverse direction tend to decrease it. This effect will be referred to as the hysteresis. For each forward voltage $V$ a set of $I(t)$ curves may be obtained, each curve corresponding to a different "history" of the plate, that is, corresponding to events in the time between $t=-\infty$ and $t=t_0$.

Similar phenomena occur when d.c. voltages are applied in the reverse direction. When for $t<t_0$ a voltage in the forward direction was applied to the rectifier and at $t=t_0$ a voltage $V$ is applied in the reverse direction, the current will reach an "instantaneous" value and then decrease, usually within a few seconds, to a constant value.

It will be clear from the preceding discussion that the d.c. characteristics can be given unambiguously only by specifying the conditions under which they were measured. The most reproducible results are obtained when before each measurement of the "instantaneous" current the rectifier is kept at the formation voltage (in the reverse direction) for a few minutes. The current in either direction is then approximately proportional to the square of the voltage. The rectification ratio, that is, the ratio of the forward and reverse current for the same absolute value of the applied voltage, may be as high as $10^4$ for a plate oxidized at about 300 volts. For the measurements described in this paper, the formation voltage was applied for a few minutes before the photographs of the a.c. characteristics were taken in order to make the initial conditions for each photograph nearly the same.

### III. THE CAPACITY OF THE RECTIFIER

In connection with the method for measuring the a.c. current-voltage characteristics (see Section IV) it is necessary first to point out some features of the equivalent circuit of the electrolytic rectifier.

It is well known that the simplest equivalent circuit for a *dry* rectifier that describes the electric properties of such a metal-insulator-semiconductor contact, consists of a non-linear resistance $R$ shunted by a non-linear capacitance $C$, the two in series with a linear resistance $r$ (Fig. 2). The capacitance $C$ arises from the insulating layer (chemical barrier layer) and a physical barrier layer (Schottky layer) existing in the semiconductor next to the insulator. The effective thickness of the latter depends on the applied voltage and hence leads to a non-linear capacitance. The voltage dependence of $C$ is most pronounced for zero bias voltage. Also, the voltage dependence of $C$ decreases with increasing thickness of the chemical barrier layer.

To investigate to what extent the circuit of Fig. 2 can be applied to the *electrolytic* rectifier, the following experiments were carried out: An aluminum plate which was 50 cm² in area, was oxidized to a formation voltage of 285 volts in a solution of ammonium-borate (sp. res. 490Ω cm). Tinfoil was used as counter electrode. The impedance of the system thus obtained was measured at zero bias voltage for frequencies between 60 and 15,000 c.p.s. The measurements were carried out by using a General Radio 716-*B* capacitance bridge and a General Radio 608-*A* oscillator. The output of the oscillator was so adjusted that the effective voltage across the rectifier was 0.5 volt. The results obtained could be accounted for over the whole frequency range by the circuit of Fig. 2 with the following numerical values: $C=1.65$ μf, $R=10^5\Omega$ and $r=23\Omega$.

The impedance of the rectifier was also measured with different bias voltages in the reverse direction. No changes in the capacitance could be detected. Similar measurements with bias voltages in the forward direction are practically impossible as a consequence of the after effect mentioned in the previous section. There is no reason to believe, however, that the capacitance

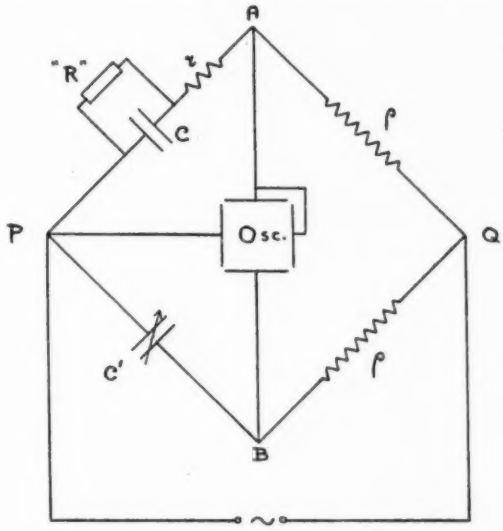


FIG. 3. Circuit for measuring the a.c. current-voltage characteristics.

would be different for voltages in the forward direction and therefore the capacitance will be treated as a constant in the following sections.

### IV. METHOD FOR MEASURING THE A.C. CHARACTERISTICS

The a.c. current-voltage characteristics of *dry* rectifiers are usually obtained by putting a known resistance $\rho$ in series. The voltage across $\rho$ gives the current through the system and may be applied to the vertical deflection plates of an oscillograph. Using the voltage across the rectifier as the time base in the horizontal direction, the current-voltage characteristic may be readily observed.

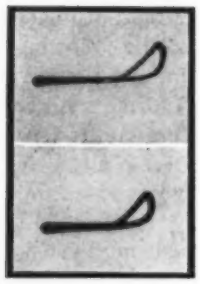

FIG. 4. Current-voltage characteristics at 2 (below) and 3 (top) cycles. Current vertical, voltage horizontal.

As a consequence of the presence of the capacitance $C$ in the equivalent circuit (Fig. 2), however, $C\omega$ may become comparable with $1/R$ at high frequencies and the characteristic will then be distorted, especially in the reverse direction. The frequencies where this occurs are sometimes very high, for instance for germanium point-rectifiers (microwave region), whereas in other cases this region may lie in considerably lower ranges. It may be noted that Lehovec[7] has pointed out that this distortion in the reverse direction may be used to determine the capacitance of a rectifier.

For the *electrolytic* rectifier considered here, distortion due to the capacitance becomes noticeable at frequencies as low as 10 c.p.s., as may easily be verified from the numerical values of $C$ and $R$ given in the preceding section. In this section a method to compensate for this effect, suggested by Dekker and van Geel, will be discussed.

In branch $PAQ$ of the bridge in Fig. 3, the rectifier is represented by a constant capacitance $C$, shunted by a rectifying element "$R$" the nature of which is the subject of the present investigation, the two in series with the resistance $r$ of the electrolyte. It should be noted that, because of the observed hysteresis (Section VI), the element "$R$" cannot be represented by a non-linear resistance only. Suppose then that an a.c. voltage $V_0e^{j\omega t}$ is applied between $P$ and $Q$. The current $I(t)$ flowing through "$R$" is some periodic function of time, depending on the input voltage, and may be developed in a Fourier series

$$I(t)=\sum_n I_n e^{jn\omega t}.$$

The voltage across the known resistance $\rho$ may be calculated from the following differential equation

$$\rho C(d/dt)\{V_0e^{j\omega t}-(1+r/\rho)V_{QA}\}+\rho I(t)=V_{QA}.$$

Assuming $V_{QA}$ can be expressed in a Fourier series, the solution is

$$V_{QA}=\rho\sum_n I_n e^{jn\omega t}\cdot\frac{1}{1+jCn\omega(r+\rho)}+j\frac{\rho C\omega V_0e^{j\omega t}}{1+jC\omega(r+\rho)}. \quad (1)$$

[7] K. Lehovec. J. App. Phys. **20**, 123 (1949).

FIG. 5. From the bottom: characteristics at 3, 15 and 30 cycles.

It is evident that for $\omega\to 0$ the voltage across $\rho$ is directly proportional to $I(t)$ and hence in that case gives the current through "$R$" directly. It is also clear from (1) that for $\omega\neq 0$ the capacitance $C$ gives rise to an "extra" capacitive current through $\rho$, leading to the second term in (1). This effect was compensated by Dekker and van Geel by using the branch $PBQ$, consisting of a variable capacitance $C'$ and a series resistance $\rho$ (equal to the one in the upper branch) in parallel with $PAQ$. Assuming that no current flows between $A$ and $B$, the following equation holds for $V_{QB}$

$$\rho C'(d/dt)(V_0e^{j\omega t}-V_{QB})=V_{QB}.$$

This leads to

$$V_{QB}=j\frac{\rho C'\omega V_0e^{j\omega t}}{1+jC'\omega\rho}. \quad (2)$$

It is evident that for $C'=C$ and $\rho\gg r$, the second term of (1) becomes equal to $V_{QB}$. Hence, by using a capacitance $C'$ equal to the capacitance of the rectifier, the voltage across $AB$ becomes

$$V_{AB}=\rho\sum_n I_n e^{jn\omega t}\frac{1}{1+jCn\omega\rho}\quad\text{for } r\ll\rho. \quad (3)$$

This expression shows that $V_{AB}$ gives a picture of $I(t)$ which is distorted in two ways: the phase of each component of the Fourier expansion is shifted and, besides, the higher terms are more suppressed than the first term. However, the hysteresis loop does not show any discontinuities or peaks and, hence, only a few terms of the expansion are of importance. Therefore, $V_{AB}$ will be approximately proportional to $I(t)$ if the condition $C\omega\rho\ll 1$ is fulfilled. For a given rectifier this condition puts a limit on the frequency range for which the method can be used.

The adjustment of $C'$ can be made simply by measuring the capacitance $C$ as indicated in Section III. A more convenient method of adjustment is the following: in the reverse direction $I(t)$ is practically zero for sufficiently low voltages. This means that $C'$ has to be so

adjusted, that $V_{AB}=0$ in the reverse direction. Both methods gave the same value for the compensating capacity within the experimental error.

It should be remarked that complete compensation of the second term in (1) may be obtained by using between $P$ and $B$ in addition to $C'$, a resistance equal to $r$ in series. This becomes mainly important at very high frequencies where $C\omega\rho$ becomes equal or larger than unity. There, however, the method breaks down for another reason given above. The effect of not using a compensation resistance for $r$ at high frequencies may be seen from (1): In the reverse direction, for $I(t)=0$, expression (1) yields

$$V_{QA}\simeq(1-r/\rho)V_0e^{j\omega t}, \quad \text{also} \quad V_{QB}\simeq V_0e^{j\omega t}.$$

Therefore, the voltage $V_{AB}$ in the reverse direction, instead of being zero and leading to a horizontal line for the characteristic, will now give rise to a line with slope $r/\rho$. This was confirmed by the experiments (Fig. 6) described in the next section.

## V. RESULTS

For investigations at frequencies below 60 cycles an oscillator of the Wien-bridge type, driving a push-pull amplifier with cathode-follower output, was built. Frequencies down to about one cycle/sec. with output of about 50 volts could be obtained with this apparatus.

Typical examples of characteristics at 2 and 3 cycles obtained with the circuit of Fig. 3 are given in Fig. 4. The rectifier consisted of an aluminum plate 50 cm² in area, oxidized in an ammonium-borate solution. The capacity of the rectifier was 0.80 $\mu$f. The resistances $\rho$ were both 50 ohms. The solution in which the characteristics were measured had a specific resistance of 76 ohm-cm, leading to a series resistance $r$ of about 0.5 ohm. Graphite counter-electrodes were used. For 3 cycles $C\omega\rho=8.10^{-4}$; hence (Section IV) the capacity has practically no influence on the shape of the loop obtained. The spot on the screen of the oscillograph follows the lower part of the loop for increasing forward voltage and returns along the upper part for decreasing forward voltage. This is in agreement with the results obtained by Dekker and van Geel at 50 cycles. In the reverse direction there is practically no current flowing and the characteristic becomes a straight horizontal line. The essential difference between Fig. 4 and the characteristic of a dry rectifier is of course the presence of the loop in the forward direction. These experiments show clearly that the loop is not due to a hysteresis in the capacity but arises from a time lag in the conduction mechanism. The characteristics are well reproducible if the formation voltage is applied for a short time before each photograph is taken.

At higher frequencies of, say 30 cycles, the following is observed: if no compensation capacity is used ($C'=0$ in Fig. 3), the characteristic in the reverse direction, instead of being a horizontal line, now "opens" up in a similar fashion as for a dry rectifier at high frequencies. This indicates that the effect is a consequence of the capacity $C$, and is confirmed by the fact that by using the circuit of Fig. 3 with $C'=C$, a straight line is again obtained in the reverse direction.

In Fig. 5 some results are shown for the plate at 3, 15 and 30 cycles. The effective voltage in each case was 34 volts. It will be noticed that the currents decrease with increasing frequency. This was observed also for other frequency ranges. The peak value of the current in the picture for 30 cycles in Fig. 5 corresponds to about 20 mA.

With increasing voltage, the general shape of the loop does not change. As a consequence of the non-linearity of the system, however, the peak value of the current increases more than linearly and the loop as a whole changes accordingly. The results of Dekker and van Geel gave a peak current approximately proportional to $V^{\frac{1}{2}}$. At higher voltages a loop in the reverse direction also becomes noticeable.

At high frequencies there is an advantage in using small plate area, since the capacity $C$ and hence the distortion of the characteristic will be reduced in this way. There is also the advantage that the currents flowing remain small and hence the internal resistance of the oscillator used does not lower appreciably the voltage in the forward direction. That this happens may be seen from Figs. 4 and 5. There is, however, the disadvantage of increasing $r$ and less sensitivity. As a consequence, compensation for $r$ as well as amplification of the signal $V_{AB}$ become necessary, unless the value of $\rho$ is increased.

Some examples of a series of characteristics obtained for a small strip of oxidized aluminum are given in

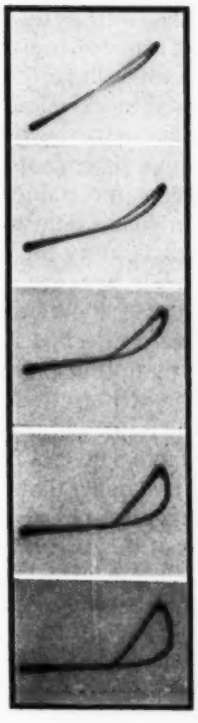

FIG. 6. Examples from a series of characteristics obtained with a small strip of oxydized aluminum. From the bottom: 20, 30, 150, 200, and 2000 cycles. No compensation for the series resistance was used in this case.

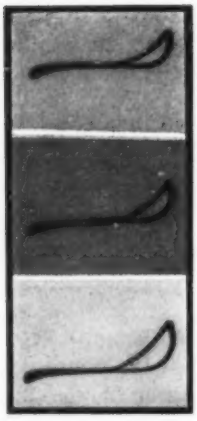

FIG. 7. Characteristics obtained for a strip of oxidized aluminum. From the bottom: 200, 300, and 400 cycles. In this case the series resistance of the electrolyte was compensated.

Fig. 6. The strip was oxidized to a formation voltage of 260 volts. Its capacity was 0.031 $\mu$f and the specific resistance of the solution was 76$\Omega$ cm. An effective voltage of 50 volts was used for all the photographs. Here again it is clear that the currents decrease with increasing frequency. Because only a capacity was used between $P$ and $B$ in Fig. 3, the effect of the series resistance $r$ shows clearly: the characteristic in the reverse direction is no longer horizontal, but has a slope increasing with frequency. That this is indeed due to $r$ may be seen from Fig. 7, where three pictures are shown obtained with a similar strip, but with a resistance to compensate for $r$ shunting the capacity $C'$.

## VI. DISCUSSION

The results obtained show definitely that the hysteresis loop is due to the conduction mechanism of the rectifying element "$R$" (Fig. 3). Therefore, any theory of the electrolytic rectifier should contain a mechanism that establishes a time lag between the current and the applied voltage. Logically, this time lag may either be caused by chemical changes in the layer which affect its conductivity, or, by processes of a physical nature that involve time, as, for instance, the building up of space charges in certain regions of the oxide.

In connection with the first possibility, experiments carried out by Störmer[8] are of interest. After preparing an oxide layer on an aluminum plate by anodic oxidation in an electrolytic solution, he applied a voltage in the forward direction for a certain length of time and used the plate thus prepared as a dry rectifier with aquadag as counter electrode. Störmer found that this treatment could improve the conductivity in the forward direction by factors up to a few hundred. He interprets his results by assuming that during the time that the forward voltage is applied to the plate in the solution, oxygen ions of the oxide are bound by hydrogen ions from the electrolyte. This leads to a semiconducting material with excess aluminum. This idea is compatible with experiments of Hartmann,[9] who found that aluminum oxide after certain heat treatments can become an excess semiconductor.

The chemical reduction, suggested by Störmer, seems the most reasonable explanation for the after effect referred to in Section II. For frequencies of the order of one cycle sec. or higher, however, it does not seem likely that changes of this type will occur and therefore the following "physical" interpretation of the hysteresis is tentatively put forward:

Suppose an aluminum plate is oxidized with a formation voltage of 300 volts. The thickness of the layer is then about 0.3 micron. For a voltage in the forward direction of, say, 30 volts, the field strength is about $10^6$ volts per cm and is of the same order as the breakdown voltages for many ionic compounds. Electrons entering the oxide from the metal side (forward voltage) are accelerated by the field and may reach sufficient energy to eject electrons from energy levels below the conduction band. In view of the fact that the thickness of the layer is large compared with the mean free path (about $10^{-7}$ cm), the same reasoning may be applied to the secondary electrons and thus a multiplication process takes place. As a consequence of this process, positive holes are created, the number of which will increase with the distance from the metal.

In connection with the nature of these holes, it is important to note that the color of the luminescence, observed under certain circumstances during the anodic oxidation, depends on the kind of impurities contained in the aluminum. It seems reasonable, therefore, to assume that in the oxide layer localized electron levels between the highest filled band and the conduction band are present.[10] Electrons ejected from these localized levels will leave immobile holes behind and give rise to a space charge. As a consequence of the multiplication process, the positive space charge density increases with increasing distance from the metal. Also, the field at the metal-oxide interface will be larger than without space charge. Therefore, when a constant forward voltage is applied to the rectifier, the current increases with time until a stationary state is established in which the number of holes produced equals the number of electrons trapped by the holes.

Suppose then that an a.c. voltage is applied across the layer and that no space charge is present initially. For small voltages in the forward direction, the electrons will not gain sufficient energy from the field to produce secondaries and the field will be constant throughout the layer. When, however, the voltage reaches a certain critical value, a space charge will be built up. This explains why the forward current remains small for low voltages and then increases rapidly in the neighborhood of the peak value. During the subsequent decrease of the forward voltage, a certain time is involved in neutralizing the space charge so that a time lag between current and voltage is established.

[8] R. Störmer, Zeits. f. Tech. Physik **16**, 508 (1935).
[9] W. Hartmann, Zeits. f. Physik **102**, 709 (1936).
[10] See S. Anderson, reference 4.

On the basis of the pre-breakdown mechanism suggested here, it is also clear that the currents should decrease with increasing frequency. This is in agreement with the experimental results.

At very low frequencies, the after effect becomes important. According to the results obtained, there seems to be a continuous transition from the hysteresis to the after effect.


## ACKNOWLEDGMENT

The authors wish to express their thanks to Dr. A. van der Ziel,* Physics Department of the University of British Columbia, Vancouver, British Columbia, Canada, for designing the oscillator for low frequencies and for many valuable and stimulating discussions.


* Now at the University of Minnesota, Minneapolis, Minnesota.

# Scheme for Analyzing Capillary Measurements on Non-Newtonian Liquids


ORRIN H. CLARK AND M. L. DEUTSCH

*Socony-Vacuum Laboratories, Research and Development Department, Paulsboro, New Jersey*



(Received January 12, 1950)



A powerful new scheme is presented for analyzing capillary flow measurements on non-Newtonian liquids. The basic disability of the capillary method, namely its inability to assign to a flow measurement any particular shear rate, or even a known range of shear rates, is overcome. This is accomplished by developing simple relations connecting the directly measured quantities, pressure and flow rate, with viscosity and shear rate. Application to Bingham bodies is easy and an illustration is given. Application to measurement at high rates of shear is immediate in principle, but there are certain allied measuring difficulties. These are discussed briefly. Finally, a simple approximate formula applicable to cases of moderate deviation from Newtonian behavior is given.


## I. INTRODUCTION

A POWERFUL new scheme is presented for analyzing the results of capillary flow measurements on non-Newtonian liquids. The classic capillary tube viscometer suffers from one intrinsic disability when applied to liquids whose viscosity varies with rate of shear. It can only measure flow corresponding to a complete range of shear rate, from zero to a maximum. Hitherto, there have been no satisfactory means of translating measurements over such a range into viscosity values at individual shear rates.[1] The present paper develops a simple method of obtaining the desired individual viscosity values from measurements of flow over a range of applied pressure.

## II. DEVELOPMENT OF ANALYSIS OF CAPILLARY FLOW MEASUREMENTS

The data obtainable from capillary flow measurements consist of values of volume flow rate corresponding to applied pressures, together with the geometric constants of the capillary tube. In the case of non-Newtonian liquids such data do not immediately reveal any information about viscosity, nor even about the range of shear rate which was applied. To obtain such information explicitly, it is necessary to develop a relation between the two measured variables, flow rate and pressure, on the one hand, and the desired variables, viscosity and shear rate, on the other.

The following symbols will be used: $Q$ = flow rate, volume per unit time; $P$ = applied pressure difference; $l$ = capillary length; $a$ = capillary radius; $r$ = radius of any annulus within the capillary ($0 \leq r \leq a$); $v$ = velocity of flow at any annular distance $r$; $S$ = rate of shear ($S = -dv/dr$); $\eta$ = viscosity.

The connection between viscosity and shear rate is immediately obtained from the differential equation appropriate to capillary flow, in which viscosity may vary with radius:

$$-Pr/l = d/dr[\eta r(dv/dr)]. \tag{1}$$

Integrating, noting that considerations of finiteness require the integration constant to be zero, and replacing $dv/dr$ by $-S$:

$$\eta = (Pr/2lS). \tag{2}$$

Specifically, at $r = a$ and for pressure $P$:

$$\eta(Pa) = [Pa]/[2lS(Pa)]. \tag{3}$$

Equation (3) gives the desired connection. However, the function, $S(Pa)$, is unknown in the case of non-Newtonian liquids. $S(Pa)$ is now obtained in terms of the (experimental) flow-pressure curve. The flow rate may be written:

$$Q = \int_0^a 2\pi r v dr. \tag{4}$$

An expression for $v$ is obtained by noting that

$$v = \int_a^r \frac{dv}{dr} dr = -\int_a^r S dr. \tag{5}$$

This involves the assumption $v = 0$ for $r = a$, i.e., there is no slippage at the wall.

[1] For example, see H. Green, *Industrial Rheology and Rheological Structures* (John Wiley and Sons, Inc., New York), Chapters 1–3.

It will be helpful to introduce two new variables, $\rho = Pr$, and $\rho_1 = Pa$. In a single experiment $\rho_1$ is constant but is variable when a range of pressure is considered. Now (4) becomes

$$Q = \frac{2\pi}{P^2}\int_0^{\rho_1} \rho v d\rho, \tag{6}$$

and (5) becomes

$$v = \frac{1}{P}\int_\rho^{\rho_1} S d\rho. \tag{7}$$

The last integral separates into two parts, one of which has constant limits.

$$v = \frac{1}{P}\int_0^{\rho_1} S d\rho - \frac{1}{P}\int_0^{\rho} S d\rho, \tag{8}$$

$$= (say) - \frac{1}{P}[A(\rho_1) - A(\rho)]. \tag{8a}$$

Introducing (8a) in (6):

$$Q = \frac{2\pi}{P^3}\left[\frac{\rho_1^2}{2}A(\rho_1) - \int_0^{\rho_1} \rho A(\rho) d\rho\right], \tag{9}$$

since $A(\rho_1)$ does not depend upon $\rho$. Differentiating (9) with respect to $\rho_1$, after placing $P = \rho_1/a$, we find

$$\frac{dQ}{d\rho_1} = -\frac{3}{\rho_1}Q + \frac{\pi a^3}{\rho_1}\frac{dA(\rho_1)}{d\rho_1}. \tag{10}$$

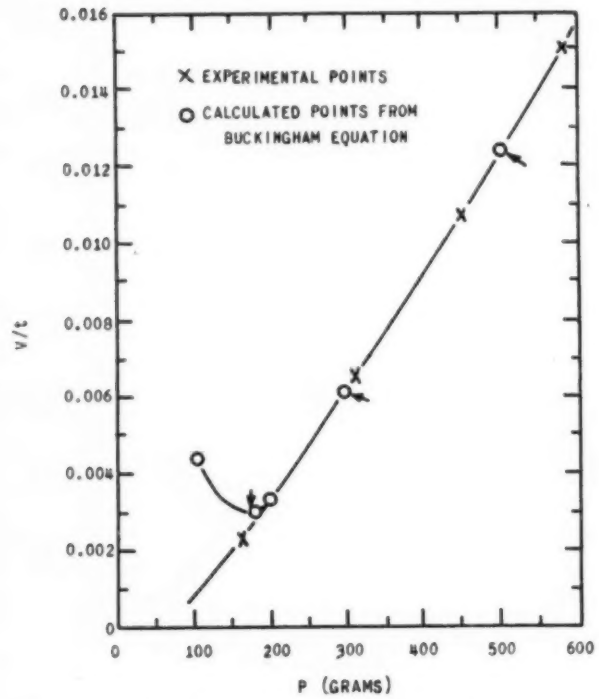


FIG. 1. Capillary flow data on a Bingham body. Reproduced by permission from *Industrial Rheology and Rheological Structures* by H. Green (John Wiley and Sons, Inc., New York, 1949).

Now noting the definition of $A(\rho_1)$,

$$dA(\rho_1)/d\rho_1 = S(\rho_1), \tag{11}$$

solving (10) for $dA(\rho_1)/d\rho_1$, and restoring the original variables we obtain

$$S(Pa) = 1/\pi a^3[3Q + P(dQ/dP)]. \tag{12}$$

Equation (12) specifies for any pressure $P$ the shear rate (at $r = a$) in terms of directly measured quantities. An expression for the viscosity corresponding to this shear rate was given in Eq. (3). A complete graph of viscosity against shear rate may be obtained merely by plotting flow against pressure, obtaining the slopes $dQ/dP$ at a number of pressures, and using Eqs. (3) and (12).

It will be noted that the shear rate given by (12) at each pressure is the maximum existing within the capillary tube, so that the range obtainable from the equations is the greatest possible, viscosity being obtained at the greatest shear rate in the liquid.

These results have great generality. It has been assumed there is no slippage at the wall. The only other limitation is implicit in Eq. (1), in which it is assumed that the applied pressure is opposed only by viscous forces, i.e., that there is no appreciable yield point or shear elasticity. This last restriction is easily removed. The yield stress bears a simple relation to the threshold pressure at which flow starts and is taken into account by a minor modification in the capillary flow equation. In the case of Bingham bodies the threshold pressure is not even required. This will be shown in the next section, which will serve to illustrate the method generally as well as the means of handling yield stress.

## III. APPLICATION TO BINGHAM BODIES

Bingham bodies are characterized by a definite yield point (denoted by $f$), viscosity being constant after flow starts. In this case (1) must be modified to include the yield stress.

$$-Pr/l + f = d/dr[\eta r(dv/dr)]. \tag{13}$$

Integrating, and taking $r = a$:

$$f = Pa/2l - \eta S, \tag{14}$$

with $S$ given by (12) as before. At the threshold pressure $S = 0$ and $f$ is obtained at once. In the case of Bingham bodies any two points on the flow-pressure curve suffice to determine $f$ and $\eta$; the constancy of $\eta$ may be verified by additional points.

An example is given using data on pigment-vehicle mixtures published by Green.[2] These are reproduced in Fig. 1. Pressure values of 200, 300 and 500 are selected. Sufficient accuracy will result from using direct differences in the table to obtain slopes, and the 300 to 500 difference will be used for pressures of 300 and 500

[2] See reference 1. Reproduced by permission.

both. Then:

$$P=200,\quad dQ/dP=0.0000289,\quad S=159,$$
$$P=300,\quad dQ/dP=0.0000315,\quad S=287,$$
$$P=500,\quad dQ/dP=0.0000315,\quad S=547.$$

Using the values for $P=200$ and $P=300$ in (14), and changing grams to dynes gives:

$$f=422 \text{ dynes/cm}^2,\quad \eta=3.92 \text{ poises}.$$

The check using points $P=300$ and $P=500$ yields the values:

$$f=428 \text{ dynes/cm}^2,\quad \eta=3.86 \text{ poises}.$$

## IV. HIGH RATES OF SHEAR

The extension of capillary flow measurements to high rates of shear encounters formidable measuring difficulties quite apart from the problem of variable shear rate which has been treated above. These difficulties arise from the necessity for high pressures and large amounts of internally developed heat, resulting in serious gradients in temperature and pressure within the capillary. Analysis of flow results including allowance for viscosity variation due to temperature and pressure effects is very difficult.

Since the starting point for the scheme just developed assumes the possession of true values of flow for given pressures, it apparently has no immediate application to these measuring difficulties. However, the development of an experimental technique for measurement at high shear rates has been pushed to an advanced stage at the Petroleum Refining Laboratory, Pennsylvania State College,[3] with the result that data are obtained which merit discussion from the viewpoint of analyzing the effect of variable shear rate.

Details of this experimental technique are not relevant to the discussion. It is sufficient to state that the method achieves the assignment of an "apparent viscosity" to each measured flow rate which is the viscosity of a Newtonian liquid producing the same flow rate at the same applied pressure. Approximate corrections for temperature and pressure effects have thus been incorporated in the apparent viscosity. For the purpose of comparative work the apparent viscosity is used directly to characterize the liquid.

If, however, a description of the fluid's non-Newtonian characteristic, i.e., its viscosity dependence upon shear rate, is desired, it is necessary to find means of assigning corresponding shear rates to the apparent viscosities resulting from capillary flow measurements. This is the very purpose for which the equations of Section II are designed. It is only necessary to translate the apparent viscosities into corresponding apparent flow rates by using Poiseuille's law. This will give the flow-pressure data needed and permit the construction of an explicit viscosity to shear rate relation.

[3] The authors are acquainted with this work through the courtesy of seeing the report to the American Petroleum Institute, P.R.L.-9-49, by Fenske, Klaus, and Dannenbrink.

TABLE I. Data for Fig. 1, experimental points.

| $P$ (g) | $V/t$ (cc/sec.) | $P$ | $V/t$ |
|---|---|---|---|
| 160.1 | 0.00230 | 100 calculated | 0.00443 |
| 307.9 | 0.00652 | 174 calculated | 0.00279 |
| 450.1 | 0.01084 | 200[a] | 0.00320 |
| 588.2 | 0.01513 | 300[a] | 0.00609 |
| 729.6 | 0.01963 | 500[a] | 0.01239 |

Radius of capillary, 0.031365 cm
Length of capillary, 3.162 cm

[a] Points taken on experimental curve for calculating $f$ and $\eta$.

It will be noted that no additional assumption is involved in applying Poiseuille's law to the apparent viscosities, for these are defined in terms of equivalence of flow rate.

A simplified procedure for assigning shear rates to the apparent viscosities is possible by introducing another Newtonian approximation. To the capillary flow in question there is assigned an effective shear rate defined as the shear rate effective in producing flow for Newtonian liquids. Thus:

$$\bar{S}=\frac{\int SdQ}{\int dQ}$$
$$=\frac{1}{Q}\int_0^a S2\pi rvdr$$
$$=\frac{1}{Q}\int_0^a \frac{Pr2\pi rP}{2l\eta 4l\eta}(a^2-r^2)dr$$
$$=(4/15)(Pa/l\eta). \qquad (15)$$

The validity of the approximation (15) will in general depend upon the magnitude of the deviation from Newtonian behavior. It should be noted, however, that in the case of the Petroleum Refining Laboratory work cited Eq. (15) constitutes an entirely satisfactory assignment of shear rate. It gives results agreeing within experimental error with those obtained by applying the method of Section II. However, one advantage does accrue from using the method of Section II; it makes possible the extension of the viscosity relation to substantially higher shear rates.

# Interpretation of Fracture Markings

J. A. Kies, A. M. Sullivan, G. R. Irwin
*Naval Research Laboratory, Washington, D. C.*
(Received March 23, 1950)

This paper presents a study of the sequence of events by which cracks "grow." A careful investigation was made of the origin, development, and characteristic pattern of level-difference markings left by rapidly moving fractures in a wide variety of materials. Characteristic markings indicating discontinuous propagation are found in fractures of plastics, polycrystalline and single-crystal materials, coal, mica, photographic film from which the emulsion was stripped, etc. Thus, the continued occurrence of essentially discontinuous initiations which comprise fracturing becomes clear. These considerations are sufficient to explain a number of well known fracture markings and to clarify what is mean by brittleness and fracture velocity.

## INTRODUCTION

THE detailed markings on fracture surfaces of metals, plastics, and ceramics show many common characteristics. A number of these are illustrated and reviewed in this paper for the purpose of showing what one may infer from these markings concerning the growth and propagation of fracturing.

## LEVEL DIFFERENCES

De Freminville,[1] Preston,[2] and others have called attention to the importance of fracture level differences and crack directions as indicators of the stress pattern in glass. The mechanism by which level differences arise has been given relatively little attention. A comparative study of metals, transparent crystals, plastics, and glass, etc., sheds new light on this mechanism.

A disconnected initiation beyond the crack head is well illustrated by Fig. 1. This shows an aluminum foil under dead weight loading. The fracture is propagated by joining a sequence of holes originating at widely separated points. T. W. George and others at NRL have shown this to be the rule in the fracture of ductile foils.

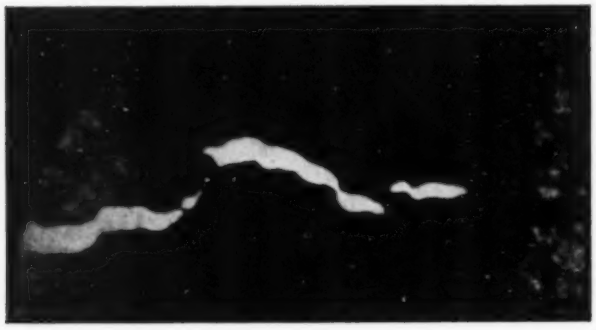

Fig. 1. (×15) Creeping fracture backlighted in 0.002-in. thick 2S aluminum foil (after T. W. George). The specimen had been under dead load for 30 days. The propagation consisted of the opening up of advance pinholes in severely strained regions followed by a joining process in which each subsidiary fracture spread backwards as well as forwards. Some such microfractures were not included in the joining process.

For the purpose of studying fracture markings in thick specimens, lucite serves as a convenient model. Figure 2 shows the fracture surface of a Lucite plate, $\frac{1}{16}$-in. thick, broken in tension. One finds that the areas separated by the parabola-like lines are at different levels. Thus, these lines owe their visibility to the existence of sharp changes in level and may be termed "level-difference lines." More details of this are shown in Fig. 3 at higher magnification. Usually there is a barely resolvable pit or hole at the focus surrounded by a circular zone of high specular reflectivity. The streamers radiating from the focus and trailing off in the direction of the crack propagation are the boundaries of various sublevels within the parabola. It can be shown that the point of origin of the fracture of fractures making up the parabola was at or very near the the focus. Similar details can be found on finer and finer scale to the limit of resolution of the ordinary microscope. This leads to the inference that all level-difference lines or edges, especially those leading in the direction of fracture can be associated with separate initiations of fracture.

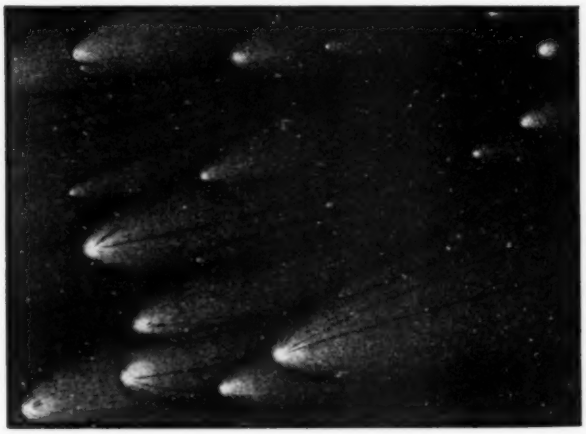

Fig. 2. Parabolic figures on the fracture surface of a Lucite plate (×75). Direction of crack propagation: Left to right. Each parabola outlines the area included in an individually initiated subsidiary fracture. The lines are visible becaues of differences in level. .

[1] Ch. de Freminville, "Caractères des Vibrations Accompagnant le Choc Déduits de l'Examen des Cassures," Rev. de Metallurgie 4, 833 (1907). "Recherches sur la Fragilité: L'Eclatement," Rev. de Metallurgie 11, 971 (1914).

[2] F. W. Preston, "A study of the rupture of glass," J. Soc. Glass Tech. X, 234 (1926).

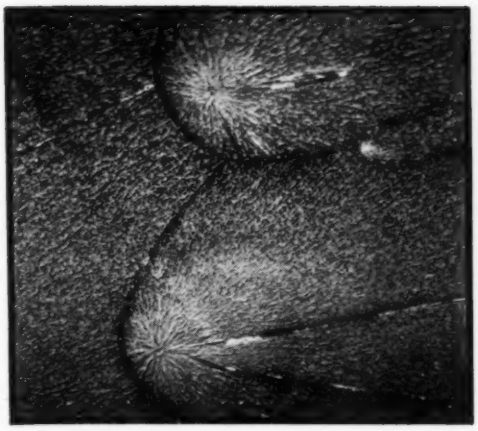

FIG. 3. Enlarged view of the foci of a group of parabolas from the preceding figure (×250). Satisfactory proof exists that fracture elements were initiated at the foci.

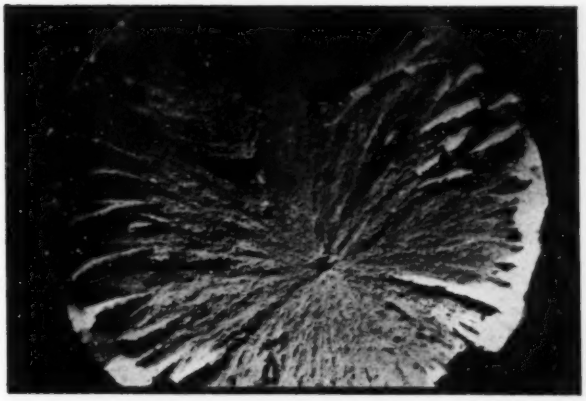

FIG. 4. (×7.5) Parabola head complete with focal pit and streamers on the fracture surface of a fine grained steel tensile bar. The vertex of the parabola points toward the spot where the main fracture first initiated. (Courtesy, Dr. W. Harris.)

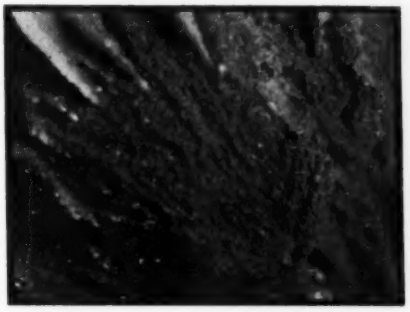

FIG. 5. (×20) Enlarged view of the parabola shown in the preceding figure. At the focus is a small crater with sheared conical walls. The weakening influence presumably within the pit is not revealed.

The structural components of the parabola in lucite have individual analogs within the comparable portions of the cup-cone fractures in ductile steel. Figure 4 shows a fracture in a tensile bar, kindly supplied to us by Dr. W. J. Harris of the NRL Metallurgy Division. The main fracture originated at the lower right and at a later time another prominent weakness at another level gave rise to a similar process starting from the focus of the parabola occurring at the upper left of center. Note that the parabola in the steel, Fig. 5, at higher magnification has a volcano-like focal crater indicating shearing at the focus. This is better illustrated in Fig. 6. Surrounding the shear is a bright granular area with streamers analogous to the pattern of Fig. 3 in Lucite. This area in the steel surrounding the focus also resembles the "mirror" in a glass fracture. Inasmuch as a granular appearance on a fracture in steel has been associated with high speeds of fracturing and low energy absorption, one may conclude that the toughest part of this fracture element was at the focus and that, once some shearing was completed, the subsequent development occurred far more rapidly. The sharp transition back to a more ductile appearance may be explained by reasoning that, at least locally, the fast fracture entailed a sudden expenditure of stored elastic energy and sudden stress relieval. This resulted in a slowing down or momentary hesitation of the crack front.

## SCALLOPED LEADING EDGE

In order to establish the time sequence of events in the generation of parabola-like figures and conchoidal markings, microscopic observations were made during the progress of fracture in cellulose acetates and in a large crystal of KBr. In the case of cellulose acetate two photographs, Figs. 7 and 8, serve to show the positions of the main crack at the instants of halt or very slow propagation in response to a controlled relieval of the force exerted on the knife blade used to propagate the crack. The arrow points to the focal spot of a parabola-like figure and at the second position new parabola heads have been created within the outline of the original one.

The leading edge was deeply scalloped with a succession of finer and finer scallops superimposed on the principal ones. Each main scallop was the leading edge of a parabola-like fracture element within which could be found an individual point of initiation.

In the case of the fracture in KBr a razor blade was forced into the material by a steady motion of a screw. In this case the scalloped leading edge of the crack more or less following a cleavage plane was essentially the same in appearance as in cellulose acetate. The main scallops were observed to progress with a rapid succession of pulses and halts self-controlled by the specimen.

Conchoidal fractures are all produced in this way except that the fracture surface is not constrained to follow a natural cleavage. It is important to recognize that such discontinuous propagation generally involves many, not just one, transitions in mode from fast to slow. During slow stages more time is allowed for plastic flow, hence a conchoidal fracture or more generally any brittle but pulsating fracture may involve local ductile

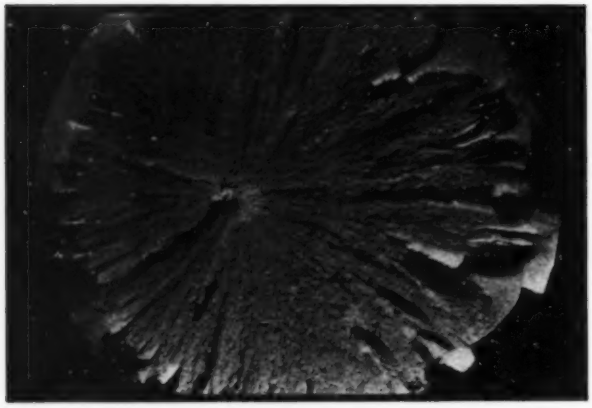

FIG. 6. (×7.5) The sector at the left was formed by radial crack propagation and corresponds to the parabolas of the preceding figures. A micro flaw is presumed to have been located at the focal pit lying within the volcano-like sheared structure. A small granular area surrounding the volcano suggests fast fracture at the expense of a local quick release of elastic energy. This was followed by slower more fibrous fracture at a somewhat lower mean stress. (Specimen supplied by Dr. W. Harris.)

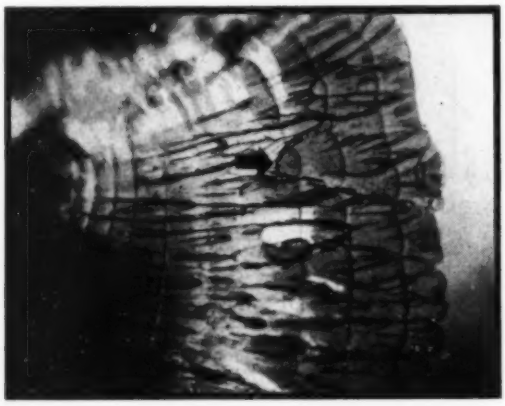

FIG. 7. (×50) A fracture, traveling to the right, viewed within cellulose acetate. Note the well formed parabola head with focal point. A chisel is being forced into the material but the crack is momentarily halted. Note the lagging crack front at points where the level changes.

behavior. Klier has recently shown examples of this in ferrite.[3]

## CHEVRON MARKINGS

The chevrons or herringbone in ship plate are easily modeled. Figure 9 shows an example of a tearing fracture in cellulose acetate. The concentration of gross fracture centers is greatest near the centerline. The fracture front obviously led at the center and lagged at the surface. However, chevrons need not point toward the origin of the running crack, provided the edges of the fracture can be made to lead. Figure 10 shows a plate of cellulose acetate in which side scratches promoted reverse herringbone.

[3] E. P. Klier, "A study of cleavage surfaces in ferrite," Pennsylvania State College, Mineral Industries Expt. Station, Final Report to ONR, October 15, 1948–1949.

Although the chevron pattern was widely considered to be indicative of brittle and therefore unsatisfactory behavior of the ship plates in failed merchant vessels, it should be understood that a considerable amount of plastic deformation was present. Tipper has pointed out that shearing was in evidence along the lines sometimes called herringbone.[4] More generally these are level-difference lines where the fracture lagged and hesitated. The final joining up of the levels by spreading towards one another involved the initiation of a new fracture front with an initially slow and therefore relatively ductile stage.

Our association here of high energy absorption with slowness of crack propagation rested partly upon the microscopic observations previously mentioned in connection with the fracture initiation foci within parabola heads in various materials. Such an association was thoroughly demonstrated on a grander scale by numerous dead loading and other more common experiments on various metal foils and plates of plastics in which central slots or scratches served to locate the beginning of fracture. In these experiments the work absorbed per unit length of crack was plotted against propagation speed and crack length. Invariably the initial or creeping stages of the crack growth required a rate of energy input several orders of magnitude higher than later, faster stages. This has been discussed by Irwin[5] and forms the main basis for his statement of the necessary and sufficient conditions for the onset of instability or the transition from ductile to brittle fracture.

## GEOMETRICAL FIGURES

It is easy to show that simple geometrical figures on fracture surfaces are to be expected as a result of the interference between neighboring fracture elements.

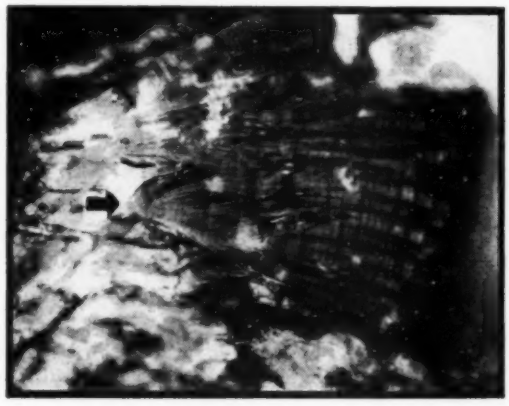

FIG. 8. (×50) An advanced stage of the fracture, traveling to the right, shown in Fig. 7. The sides of the main parabola are greatly developed and newer, smaller parabolas have been created within the main one.

[4] C. F. Tipper, "The fracture of mild steel plate," Report No. R3, Admiralty Ship Welding Committee, London, 1948.

[5] G. R. Irwin, "Fracture dynamics," "Fracturing of metals," Am. Soc. Metals, 147 (1948).

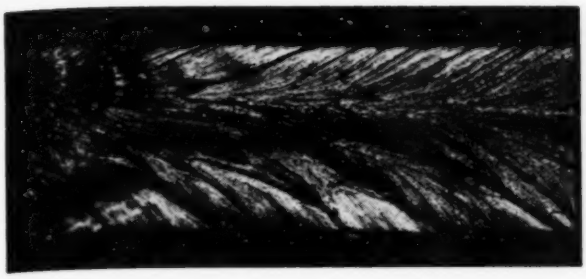

FIG. 9. (×50) Herringbone or chevron fracture produced in a cellulose acetate plate. The fracture propagation was left to right. The heads of parabolas are clearly shown as concentrated at the center of the plate thus showing centrally located but discontinuous initation and propagation to be the reasons for such markings. The scalloped crack front was generally normal to the sides of the parabolas. Note that some figures become rapidly divergent and have hyperbolic outlines. This is due to local speed effects.

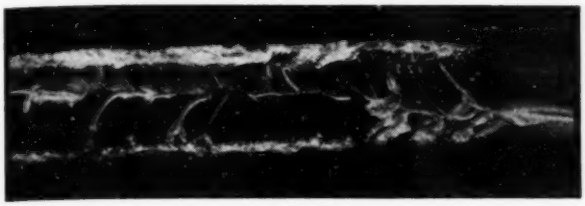

FIG. 10. (×7.5) Reversed chevrons or herringbone fracture in a cellulose acetate plate. Side scratches promoted initiation near the plate surface rather than in the center. As the fracture proceeded from left to right the fracture led at the surface and lagged in the middle contrary to normal chevrons in ship plate. Parabola heads are present but too small to be seen at this magnification.

For example, a rectilinearly propagating crack with a straight line front and a radially propagating crack with a circular front both in the same plane will meet on a conic section. If the velocities are equal, the figure is a parabola. If the circular- or disk-shaped crack is the slower, an ellipse will result. An example of this is shown in Fig. 11. A slight level difference for the two fractures makes the figure easily visible. In any case a relatively slow element will be surrounded and stopped by its faster neighbors. The ensiform tips in Fig. 11 thus represent extinctions of fracture elements. These are also junction points in river systems to be mentioned later. A hyperbola-like figure is to be expected as the boundary of a fast fracture element if it spreads more rapidly than its neighboring fracture elements. Such an outline is suggested at several places in Fig. 9.

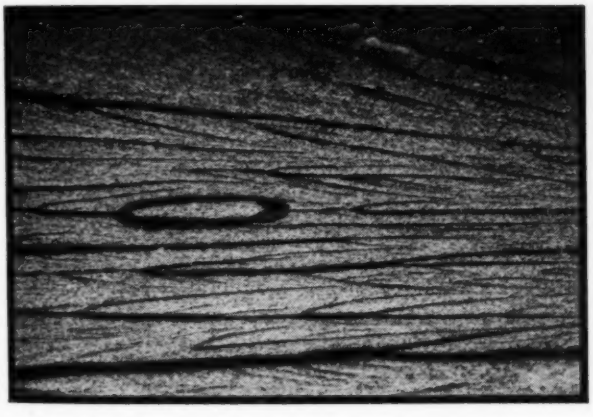

FIG. 11. (×50) Fracture surface in cellulose acetate created by a crack traveling right to left at 0.01 in./sec. Note the elliptical figure swept out by a fracture element which was engulfed and cut off by surrounding elements which ran ahead. Each ensiform tip is the trailing end of a fracture element which was crowded out by faster adjoining elements. Parabola heads are too small to show at this magnification.

River systems result from the consolidation of level differences as the faster elements shoot ahead and stop the slower ones. Many such examples have been shown without this explanation in publications by Zapffe and others.[6] A large scale example of river systems is shown in Fig. 12. This is a face spall in steel armor. The rod-shaped pieces lying within the overlap of neighboring fracture elements are often thrown off as fragments designated (in French) by De Freminville as "stries". A complete understanding of the origin of these shards and the separate fracture elements creating them cannot be gained by the observation of fractures in glass and hardened steel alone since in these materials the scale of events is too fine or is obscured by crystallinity. In plastics, however, each tributary of a river system can be seen to be a level difference between fracture elements originating from separate initiation points or operative flaws. In general, only one limb of the parabola-like figure associated with each initiation persists with enough level difference to be noted as a tributary in the system. The flaw-like nature of these initiations is demonstrated by Fig. 13 in which the boundaries of poorly molded particles of Lucite provide many such points for fracture initiation. Such examples lead to the inference that operative flaws play a promi-

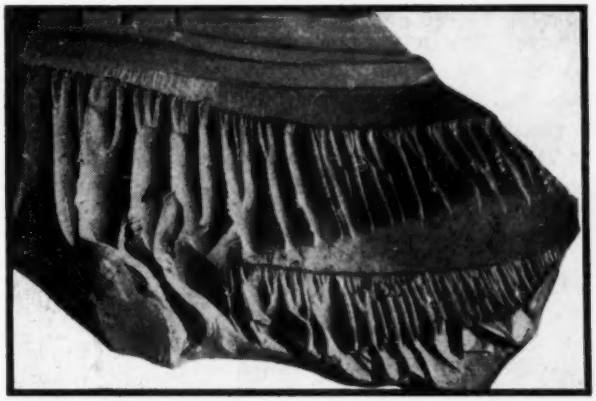

FIG. 12. (×.5) Face spall in 4-in. thick Class *A* armor. The fracture initiated at the top of the picture. Note the banded structure with repeating river systems. Each tributary marks a difference in level between adjoining components of the fracture. Tributaries converge because some fracture elements were too slow to compete. Each band edge is a position of the crack front at an instant of hesitation in the propagation.

[6] C. A. Zapffe and F. K. Landegraff, "Fractographic examination of tungsten," Am. Soc. Metals 41, 396 (1949).

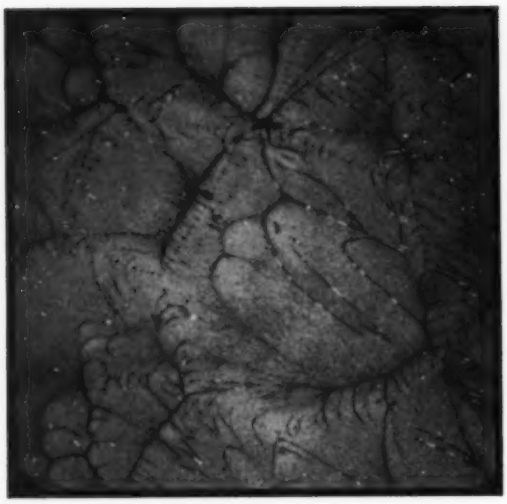

FIG. 13. (×250) "Grain boundary" weakness in imperfectly molded Lucite.

FIG. 14. (×50) Multiplicity of fracture initations contributing to a high speed shattering fracture in Lucite. The star-like components have spread more or less concurrently so that a system of honeycomb boundaries separates the components lying at slightly different levels. There is no evidence of a main crack front here. The presence of such a system is enough to insure low ductility and low $dw/dx$.

nent role in the propagation of fractures in all materials showing gross fracture patterns of the kinds described here.

## EXPLOSIVE FRACTURE

The conditions of propagation as modified by high overstress can be indicated by the system of star-like fracture components shown in Fig. 14. Each one resembles the star in a tensile fracture of steel. Their independence of the main fracture results in their circular form. The regions between the initiations were evidently encroached on by many spreading fractures and thus little opportunity for plastic action was permitted. It is conceivable that operative flaws, e.g., lattice imperfections or dislocations, may be created anywhere in any solid material provided that there is sufficient time and an appropriate set of stresses. It follows that any material, however tough in static tests, can be made to fracture in a brittle manner provided that many flaws become operative simultaneously. This condition is readily achieved in suitable explosion tests of steel plate and hollow vessels. In such cases the over-all or apparent fracturing consists of many widely separated fractures joining together in more or less orderly sequence.

## CONCLUSIONS

In conclusion, it may be stated that:

(1) The propagation of fracture is, in carefully observed cases, essentially and generally discontinuous and consists of the joining up of multitudes of separately initiated components of fracture.

(2) The more brittle the substance, the more striking are the effects of speed variations in creating markings usually called clam shell or conchoidal. Speed differences between components are responsible for the flowing together of markings resembling river systems and for the creation of geometrical patterns visible as parabolas, ellipses, and hyperbolas.

(3) Chevron or herringbone markings on ship plate may be explained on the basis of centrally concentrated gross initiation coupled with a centrally leading but scalloped crack front. Some initiations may be far in advance of the main crack and backwards propagation must occur locally.

(4) The transition from slow to moderately fast but not explosive fracture in hardened steel is accompanied by finer and finer scaled elements initiating closer and closer to the leading edge of the main crack as the local velocity of propagation increases. Fewer and fewer main elements persist with individually smoother faces.

(5) The over-all velocity of propagation of a crack is governed by the rate and distance at which advance initiations can occur and the rapidity with which subsidiary multiple fractures can be joined up. Many component joinings may occur simultaneously. This may be described as explosive fracture.

(6) In cases of high speed fractures traveling in high stress fields, the great number of fracture elements operating simultaneously tends to produce a condition in which the material in the path of the oncoming crack is permeated by multitudes of local stress raisers and flow restricters. Material surrounded by initiating fractures is subjected to a condition similar to that in a sharply notched tensile impact bar. Low ductility is a consequence.

The authors gratefully acknowledge the help and cooperation received from the following: Dr. W. Harris of the NRL Metallurgy Division, who supplied us with the tensile fractures in steel. Mr. C. Hauver, Head of the Photographic Section, Mechanics Division, NRL, who prepared some of the photographs. Messrs. H. L. Smith and W. J. Ferguson of the Mechanics Division, NRL, who performed many necessary fracture experiments contributing to this report. Dr. W. H. Sanders, Consultant, Mechanics Division, NRL, who assisted by editorial criticism and advice.

# Letters to the Editor

## An Absolute Measurement of Copper-Copper Interfacial Free Energy

G. W. Sears
*General Electric Research Laboratory, Schenectady, New York*
March 31, 1950

It has been proposed by Smith[1] that the dihedral angles formed by three intersecting grain and phase boundaries are determined by a simple mechanical balancing of the interfacial tensions. He presented a mass of evidence to substantiate his assumption. On this basis he measured the ratio of copper(solid)-copper(solid) to copper(solid)-lead(liquid) interfacial free energies to be 0.59 from measurements of the dihedral angles formed at the junction of a pair of copper grains with liquid lead.

Following a suggestion of Fisher[2] the equilibrium angles at the edges of liquid lead drops equilibrated on a copper single crystal at high temperature were studied in an attempt to obtain an absolute value for the copper(solid)-lead(liquid) interfacial free energy and in conjunction with Smith's data an absolute value of the copper grain boundary free energy.

Outgassed cylinders of OFHC copper were polished on one end. The samples were placed polished side up in a hydrogen atmosphere and dusted lightly with lead powder. The specimens were heated for 8 hr. at 800°C.

After cooling, the samples were plated with 0.012 in. of copper. The specimens were cross-sectioned and polished normal to the lead-covered surface. The polished face was given a light dichromate etch and examined at 500× with a Bausch and Lomb metallograph.

After measuring approximately 500 dihedral angles at the edge of lead drops, it was established that they had distorted upon solidification while cooling to room temperature.

At the suggestion of W. Schockley it was assumed that shape of the drops remained undistorted upon solidification. On this basis the angles were calculated from measured lengths and thicknesses of the lenticular lead drops. The preliminary results on these measurements yield angles consistent with the random cross sectioning of lenticular drops normal to their median planes and having constant dihedral angles at their edges. Recent high temperature microscopic studies have independently confirmed Shockley's suggestion.

A preliminary value of 510 ergs/cm² has been obtained for the copper(solid)-lead(liquid) interfacial free energy. In addition a value of 720 ergs/cm² for the copper(solid)-lead(vapor) surface free energy was found. This differs from the value of 1370 ergs/cm for the copper(solid)-copper(vapor) surface free energy measured by Udin, Shaler, and Wulff.[3]

In conjunction with Smith's data a copper(solid)-copper(solid) interfacial free energy of 860 ergs/cm² has been determined. This represents the first absolute measurement of a solid-solid interfacial free energy to be reported in the literature.

[1] C. S. Smith, Met. Tech., T.P. 2387 (1948).
[2] J. C. Fisher, Met. Tech., T.N. 1 (1948).
[3] Udin, Shaler, and Wulff, J. Metals 1, 762 (1949).

## Limiting Negative Pressure of Water

Lyman J. Briggs
*National Bureau of Standards, Washington, D. C.*
February 20, 1950

At the 1949 meeting of the National Academy of Sciences in Washington I presented the results of some measurements, by a new method, of the limiting negative pressure of water. Improvements in technique have since led to values higher than those provisionally reported.[1] In particular, the investigation of the effect of temperature has disclosed a remarkable 10-fold change in the limiting negative pressure of water between 0° and 6°C.

The liquid under examination by this method is held in a capillary tube *open at both ends*. About 1 cm from each end the tube is bent back upon itself through an angle of 140° to form a Z. After thorough cleaning the tube is cemented (with thinned Duco) symmetrically to the web of a spinner of I-beam cross section. The spinner is mounted at its center on the upper end of the vertical shaft of a high speed three-phase induction motor, driven by a variable-speed motor-generator, equipped with an electric tachometer.

The motor and spinner are enclosed in a cylinder 25 cm in diameter, fitted with soft rubber gaskets at both ends and resting on the base supporting the motor. A tempered glass plate closes the top. When operating, the internal air pressure is reduced to 3 or 4 cm Hg.

The capillary tube spins in its Z plane, which is horizontal and is so mounted that its *center intersects the projected spin axis*. Consequently, the liquid column at this point is visible even at high angular speeds. The breaking of the column is signalized by a marked change in the refraction of the tube.

When the liquid under examination is an electrolyte, the rupture of the column can also be conveniently detected in the following way. A strip of filter paper 3 cm wide is cemented by its edges to the inside of the cylinder at the height of the spinner. Over this a continuous strip of open-mesh metal gauze 2.5 cm wide is cemented by its edges to the filter paper. The gauze and cylinder are connected in series with a 135-v $B$ battery and a 25-v voltmeter. Normally the voltmeter shows no deflection. But the instant the column breaks and the electrolyte is thrown against the filter paper, a strong kick on the voltmeter is observed. In working with pure water, the filter paper is first activated by moistening with a solution of NaCl and then dried.

In the centrifugal field, one-half of the liquid column is pulling against the other. If one meniscus is nearer the spin axis than the other when the motor starts, it immediately retreats and the other advances until equilibrium is restored. The maximum stress is at the center. If $L$ is the measured distance between the menisci in the bent legs of the tube, the effective length of the column is $r=L/2$.

The force exerted on any element of liquid in the column of length $dx$ is $a\rho\omega^2 r\,dx$, where $a$ is the cross section in cm², $\rho$ is the density of the liquid, and $\omega$ is the angular velocity in radians per second. Integrating, from 0 to $r$, $F=\frac{1}{2}\rho\omega^2 r^2$ dynes/cm². The nega-

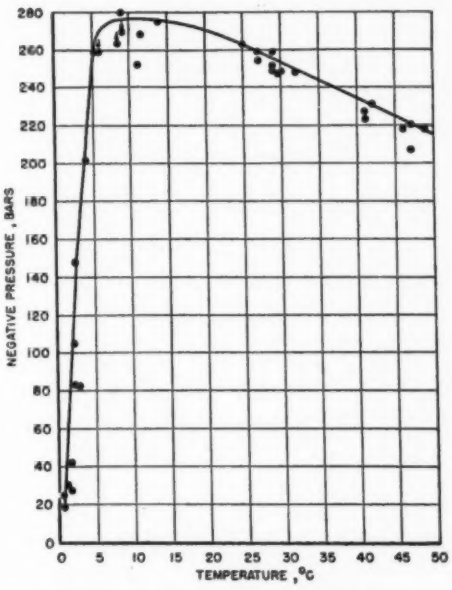


Fig. 1. The limiting negative pressure of water between 0° and 50°C.

tive pressure is given in bars (1 bar $=10^6$ dynes/cm$^2$ $=0.987$ standard atmosphere).

Scrupulous cleanliness is necessary in the measurement of negative pressure. The open-ended tube possesses a great advantage in being easy to clean and fill. To aid in these operations, the open ends of the tube project about 3 mm beyond the side of the supporting spinner.

The results of the measurements are presented in graphical form in Fig. 1. Points with arrows mean that the water column was subjected to the indicated negative pressure without rupture. It will be noted that the negative pressure is greatest (277 bars) around 10°C and decreases as the temperature is increased to 50°C. This decrease was expected, for at the critical temperature the negative pressure must be zero. The temperature coefficient from 25° to 50°C is about $-2$ bar/°C.

Between 5° and 0°C, the limiting negative pressure of water undergoes an enormous change, dropping to less than 10 percent of the maximum value. It presents another anomaly in the behavior of water in this interesting region. It cannot be accounted for by the change in density alone, for the density of water at 0° is only 0.00013 less than at 4°C; whereas a decrease in density of 0.009 occurs in raising the temperature of water from 25° to 50°C, which is accompanied by a change of only 20 percent in the limiting negative pressure.

The negative pressure measurements given in Fig. 1 are believed to be correct within three percent (one percent for $\omega$ and 0.5 percent for $L$). The temperatures corresponding to high values of the negative pressure are somewhat uncertain. The work done by the spinner on the residual gas in the chamber progressively raised its temperature and it is not known how closely the glass-enclosed liquid at the center of the column follows the temperature of the gas. Further measurements by a modified method are in progress.

The distilled water used in these measurements cannot be said to be air-free. The container from which the capillary tube was to be filled was completely immersed in distilled water and boiled vigorously. Inasmuch as the solubility of air in water decreases as the temperature is increased, it is assumed that the residual air in the boiled water was in a state of true solution at the lower temperatures at which the experiments were carried out.

Finally it must be emphasized that with this method we cannot tell whether the rupture of the column originates on the wall of the capillary (loss of adhesion) or in the body of the liquid (loss of cohesion). Strictly speaking, the measurements reported should be considered as applying to boiled water in a Pyrex glass capillary 0.6–0.8 mm internal diameter.

A fuller account of this work with additional data will appear in the *Journal of Research of the National Bureau of Standards*.

[1] Science **109**, 440 (1949).

## The Effective Permeability of Iron Dust Particles

LEONARD LEWIN
*Standard Telecommunication Laboratories, Ltd., Enfield, Middlesex, England*
March 30, 1950

IN a recent paper on attenuators,[1] Theodore Miller quoted a formula on loaded materials from my paper "The electrical constants of a material loaded with spherical particles."[2]

As he says that the radii of the particles do not enter into the formula, I think there must have been some misunderstanding of the symbols I have employed, since the formula certainly contains the particle radius, although it is not shown explicitly.

The formula for the permeability, $\mu_m$ of the mixture is

$$\mu_m=\mu_b\left(1+\frac{3f}{(\mu_p+2\mu_b)/(\mu_p-\mu_b)-f}\right),$$

where $\mu_b$ is the permeability of the binder, usually unity, $\mu_p$ is the effective permeability of the particles at the frequency under consideration, and $f$ is the volume ratio of particles to total volume.

The trouble arises over $\mu_p$, which is *not* the permeability of the material from which the particles are made. If we call this latter permeability $\mu_2$, then $\mu_p=\mu_2$ only when the radius of the particle is so small that the field completely penetrates the article. The general relation is

$$\mu_p=\mu_2F(\theta)$$

where

$$F(\theta)=\frac{2(\sin\theta-\theta\cos\theta)}{(\theta^2-1)\sin\theta+\theta\cos\theta}\simeq 1+\frac{\theta^2}{10}+\frac{9\theta^4}{700}\text{ for }\theta\text{ small},$$

and $\theta=ka(\mu_2K_2)^{\frac{1}{2}}$, $k=2\pi/\lambda$ ($\lambda$ is the free-space wave-length in cm), $a$ = particle radius in cm, $K_2$ = complex permittivity of the particle material. For a metal $K_2=-j60\lambda\sigma$, where $\sigma$ is the conductivity in mho/cm. If the particle radius is much greater than the skin depth this gives $\mu_p=-j(\lambda/\pi a)(\mu_2/K_2)^{\frac{1}{2}}$, which is much smaller than $\mu_2$. The general agreement which Miller obtains between theory and experiment probably points to the particle size being small enough for the approximation $F(\theta)\simeq 1$ to be used in most cases. The discrepancies actually recorded correspond to a value of $F$ less than 1, which is in agreement with the formula for $F$, since $\theta^2$ is negative for the values of the constants used.

[1] Theodore Miller, J. App. Phys. **20**, 878 (1949).
[2] L. Lewin, J. Inst. Elec. Eng. **94**, 64 (1947).

## Magnetically Controlled Wave-Guide Attenuators

THEODORE MILLER
*Electronics and Nuclear Physics Department, Westinghouse Research Laboratories, Pittsburgh, Pennsylvania*
April 7, 1950

I WISH to thank Mr. Lewin for bringing to my attention an erroneous impression which I unwittingly created in a reference to his article which appeared in my paper "Magnetically controlled wave-guide attenuators."[1] I did not mean to imply that Mr. Lewin did not include the radii of particles in his general derivation for the effective permeability of a dielectric loaded with spherical particle, but rather that my application of his formula did not involve the radii.

Mr. Lewin's formula for the permeability of a loaded dielectric $\mu_m$ is[1]

$$\mu_m=\mu_b\left[1+\frac{3f}{(\mu_p-2\mu_b)/(\mu_p-\mu_b)-f}\right],$$

where $f$ is the volume ratio of particles to total volume, $\mu_d$ is the permeability of dielectric, and $\mu_p$ is the high frequency permeability of the particles.

In his paper, Mr. Lewin relates the permeability of iron particles with the wave-length through an equation involving the particle radii, the conductivity, and the low frequency permeability of the iron material. However, since there was considerable uncertainty as to what values to assign to the conductivity and low frequency permeability of the iron material, it was decided to use Kittel's[3] value for the high frequency permeability of a thin film (2.5$\mu$ thick) instead of applying Mr. Lewin's equation which in part reads

$$\mu_p=\mu_2F(\theta),$$
$$\theta=ka(\mu_2K_2)^{\frac{1}{2}},$$
$$K_2=-j60\lambda\sigma$$

where $\mu_2$ is the permeability of iron material, $\sigma$ is the conductivity, $a$ is the radii of iron particles, and $k=2\pi/\lambda$.

[1] Theodore Miller, J. App. Phys. **20**, 878 (1949).
[2] Leonard Lewin, J. Inst. Elec. Eng. **94**, 64 (1947), Eq. (11).
[3] C. Kittel, Phys. Rev. **70**, 281 (1946).

# A Note on the Error Coefficients of a Servo Mechanism

JOHN L. BOWER
*Department of Electrical Engineering, Yale University, New Haven, Connecticut*
March 24, 1950

IN a linear servo system, it is convenient to be able to relate the error to the various disturbances on the system, the primary one of which is the input, $\theta_i$. For a system initially at rest, one can write the following expression for that part of the error due to $\theta_i$:

$$\epsilon(t)=\int_0^\infty d\lambda w(\lambda)\theta_i(t-\lambda). \tag{1}$$

The weighting function, $w(\lambda)$, is the inverse transform of the familiar transfer function relating the error to the disturbance, $\theta_i$. For all physical systems, it includes a delta-function of order zero and of unit amplitude at the origin. If we assume $\theta_i$ to be a function which is differentiable through order $n$ for all $\lambda$ up to some $\lambda_d$, then we can write Maclaurin's formula for $\theta_i(t-\lambda)$ as a function of $\lambda$:

$$\theta_i(t-\lambda)=\theta_i(t)-\lambda\theta_i'(t)+\tfrac{1}{2}\lambda^2\theta_i''(t)+\cdots\frac{(-\lambda)^{n-1}}{(n-1)!}\theta_i^{(n-1)}(t)+R_n,\quad 0<\lambda<\lambda_d. \tag{2}$$

Here, $R_n$ will be given the form,

$$R_n=\frac{(-\lambda)^n}{n!}\theta_i^{(n)}(t-\Delta\lambda)\text{ where }0<\Delta<1\text{ and }0<\lambda<\lambda_d. \tag{3}$$

We use the form $\theta_i^{(r)}(t-\lambda)$ to designate the $r$th derivative of $\theta_i$ with respect to the bracketed quantity. By inserting the identity (2) into (1), we have immediately an expression for error in terms of the derivatives of the input, $\theta_i$, evaluated at $t$:

$$\epsilon(t)=C_0\theta_i(t)+C_1\theta_i'(t)+\frac{C_2}{2}\theta''(t)+\cdots\frac{C_{n-1}}{(n-1)!}\theta_i^{(n-1)}(t)+\frac{K_R}{n!}+K_d \tag{4}$$

where

$$C_r=\int_0^{\lambda_d}d\lambda(-\lambda)^r w(\lambda); \tag{5}$$

$$K_R=\int_0^{\lambda_d}d\lambda(-\lambda)^n\theta_i^{(n)}(t-\Delta\lambda)\cdot w(\lambda);$$

$$K_d=\int_{\lambda_d}^\infty d\lambda w(\lambda)\theta_i(t-\lambda). \tag{6}$$

It is obvious that the above series is most useful only when the last two terms are small enough to be neglected in the computation of $\epsilon(t)$. If the first $m$ derivatives of the input are known to exist over all time, if the $m$th derivative is bounded by $\pm M$, and if $m$ is sufficiently large that the corresponding remainder is negligible, we can represent the error by use of the coefficients up through $C_{m-1}$. The conditions here make for a simple calculation of the remainder, since $\lambda_d=\infty$, $K_d=0$, and

$$|K_R|\leq M\int_0^\infty d\lambda\lambda^m|w(\lambda)|. \tag{7}$$

Such a case as this might arise, for example, where the $m$th derivative is a stationary time series. The matter of evaluating the coefficients from (5) can be handled simply if the transfer function $H(s)$ relating the error to the input is known, for by definition of $w(\lambda)$,

$$H(s)=\int_0^\infty d\lambda\epsilon^{-s\lambda}w(\lambda). \tag{8}$$

By differentiating $r$ times with respect to $s$, and taking $s$ to zero in the result, we have

$$\left.\frac{d^rH(s)}{ds^r}\right|_{s=0}=\int_0^\infty d\lambda(-\lambda)^r w(\lambda)=C_r,\text{ for }\lambda_d=\infty. \tag{9}$$

These steps are clearly valid for any stable system, since its transfer function, $H(s)$, must be analytic in the neighborhood of the origin. The expression (9) places the coefficients of the power series in the familiar form shown in textbooks.[1] The inverses of $C_0$, $C_1$, and $C_2/2$, respectively, are referred to as the position-, velocity-, and acceleration-error coefficients of the servo.

For the ordinary rational fractional forms of $H(s)$ with simple poles, an upper limit for (7) can be obtained easily. We note that

$$\int_0^\infty d\lambda\lambda^m|w(\lambda)|=\left|\frac{d^m}{ds^m}\int_0^\infty d\lambda\epsilon^{-s\lambda}|w(\lambda)|\right|_{s=0}. \tag{10}$$

An upper bound for this quantity can be obtained by making a partial-fraction expansion of $H(s)$, substituting magnitudes of residues for the residue coefficients and replacing the poles by their real parts, after which the differentiation in $s$ is performed and $s$ is taken to zero. The result, placed in (7), is

$$K_R\leq M\int_0^\infty d\lambda\lambda^m|w(\lambda)|\leq Mm!\sum_{k=1}^N\frac{|a_k|}{(R\alpha_k)^{m+1}}, \tag{11}$$

where the $\alpha_k$ are the locations of the $N$ poles of $H(s)$, whose real parts are indicated by $R\alpha_k$, and whose residues are $a_k$. The form of (11) shows the tendency to weight most heavily the poles nearest the origin when $m$ is large. For the usual servo these poles will be close to the real axis, which circumstance will make this bound on $K_R$ approximate the value $M|C_R|$.

The series (4) may be useful even though the derivatives of sufficient order for application of the above method do not exist over all time. If the $n$th derivative fails at some $\lambda_d$ which is sufficiently large that $K_d$ from (6) is known to be small, and if (7) and (9) are good approximations for $K_R$ and $C_r$, respectively, we can proceed as in the earlier case.

It might be mentioned that the above relations are valid for servo systems whose weighting functions, $w(\lambda)$ vary with time, $t$, as a parameter, in such a way that the law of superposition applies for each value of $t$.

[1] See James, Nichols, and Phillips, *Theory of Servomechanisms* (McGraw-Hill Book Company, Inc., New York, 1947), p. 147.

---

# Erratum: Radiofrequency Mass Spectrometer

[J. App. Phys. 21, 143 (1950)]
WILLARD H. BENNETT
*National Bureau of Standards, Washington, D. C.*

FIGURE 12 of this article was improperly provided with a mass number scale which should have been as shown below.

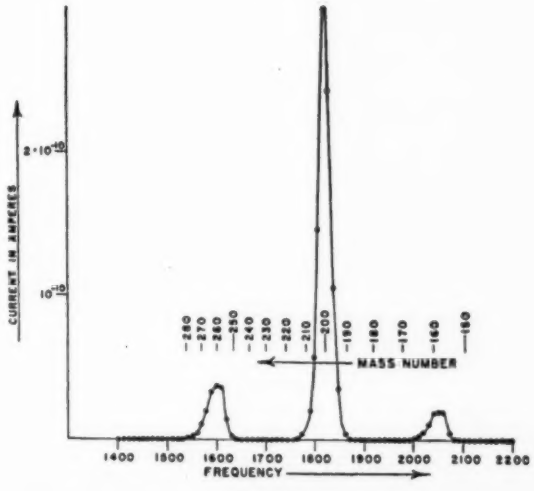


FIG. 12.

## The Use of Critical Point Phenomena in Preparing Specimens for the Electron Microscope*

THOMAS F. ANDERSON
*Johnson Research Foundation, University of Pennsylvania, Philadelphia, Pennsylvania*
April 21, 1950

A SERIOUS handicap in the use of the electron microscope has been the fact that specimens must be dried before they can be examined in the high vacuum of the instrument. Delicate biological specimens are particularly susceptible to damage by the force of surface tension which flattens and sometimes disrupts them in the last stages of evaporation of the suspending medium. We report here a technique which eliminates the passage of a phase boundary through the specimen while it is being dried. After the specimen has been fixed, its water is replaced by alcohol, and the alcohol replaced in turn by each of a series of miscible liquids, the last in the series being one which has a conveniently low critical temperature. The temperature of the specimen in a bomb completely filled with the latter liquid is then raised above the critical point where the liquid changes imperceptibly into a gas. Then the gas is allowed to escape at the higher temperature leaving behind a dried specimen through which no phase boundary has passed. As a result, specimens like the hemolysed human red cells shown in the stereoscopic pair of electron micrographs of Fig. 1 retain their round shapes when dried in this way rather than being pressed flatly against the supporting Formvar membrane by the tension in the surface of an evaporating water droplet as they would have been in the conventional method of mounting specimens.

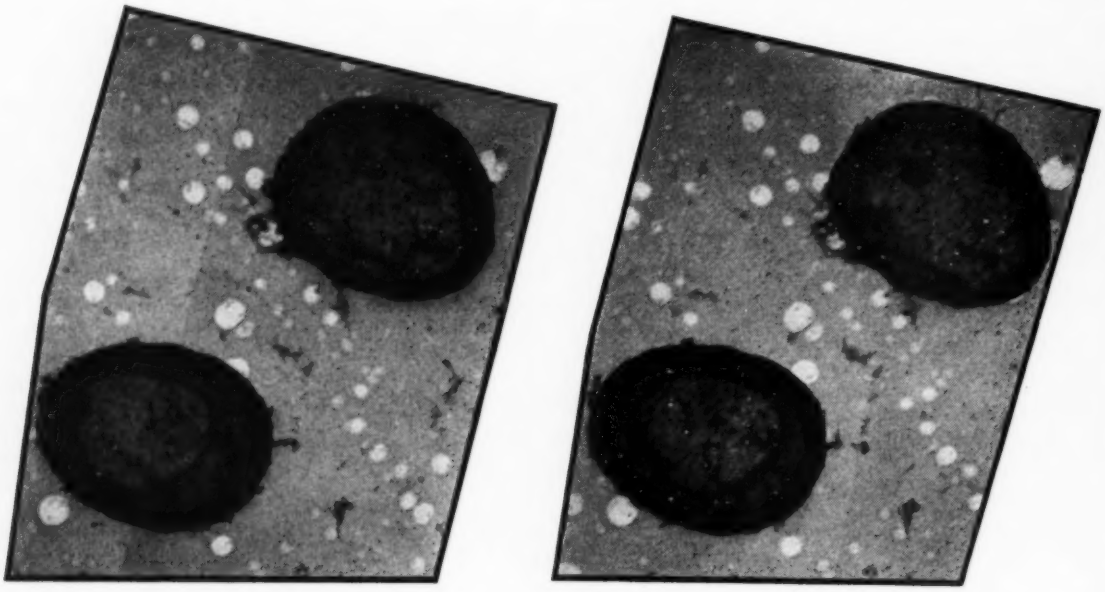

FIG. 1. Stereoscopic pair of micrographs of hemolysed red cells. Whole blood was diluted 1:10 in physiological saline, and the hemoglobin removed from the cells by the addition of an equal volume of water. A droplet of the hemolysed cells was then placed on a Formvar-coated specimen screen, fixed in osmic acid vapor, taken through alcohol to amyl acetate and then to liquid nitrous oxide in a pressure bomb at 25°. The temperature was then raised to 45° and the now gaseous nitrous oxide allowed to escape. The hollow "ghosts" of the cells may be seen adhering to the Formvar membrane.

* This work was supported by Contract N6 ori 168 T.O. II between the ONR and the Trustees of the University of Pennsylvania, and the Government is hereby granted royalty-free right of reproduction of this article.

## International Congress on Electron Microscopy at Paris, September 14–22, 1950

A preliminary announcement has been received in this country concerning the above meeting. The following information has been abstracted from this announcement:

1. The Congress will include Sections on Electron Optics and Microscopes, Electron Diffraction, Metallurgical Applications, Chemical Applications, and Biological Applications as well as an Exhibition devoted to "The Microscope" and an Exhibition of the work of those attending.
2. The official language will be French but papers may be presented in English.
3. Titles and abstracts of papers should be submitted by June 1st to the General Secretary of the Congress, M. Locquin, Lab. de Cryptogamie, 12 rue de Buffon, Paris 5°, France.
4. The manuscripts of papers should be submitted by August 1st. The Congress reserves to itself the right to publish such manuscripts unless it has given a written release to the contrary.

Further details may be obtained from C. J. Burton, American Optical Company, Southbridge, Massachusetts.